JSCSEN 90(9) 1015-1146(2025)

ISSN 1820-7421(Online)

Journal of the Serbian Chemical Society

Electronic version

VOLUME 90

No 9

BELGRADE 2025

Available on line at

www.shd.org.rs/JSCS/

The full search of JSCS is available through

DOAJ DIRECTORY OF OPEN ACCESS JOURNALS

www.doaj.org

The **Journal of the Serbian Chemical Society** (formerly Glasnik Hemijskog društva Beograd), one volume (12 issues) per year, publishes articles from the fields of chemistry. The **Journal** is financially supported by the **Ministry of Education, Science and Technological Development of the Republic of Serbia.**
Articles published in the **Journal** are indexed in **Clarivate Analytics products: Science Citation Index-Expanded™** – accessed *via* **Web of Science®** and **Journal Citation Reports®**.
Impact Factor announced on 28 June, 2023: **1.000; 5-year Impact Factor**: **1.100**.
Articles appearing in the **Journal** are also abstracted by: **Scopus, Chemical Abstracts Plus (CAplus℠), Directory of Open Access Journals, Referativnii Zhurnal (VINITI), RSC Analytical Abstracts, EuroPub, Pro Quest** and **Asian Digital Library.**

Publisher:	**Serbian Chemical Society**, Karnegijeva 4/III, P. O. Box 36, 1120 Belgrade 35, Serbia tel./fax: +381–11–3370–467, E-mails: **Society** – shd@shd.org.rs; **Journal** – jscs@shd.org.rs Home Pages: **Society** – http://www.shd.org.rs/, **Journal** – http://www.shd.org.rs/JSCS/
Internet Service:	Contents, Abstracts and full papers (from Vol 64, No. 1, 1999) are available in the electronic form at the Web Site of the **Journal** (http://www.shd.org.rs/JSCS/).
Former Editors:	**Nikola A. Pušin** (1930–1947), **Aleksandar M. Leko** (1948–1954), **Panta S. Tutundžić** (1955**–**1961), **Miloš K. Mladenović** (1962–1964), **Đorđe M. Dimitrijević** (1965–1969), **Aleksandar R. Despić** (1969–1975), **Slobodan V. Ribnikar** (1975–1985), **Dragutin M. Dražić** (1986–2006).
Editor-in-Chief:	BRANISLAV Ž. **NIKOLIĆ**, Serbian Chemical Society (E-mail: jscs-ed@shd.org.rs)
Deputy Editor:	DUŠAN **SLADIĆ**, Faculty of Chemistry, University of Belgrade
Sub editors:	
Organic Chemistry	DEJAN **OPSENICA**, Institute of Chemistry, Technology and Metallurgy, University of Belgrade JÁNOS **CSANÁDI**, Faculty of Science, University of Novi Sad
Biochemistry and Biotechnology	OLGICA **NEDIĆ**, INEP – Institute for the Application of Nuclear Energy, University of Belgrade
Inorganic Chemistry	BILJANA **GLIŠIĆ**, Faculty of Science, University of Kragujevac
Theoretical Chemistry	MATIJA **ZLATAR**, Institute of Chemistry, Technology and Metallurgy, University of Belgrade MILOŠ **MILIČIĆ**, Faculty of Chemistry, University of Belgrade
Physical Chemistry	LJILJANA **DAMJANOVIĆ-VASILIĆ**, Faculty of Physical Chemistry, University of Belgrade
Electrochemistry	SNEŽANA **GOJKOVIĆ**, Faculty of Technology and Metallurgy, University of Belgrade
Analytical Chemistry	RADA **BAOŠIĆ**, Faculty of Chemistry, University of Belgrade
Polymers	BRANKO **DUNJIĆ**, Faculty of Technology and Metallurgy, University of Belgrade
Thermodynamics	MIRJANA **KIJEVČANIN**, Faculty of Technology and Metallurgy, University of Belgrade
Chemical Engineering	TATJANA **KALUĐEROVIĆ RADOIČIĆ**, Faculty of Technology and Metallurgy, University of Belgrade
Materials	RADA **PETROVIĆ**, Faculty of Technology and Metallurgy, University of Belgrade
Metallic Materials and Metallurgy	ANA **KOSTOV**, Mining and Metallurgy Institute Bor, University of Belgrade
Environmental and Geochemistry	VESNA **ANTIĆ**, Faculty of Agriculture, University of Belgrade
History of and Education in Chemistry	DRAGICA **TRIVIĆ**, Faculty of Chemistry, University of Belgrade
English Language Editors:	LYNNE **KATSIKAS**, Serbian Chemical Society VLATKA **VAJS**, Serbian Chemical Society JASMINA **NIKOLIĆ**, Faculty of Technology and Metallurgy, University of Belgrade
Technical Editors:	VLADIMIR **PANIĆ**, Institute of Chemistry, Technology and Metallurgy, University of Belgrade, MARIO **ZLATOVIĆ**, Faculty of Chemistry, University of Belgrade
Journal Manager & Web Master:	MARIO **ZLATOVIĆ**, Faculty of Chemistry, University of Belgrade
Office:	VERA **ĆUŠIĆ**, Serbian Chemical Society

Editorial Board
From abroad: **R. Adžić**, Brookhaven National Laboratory (USA); **A. Casini**, University of Groningen (The Netherlands); **G. Cobb**, Baylor University (USA); **D. Douglas**, University of British Columbia (Canada); **G. Inzelt**, Etvos Lorand University (Hungary); **J. Kenny**, University of Perugia (Italy); **Ya. I. Korenman**, Voronezh Academy of Technology (Russian Federation); **M. D. Lechner**, University of Osnabrueck (Germany); **S. Macura**, Mayo Clinic (USA); **M. Spiteller**, INFU, Technical University Dortmund (Germany); **M. Stratakis**, University of Crete (Grecce); **M. Swart**, University de Girona (Cataluna, Spain); **G. Vunjak-Novaković**, Columbia University (USA); **P. Worsfold**, University of Plymouth (UK); **J. Zagal**, Universidad de Santiago de Chile (Chile).
From Serbia: **B. Abramović**, **V. Antić**, **R. Baošić**, **V. Beškoski**, **J. Csanadi**, **Lj. Damjanović-Vasilić**, **A. Dekanski**, **V. Dondur**, **B. Dunjić**, **M. Đuran, B. Glišić, S. Gojković**, **I. Gutman**, **B. Jovančićević**, **I. Juranić**, **T. Kaluđerović Radiočić**, **L. Katsikas**, **M. Kijevčanin**, **A. Kostov**, **V. Leovac**, **S. Milonjić**, **V.B. Mišković-Stanković**, **O. Nedić**, **B. Nikolić**, **J. Nikolić**, **D. Opsenica**, **V. Panić**, **M. Petkovska**, **R. Petrović**, **I. Popović**, **B. Radak**, **S. Ražić**, **D. Sladić**, **S. Sovilj**, **S. Šerbanović**, **B. Šolaja**, **Ž. Tešić**, **D. Trivić**, **V. Vajs, M. Zlatović**.

Subscription: The annual subscription rate is **150.00 €** including postage (surface mail) and handling. For Society members from abroad rate is **50.00 €**. For the proforma invoice with the instruction for bank payment contact the Society Office (E-mail: shd@shd.org.rs) or see JSCS Web Site: http://www.shd.org.rs/JSCS/, option Subscription.
Godišnja pretplata: Za članove SHD: **2.500,00 RSD**, za penzionere i studente: **1000,00 RSD**, a za ostale: **3.500,00 RSD**:za organizacije i ustanove: **16.000,00 RSD**. Uplate se vrše na tekući račun Društva: **205-13815-62**, poziv na broj **320**, sa naznakom "pretplata za JSCS".

Nota: Radovi čiji su svi autori članovi SHD prioritetno se publikuju.
Odlukom Odbora za hemiju Republičkog fonda za nauku Srbije, br. 66788/1 od 22.11.1990. godine, koja je kasnije potvrđena odlukom Saveta Fonda, časopis je uvršten u kategoriju međunarodnih časopisa (**M-23**). Takođe, aktom Ministarstva za nauku i tehnologiju Republike Srbije, 413-00-247/2000-01 od 15.06.2000. godine, ovaj časopis je proglašen za publikaciju od posebnog interesa za nauku. **Impact Factor** časopisa objavljen 2024. godine je **0,700**, a petogodišnji **Impact Factor 0,900**. **Journal Citation Indicator** časopisa za period 2020–2024 je **0,16**.

Journal of the Serbian Chemical Society
JSCS-info@shd.org.rs • www.shd.org.rs/JSCS

J. Serb. Chem. Soc. Vol. 90, No. 9 (2025)

CONTENTS*

Published by the Serbian Chemical Society
Karnegijeva 4/III, P.O. Box 36, 11120 Belgrade, Serbia
Printed by the Faculty of Technology and Metallurgy
Karnegijeva 4, P.O. Box 35-03, 11120 Belgrade, Serbia

* For colored figures in this issue please see electronic version at the Journal Home Page: http://www.shd.org.rs/JSCS/

Journal of the Serbian Chemical Society
JSCS-info@shd.org.rs • www.shd.org.rs/JSCS
J. Serb. Chem. Soc. 90 (9) 1015–1025 (2025)
JSCS–5436
Original scientific paper
Published 30 September, 2025

Synthesis of poly(itaconic acid) and its application for synthesis of pyrrolinones as a reusable homogeneous catalyst

PARYA HAMDI MOHAMADABAD, DAVOOD SETAMDIDEH* and FATEMEH GHANBARY

Department of Chemistry, Mahabad Branch, Islamic Azad University, Mahabad, Iran

(Received 27 August 2024, revised 6 January, accepted 1 August 2025)

Abstract: In this context, poly(itaconic acid) (PIA) was synthesized through the polymerization of itaconic acid in the presence of $K_2S_2O_8$ and NaH_2PO_4, achieving satisfactory yields of 80 % within 48 h at 55 °C. The PIA served as a homogeneous catalyst in MeOH for the synthesis of pyrrolin-2-ones from aromatic aldehydes, anilines and dimethyl acetylenedicarboxylate (DMAD). The reactions proceeded efficiently, yielding excellent results with conversion rates of 90–95 % within 8 h at room temperature. The synthesized products were characterized by combustion analysis (CHN), ^{1}H-NMR, ^{13}C-NMR and FT-IR spectra. This method is eco-friendly and aligns with the principles of green chemistry.

Keywords: poly(itaconic acid); pyrrolin-2-ones; green chemistry; homogeneous catalyst.

INTRODUCTION

Polymer catalysts are useful for performing chemical reactions. Polymer catalysts are polymers that possess catalytically active sites. Typically, these active moieties are incorporated into the polymer chains. Examples include the asymmetric Diels–Alder reaction catalyzed by a helical polymer (optically active),[1] the preparation of N-methylated compounds from alcohols and urea from carbamates or CO_2 fixation by copper nanoparticles on triazine–triamine as a porous organic polymer[2] and epoxidation reactions by [Cu(H_2btec)(bipy)] as a metal––organic polymer catalyst.[3] Other examples are the epoxidation of olefins by a one-dimensional polyoxomolybdate polymer,[4] cascade carbon–carbon bond-forming reactions by CBAP-1(EDA-SO_3H) as a dual-functionalized porous organic polymer[5] and the acetalization of carbonyl compounds with alcohols by a hierarchical porous organic polymer.[6] Additionally, examples include a pro-

* Corresponding author. E-mail: dsetamdideh@iau.ac.ir; davood.setamdideh@gmail.com
https://doi.org/10.2298/JSC240827058M

moted Suzuki reaction using palladium chloride anchored on a polymer,[7] the synthesis of biomass-derived alkyl levulinates by a sulfonic acid-functionalized organic polymer[8] and a one-pot multistep organic transformation by a tri-functional covalent triazine and carbonyl-based polymer.[9] To continue our investigation into the application of DOWEX, a cross-linked copolymer functionalized to act as a heterogeneous catalyst,[10] we have decided to explore the catalytic properties of poly(itaconic acid) (PIA). Because, a comprehensive review of the chemical literature indicates that the catalytic potential of PIA remains unexplored to date. PIA was originally synthesized directly from itaconic acid (IA) by Marvel and Shepherd in 1959.[11] The PIA is a major component in some chemical material such as magnetite nanocomposites[12] and hydrogels[13] (as adsorbent materials), self-assembled clay-polyelectrolyte hydrogels,[14] gelatin-based films (antimicrobial-active food packaging),[15] superabsorbent (a polymer network for application in concrete as an internal curing agent),[16] encapsulator of PCMs (the phase change materials),[17] hydrogels (for human pluripotent stem cell culture),[18] electrospun nanofibers[19] and highly stable fluorescent polymer.[20] In this context, PIA was synthesized using a modified method from IA in the presence of $K_2S_2O_8$ and NaH_2PO_4.

On the other hand, literature surveys indicate that the preparation of pyrrolinone derivatives has been of considerable synthetic interest, driven by the moiety's significant biological activity in numerous natural products and pharmaceutical compounds.[21]

Building on our experience in synthesizing pyrrolin-2-ones,[21] we evaluated the catalytic properties of PIA through the synthesis of these classes of compounds, as illustrated in Scheme 1.

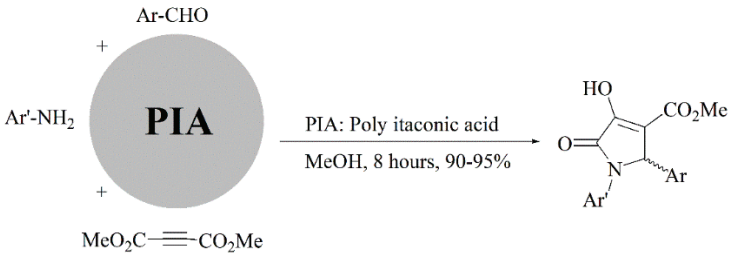

Scheme 1. The synthesis of pyrrolin-2-ones by poly(itaconic acid) as a homogeneous catalyst in MeOH.

EXPERIMENTAL

All substrates and reagents were obtained from Sigma-Aldrich Company. FT-IR spectra were recorded using a PerkinElmer FT-IR RXI instrument. ^{1}H- and ^{13}C-NMR spectra were obtained on Bruker spectrometers operating at 250, 300 and 400 MHz frequencies. Gel permeation chromatography (GPC) experiments were conducted on an Agilent 1100 series system. The monitoring of reaction progress was performed using Merck silica gel 60 F_254

aluminum sheets. The mass spectra were recorded using a Agilent 5973N spectrometer at 70 eV. The elemental analysis was performed on the LECO-TruSpec elemental analyzer (CHN, USA). Additionally, ^{1}H-NMR spectroscopy and combustion analysis were utilized to assess the purity of the synthesized products.

Synthesis of the poly(itaconic acid)(PIA)

A 250 mL flask, equipped with a magnetic stirrer and condenser, was used. An aqueous solution was prepared consisting of itaconic acid (20 g, 153 mmol), sodium dihydrogen phosphate (NaH_2PO_4, 10 g, 83 mmol), and potassium persulfate ($K_2S_2O_8$, 0.2 g, 0.739 mmol) in 100 mL of H_2O. This solution was stirred at a temperature of 55 °C for 48 h. After this, the solution was gradually added to acetone. The PIA was precipitated out of the solution and was then collected through filtration and redissolved in water. This was followed by reprecipitation from acetone, and then the precipitate was dried under reduced pressure. The PIA was obtained as a white powder, with a yield of 80 % or 16 g.

*A typical procedure: The synthesis of 1,5-diphenyl-3-hydroxy-4-methoxycarbonyl-3-pyrrolin--2-one (**1a**) in the presence of the PIA as a homogeneous catalyst in MeOH*

A mixture of benzaldehyde (0.106 g, 1 mmol), aniline (0.93 g, 1 mmol) and PIA (0.2 g) was prepared in a 25 mL round-bottomed flask using 5 mL of methanol. This mixture was stirred at room temperature for 30 min using a magnetic stirrer. After that, dimethyl acetylenedicarboxylate (DMAD, 0.142 g, 1 mmol) was added to the reaction mixture. The reaction was monitored by thin layer chromatography (TLC) using an ethyl acetate/*n*-hexane solvent system (1:1 ratio) and completed within 8 h. Following the completion of the reaction, the precipitate was filtered and washed with distilled water (3×5 mL). The product was then purified through crystallization from ethanol (which was dried over anhydrous sodium sulfate). The corresponding pyrrolin-2-one was obtained in an excellent yield of 90 % (0.28 g) as a white powder with a melting point range of 182–183 °C (180–182 °C[21]). The product was characterized using by combustion analysis (CHN), ^{1}H-NMR, ^{13}C-NMR and FT-IR spectra. The corresponding data are given in the Supplementary material to his paper.

Additionally, PIA was recovered from water by the addition of acetone, achieving a yield of 95 % (0.19 g). In this procedure, water was initially evaporated using a laboratory rotary evaporator, leaving behind 12–13 mL of water. This method was employed to minimize acetone usage.

RESULT AND DISCUSSION

Marvel *et al.* synthesized poly(itaconic acid) from itaconic acid using potassium persulfate ($K_2S_2O_8$) and hydrochloric acid (HCl, 0.5 M), achieving low yields of 35 %.[11] To improve this process, several methods have been published, and the results of these modifications have been summarized in Table I.

The PIA was synthesized following the protocol outlined by Marvel *et al.* (entry 2, Table I), with modifications (entry 1, Table I) as presented in Scheme 2. The polymerization process was conducted at 55 °C to prevent decarboxylation. The new conditions provide several benefits, such as the ready availability of reagents, safer handling, and increased yield, along with reduced processing times compared to some existing protocols.

The PIA obtained was characterized by an FT-IR, ^{1}H-NMR and GPC spectra. In the FT-IR spectrum of itaconic acid (Fig. 1), bands appear at 3027

cm^{-1} (attributed to =C–H stretching vibration), 1636 cm^{-1} (attributed to C=C stretching vibration) and 913 cm^{-1} (attributed to =C–H bending vibration). These absorptions were not present in the PIA spectrum, indicating successful synthesis of the polymer. It is important to note that although the acid has the potential to form polyester by creating ester bonds, the stretching band for the C=O in the FT-IR spectrum of PIA (Fig. 1B) appeared at 1717 cm^{-1}, which does not align with the expected stretching band for C=O esters in the range of 1735–1750 cm^{-1}. Therefore, it can be concluded that polyester formation does not occur under these conditions.

TABLE I. Synthesis of poly(itaconic acid) (PIA) by different protocols from itaconic acid (IA)

Entry	Reagents	*t* / °C	Time, h	Yield / %	Reference
1	IA (77 mmol in 50 mL H_2O), $K_2S_2O_8$ (2.9 % in H_2O), NaH_2PO_4 (9 % in H_2O)	55	48	80	Current work
2	IA (145 mmol), $K_2S_2O_8$ (0.37 mmol), HCl (0.5 M, 50 mL)	50	68	35	11
3	IA (38.5 mmol), $K_2S_2O_8$ (0.92 mmol), $K_2S_2O_5$ (1.1 mmol), HCl (0.1 M, 50 mL)	25	72	70	22,23
4	IA (770 mmol), NaOH (31 g, in 50 mL H_2O), *tert*-butyl hydroperoxide (0.5 mL, 70 %)	80	1	90	24
5	IA (39 mmol, in 25 mL H_2O), $(NH_4)_2S_2O_8$ (2 mmol), choline chloride (0.91 g)	55	48-96	50-62	25
6	IA (20 mmol), choline chloride (20 mmol), $(NH_4)_2S_2O_8$ (1 mmol in 0.36 ml of distilled water)	110/1 h 65/2 h	3	80	26

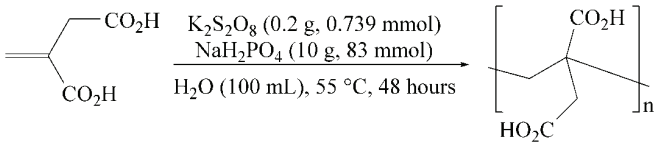

(20 g, 153 mmol) (16 g, yield: 80%)

Scheme 2. The polymerization of the itaconic acid (IA) to the poly(itaconic acid) (PIA).

The ^{1}H-NMR spectrum for poly(itaconic acid) was recorded in D_2O. The absence of peaks corresponding to olefinic hydrogens suggests that no monomeric itaconic acid remained within the polymer network, confirming successful polymerization. The other observed peaks in the spectrum were assigned to the appropriate hydrogen groups, as illustrated in Fig. 2.

The polymers were characterized using gel permeation chromatography (GPC). A Waters chromatography system was utilized for the GPC measurements, which employed 0.1 M $NaNO_3$ as the eluent at a flow rate of 1 mL min^{-1}. The samples were analyzed at a concentration of 1 mg mL^{-1} and a temperature of 23 °C. Calibration was effectively performed using polystyrene standards sup-

plied by Polymer Standards Service. The obtained chromatogram is shown in Fig. 3. The results of the GPC measurements for synthesized poly(itaconic acid) are summarized in Table II.

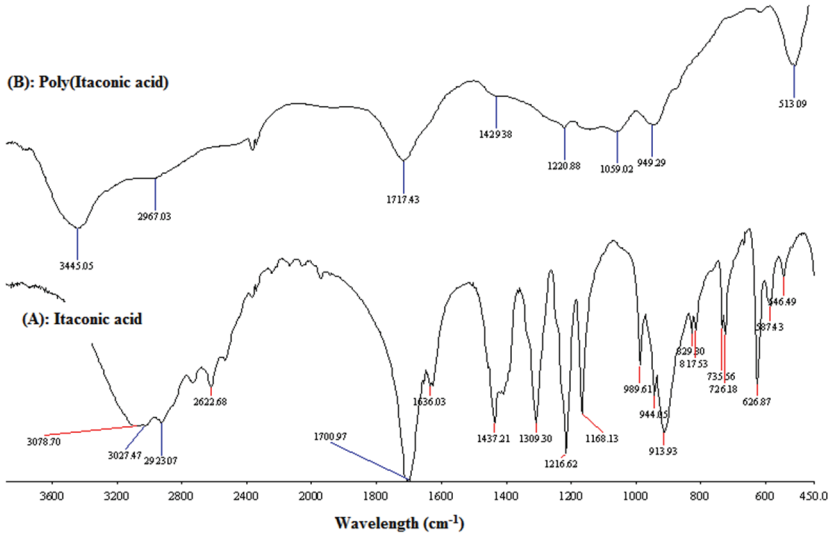

Fig. 1. FT-IR (KBr) spectra of: A) the itaconic acid; B) the poly(itaconic acid).

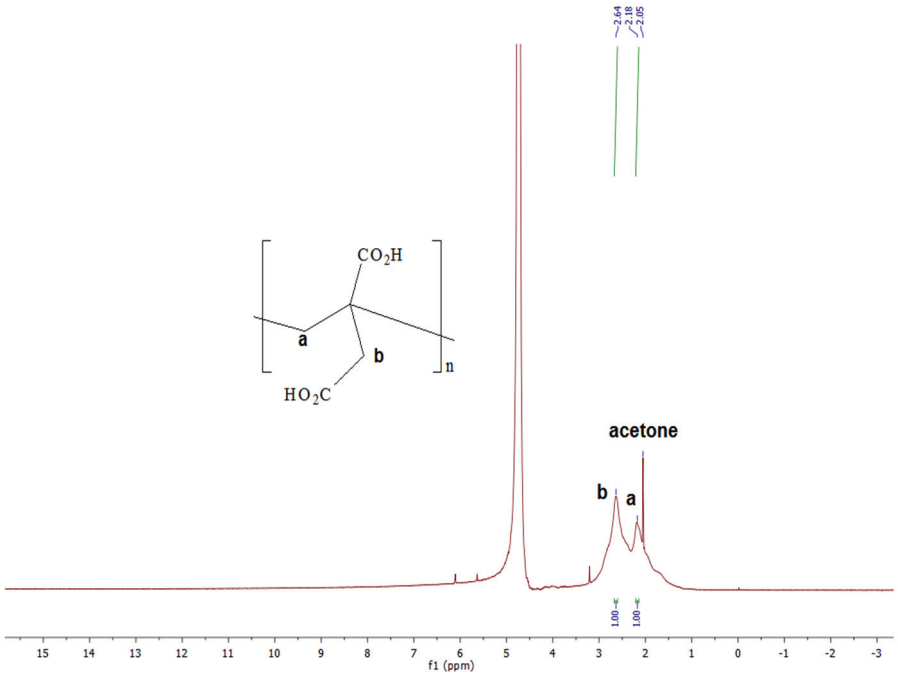

Fig. 2. ^{1}H-NMR of poly(itaconic acid) sample in D_2O.

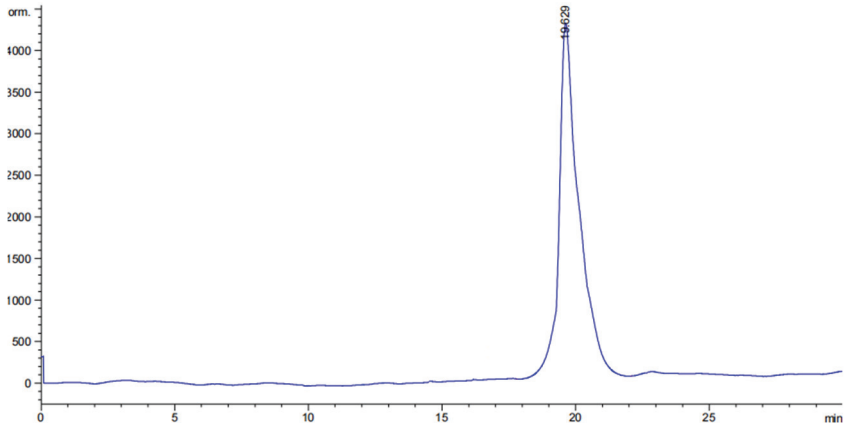

Fig. 3. Gel permeation chromatography (GPC) trace of poly(itaconic acid).

TABLE II. Synthesis parameters and GPC results of poly(itaconic acid) polymerized at 55 °C for 48 h. *Z*-average molecular weight (M_z), number average molecular weight (M_n), weight average molecular weight (M_w) and polydispersity index (PDI) = M_w/M_n calculated from GPC data

Retention time min	Peak area %	M_z g mol^{-1}	M_w g mol^{-1}	M_n g mol^{-1}	*PDI*
19.629	100	49251	41654	34879	1.1942

Analysis of the GPC chromatogram data revealed one distinct peak with a retention time of 19.629 min with accounts for a percentage of 100 % total peak area, indicating that it constitutes the major component of the sample. Furthermore, ^{1}H-NMR and FT-IR spectroscopic analyses have detected no impurities, by-products or additives. Therefore, the chromatographic result is consistent with other analytical methods, ruling out the presence of non-polymer materials.

PIA demonstrates versatile solubility properties, being soluble in methanol and water which makes it a potential candidate for use as a homogeneous catalyst, especially due to the acidic nature (pH 4) of its aqueous solution. This feature allows it to effectively load hydronium ions in methanol-based reactions, creating a moderately acidic environment ideal for moisture-insensitive organic reactions.

A review of the chemistry literature revealed that the catalytic properties of PIA have not been explored to date. The catalytic capabilities of PIA can be explored in a variety of organic reactions. Additionally, this polymer is insoluble in ethanol, propanol and acetone but exhibits solubility in water and methanol.[11] Given that pyrrolin-2-ones are frequently synthesized in methanol,[21] the use of PIA in this synthesis presents a valuable opportunity to evaluate its catalytic efficiency. The synthesis of pyrrolin-2-one derivatives using PIA as a homogeneous catalyst in methanol could provide significant insights into its catalytic properties and potential applications in organic synthesis.

A one-pot and three-component synthesis was carried out for the preparation of 3-acyl-5-hydroxy-3-pyrrolin-2-ones from ArCHO, $ArNH_2$ and dimethyl acetylenedicarboxylate (DMAD) by PIA as a homogeneous catalyst in MeOH as shown in Scheme 3. The synthesis process of 3-acyl-5-hydroxy-3-pyrrolin-2--ones demonstrates efficiency when PIA is used as a catalyst. Using 0.2 g of PIA has been identified as the optimally efficient quantity for converting benzaldehyde, aniline and dimethyl acetylenedicarboxylate in methanol at room temperature. This highlights the usefulness of PIA in this context. In particular, the derivative 1,5-diphenyl-3-hydroxy-4-methoxycarbonyl-3-pyrrolin-2-one (**1a**) achieved high yields of 90 % within 8 h in methanol. Comparing this to the lack of significant yield without a catalyst or with itaconic acid further emphasizes the superior catalytic role of PIA in this synthesis.

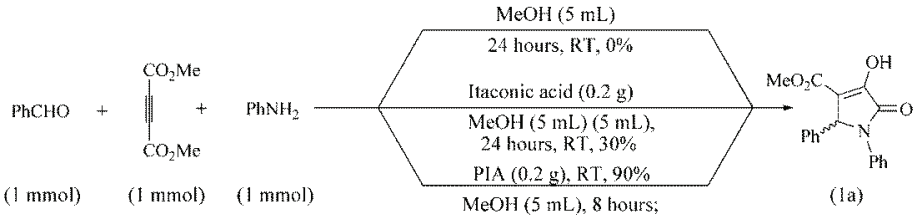

Scheme 3. Comparison of the synthesis of 1,5-diphenyl-3-hydroxy-4-methoxycarbonyl-3-pyrrolin-2-one (**1a**) without catalyst and by the PIA as a heterogeneous catalyst in ethanol.

The efficiency of these procedures was evaluated through the synthesis of additional derivatives of 3-acyl-5-hydroxy-3-pyrrolin-2-one under optimized reaction conditions. The corresponding products were synthesized with excellent yields of 90–95 % were achieved in MeOH as indicated in Table III. The products were characterized by CHN, ^{1}H-NMR, ^{13}C-NMR and FT-IR (KBr). Also, the melting point was measured and compared with appropriate references.

TABLE III. The synthesis of pyrrolin-2-ones from Ar-CHO (1 mmol), Ar-NH_2 (1 mmol), DMAD (1 mmol) and the PIA (0.2 g) in MeOH (5 mL) at room temperature; the yields were referred to isolated products. The purity of the products was determined by ^{1}H-NMR

Entry	Ar-CHO	Ar-NH_2	m.p. / °C	m.p. (lit.) / °C	Yield / %
1a[21,27,28]	Ph	Ph	182–183	180–182	90
2a[21,27]	4-Br-Ph	4-Br-Ph	217–219	218–220	92
3a[30]	Ph	4-MeO-Ph	171–173	170–171	90
4a[21]	2-Cl-Ph	4-MeO-Ph	191–193	192–194	90
5a[21]	4-Br-Ph	4-Me-Ph	170–172	170–172	95
6a[21]	2-Cl-Ph	4-Me-Ph	192–194	193–194	90
7a[21]	3-Br-Ph	4-MeO-Ph	170–171	170–171	94

As illustrated in Scheme 4, the synthesis of pyrrolin-2-ones involves a multi--step process, where PIA plays a crucial role in activating and transforming the

reactants. The first step involves the acid surface of PIA activating the aldehyde functional group, enabling it to react with aniline and form an imine intermediate. In the subsequent condensation reaction, water molecules are released and react with dimethyl acetylenedicarboxylate, generating a 1,3-dipolar intermediate.[29] This intermediate then adds to the activated imine. The following reaction involves the amino group attacking one of the ester groups through an intramolecular process. The reaction proceeds through five-membered ring formation, establishing the pyrrolin-2-one system. Notably, the enol form represents the more stable configuration in these compounds. It is noteworthy that PIA facilitates this step of the reaction, further highlighting its catalytic proficiency in the synthesis of pyrrolin-2-ones. The PIA, once recovered, can be used in subsequent reaction cycles without any limitations. Despite this, there was no observation of leakage from the catalyst or its components in the products.

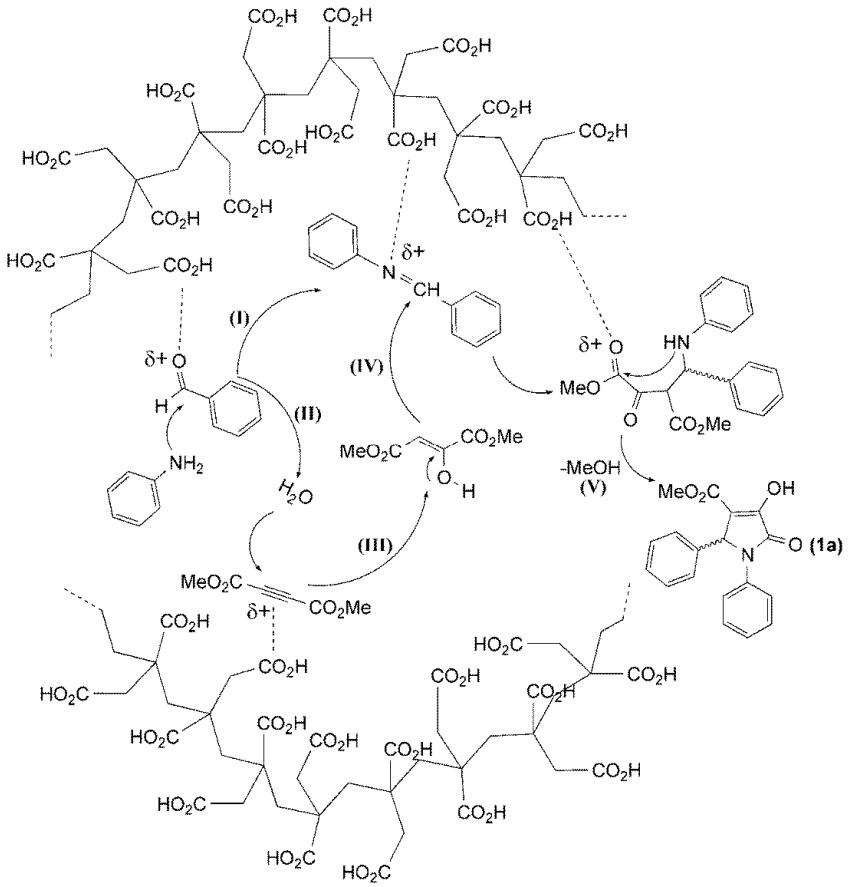

Scheme 4. The proposed mechanism for the synthesis of pyrrolin-2-one derivatives by the PIA.

Comparisons between these protocols and other reported methods for synthesizing pyrrolin-2-one derivatives are presented in Table IV. Based on the results obtained, the PIA catalyst exhibits a favorable profile for the synthesis of the pyrrolinone skeleton. The higher product yields, shorter reaction times, and the polymer's recyclability, compared to some existing methods, represent its key catalytic advantages.

TABLE IV. Comparison of synthesis of product **1a** by different methods in the litrature[21]

Entry	Protocol	Yield / %	Time	Reusable catalyst	Reference
1	PIA in MeOH	90	8 h	Yes	Current
2	Fe_3O_4@PEG-400@OA	94	24 h	Yes	21a
3	AmberChrom/EtOH	90	24 h	Yes	21b
4	Fe_3O_4@NH_2@OA	95	8 h	Yes	21c
5	TiO_2 admicelle/H_2O	75	18 h	Non	27
6	Fe_3O_4@SiO_2@propyl–ANDSA/EtOH	87	8 h	Yes	28
7	P-TsOH/EtOH	62	24 h	Non	29
8	EtOH/H_2O	87	15 h	Non	30
9	Citric acid/US/EtOH	90	20 min	Non	31
10	P-TsOH/MW/EtOH	96	6 min	No	32
11	[bmim]BF_4/PEG-400	89	1 h	Yes	33
12	MW/[BBSI]Cl/glycol	90	5 min	Yes	34
13	[BBSI]Cl/ball milling	90	25 min	Yes	35

CONCLUSION

In this study, poly(itaconic acid) (PIA) was synthesized using potassium persulfate and sodium dihydrogen phosphate with a good yield of 80 % within 48 h at 55 °C. Notably, this represents the first reported application of PIA as a homogeneous catalyst. When employed in methanol for pyrrolin-2-one synthesis, PIA demonstrated satisfactory catalytic performance. Compared to some existing methods, this polymer offers significant catalytic advantages, such as higher product yields, shorter reaction times and recyclability. Consequently, PIA can be introduced as a convenient and reusable catalyst for conducting organic reactions with a green profile. Future research could be directed toward examining the catalytic properties of PIA derivatives, such as novel co-polymers, for executing organic reactions.

SUPPLEMENTARY MATERIAL

Additional data and information are available electronically at the pages of journal website: https://www.shd-pub.org.rs/index.php/JSCS/article/view/13026, or from the corresponding author on request.

Acknowledgement. The authors extend their sincere gratitude for the financial support provided for this research by the Research Council of the Islamic Azad University, Mahabad Branch.

И З В О Д

СИНТЕЗА ПОЛИ(ИТАКОНСКЕ КИСЕЛИНЕ) И ЊЕНА ПРИМЕНА КАО ВЕШЕКРАТНОГ ХОМОГЕНОГ КАТАЛИЗАТОРА ЗА СИНТЕЗУ ПИРОЛИНОНА

PARYA HAMDI MOHAMADABAD, DAVOOD SETAMDIDEH и FATEMEH GHANBARY

Department of Chemistry, Mahabad Branch, Islamic Azad University, Mahabad, Iran

Поли(итаконска киселина) (PIA) је синттисана полимеризацијом итаконске киселине у присуству $K_2S_2O_8$ и NaH_2PO_4, у добром приносу од 80 %, током 48 h, на температури од 55 °C. PIA је коришћена као хомогени катализатор за синтезу пиролин-2-она из ароматичних алдехида, анилина и диметил-ацетилендикарбоксилата (DMAD). Реакција се врши у метанолу, у кратком реакционом времену, у одличном приносу од 90–95 %, током 8 h на собној температури. Синтетисани производи окракатреисани су микроанализом (CHN), ^{1}H-NMR, ^{13}C-NMR и FT-IR спектрима. Описана метода је еколошки прихватљива и у складу је са принципима зелене хемије.

(Примљено 28. августа 2024, ревидирано 6. јануара, прихваћено 1. августа 2025)

REFERENCES

1. H. Wang, N. Li, J. Zang, X. Wan, *Chirality* **27** (2015) 523 (https://doi.org/10.1002/chir.22448)
2. N. Haque, S. Biswas, P. Basu, I. Haque Biswas, R. khatun, A. Khan, S. M. Islam, *New J. Chem.* **44** (2020) 15446 (https://doi.org/10.1039/D0NJ02798G)
3. P. Aguirre, K. Brown, D. Venegas-Yazigi, V. Paredes-Garcıa, E. Spodine, *Macromol. Symp.* **304** (2011) 65 (https://doi.org/10.1002/masy.201150609)
4. M. Najafi, A. Abbasi, M. Masteri-Farahani, H. Shahbaazi, M. Ahmadniai Motlagh, J. Janczak, *RSC Adv.* **6** (2016) 29944 (https://doi.org/10.1039/C6RA02248K)
5. P. Puthiaraja, Y. M. Chung, W. S. Ahna, *Mol. Catal.* **441** (2017) 1 (https://doi.org/10.1016/j.mcat.2017.08.002)
6. J. J. Kim, C-R, Lim, B. M. Reddy, S. E. Park, *Mol. Catal.* **451** (2018) 43 (https://doi.org/10.1016/j.mcat.2017.10.022)
7. G. Fan, H. Zhang, S. Cheng, Z. Ren, Z. Hu, Z. Wang, *Aus. J. Chem.* **61** (2008) 610 (https://doi.org/10.1071/CH08066)
8. Y. Tian, R. Zhang, W. Zhao, S. Wen, Y. Xiang, X. Liu, *Catal. Lett.* **150** (2020) 3553 (https://doi.org/10.1007/s10562-020-03253-5)
9. A. Ahmed Raza, S. Ravi, S. S. Tajudeen, A. K. Ibrahim Sheriff, *React. Funct. Polym.* **167** (2021) 105011 (https://doi.org/10.1016/j.reactfunctpolym.2021.105011)
10. D. Setamdideh, *J. Serb. Chem. Soc.* **81** (2016) 971 (https://doi.org/10.2298/JSC160202050S)
11. C. S. Marvel, T. H. Shepherd, *J. Org. Chem.* **24** (1959) 599 (https://doi.org/10.1021/jo01087a006)
12. a) P. Kulal, V. Badalamoole, *Int. J. Biol. Macromol.* **193** (2021) 2232 (https://doi.org/10.1016/j.ijbiomac.2019.11.181); b) H. Ge, Z. Zhang, X. Zhao, H. Li, J. Sun, X. Jv, *Can. J. Chem. Eng.* **99** (2021) S157 (https://doi.org/10.1002/cjce.24014)
13. a) G. Sharma, A. Kumar, M. Naushad, B. Thakur, D. V. N. Vo, B. Gao, A. A. Al-Kahtanid, F. J . Stadler, *J. Hazard. Mater.* **416** (2021) 125714 (https://doi.org/10.1016/j.jhazmat.2021.125714); b) S. Dan, S. Banivaheb, H. Hashemipour, M. kalantari, *Polym. Bull.* **78** (2021) 1887 (https://doi.org/10.1007/s00289-020-03190-8); c) T. Sharika, A. Mohanan, *Mater. Today: Proc*. **41** (2021) 744 (https://doi.org/10.1016/j.matpr.2020.08.421)

14. S. Bujok, M. Konefal, R. Konefal, M. Nevoralová, S. Bednarz, K. Mielczarek, H. Benes, *J. Colloid Interface Sci.* **610** (2022) 1 (https://doi.org/10.1016/j.jcis.2021.12.055)
15. C. Cottet, A. G. Salvay, M. A. Peltzer, M. Fernandez-Garcia, *Polymers* **13** (2021) 200 (https://doi.org/10.3390/polym13020200)
16. L. Wang, G. Guan, J. Wang, *Iran. Polym. J.* **30** (2021) 1149 (https://doi.org/10.1007/s13726-021-00959-0)
17. G. Z. Yin, J. L. Palencia, D. Y. Wang, *Compos. Commun.* **27** (2021) 100893 (https://doi.org/10.1016/j.coco.2021.100893)
18. T. C. Sung, M. W. Lu, Z. Tian, H. H. C. Lee, J. Pan, Q. D. Ling, A. Higuchi. *J. Mater. Chem., B* **9** (2021) 7662 (https://doi.org/10.1039/D1TB01555A)
19. H. Baskan, L. Esentürk, S. Dösler, A. S. Sarac, H. Karakas, *J. Ind. Text.* **50** (2019) 1594 (https://doi.org/10.1177/1528083719868170)
20. G. Zhu, H. Hub, T. Yang, J. Ma, H. Zhang, X. He, *RSC Adv.* **11** (2021) 20720 (https://doi.org/10.1039/D1RA03109K)
21. a) S. Esmaielzadeh, D. Setamdideh, *J. Serb. Chem. Soc.* **86** (2021) 1039 (https://doi.org/10.2298/JSC210521059E); b) P. Hamdi Mohamadabad, D. Setamdideh, *Org. Prep. Proced. Int.* **55** (2023) 265 (https://doi.org/10.1080/00304948.2022.2141044); c) S. Esmaielzadeh, D. Setamdideh, F. Ghanbary, *J. Mex. Chem. Soc.* **68** (2024) 234 (https://doi.org/10.29356/jmcs.v68i2.1910)
22. E. Grespos, D. J. T. Hill, J. H. O'Donnell, P. W. O'Sullivan, T. L. Young, J. C. East, K. J. Ivin, *Makromol. Chem. Rapid Commun.* **5** (1984) 489 (https://doi.org/10.1002/marc.1984.030050901)
23. J. Velickovic, J. Filipovic, D. P. Petrovic, *Polym. Bull.* **32** (1994) 169 (https://doi.org/10.1007/BF00306384)
24. M. Cao, *Synthesis and properties of poly(itaconic acid)*, University of New Hampshire, Durham, NH, 2008
25. S. Bednarz, A. Błaszczyk, D. Błażejewska, D. Bogdał, *Catal. Today* **257** (2015) 297 (https://doi.org/10.1016/j.cattod.2014.07.021)
26. S. Bednarza, G. Kowalskib, R. Konefałc, *Eur. Polym. J.* **115** (2019) 30 (https://doi.org/10.1016/j.eurpolymj.2019.03.021)
27. R. Sarkar, C. Mukhopadhyay, *Tetrahedron Lett.* **54** (2013) 3706 (https://doi.org/10.1016/j.tetlet.2013.05.017)
28. R. Ghorbani-Vaghei, N. Sarmast, J. J. Mahmoodi, *Appl. Organomet. Chem.* **31** (2017) e3681 (https://doi.org/10.1002/aoc.3681)
29. J. Sun, Q. Wu, E. Y. Xia, C. G. Yan, *Eur. J. Org. Chem.* (2011) 2981 (https://doi.org/10.1002/ejoc.201100008)
30. A. M. Zonouz, I. Eskandari, B. Notash, *Synth. Commun.* **45** (2015) 2115 (https://doi.org/10.1080/00397911.2015.1065506)
31. H. Ahankar, A. Ramazani, K. Slepokura, T. Lis, S. W. Joo, *Green Chem.* **18** (2016) 3582 (https://doi.org/10.1039/c6gc00157b)
32. K. S. Marapala, N. Venkatesh, M. Swapna, P. R. Venkateswar, *Int. J. ChemTech Res*. **13** (2020) 227 (https://doi.org/10.20902/ijctr.2019.130128)
33. S. Pervaram, D. Ashok, C. Venkata Ramana Reddy, M. Sarasija, A. Ganesh, *Chem. Data Collect.* **29** (2020) 100508 (https://doi.org/10.1016/j.cdc.2020.100508)
34. N. Ghaffari Khaligh, T. Mihankhah, M. Rafie Johan, S. J. J. Titinchi, *Green Process Synth.* **8** (2019) 373 (https://doi.org/10.1515/gps-2019-0004)
35. N. Ghaffari Khaligh, T. Mihankhah, M. Rafie Johan, M. *Synth. Commun*. **49** (2019) 1334 (https://doi.org/10.1080/00397911.2019.1601225).

Journal of the Serbian Chemical Society
JSCS@tmf.bg.ac.rs • www.shd.org.rs/JSCS
J. Serb. Chem. Soc. 90 (9) S310–S324 (2025) *Supplementary material*

SUPPLEMENTARY MATERIAL TO

Synthesis of poly(itaconic acid) and its application for synthesis of pyrrolinones as a reusable homogeneous catalyst

PARYA HAMDI MOHAMADABAD, DAVOOD SETAMDIDEH* and FATEMEH GHANBARY

Department of Chemistry, Mahabad Branch, Islamic Azad University, Mahabad, Iran

J. Serb. Chem. Soc. 90 (9) (2025) 1015–1025

*1,5-diphenyl-3-hydroxy-4-methoxycarbonyl-3-pyrrolin-2-one (**1a**)*

White powder, MeOH (8 hours, yields: 90%), mp 182-183 °C (180-182 °C [21, 27-28]). FT-IR (KBr)(cm^{-1}): 3260 (OH), 2958, 1702 (C=O), 1680 (C=O), 1498, 1382, 1232, 1002. ^{1}H-NMR (400 MHz, DMSO-d6): δ 3.60 (s, 3H, CH_3), 6.10 (s, 1H, CH), 7.07–7.62 (m, 10 H, Ar and OH); ^{13}C NMR (100 MHz, DMSO-d6): δ 50.55, 61.05, 112.35, 122.96, 125.80, 128.13, 128.38, 128.73, 129.13, 136.74, 137.00, 153.14, 162.96 (C=O), 164.49 (C=O). Anal. Calcd for $C_{18}H_{15}NO_4$: C (%), 69.89; H (%), 4.89; N (%), 4.53. Found: C (%), 69.92; H (%), 4.81; N (%), 4.48.

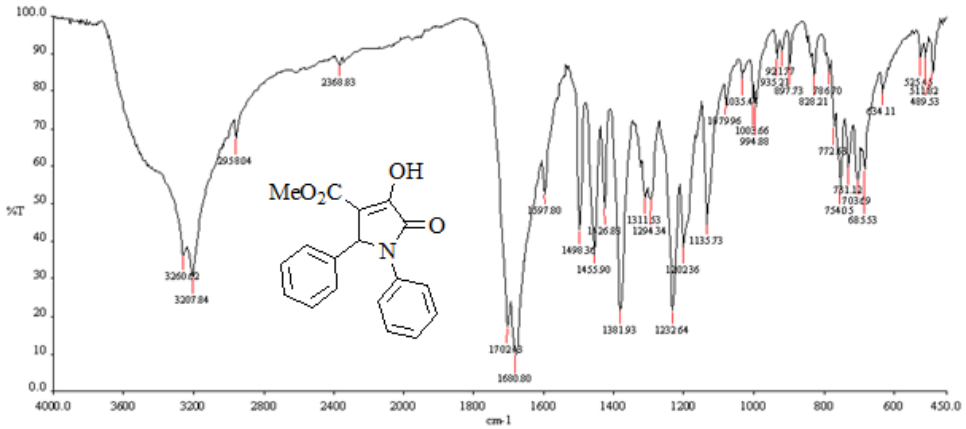

Fig. S-1. FT-IR (KBr, cm^{-1}) spectrum of compound 1a.

* Corresponding author. E-mail: dsetamdideh@iau.ac.ir; davood.setamdideh@gmail.com

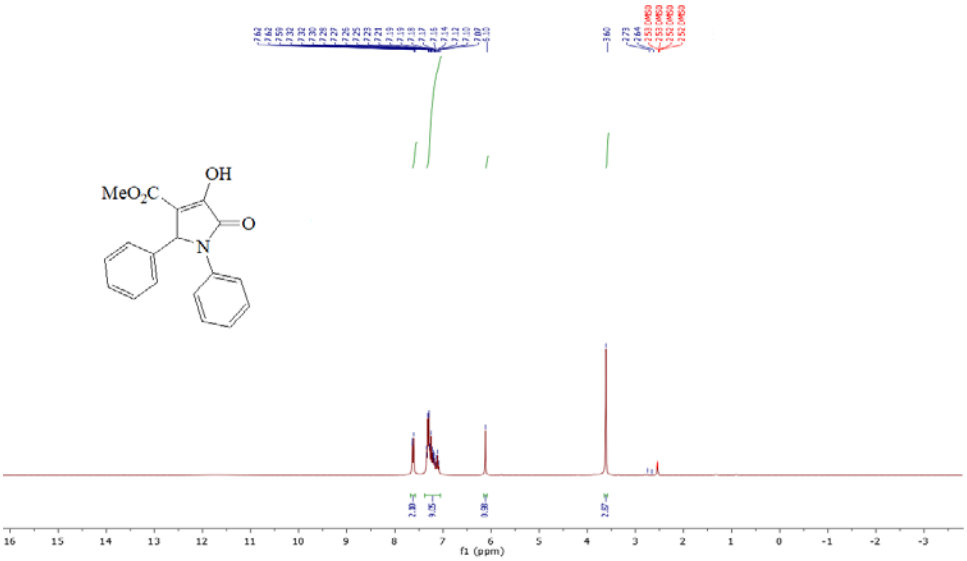

Fig. S-2. ^{1}H-NMR (400 MHz, DMSO-d6, δ/ppm) spectrum of compound 1a.

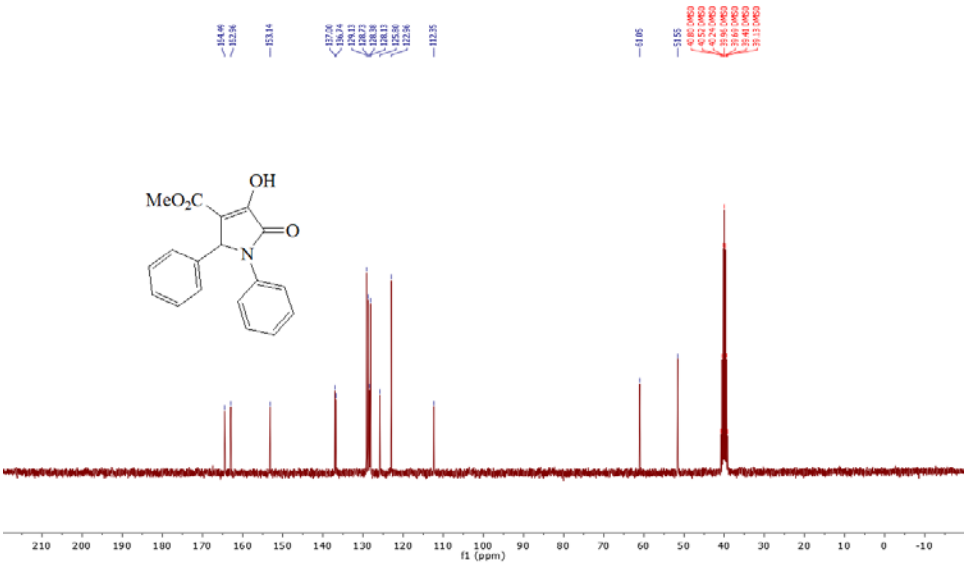

Fig. S-3. ^{13}C-NMR (100 MHz, DMSO-d6, δ/ppm) spectrum of compound 1a.

1-(4-bromophenyl)-5-(4-bromophenyl)-3-hydroxy-4-methoxycarbonyl-3-pyrrolin-2-one (2a)

The white solid, MeOH (8 hours, yields: 92%), mp 217-219 °C (218-220 °C [21, 27]). FT-IR (KBr): ν_{max}(cm^{-1}) :3234 (OH), 2951, 1709 (C=O), 1684 (C=O), 1491, 1372, 1233, 1133;^{1}H-NMR (400 MHz, DMSO-d6) δH: 3.83 (s, 3H, OCH_3), 6.07 (s, 1H, CH), 7.24–8.63 (m, 8 H, Ar). ^{13}C-NMR (100 MHz, DMSO-d6) δ C: 51.35, 60.10, 110.15, 118.05, 121.43, 124.61, 130.40, 131.66, 132.04, 136.13, 137.17, 155.27, 163.26, 165.28 (C=O). Anal. Calcd for $C_{18}H_{13}Br_2NO_4$: C (%), 46.28; H (%), 2.81; N (%), 3.00. Found: C (%), 46.38; H (%), 2.75; N (%), 2.93.

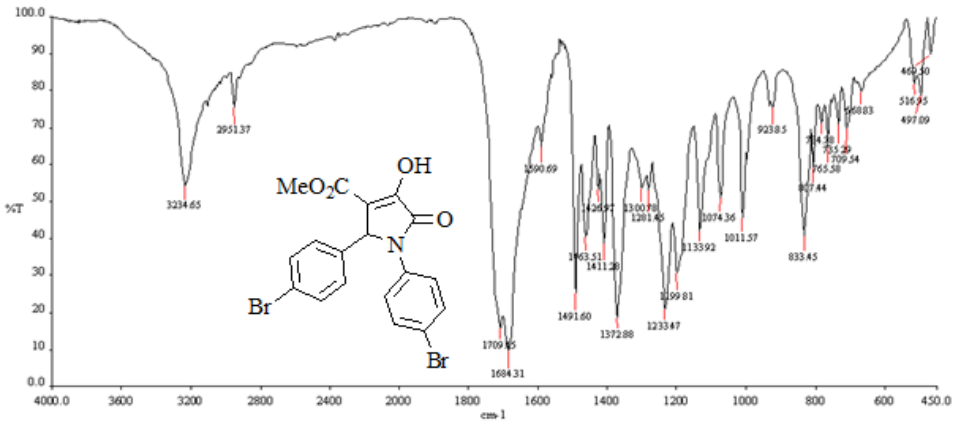

Fig. S-4. FT-IR (KBr, cm-1) spectrum of compound 2a.

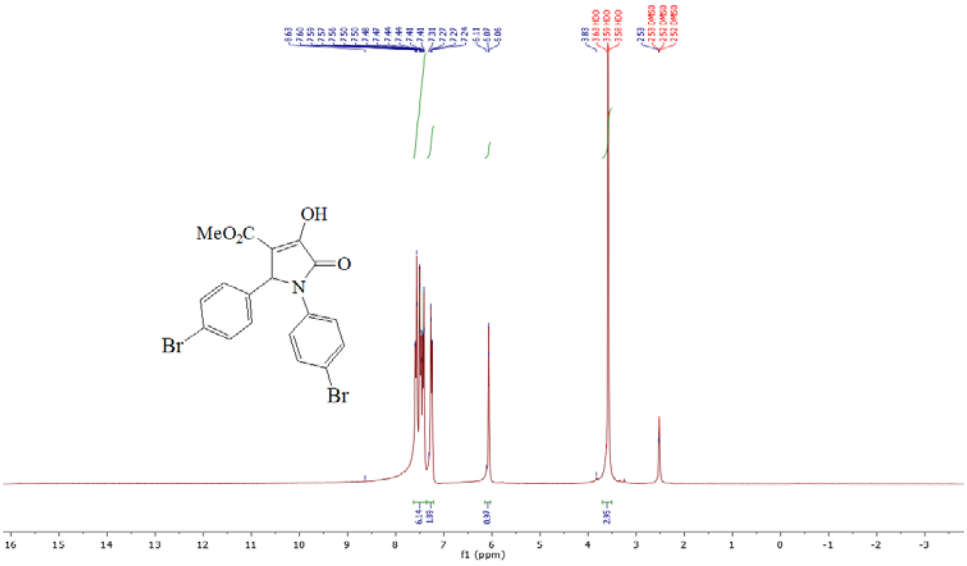

Fig. S-5. ^{1}H-NMR (400 MHz, DMSO-d6, δ/ppm) spectrum of compound 2a.

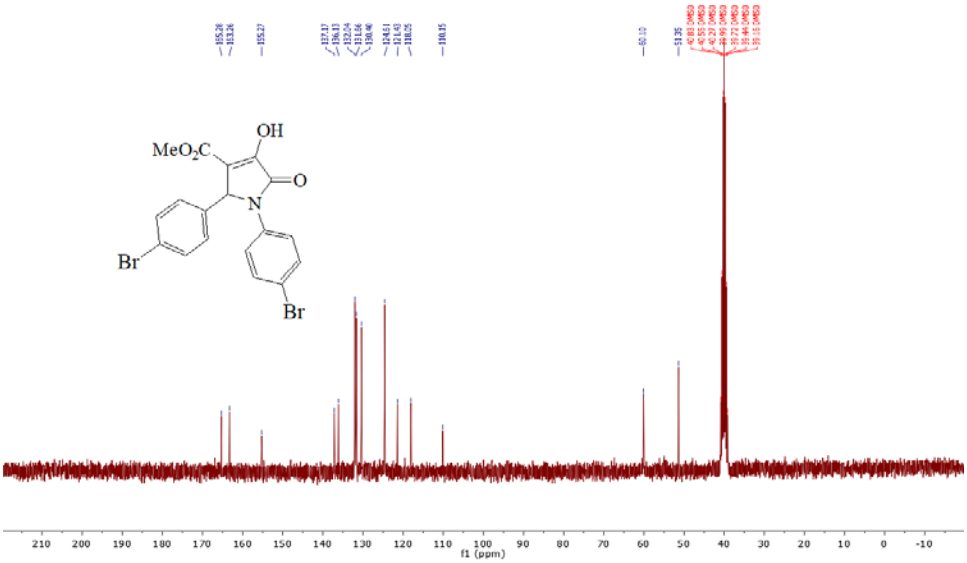

Fig. S-6. ^{13}C-NMR (100 MHz, DMSO-d6, δ/ppm) spectrum of compound 2a.

1-(4-methoxyphenyl)-5-phenyl-3-hydroxy-4-methoxycarbonyl-3-pyrrolin-2-one (3a)

White solid, MeOH (8 hours, yields: 90%), 171-173 °C (170-171°C [30]). FT-IR (KBr): ν_{max}(cm^{-1}) :3232 (OH), 2952, 1709 (C=O), 1679 (C=O), 1494, 1374, 1231, 1134; ^{1}H-NMR (250.13 MHz, $CDCl_3$) δH: 3.72 (s, 3H, OCH_3), 5.69 (s, 1H, CH), 7.21–7.36 (m, 9 H, Ar). The ^{13}C-NMR (62.90 MHz, $CDCl_3$) δ C: 52.10, 58.47, 61.43, 112.99, 119.03, 123.48, 127.35, 128.81, 132.03, 134.62, 135.30, 155.87, 162.83 (C=O), 165.11 (C=O). Anal. Calcd for $C_{19}H_{17}NO_5$: C (%), 67.25; H (%), 5.05; N (%), 4.13. Found: C (%), 67.31; H (%), 4.98; N (%), 4.00.

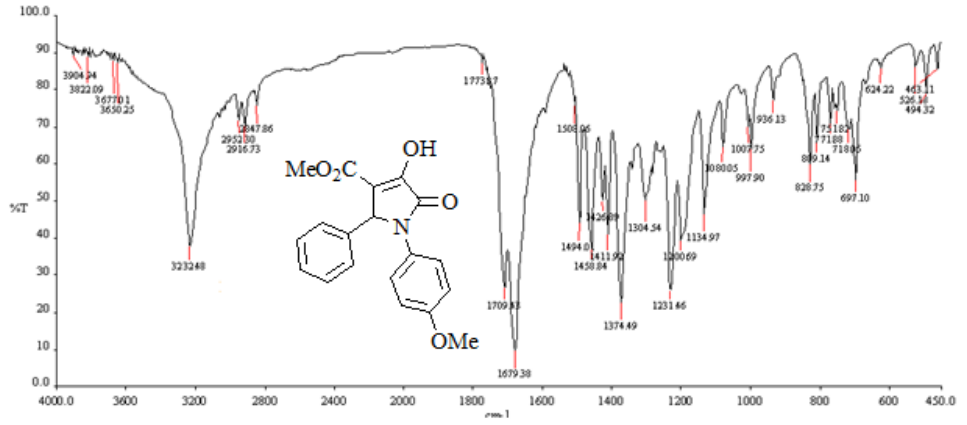

Fig. S-7. FT-IR (KBr, cm-1) spectrum of compound 3a.

Fig. S-8. ^{1}H-NMR (250 MHz, $CDCl_3$, δ/ppm) spectrum of compound 3a.

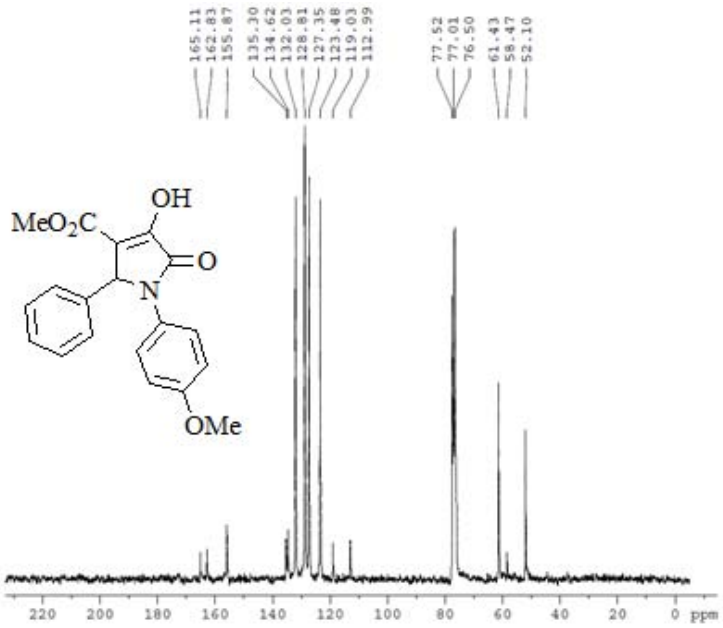

Fig. S-9. ^{13}C-NMR (62.90 MHz, $CDCl_3$, δ/ppm) spectrum of compound 3a.

1-(4-methoxyphenyl)-5-(2-chlorophenyl)-3-hydroxy-4-methoxycarbonyl-3-pyrrolin-2-one (4a)

The brown solid, MeOH (8 hours, yields: 90%), m.p. 191-193°C (192-194 °C [21]. FT-IR (KBr)(cm^{-1}): 3198 (OH), 2954, 1701 (C=O), 1684 (C=O), 1533, 1351, 1250, 1029. ^{1}H-NMR ((250.13 MHz, $CDCl_3$)) δ 3.62 (s, 3H, OCH_3), 3.71 (s, 3H, OCH_3), 6.37 (s, 1H, CH), 6.77–7.37 (m, 8 H, Ar), 9.11 (br s, 1H, OH). ^{13}C-NMR (63 MHz, $CDCl_3$) δ 52.03, 55.30, 57.05, 112.40, 114.24, 123.77, 126.91, 127.44, 128.82, 129.77, 132.67, 134.96, 156.86, 157.60, 162.72 (C=O), 165.09 (C=O). Anal. Calcd. for $C_{19}H_{16}ClNO_5$ (373.79) C (%), 61.05; H (%), 4.31; Cl (%), 9.48; N (%), 3.75. Found: C (%), 61.15; H (%), 4.39; Cl (%), 9.37; N (%), 3.90.

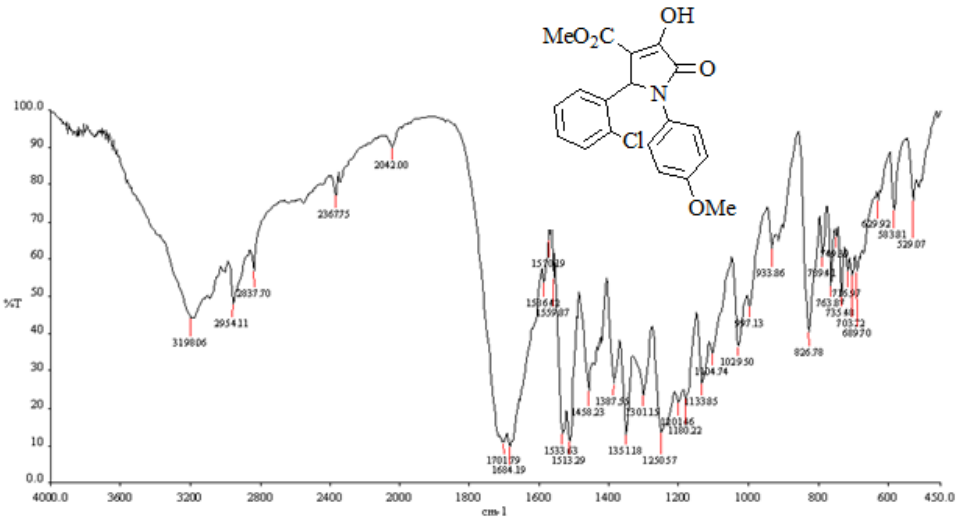

Fig. S-10. FT-IR (KBr, cm-1) spectrum of compound 4a.

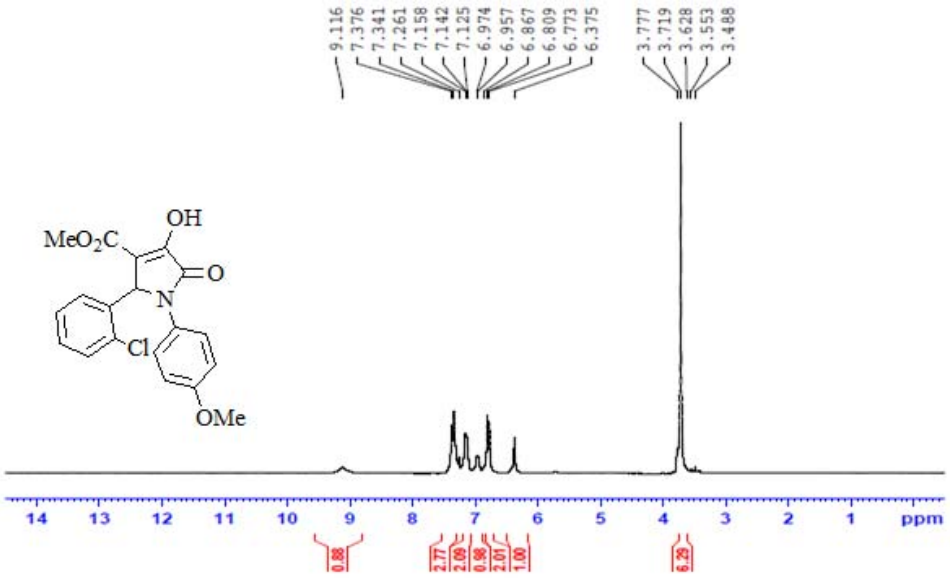

Fig. S-11. ^{1}H-NMR (250 MHz, $CDCl_3$, δ/ppm) spectrum of compound 4a.

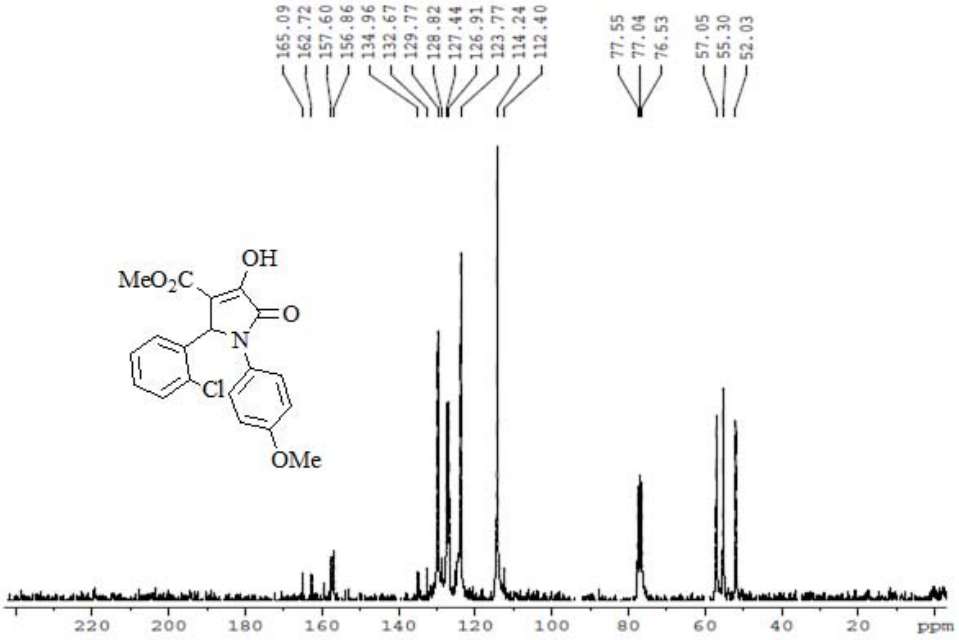

Fig. S-12. ^{13}C-NMR (63 MHz, $CDCl_3$, δ/ppm) spectrum of compound 4a.

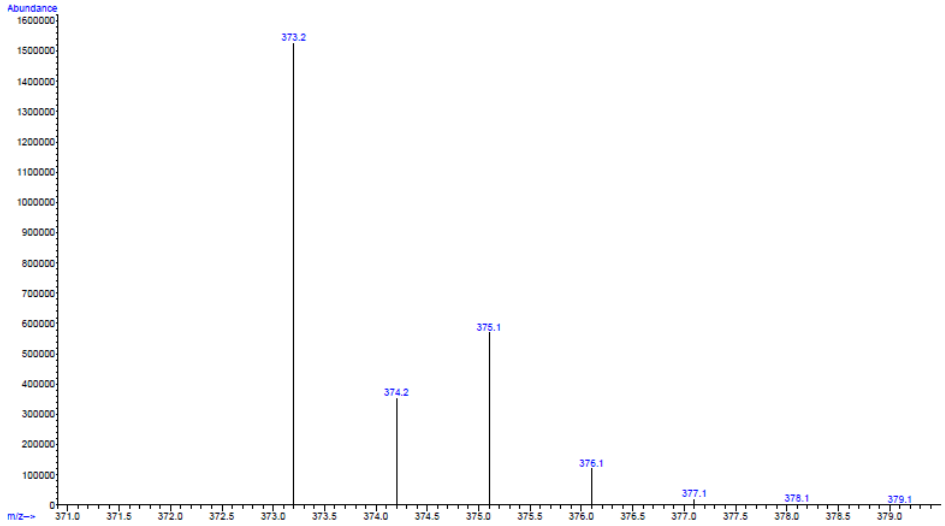

Fig. S-13. Mass spectrum of compound 4a.

1-(4-bromophenyl)-5-(4-methylphenyl)-3-hydroxy-4-methoxycarbonyl-3-pyrrolin-2-one (5a)

The cream powder; MeOH (8 hours, yields: 95%), m.p. 170-172 °C (170-172 °C [21]. FT-IR (KBr): ν_{max}(cm^{-1}) :3167 (OH), 2951, 1724 (C=O), 1667 (C=O), 1515, 1383, 1230, 1010; ^{1}H-NMR (250.13 MHz, $CDCl_3$) δH: 2.16 (s, 3H, CH_3), 3.56 (s, 3H, OCH_3), 6.02 (s, 1H, CH), 7.04–7.42 (m, 8 H, Ar), 11.90 (br s, 1H, OH). ^{13}C-NMR (62.90 MHz, $CDCl_3$) δ C: 20.85, 51.57, 60.39, 111.72, 121.46, 122.97, 129.65, 130.40, 131.65, 133.95, 136.66, 153.38, 162.88 (C=O), 164.16 (C=O). Mass (m/z): 403.1 (M^++2), 401.1 (M^+), 369.1, 342.1, 267.0, 236.0, 208.0, 180.0, 157.1 (100%), 133.1, 115.1, 91.2, 65.2.). Anal. Calcd for $C_{19}H_{16}BrNO_4$: C (%), 56.73; H (%), 4.01; N (%), 3.48. Found: C (%), 56.55; H (%), 4.15; N (%), 3.60.

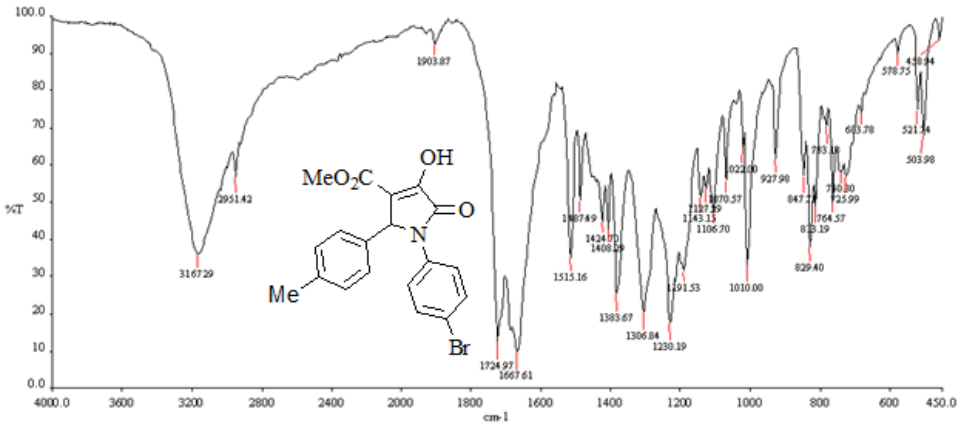

Fig. S-14. FT-IR (KBr, cm-1) spectrum of compound 5a.

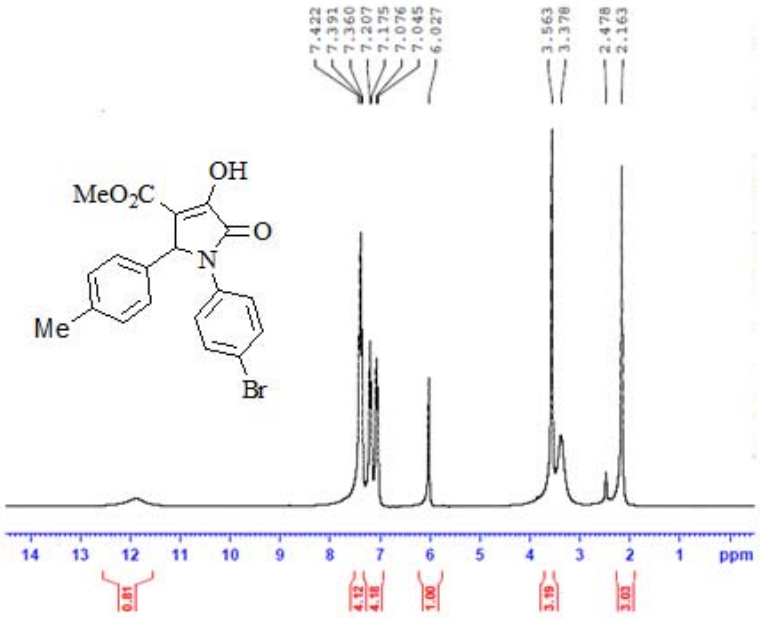

Fig. S-15. ^{1}H-NMR (250 MHz, $CDCl_3$, δ/ppm) spectrum of compound 5a.

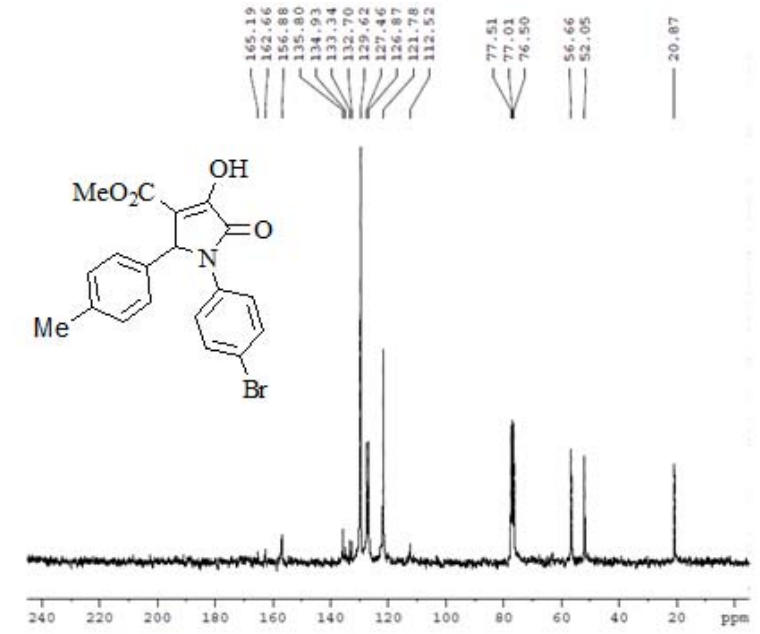

Fig. S-16. ^{13}C-NMR (62.9 MHz, $CDCl_3$, δ/ppm) spectrum of compound 5a.

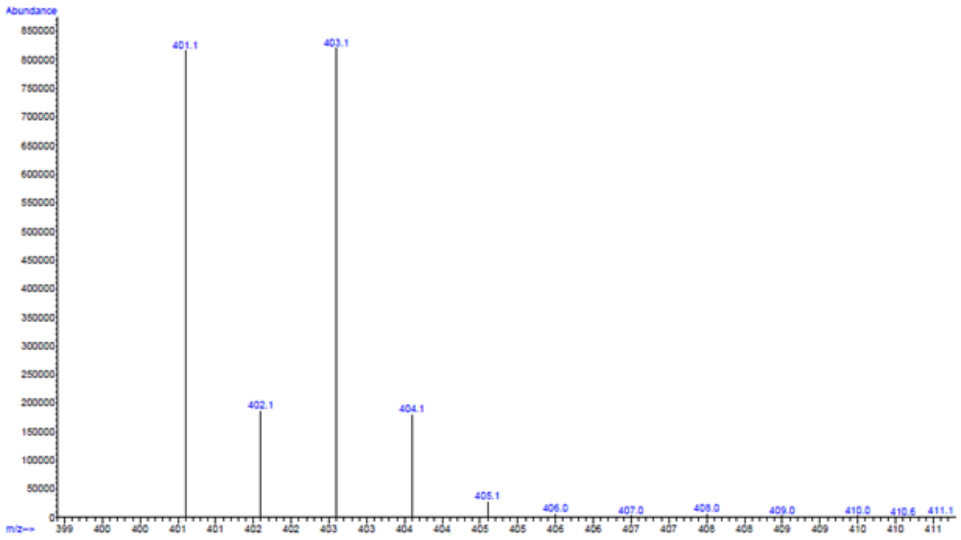

Fig. S-17. Mass spectrum of compound 5a.

1-(4-methylphenyl)-5-(2-cholorophenyl)-3-hydroxy-4-methoxycarbonyl-3-pyrrolin-2-one (6a)

The white solid, MeOH (8 hours, yields: 90%), m.p. 192-194 °C (193-194 °C [21]. FT-IR (KBr): ν_{max}(cm^{-1}) :3310 (OH), 2954, 1706 (C=O), 1680 (C=O), 1516, 1374, 1222, 1009; ^{1}H-NMR (250.13 MHz, $CDCl_3$) δH: 2.23 (s, 3H, CH_3), 3.72 (s, 3H, OCH_3), 6.40 (s, 1H, CH), 6.96–7.38 (m, 8 H, Ar), 9.10 (br s, 1H, OH). ^{13}C-NMR (62.90 MHz, $CDCl_3$) δ C: 20.87, 52.05, 56.66, 112.52, 121.78, 126.87, 127.46, 129.62, 132.70, 133.34, 135.80, 156.88, 162.66 (C=O), 165.19 (C=O). Mass (m/z): 359.2 (M^++2), 357.2 (M^+), 325.1, 290.1, 262.1, 228.1, 164.1 (100%), 133.1, 115.1 91.1, 65.1.). Anal. Calcd for $C_{19}H_{16}ClNO_4$: C (%), 63.78; H (%), 4.51; N (%), 3.91. Found: C (%), 63.59; H (%), 4.40; N (%), 3.77.

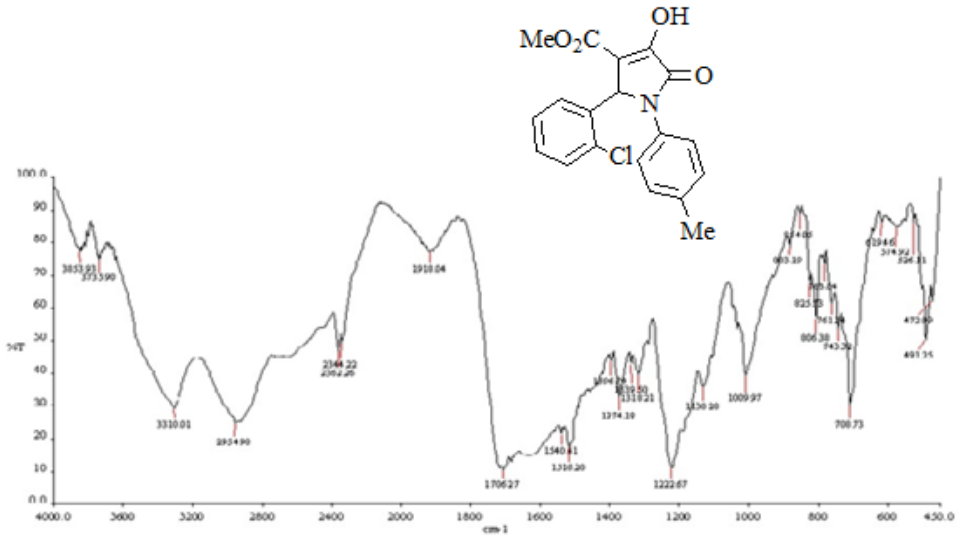

Fig. S-18. FT-IR (KBr, cm-1) spectrum of compound 6a.

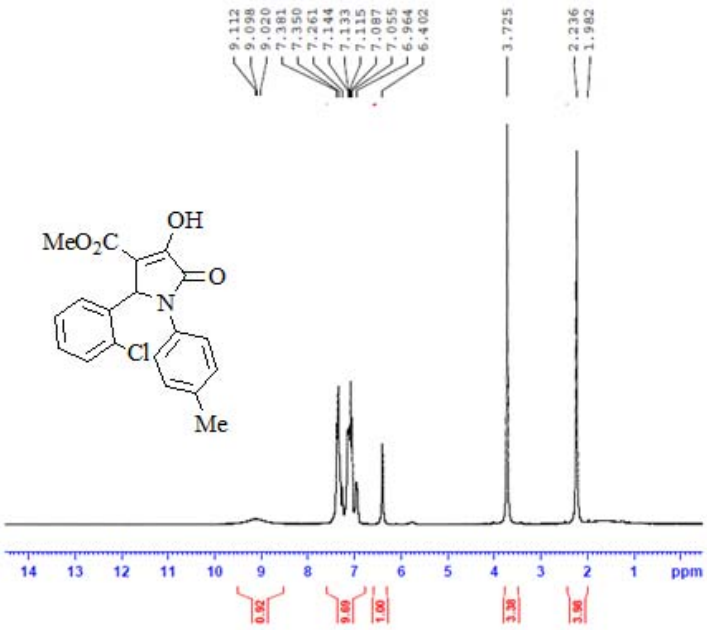

Fig. S-19. ^{1}H-NMR (250 MHz, $CDCl_3$, δ/ppm) spectrum of compound 6a.

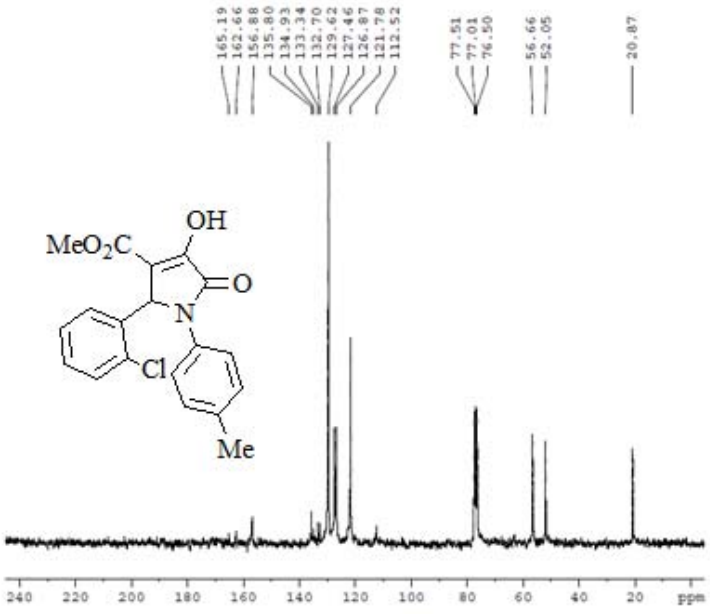

Fig. S-20. ^{13}C-NMR (62.9 MHz, $CDCl_3$, δ/ppm) spectrum of compound 6a.

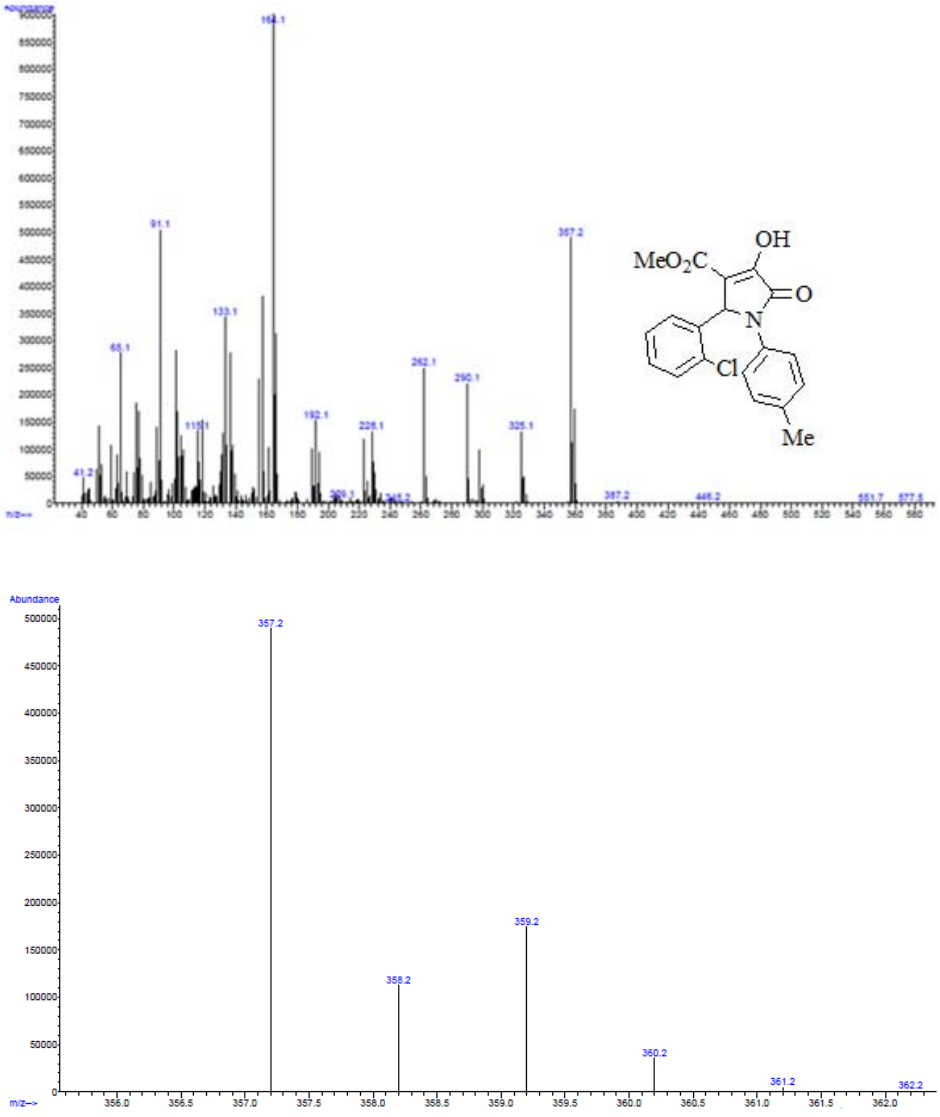

Fig. S-21. Mass spectrum of compound 6a.

1-(4-methoxyphenyl)-5-(3-bromophenyl)-3-hydroxy-4-methoxycarbonyl-3-pyrrolin-2-one (7a)

The cream solid, MeOH (8 hours, yields: 94%), 170-171 °C (170-171 °C [21]. FT-IR (KBr): ν_{max}(cm^{-1}) :3198 (OH), 2954, 1707 (C=O), 1683 (C=O), 1514, 1385, 1254, 1132; ^{1}H-NMR (250.13 MHz, $CDCl_3$) δH: 3.72 (s, 3H, OCH_3), 3.74 (s, 3H, OCH_3), 5.59 (s, 1H, CH), 6.78–7.36 (m, 8H, Ar). ^{13}C-NMR (62.90 MHz, $CDCl_3$) δ C: 52.10, 55.34, 61.56, 112.17, 114.37, 122.59, 124.44, 126.28, 128.62, 130.22, 130.46, 131.78, 137.53, 156.22, 157.80, 162.77 (C=O), 164.83 (C=O). Mass (m/z): 419.1 (M^++2), 417.1 (M^+), 387.1, 208.0, 149.2 (100%), 101.1, 77.2. Anal. Calcd for $C_{19}H_{16}BrNO_5$: C (%), 54.56; H (%), 3.86; N (%), 3.35. Found: C (%), 54.45; H (%), 3.98; N (%), 3.48.

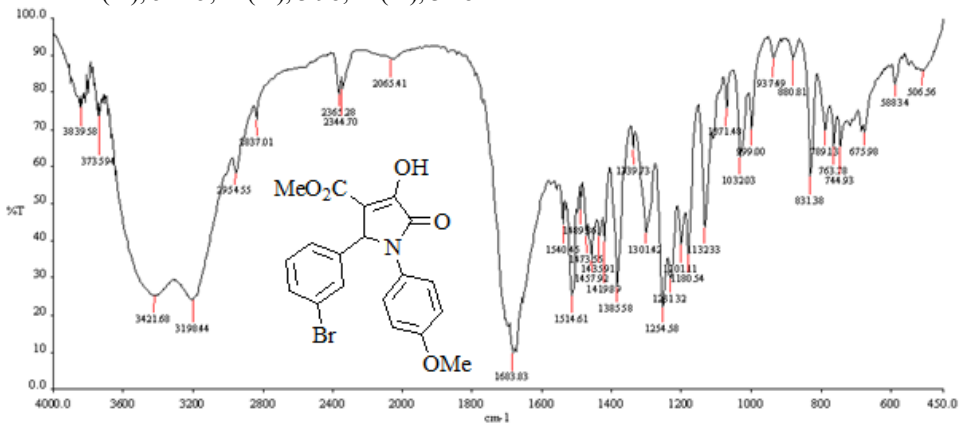

Fig. S-22. FT-IR (KBr, cm-1) spectrum of compound 7a.

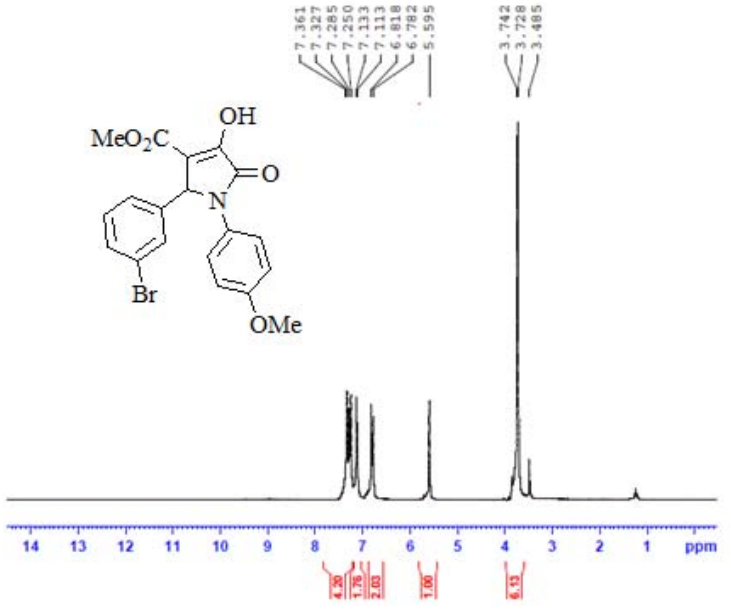

Fig. S-23. ^{1}H-NMR (250 MHz, $CDCl_3$, δ/ppm) spectrum of compound 7a.

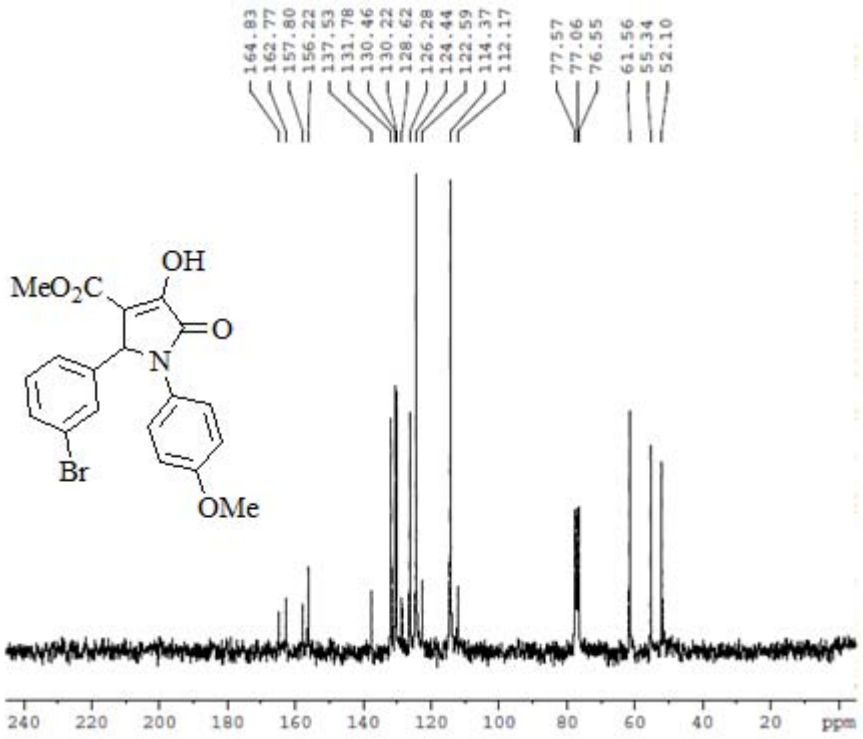

Fig. S-24. ^{13}C-NMR (62.9 MHz, $CDCl_3$, δ/ppm) spectrum of compound 7a.

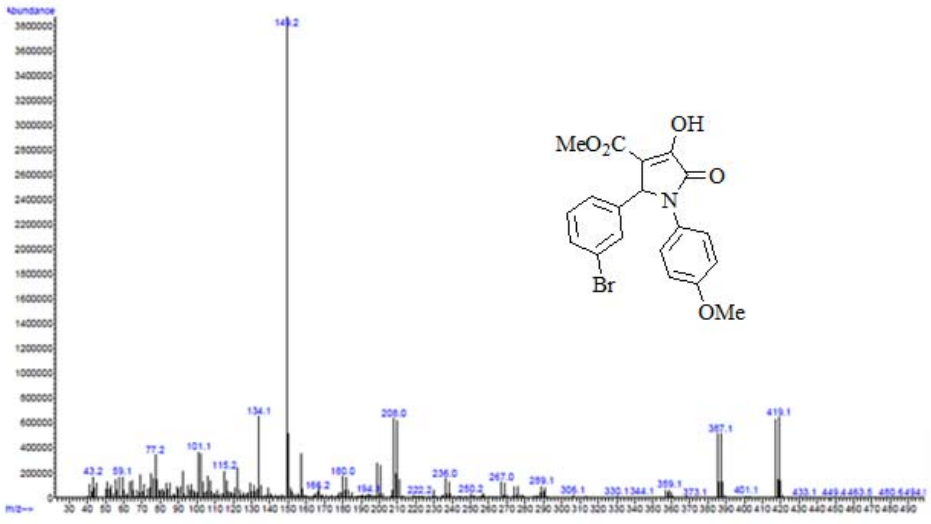

Fig. S-25. Mass spectrum of compound 7a.

Journal of the Serbian Chemical Society
JSCS-info@shd.org.rs • www.shd.org.rs/JSCS
J. Serb. Chem. Soc. *90* (9) 1027–1040 (2025)
JSCS–5437
Original scientific paper
Published 30 September, 2025

Binding elucidation of azo dye with DNA *via* spectroscopic approaches and molecular docking techniques

SHABNAM JAMPOUR-KOLOUR and HAMID DEZHAMPANAH*

Department of Applied Chemistry, Faculty of Chemistry, University of Guilan, P.O.B. 1914, Rasht 0098, Iran

(Received 23 March; revised 10 April; accepted 16 July 2025)

Abstract: In this study, the interaction between a synthesized monoazo disperse dye and calf thymus DNA (Ct-DNA) was investigated *via* UV–Vis spectroscopy, fluorescence and FT-IR spectroscopy and molecular docking calculations. Hypochromic effects on the absorbance and quenching of fluorescence were observed, revealing the binding of azo dye to Ct-DNA. Upon the addition of Ct-DNA, the azo dye showed a hypochromic effect and a small redshift in the wavelength of the absorption spectra, suggesting a groove binding mode of interaction of this probe with Ct-DNA, which was confirmed by the molecular docking results. The values of the binding constant were calculated from the maximum absorption spectra of the azo dye at various Ct-DNA concentrations at several temperatures and the corresponding thermodynamic parameters $\Delta G°$, $\Delta H°$ and $\Delta S°$ were obtained. In addition, fluorescence resonance energy transfer showed that the distance between the donor (EB–Ct-DNA) and acceptor (azo dye) is suitable for energy transfer. Molecular docking analysis revealed that hydrogen bonds and π-electrons on the benzene ring of the azo dye are crucial for binding the azo dye to Ct-DNA. The results of the molecular docking investigations corroborate well with those of the spectral studies and these probes bind to the minor groove of Ct-DNA.

Keywords: calf thymus DNA; fluorescence spectroscopy; molecular modeling; UV–Vis spectroscopy; synthesized azo dyes.

INTRODUCTION

Deoxyribonucleic acid (DNA) and ribonucleic acid (RNA) are the two main forms of nucleic acid. All living organisms, including multicellular mammals and single-celled bacteria, have DNA as their genetic material.[1] DNA is a medium for storing information. For DNA to serve this purpose and maintain information

* Corresponding author. E-mail: h.dpanah@guilan.ac.ir
https://doi.org/10.2298/JSC250328047J

for an organism's lifetime, which for certain trees may span many millennia, it must be incredibly stable. DNA is found in the nucleus of eukaryotic cells, as well as in organelles such as mitochondria and chloroplasts. Like most biological molecules, the structure of DNA is closely related to its function, which involves storing genetic information.

A single strand can always be converted into a complimentary strand owing to the particular hydrogen bond pairing between the GC and AT bases. While these hydrogen bonds help stabilize the double helix structure, they can be disrupted when the DNA needs to be accessed.[2]

When proteins are translated, the information needed to code for amino acids is contained in the base sequence. Through interactions with proteins involved in DNA packaging and regulation, DNA sequences that do not directly encode amino acids can transmit crucial information. The sequences that are accessible to DNA-interacting proteins can vary according to the major and minor grooves of DNA.[3]

DNA serves as a crucial intracellular target, making the design and synthesis of DNA-binding ligands an important area of focus in cancer therapy. The binding of these ligands can cause significant changes in the locations and affinities of DNA binding modes. This offers critical information for creating DNA probes specific to certain sites and possible chemotherapeutic drugs.[4] In recent years, extensive research has been conducted on the interactions between bioactive molecules and DNA, as these studies offer insights into the origins of diseases and the structural properties of DNA and contribute to the design of new chemotherapeutic agents.[5]

Azo dyes are the oldest and most widely used class of industrially manufactured organic dyes because of their many uses in biological research and applications and in the coloring of textiles, leather, paper, food and cosmetic items. Additionally, they are employed in high-tech fields such as dye-sensitized solar cells, lasers and photodynamic treatment.[6] Azo dyes, particularly azo dispersion dyes, contain hydrogen atoms in their molecules; they are traditionally utilized primarily for their classical application in dyeing fibers, for example. In the research of solvent and substituent effects on the λ_{max} values of produced dyes, azobenzene dyes with donor and acceptor terminal groups in conjugated systems of dyes have been used and applied in recent years.[7] These dyes demonstrate notable biological properties and their antibiotic, antifungal and anti-HIV effects render them highly valuable in medicinal chemistry. However, despite their broad applications, azo dyes are known to be carcinogenic when they interact with DNA, leading to mutations.[8–10]

Many studies conducted recently have concentrated on the synthesis and structural characteristics of azo dyes. These advancements have inspired inorg-

anic chemists to explore new techniques for developing more effective and targeted drugs involving azo dyes.[11–13]

The intriguing physicochemical properties of azo compounds have made them compelling subjects of study in physical biochemistry. Their potential to interact with biomolecules such as DNA through intercalation or groove binding offers a unique platform for exploring fundamental molecular interactions. Investigating these interactions not only enhances our understanding of DNA–drug binding mechanisms but also contributes to the rational design of bioactive compounds with diagnostic or therapeutic applications.[14] Therefore, this study aims to bridge the gap between synthetic azo chemistry and the biophysical exploration of Ct-DNA interactions.

In the present research, the molecular details of the interaction between the synthetic azo dye (Scheme 1) and calf thymus DNA (Ct-DNA) were investigated systematically via various spectral techniques, such as synchronous fluorescence, Fourier transform infrared (FT-IR) spectroscopy, ultraviolet–visible spectroscopy and molecular docking studies. The main objectives, therefore, of the present study are to determine the binding constant, binding mode, Stern–Volmer constant (K_{SV}) and rate constant for quenching (k_q), which can be determined by optical absorption, fluorescence spectroscopy and molecular docking. A complete understanding of the BAE–Ct-DNA binding mechanism and the factors that influence it would contribute to the design of new anticancer, antiviral and antibacterial drugs. The chemical structure and IUPAC name of this mono-azo disperse dye derivative are given in Scheme 1, and the abbreviation BAE is used in this document.

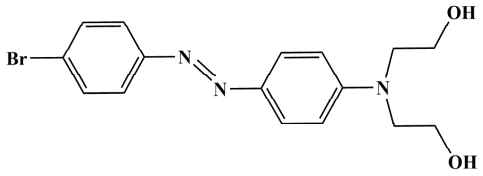

Scheme 1. Molecular structure of (*E*)-2,2'-((4-((4-bromophenyl)diazenyl)phenyl)azanediyl)-bis(ethan-1-ol) (BAE).

EXPERIMENTAL

Materials

Calf thymus DNA from Sigma–Aldrich was dissolved in double-distilled water and stored in the dark at 4 °C. The Ct-DNA solution concentration (3.44×10^{-3} M) was determined *via* an extinction coefficient of 13200 M^{-1} cm^{-1} at 260 nm.[15]

The azo dye BAE was synthesized based on established literature.[16] A stock solution of the azo dye (2×10^{-3} M) was prepared in ethanol and then diluted with 5 mM phosphate buffer to the final concentration. The dye solution was stored in the dark at 4 °C and used fresh after preparation. All the analyses were conducted with 5 mM phosphate buffer at pH 7.20.[17]

UV–Vis absorption spectroscopy

A UV–Vis spectrometer was used to record absorption spectra under simulated physiological conditions (pH 7.2) *via* an Agilent Technologies UV-1601 spectrophotometer. The absorption measurements were taken at a constant concentration of azo dye (67.63 μM) and various concentrations of Ct-DNA (0–31 μM) across temperatures ranging from 298.2 to 313.2 K. A 10 mm quartz cell was employed for measurements in the wavelength range of 300–550 nm. The UV–Vis titration experiments were conducted by adding the Ct-DNA stock solution to a 1 ml cuvette containing the azo dye solution at the appropriate concentration.

Fluorescence spectroscopy study

Similar to the absorption spectra titration experiments, the emission spectra of ethidium bromide (EB) bound to Ct-DNA in the absence and presence of BAE were recorded using a Varian Cary Eclipse spectrofluorometer. A 1.5 ml sample of an EB solution with a fixed concentration (70 μM) was mixed with 330 ml of Ct-DNA solution (209 μM) in a 10 mm quartz cuvette at 25 °C. The mixture of EB–Ct-DNA was titrated with 5 to 463 μl of BAE solution in phosphate buffer. The solutions were excited at 450 nm, and the emitted light intensity was measured at 550–700 nm. The temperature was held constant at ±1 °C during the titration experiments.

The fluorescence intensity of EB–Ct-DNA complex was corrected for the inner filter effect using the following equation:[18]

$$F_{cor} = 10^{(A_1+A_2)/2} F_{obs} \quad (1)w$$

where F_{cor} is the corrected fluorescence intensity, F_{obs} is the observed fluorescence intensity in the experiment, and A_1 and A_2 are the total absorbances of all the components at the excitation wavelength (λ_1) and the emission wavelength (λ_2), respectively.

FT-IR spectroscopic measurements

FT-IR measurements were conducted at room temperature using an Alpha FT-IR spectrometer (Bruker). The Ct-DNA concentration was constant at 500 μM, while the dye concentration was 40 μM. The pellets were prepared by mixing the freeze-dried samples with KBr and compressing them under vacuum for 3 min.[19]

Energy transfer measurements

FRET is broadly used to assign proximities, distances, orientations and dynamic properties of biomolecular structures. The absorption spectrum of BAE and the fluorescence spectrum of DNA–BAE were recorded, covering a wavelength range of 530–700 nm with 12.10 μM of BAE and DNA at 298.2 K.

Molecular docking

Molecular docking is an effective technique for understanding the interaction between ligands and biological targets and is crucial for clinical treatment and the recognition of nucleic acid molecules.[20] In this case, AutoDock 4.2 software was used to study molecular docking.[21] The 3D structure of BAE was determined via Gauss View 5.0. The geometry of the BAE ligand was optimized *via* density functional theory (DFT) (B3LYP/6-31G*(d,p)) *via* Gaussian 03. Additionally, the Ct-DNA structure was taken from the protein data bank (http://rcsb.org, PDB ID: 1bna); then, all the ligands and water molecules were removed and hydrogen atoms were added. Here, AutoDock tools software was used to convert DNA and ligands to pdbqt format, and the connection between the two was performed *via* AutoDock Vina software. The grid box used in this study was defined with dimensions of 30 Å×30 Å×50

Å and a grid spacing of 1 Å, centered at coordinates (15.422, 21.448, 8.999). Finally, the model and binding sites were evaluated *via* Discovery Studio, and the atoms in the hydrogen bonds and hydrophobic residues in the complex were evaluated *via* Ligaplot.

RESULTS AND DISCUSSION

UV–Vis study of the BAE interaction with Ct-DNA

UV–Vis spectroscopy is an easily available technique for investigating ligand-binding reactions, enzyme catalysis and conformational change transitions in proteins and nucleic acids.

The changes in the absorption spectra of dye (ligand) in terms of wavelength changes, hyperchromic/hypochromic effects, and isosbestic points can be used to study the interactions of certain functional groups with $\pi \rightarrow \pi^*$ and $n \rightarrow \pi^*$ transitions with Ct-DNA. These spectrum characteristics result from molecular interactions that are intimately linked to variations in bonding energy levels.[22]

Generally, hyperchromic/hypochromic are the two spectral features, which are closely related to the double helix structure of Ct-DNA.[23] The hyperchromic effect (increase in absorption of the DNA band) and the hypochromic effect (decrease in absorption of the Ct-DNA band) are the spectral changes typical of the interaction of a compound with Ct-DNA helix. Hypochromic effect results from contraction of the Ct-DNA helix as well as changes in its conformation, while hyperchromic effect is due to the damage to the Ct-DNA double helix structure. Moreover, the binding of an intercalative molecule to Ct-DNA is accompanied by hypochromic effect (30 %) and a significant red shift (> 15 nm) is characteristic of strong π–π stacking interaction between the aromatic chromophore of the ligand and Ct-DNA base pairs. On the other hand, groove binding results only in a small shift and moderate hypochromic effect in the absorption spectra.

The characteristic change in the maximum absorption wavelength of BAE (454 nm) during the titration of Ct-DNA is shown in Fig. 1. Upon the addition of varying concentrations of Ct-DNA, the absorption intensity gradually decreases and shifts to longer wavelengths (bathochromic shift) by approximately 3 nm in terms of the absorption maxima, indicating a shift to a more polar environment upon interaction. These remarkable hypochromic effects and small red shift indicate the existence of strong interactions between BAE and Ct-DNA, most likely *via* the groove binding mode. These spectral properties indicate a high affinity of the complex for binding to Ct-DNA.

On the basis of the changes in the absorbance of BAE at 454 nm during titration with Ct-DNA, the intrinsic binding constant (K_b) between BAE and Ct--DNA was calculated *via* following equation:

$$\frac{A_0}{A - A_0} = \frac{\varepsilon_d}{\varepsilon_{H\text{-}d} - \varepsilon_d} + \frac{\varepsilon_d}{\varepsilon_{H\text{-}d} - \varepsilon_d} \frac{1}{K_b[DNA]} \quad (2)$$

Here, A_0 and A represent the absorbances of the BAE in the absence and presence of Ct-DNA, respectively. ε_d and $\varepsilon_{H\text{-}d}$ are the corresponding absorption coefficients of free BAE and BAE in the presence of Ct-DNA (fully bound form), respectively. A plot of $A_0/(A–A_0)$ *versus* 1/[DNA] yields a slope of $(\varepsilon_d/(\varepsilon_{H\text{-}d} - \varepsilon_d)(1/K_b)$ and a *Y*-intercept equal to $(\varepsilon_d/(\varepsilon_{H\text{-}d} - \varepsilon_d)$, where K_b is the ratio of the intercept to the slope. The linear plot for the binding of BAE to Ct-DNA is shown in Fig. S-1 of the Supplementary material to this paper, and the intrinsic binding constant, K_b ($(4.91\pm0.04)\times10^6$ L mol^{-1}) at 454 nm was calculated on the basis of the ratio of the intercept to the slope of the corresponding linear equation. The results are shown in Table I at various temperatures ranging from 298.2 to 318.2 K. The observed values of K_b have also revealed that the BAE azo dye binds to Ct-DNA *via* groove mode.[23]

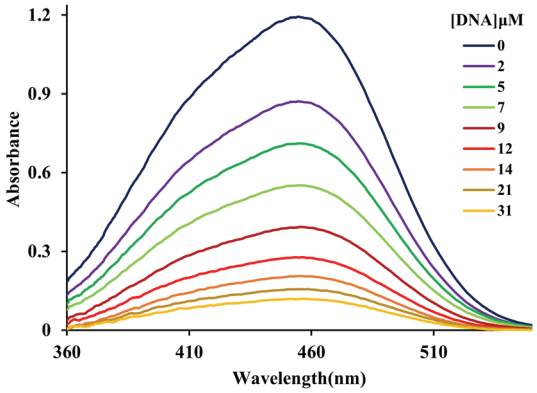

Fig. 1. UV–Vis absorption spectra of Ct-DNA-BAE at 298.2 K in 5 mM phosphate buffer (pH 7.2) with various concentrations of Ct-DNA ranging from 0 to 22.43 μM.

Determination of thermodynamic functions

To facilitate the binding of a small molecule to a biological macromolecule, hydrogen bonding, van der Waals interactions, electrostatic forces and hydrophobic contacts play crucial roles. The primary forces involved in the binding process can be explained by the signs and significance of thermodynamic parameters, such as the entropy change ($\Delta S°$) and enthalpy change ($\Delta H°$). Therefore, the van't Hoff equation was used to evaluate the thermodynamic parameters related to the acquired binding constants:

$$\ln K = -\frac{\Delta H^\circ}{RT} + \frac{\Delta S^\circ}{R} \tag{3}$$

where K is the binding constant at the appropriate temperature, and R and T are the gas constant and absolute temperature, respectively. The effects of temperature variation on the binding constant were investigated at 298.2, 303.2, 313.2

and 318.2 K. The plots of ln *K versus* 1/*T* can be used to determine the values of $\Delta H°$ and $\Delta S°$. The value of $\Delta H°$ can be considered temperature-independent when the temperature varies only slightly. Therefore, Eq. (4) can be used to determine the free energy change ($\Delta G°$):

$$\Delta G^\circ = \Delta H^\circ - T\Delta S^\circ = -RT \ln K \quad (4)$$

Based on the binding constants of BAE to Ct-DNA at various temperatures, the thermodynamic parameters ($\Delta H°$, $\Delta G°$ and $\Delta S°$) were calculated *via* these equations, with the results presented in Fig. S-2 and Table I. The negative values of $\Delta G°$ under all the conditions indicate that the interaction was spontaneous.[24]

TABLE I. Binding constant and thermodynamic parameters for the BAE–Ct-DNA system from UV–Vis data at different temperatures

T / K	$K_b \times 10^{-6}$/ L mol^{-1}	$\Delta H°$ / kJ mol^{-1}	$\Delta S°$ / J mol^{-1} K^{-1}	$\Delta G°$ / kJ mol^{-1}
298.2	4.91±0.04	28.62±0.04	224.10±0.01	–38.17±0.01
303.2	6.07±0.05		224.30±0.02	–39.35±0.01
313.2	8.48±0.06		224.00±0.01	–41.51±0.02
318.2	10.3±0.3		224.20±0.02	–42.69±0.01

The sign and magnitude of the thermodynamic parameters for different types of interactions in protein association processes were described by Ross and Subramanyam.[25] Considering the water structure, a positive value of $\Delta S°$ is commonly considered proof of hydrophobic interactions. The interaction process is spontaneous, as indicated by the negative value of $\Delta G°$. The positive enthalpy and entropy changes of the interaction between BAE and Ct-DNA indicate that the binding is primarily entropy-driven, with enthalpy change being unfavorable for this process. Thus, hydrophobic forces play a major role in the binding BAE to Ct-DNA.[24] Overall, the consistency between the molecular docking results and the thermodynamic data reinforces the reliability of our findings.

Fluorescence studies of Ct-DNA and BAE

Fluorescence quenching measurement is an important method for studying interactions between small molecules and biomolecules. Upon the addition of increasing concentrations of BAE (0–168 μM) to the EB–Ct-DNA system, the fluorescence peak slightly red-shifted at 604 nm, and the intensity of the EB–Ct--DNA system attenuated regularly with increasing concentrations of BAE, which indicated that interactions occurred between BAE and the EB–Ct-DNA system. The results are shown in Fig. S-3 of the Supplementary material. This finding indicated that BAE binding with EB–Ct-DNA formed a new non-fluorescent EB–Ct-DNA–BAE complex, which decreased the fluorescence intensity of EB––Ct-DNA. The results revealed that BAE cannot intercalate into Ct-DNA in the presence of EB. Then, the intensity of the EB–Ct-DNA system fluorescence dec-

reased because BAE bound with EB–Ct-DNA. The fluorescence emission peak slightly red-shifted by 2 nm, but the peak shape did not significantly change, which meant that the microenvironment of the EB had changed and that BAE had reacted with EB–Ct-DNA.[26] To further elucidate the quenching mechanism, fluorescence quenching was examined *via* the Stern–Volmer equation:

$$\frac{F_0}{F} = 1 + K_{SV}[Q] = 1 + k_q \tau_0 [Q] \quad (5)$$

where F_0 and F are the fluorescence intensities of EB–Ct-DNA in the absence and presence of the quencher BAE, respectively; K_{SV} is the Stern–Volmer quenching constant; k_q is the EB–Ct-DNA complex quenching rate constant; τ_0 is the fluorophore's typical lifetime in the absence of BAE (10^{-8} s); and [Q] is the BAE concentration.[27]

Fig. S-4 of the Supplementary material shows the Stern–Volmer plot for the fluorescence quenching of the EB–Ct-DNA complex by BAE, which has good linearity (R^2 = 0.98). The quenching constants K_{SV} and k_q are shown in Table II for BAE, the calculated value of k_q was much greater than the diffusion-controlled quenching rate constant of various quenchers with the biopolymer (2×10^{10} L mol^{-1} s^{-1}) in aqueous medium.[28] Thus, the fluorescence enhancement is not initiated by a dynamic process. It is suggested that a static process involves complex formation in the ground state.[29]

TABLE II. Quenching constants (K_{SV} and k_q) obtained from the fluorescence measurements

Dye	T / K	K_{SV} / L mol^{-1}	k_q / L mol^{-1} s^{-1}	R^2
BAE	298.2	$(1.29\pm0.03)\times10^4$	$(1.29\pm0.03)\times10^{12}$	0.98

Energy transfer between EB–Ct-DNA and BAE

Fluorescence resonance energy transfer (FRET) occurs when the emission spectrum of a fluorophore (donor) overlaps with the absorption spectrum of another molecule (acceptor) and the distance between them is less than 8 nm.[30]

To enhance FRET efficiency, the EB–Ct-DNA complex was used as the energy donor and BAE as the energy acceptor. The distance between the donor and the acceptor can be ascertained *via* FRET measurements. In our experiment, Förster energy transfer was used to determine the binding distance (r) for energy transfer from EB–Ct-DNA and BAE azo dye. The energy transfer parameter can be computed *via* the following equation:[31]

$$E = 1 - \frac{F_0}{F} = \frac{R_0^6}{R_0^6 + r^6} \quad (6)$$

where F_0 and F are the fluorescence intensities of EB–Ct-DNA and BAE–Ct--DNA–EB, respectively. R_0 is the critical distance when 50 % of the excitation energy is shifted to the acceptor. R_0 can be calculated *via* the following equation:[32]

$$R_0^6 = 8.79\times10^{-25} K^2 n^{-4} \phi J \tag{7}$$

This formula includes the dipole's spatial orientation factor (K^2), the medium's refractive index (n), the donor's fluorescence quantum yield (ϕ) and the spectral overlap effect between the donor's emission and acceptor's absorption spectra (J), which is determined *via* the following formula:

$$J = \frac{\int_0^\infty F(\lambda)\varepsilon(\lambda)\lambda^4 \mathrm{d}\lambda}{\int_0^\infty F(\lambda)\mathrm{d}\lambda} \tag{8}$$

In this formula, $F(\lambda)$ is the fluorescence intensity of the donor and $\varepsilon(\lambda)$ represents the molar absorption coefficient of the acceptor at wavelength λ.[33] Fig. S-5a and b of the Supplementary material show the overlap between the absorption spectrum of BAE and the fluorescence emission spectrum of EB–Ct-DNA, which is K^2 = 2/3, n = 1.33 and ϕ = 0.16 for EB–Ct-DNA.[34] According to Eqs. (6)–(8), the parameters J, R_0, E and r were 1.21×10^{13} cm^3 L mol^{-1}, 2.26 nm, 0.10 nm and 2.99 nm, respectively. The value of r is the distance from the BAE to the EB–Ct-DNA, is less than 8 nm and $0.5R_0 < r < 1.5R_0$. This result indicates that the binding obeyed the conditions of Förester's energy transfer theory and energy transfer from EB–Ct-DNA to the BAE has a high probability.[35]

FT-IR studies of Ct-DNA and BAE

To verify the structural changes in Ct-DNA upon the addition of BAE, FT--IR spectroscopy was employed to analyze and examine the secondary structure of both the Ct-DNA and BAE–Ct-DNA complexes. The FT-IR spectra of the BAE–Ct-DNA system at 950–1750 cm^{-1} are presented in Figs. S-6 and S-7 of the Supplementary material. The concentrations of Ct-DNA and BAE were fixed at 500 and 40 μM, respectively. The intensity of the absorption spectra generally significantly increased with the addition of BAE.

The stretching vibrations of C=O and C=N bonds, as well as the bending vibrations of exocyclic –NH_2 groups found in Ct-DNA bases, are the main sources of the first region (approximately 1600–1750 cm^{-1}) of the infrared spectrum of Ct-DNA.[36] Purine and pyrimidine ring vibrations are the main sources of the second region (~1600–1500 cm^{-1}), and the symmetric and asymmetric stretching of PO_2 groups within the phosphodiester-deoxyribose backbone constitutes the third region (~950–1250 cm^{-1}).

Strong bands originating from the carbonyl stretching modes of DNA bases are found in the 1750–1550 cm^{-1} region. These modes are superposed to form the spectrum in this area. Certain bands could have frequencies that are near those of nearby peaks. These summits may be concealed or covert. We used the second derivative approach to perform spectral decomposition for free Ct-DNA and BAE–Ct-DNA, as shown in Figs. S-8 and S-9 of the Supplementary material, to further examine the associated vibrations. Table III summarizes the proposed assignment of the individual vibration bonds of Ct-DNA.

TABLE III. The assignments of individual peaks in the Ct-DNA spectra

Abs.max., cm^{-1}	Band's vibrations of Ct-DNA	Abs.max., cm^{-1}	Band's vibrations of Ct-DNA
1688	C2=O of thymine	1579	C=N(H2) of guanine
1673	C6=O of guanine	1573	C=N7 of guanine
1658	C4=O of thymine	1105	Group PO_2 (symmetrical)
1641	Thymine ring	1058	C–O of deoxyribose
1619	Adenine ring	1028	Deoxyribose ring

The vibrations for the decomposed bands of DNA are C2=O for thymine, C6=O for guanine, C4=O for thymine, the thymine ring, the adenine ring, C=N(H2) for guanine and C=N7 for guanine.

Based on the data in Table S-I and Fig. S-8 and Fig. S-9, it can be concluded that the most pronounced changes are in the relative intensity of thymine ring. Additionally, guanine bands are more sensitive to small BAE–Ct-DNA. In the 1100–800 cm^{-1} region, there was a shift in the 1028 cm^{-1} band (most likely corresponding to the deoxyribose ring) to 1030 cm^{-1}. For BAE–Ct-DNA and C–O of deoxyribose, a slight shift and a 10 cm^{-1} shift in the 1105 cm^{-1} band (arising from the symmetric vibration of the O=P=O group) were observed. Thus, our data revealed the preferred binding of BAE to guanine bases and demonstrated good agreement with previous results. The structures of free Ct-DNA alone and upon interaction with BAE were quantitatively analyzed by fitting analysis, and the results are presented in Table S-I. These results are consistent with the FT-IR spectroscopy findings, which showed that BAE binding induces structural changes in Ct-DNA.[37]

Molecular docking studies

Molecular docking is a valuable tool for validating experimental data and providing deeper insight into ligand–Ct-DNA interactions. Molecular modeling was performed to predict the possible orientation of the newly formed complex between the Ct-DNA and the ligand. The interaction of Ct-DNA with ligands is shown in Figs. 2 and S-10 of the Supplementary material. It is caused by hydrophobic forces and hydrogen bonds.[38,39] The ligand can slide between DG4 and N3 with –29.4 kJ mol^{-1} into the Ct-DNA; this mode, which has the lowest

energy and the highest binding affinity, was chosen as the most favorable binding site. Therefore, it can be concluded that the results of molecular binding can further confirm the above experimental results.

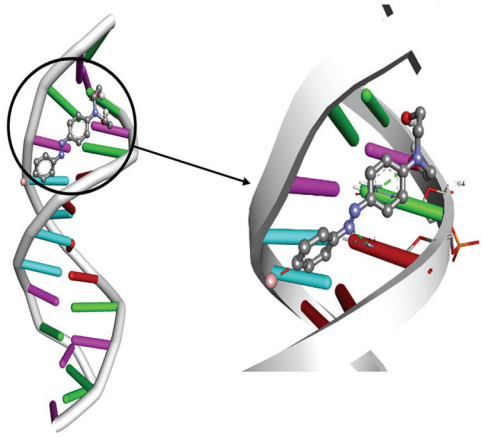

Fig. 2. Complex structure used in molecular docking.

The azo dye molecule is embedded within the groove of the Ct-DNA. The molecule is aligned along the groove without significant disruption of base stacking, indicating that it fits into the DNA structure without being inserted between base pairs. This observation is supported by the ligplot (Fig. S-10), which highlights specific hydrogen bonding and van der Waals interactions between the azo compound (Unk1) and nearby nucleotide residues (such as dg22 and dc23). A hydrogen bond at a distance of 3.06 Å further confirms the stable, non-covalent interaction typically observed in groove binders. The positions near the sugar--phosphate backbone and bases such as dc21, da6 and dg4 also align with minor groove accessibility. Collectively, these data strongly indicate that the azo dye interacts with Ct-DNA through minor groove binding, which is stabilized by hydrogen bonding and hydrophobic interactions. This type of interaction is particularly relevant in biophysical studies, as it may influence Ct-DNA conformation and gene expression without causing strand separation, making azo dyes potential candidates for gene-targeted diagnostics or therapeutics.[40]

CONCLUSION

The binding interactions between the monoazo dispersion dye (BAE) and Ct-DNA were thoroughly investigated, in this study, using molecular docking in conjunction with a variety of biophysical techniques. FT-IR spectroscopy, fluorescence and UV–Vis absorption analyses confirmed the formation of the BAE––Ct-DNA complex, and the calculated binding constant (~10^6 M^{-1}) is consistent with a groove-binding mode. Förster resonance energy transfer (FRET) analysis

showed a donor–acceptor distance of 2.99 nm between EB–Ct-DNA and BAE, indicating close proximity suitable for energy transfer. Thermodynamic parameters indicated that the binding is primarily entropy-driven ($\Delta S° > 0$) and endothermic ($\Delta H° > 0$), with the spontaneous nature of the interaction supported by negative free energy changes ($\Delta G° < 0$). Additionally, thermodynamic characteristics indicated that hydrophobic forces dominate the binding interaction, with hydrogen bonding playing a minimal role. This conclusion was corroborated by molecular docking experiments, which demonstrated a favorable binding energy and particular interactions between BAE and guanine-rich areas inside the DNA minor groove. Crucially, FT-IR spectroscopy revealed significant alterations in the thymine ring and phosphate backbone vibrational frequencies, suggesting that BAE interacts with DNA *via* the minor groove.

These results collectively offer strong proof that BAE primarily binds to Ct--DNA through minor groove binding, which is maintained by hydrogen bonding and hydrophobic interactions. This study advances our knowledge of azo dyes' DNA-binding capabilities and establishes a framework for future research into their biological activity and possible genotoxic consequences.

SUPPLEMENTARY MATERIAL

Additional data and information are available electronically at the pages of journal website: https://www.shd-pub.org.rs/index.php/JSCS/article/view/13313, or from the corresponding author on request.

Acknowledgement. This work has been supported by the University of Guilan.

ИЗВОД

ИСПИТИВАЊЕ ВЕЗИВАЊА АЗО БОЈЕ ЗА ДНК ПРИМЕНОМ СПЕКТРОСКОПСКИЈЕ И МЕТОДЕ МОЛЕКУЛСКОГ МОДЕЛОВАЊА

SHABNAM JAMPOUR-KOLOUR и HAMID DEZHAMPANAH

Department of Applied Chemistry, Faculty of Chemistry, University of Guilan, P.O.B. 1914, Rasht 0098, Iran

У овој студији је испитивана интеракција између синтетисане моноазо дисперзне боје и ДНК тимуса телета (Ct-DNA) применом UV–Vis, флуоресцентне и FT-IR спектроскопије и молекулског моделовања. На апсорпционим и флуоресцентним спектрима је уочен хипохромни ефекат и ефекат гашења, што је потврдило везивање азо боје за Ct-DNA. Након везивања за ДНК, азо боја је изазвала хипохромни ефекат и мало померање спектра ка црвеном делу, што је указало да везивање обухвата жљеб ДНК и накнадно је потврђено резултатима молекулског моделовања. Израчунате су константе везивања из интензитета максимума апсорпционих спектара за азо боју и различите концентрације Ct-DNA, на неколико температура, као и термодинамички параметри $\Delta G°$, $\Delta H°$ и $\Delta S°$. Флуоресцентни резонантни енергетски трансфер је показао да је размак између донора (Ct-DNA) и акцептора (азо боја) одговарајући за пренос енергије. Молекулско моделовање је показало да су водоничне везе и π-електрони бензеновог прстена азо боје кључни за везивање. Резултати молекулског моделовања потврђују резултате спектралне анализе, односно да се боја везује за мали жљеб Ct-DNA.

(Примљено 28. марта, ревидирано 10. априла, прихваћено 16. јула 2025)

REFERENCES

1. A. Travers , G. Muskhelishvili, *FEBS J.* **282** (2015) 2279 (https://doi.org/10.1111/febs.13307)
2. C. Nieuwland, T. A. Hamlin , C. F. Guerra , G. Barone , F. M. Bickelhaupt, *Chem. Open* **11** (2022) 2 (https://doi.org/10.1002/open.202100231)
3. S. Minchin, J. Lodge, *Essays Biochem.* **63** (2019) 433 (https://doi.org/10.1042/EBC20180038)
4. S. Gupta, S. Aggarwal, M. Munde, *ACS Omega* **8** (2023) 4554 (http://doi.org/10.1021/acsomega.2c01557)
5. K. Shridhar, G. K.Walia, A. Aggarwal, S. Gulati, A. Geetha, D. Prabhakaran, P. K. Dhillon, P. Rajaraman, *Oral Oncology* **53** (2016) 1 (http://doi.org/10.1016/j.oraloncology.2015.11.012)
6. S. Benkhaya, S. E. Mrabet, A. Harfi, *Heliyon* **6** (2020) 03271 (http://doi.org/10.1016/j.heliyon.2020.e03271)
7. Y. X. Liu, H. W. Mo, Z. Lv, F. Shen, C. L. Zhan, Y. Y. Qi, Z. Mao, X. Y. Le, *Trans. Met. Chem*. **43** (2018) 259 (http://doi.org/10.1007/s11243-018-0211-y)
8. M. Maliyappa, J. Keshavayya, N. Mallikarjuna, P. M. Krishna, N. Shivakumara, T. Sandeep, K. Sailaja, M. A. Nazrulla, *J. Mol Struct*. **1179** (2019) 630 (http://doi.org/10.1016/j.molstruc.2018.11.041)
9. A. S. Mondal, A. K. Pramanik, L. Patra, C. K. Manna, T. K. Mondal, *J. Mol. Struct.* **1146** (2017) 146 (http://doi.org/10.1016/j.molstruc.2017.05.131)
10. Y. Ali, S. Abd Hamid, U. Rashid, *Med. Chem.* **18** (2018) 1548 (http://doi.org/10.2174/1389557518666180524113111)
11. M. Y. Zhao, Y. F. Tang, G. Z. Han, *Molecules* **28** (2023) 6741 (http://doi.org/10.3390/molecules28186741)
12. N. Venugopal, G. Krishnamurthy, H. S. Bhojya Naik, J. D. Manohara, *J. Inorg. Organomet. Polym. Mat.* **30** (2020) 2608 (http://doi.org/10.1007/s10904-019-01394-8)
13. S. Qamar, Z. Akhter, S. Yousuf, H. Bano, F. Perveen, *J. Mol. Struct*. **1197** (2019) 345 (https://doi.org/10.1016/j.molstruc.2019.07.069)
14. S. Benkhaya, S. M'rabet, A. El Harfi. *Heliyon* **6** (2020) 3072. (https://doi.org/10.1016/j.heliyon.2020.e03271)
15. S. Das, S. Chatterjee, S. Pramanik, P. S. Devi, G. S. Kumar, *J. Photochem. Photobiol., B* **178** (2018) 339 (https://doi.org/10.1016/j.jphotobiol.2017.10.039)
16. M. R. Yazdanbakhsh, A. Mohammadi, *J. Mol. Liq*. **148** (2009) 35 (http://doi.org/10.1016/j.molliq.2009.06.001)
17. J. Albani, *Principles and applications of fluorescence spectroscopy*, Wiley-Blackwell, Hoboken, NJ, 2007 (http://doi.org/10.1002/9780470692059)
18. B. Kavitha, M. Sravanthi, P. Saritha Redd, *J. Mol. Struct*. **1185** (2019) 153 (https://doi.org/10.1016/j.molstruc.2019.02.093)
19. L. Hana, Y. Zhoub, X. Huangb, M. Xiaoa, L. Zhoua, J. Zhoua, A. Wangc, J. Shena, *Spectrochim. Acta, A* **123** (2014) 497 (http://dx.doi.org/10.1016/j.saa.2013.11.088)
20. X. Li, Y. Yuan, Y. Wang, F. Zhang, R. Zhao, D. Shao, S. Bi, *Process Biochem*. **108** (2021) 26 (http://doi.org/10.1016/j.procbio.2021.05.023)
21. J. Antosiewicz, D. Shugar, *Biophys. Rev*. **8** (2016) 163 (http://doi.org/10.1007/s12551-016-0197-7)
22. Y. Pin, Z. Chunqiong, *Acta Chim. Sin.* **61** (2003) 1455 (in Chinese) (https://sioc-journal.cn/Jwk_hxxb/EN/Y2003/V61/I9/1455#1)

23. Z. Shokohi-Pour, H. Chiniforoshan, M. R. Sabzalian, S. A. Esmaeili, A. A. Momtazi--Borojeni, *J. Biomol. Struct. Dyn*. **36** (2018), 532 (http://dx.doi.org/10.1080/07391102.2017.1287006)
24. K. Xia, G. Zhang, S. Li, D. Gong, *J. Fluoresc*. **27** (2017) 1815 (http://doi.org/10.1007/s10895-017-2119-x)
25. P. D. Ross, S. Subramanian, *Biochemistry* **20** (1981) 3096 (http://doi.org/10.1021/bi00514a017)
26. B. Shen, H. Yang, J. C. X. Liu, M. Zhou, *Spectrochim. Acta, A* **261** (2021) 1386 (https://doi.org/10.1016/j.saa.2021.119998)
27. S. Ansari, I. Yousuf, F. Arjmand, M. K. Siddiqi, S. Naqvi, *Int. J. Biol. Macromol*. **116** (2018) 1105 (http://doi.org/10.1016/j.ijbiomac.2018.05.052)
28. W. R. Ware, *J. Phys. Chem.* **66** (1962) 455 (https://doi.org/10.1021/j100809a020)
29. W. He, Y. Li, J. Tang, F. Luan, J. Jin, Z. Hu, *Int. J. Biol. Macromol*. **39** (2006) 165 (https://doi.org/10.1016/j.ijbiomac.2005.11.003)
30. X. Y. Cao, S. Wang, S. Q. Tian, H. Lou, Y. C. Kong, Z. J. Yang, J. L. Liu, *Spectrochim. Acta, A* **203** (2018) 301 (http://doi.org/10.1016/j.saa.2018.05.091)
31. S. S. Ansari, I. Yousuf, F. Arjmand, M. K. Siddiqi, S. Naqvi, *Int. J. Biol. Macromol*. **116** (2018) 1105 (http://doi.org/10.1016/j.ijbiomac.2018.05.052)
32. H. Li, H. Dou, Y. Zhang, Z. Li, R. Wang, J. Chang, *Spectrochim. Acta, A* **136** (2015) 416 (https://doi.org/10.1016/j.saa.2014.09.051)
33. N. Vandenberk, A. Barth, D. Borrenberghs, J. Hofkens, J. Hendrix, *J. Phys. Chem., B* **122** (2018) 4249 (http://doi.org/10.1021/acs.jpcb.8b00108)
34. X. Li, Y. Yuan, Y. Wang, F. Zhang, R. Zhao, D. Shao, S. Bi, *Process Biochem*. **108** (2021) 26–33 (https://doi.org/10.1016/j.procbio.2021.05.023)
35. *Principles of Fluorescence Spectroscopy*, 3rd ed., J. R. Lakowicz, Ed., Springer, Boston, MA, 2006 (http://doi.org/10.1007/978-0-387-46312-4)
36. S. Bi, X. Li, Z. Ren, B. Yang, Y. Wang, F. Zhang, Y. Yuan, D. Shao, R. Zhao, *Luminescence* **37** (2022) 1275 (http://doi.org/10.1002/bio.4293)
37. E. Tymchenko, V. Glova, A. Soldatova, E. Chikhirzhina, A. Polyanichko, *J. Phys.: Conf. Ser.* **1400** (2019) 1742 (http://doi.org/10.1088/1742-6596/1400/3/033004)
38. S. Ponkarpagam, K. N. Vennila, K. P. Elango, *Spectrochim. Acta, A* **278** (2022) 121351 (http://doi.org/10.1016/j.saa.2022.121351)
39. B. Shen, H. Yang, J. Chen, X. Liu, M. Zhou, *Spectrochim. Acta, A* **261** (2021) 119998 (https://doi.org/10.1016/j.saa.2021.119998)
40. E. S. Istifli, *Colorants* **1** (2022) 236 (https://doi.org/10.3390/colorants1020015).

Journal of the Serbian Chemical Society
JSCS@tmf.bg.ac.rs • www.shd.org.rs/JSCS
J. Serb. Chem. Soc. 90 (9) S325–S331 (2025) *Supplementary material*

SUPPLEMENTARY MATERIAL TO

Binding elucidation of azo dye with DNA *via* spectroscopic approaches and molecular docking techniques

SHABNAM JAMPOUR-KOLOUR and HAMID DEZHAMPANAH*

Department of Applied Chemistry, Faculty of Chemistry, University of Guilan, P.O.B. 1914, Rasht 0098, Iran

J. Serb. Chem. Soc. 90 (9) (2025) 1027–1040

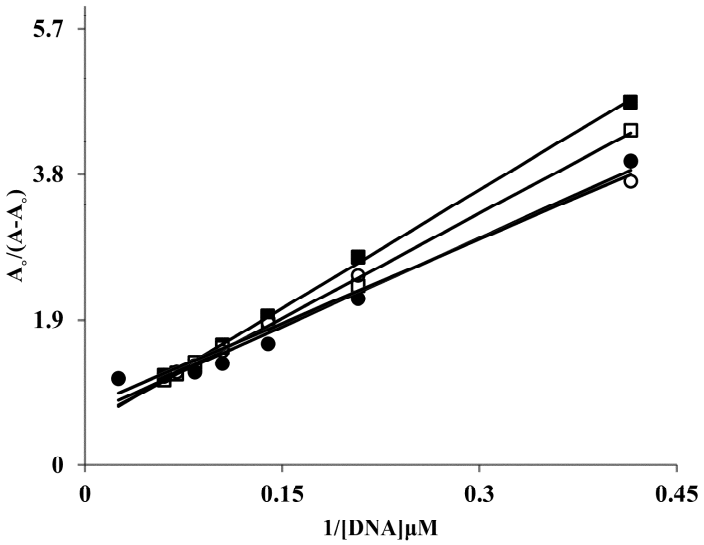

Fig. S-1. Benesi Hildbrand plots for the interactions of Ct-DNA-BAE. (■298.2K, □ 303.2K, ○ 313.2K, ● 318.2K)

* Corresponding author. E-mail: h.dpanah@guilan.ac.ir

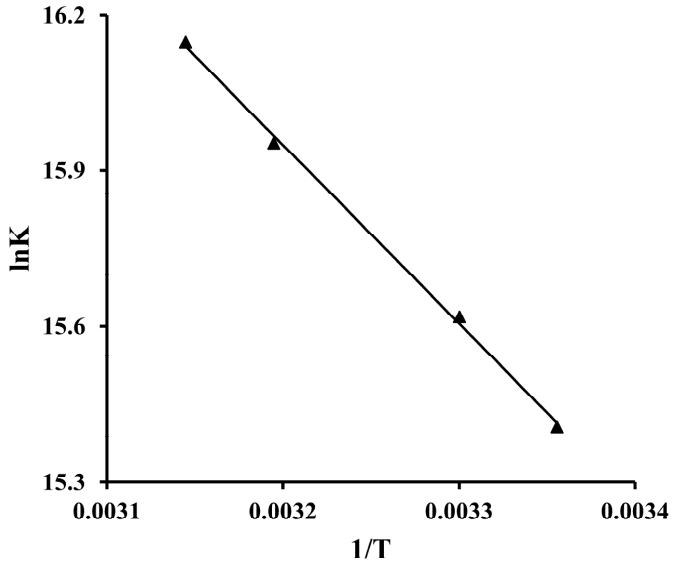

Fig. S-2. Plots of lnK vs. 1/T for the determination of thermodynamic parameters.

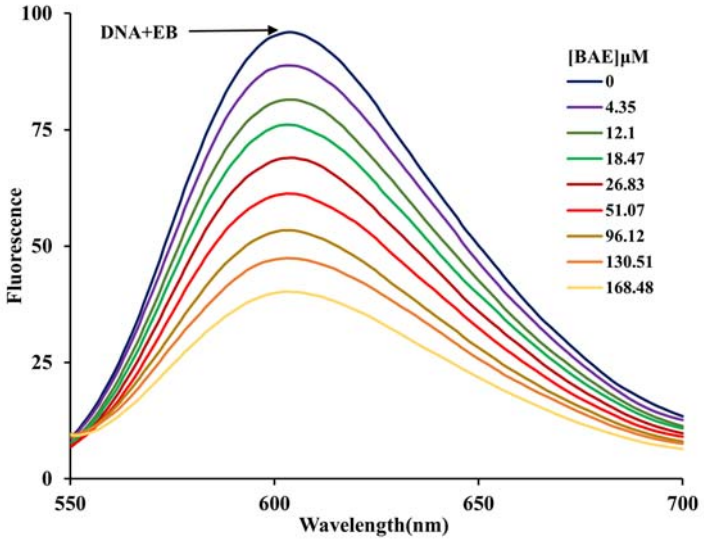

Fig. S-3. Fluorescence quenching EB-Ct-DNA system in the absence and presence of BAE: [Ct-DNA] = 160 µM, [EB] = 320 µM, and [BAE] azo dye from 0 to 168 µM.

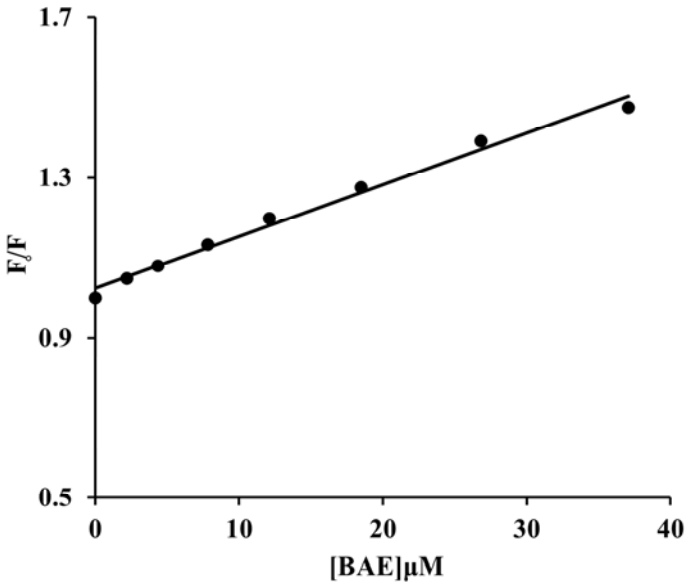

Fig. S-4. Linear Stern–Volmer plot of the EB-Ct-DNA system in the absence and presence of BAE at 298.2 K.

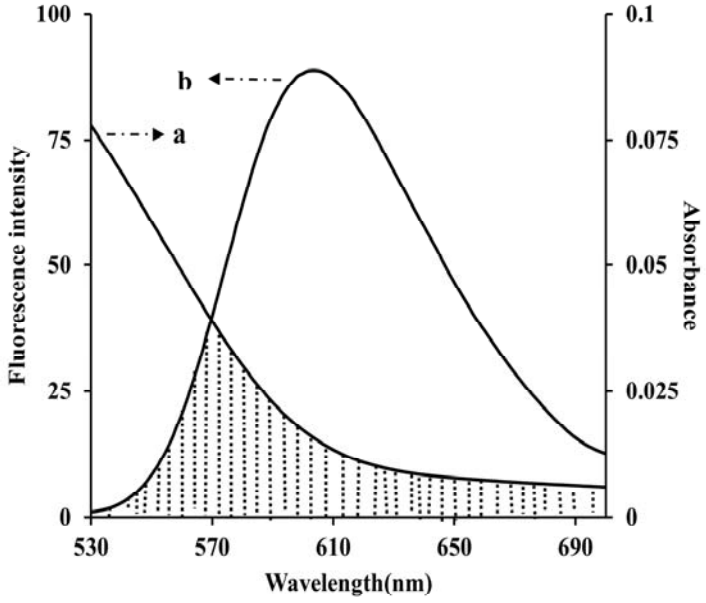

Fig. S-5. Overlap of the absorption spectra of BAE (a) with fluorescence emission of Ct-DNA-EB (b) in 5 mM phosphate buffer, pH = 7.2, at 298.2 K, λ_{ex} = 450 nm [BAE] = [Ct-DNA-EB] = 12.10 μM.

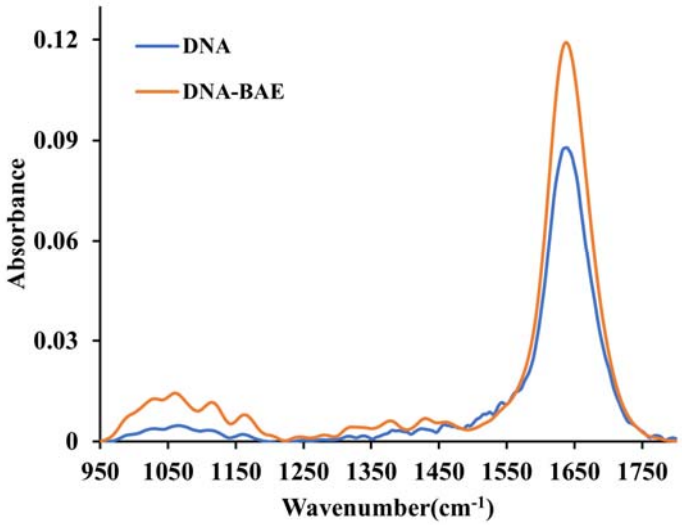

Fig. S-6. FT-IR spectra of the BAE-Ct-DNA system. The concentration of Ct-DNA was fixed at 500 μM, and the BAE concentration was fixed at 40 μM.

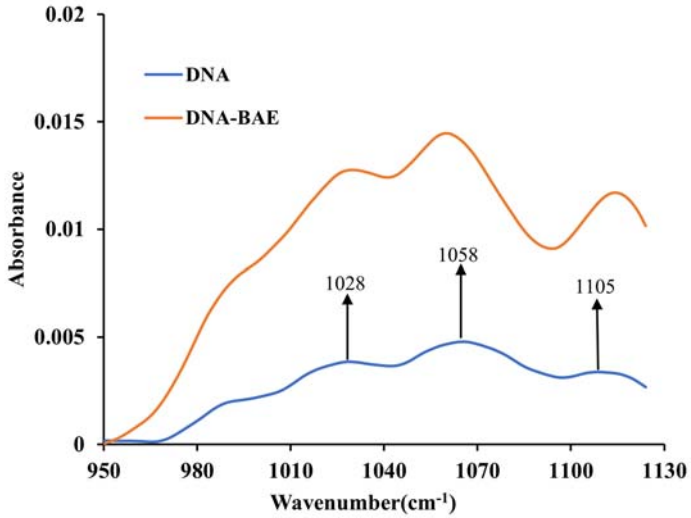

Fig. S-7. Highlights of the FT-IR spectra of the BAE-Ct-DNA system at 950-1130 cm^{-1} region. The concentration of Ct-DNA was fixed at 500 μM, and the BAE concentration was fixed at 40 μM.

TABLE S-I. the relative contribution of bands to the total absorption in 1750–1550 cm^{-1} region in %

Peak	Ct-DNA%	Ct-DNA-BAE%
1688	11.98	16.67
1673	7.02	6.54
1658	12.75	13.08
1641	29.84	26.16
1619	23.88	22.76
1579	7.52	5.03
1573	7.01	9.45

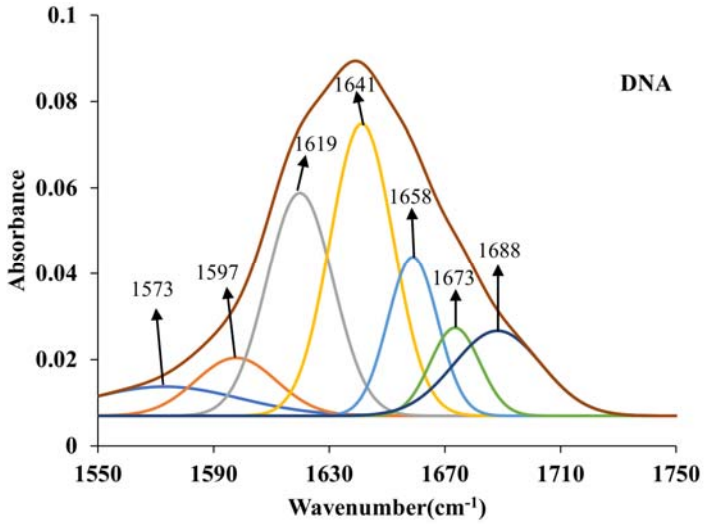

Fig. S-8. FT-IR spectra, Gaussian function fitting curves and deconvoluted spectra Ct-DNA band region (1550–1750 cm^{-1}) at 298 K and pH = 7.2.

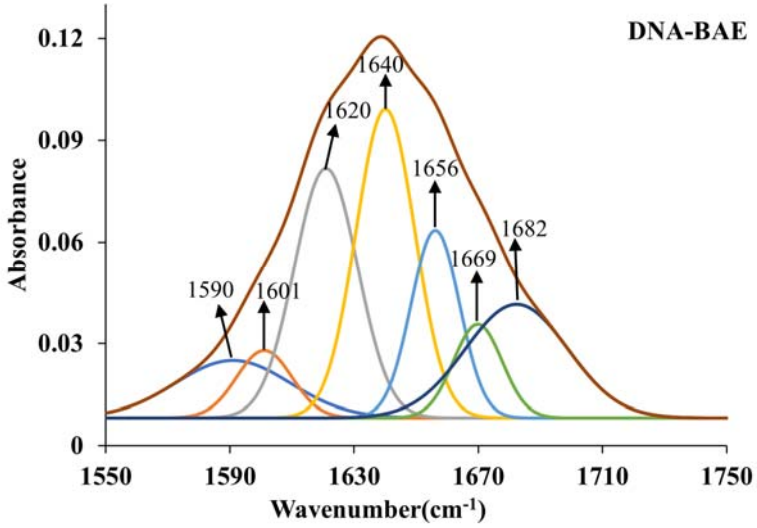

Fig. S-9. FT-IR spectra, Gaussian function fitting curves and deconvoluted spectra Ct-DNA-BAE band region (1550–1750 cm^{-1}) at 298 K and pH = 7.2.

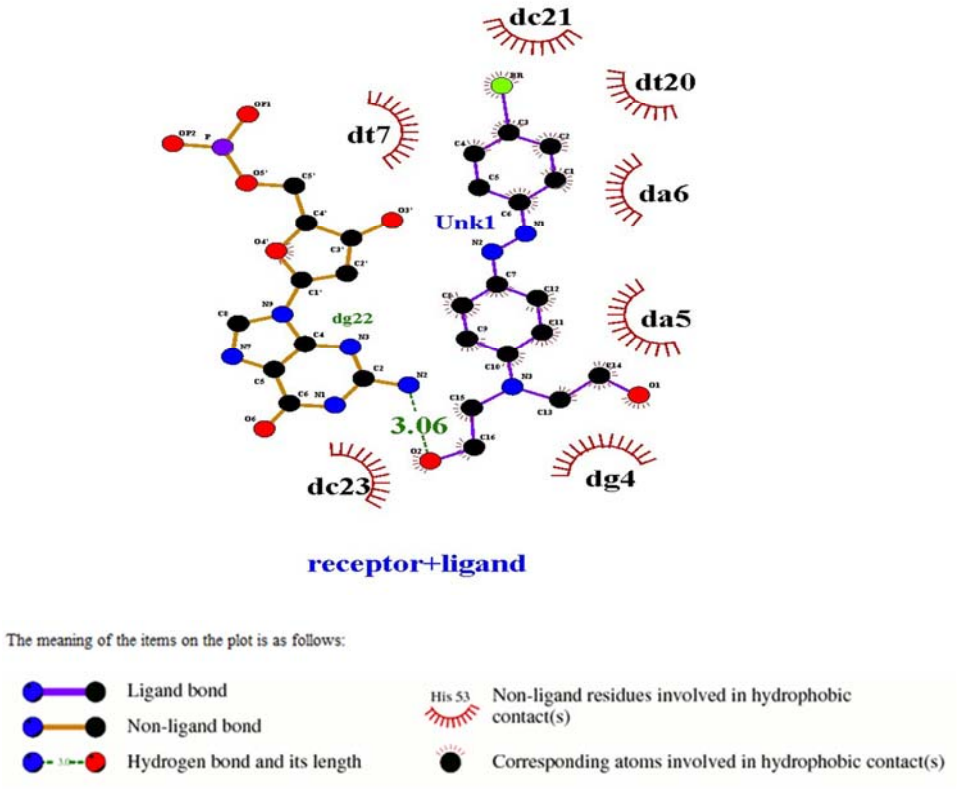

Fig. S-10. Hydrophobic interactions and hydrogen bonds in the interaction model of BAE with Ct-DNA

Journal of the Serbian Chemical Society
JSCS@tmf.bg.ac.rs • www.shd.org.rs/JSCS
J. Serb. Chem. Soc. *90* (9) 1041–1054 (2025)
JSCS–5438
Original scientific paper
Published 26 September, 2025

Dibutyltin(IV) formulations: Synthetic aspect, spectroscopic interpretation and computational calculation

SUCHITRA BUDANIA, ANKUR M KUMAR, POONAM CHAND and ASHA JAIN*

Department of Chemistry, University of Rajasthan, Jaipur-302004, Rajasthan, India

(Received 6 March, revised 15 May, accepted 10 July 2025)

Abstract: This research article reports a series of dibutyltin(IV) complexes, Bu2SnL(n)A (**1a**–**d**), synthesized by the reaction of sodium salts of substituted pyrazolones (L(n)H) and aromatic carboxylic acid (AH) with dibutyltin dichloride in dried THF solvent. The newly synthesized dibutyltin(IV) complexes were characterized by FT-IR, NMR (^{1}H, ^{13}C, ^{119}Sn) spectroscopy and mass study. The coordination mode of both ligands with central tin atom was explicated with spectroscopic analysis of the complexes. The spectroscopic results revealed that the substituted pyrazolone ligand coordinates to the tin atom in a bidentate fashion *via* enolic oxygen and a carbonyl oxygen atom. In contrast, the aromatic carboxylic acid ligand coordinates in a monodentate manner through the carboxylic oxygen atom, resulting in a penta-coordinated environment around the central tin atom. Computational calculations using density functional theory (DFT) provide insights into the optimized molecular structures, energies, Mulliken charges and distortion in bond lengths and bond angles of the newly generated complexes. The global reactivity descriptors and the frontier molecular orbitals (FMOs) were calculated to understand the structural and electronic properties of dibutyltin(IV) formulations. The theoretical study explores the proposed penta-coordinated environment around tin atoms, revealing a distortion in the geometry of the complexes.

Keywords: dibutyltin(IV) complexes; carboxylic acid; substituted pyrazolones; DFT.

INTRODUCTION

The study of organotin(IV) complexes constitutes a significant portion of organometallic chemistry and is gaining attention due to their ability to interact with various biomolecules.[1–3] Some of these complexes have demonstrated anticancer,[4–8] DNA binding,[8,9] antimicrobial,[3,7,10–12] antidiabetic,[13,14] anti-inflam-

* Corresponding author. E-mail: aashajain27@gmail.com
https://doi.org/10.2298/JSC250306051B

matory,[7,12] antituberculosis,[12,15] antileishmanial,[7] antioxidant[7,9,10,16,17] and enzyme inhibition properties.[7] The biological activity of organotin(IV) complexes is influenced by several factors such as the number of Sn–C bonds, nature of alkyl or aryl substituents attached to tin centre, coordinating ligands and the gradual hydrolytic cleavage of complexes.

Focusing on the industrial,[18] agricultural[19] and biological uses[3–17] of organotin complexes, it is crucial to comprehend their structural coordination. Advanced spectroscopic and structural approaches have been used to investigate their chemistry.[20,21] According to reported literature, many ligand systems, including Schiff bases, oximes, carboxylic acids, phenols, diketones and others, are present in structurally distinct organotin(IV) complexes.[22] The nature of ligand plays pivotal role in determining the activity of these organotin(IV) complexes as it can modify their physicochemical properties. The synergistic interaction of organotin moiety with different functional ligands has led to the development of novel complexes with enhanced pharmacological activity when compared to the corresponding free ligands.[3,11,13,15,16]

Recognizing the significance of substituted pyrazolones[23] and carboxylic acids[24] as an organic moiety, along with the substantial bioactivity of organotin complexes, our research focuses on exploring the chemistry of hybrid organotin(IV) complexes. This study involves the synthesis and structural analysis of the newly generated dibutyltin(IV) complexes using spectroscopic methods. The DFT-based quantum-chemical study gives insights into the electronic structure of molecules and their correlation with synthetic and biological properties.[3,11,13] Therefore, a conceptual computational technique, DFT integrated with experimental approach has been employed to explore global and local descriptors, as well as the structural characteristics of newly synthesized dibutyltin(IV) complexes. This combined approach provides a better understanding of electronic structure and reactivity of complexes.

EXPERIMENTAL

Mandelic acid (AH) and dibutyltin dichloride were obtained from Sigma–Aldrich Chemical Co. and utilized without additional purification. Four types of substituted pyrazolones ($L_{(1)}H$, $L_{(2)}H$, $L_{(3)}H$ and $L_{(4)}H$) were synthesized using Jensen's method.[25] The standard literature procedures were used to dry the solvents which were employed in the experimental procedure. The experimental work was carried out under a strictly anhydrous atmosphere. Tin was estimated as tin(IV) oxide. Melting points of newly synthesized complexes (**1a**–**d**) were determined in sealed capillaries. Synthesized complexes **1a**–**d** were characterized using spectroscopic techniques. IR spectra of the complexes were recorded on a Perkin Elmer – Spectrum RX-IFTIR using KBr pellets in the range 4000–400cm^{-1}. ^{1}H- and ^{13}C-NMR spectra of organotin(IV) complexes were recorded on the ECS400 MHz (JEOL) NMR spectrometer, and ^{119}Sn NMR spectrum of complex **1a** was recorded on the Bruker Advance NEO 500 MHz NMR spectrometer. Mass spectra of complexes **1a** and **1d** were carried out on Xevo G2-S Q (Tof

(Waters, USA) mass spectrometer (APCI) whereas the mass spectra of dibutyltin(IV) complexes **1b** and **1c**, were obtained using Agilant MassHunter-6470A LC/MS system using electrospray ionizaton(ESI). DFT calculation of synthesized complexes **1a**–**d** was carried out by using the DFT/B3LYP/6-31G* basis set in Spartan 20 molecular modeling software.[3,13,15,16]

The detailed synthetic procedures of dibutyltin(IV) complexes are described below.

*Synthesis of $Bu_2SnL_{(1)}A$ (**1a**)*

A dry THF solution of sterically demanding substituted pyrazolone $L_{(1)}H$ (292.2 mg, 1.35 mmol) and mandelic acid AH (205.7 mg, 1.35 mmol), was added to a methanolic solution of sodium (62.1 mg, 2.70 mmol). The reaction mixture was refluxed over a period of 6 h. Subsequently, the mixture of sodium salts of both ligands was mixed with a dry THF solution of dibutyltin dichloride (410.8 mg, 1.35 mmol). After that, the components of the reaction underwent refluxing for approximately 8 h. The solid sodium chloride (0.157 g) that was produced as a byproduct of the reaction was filtered. To get crude solid product, the volatile solvent fraction of the remaining reaction mixture was extracted at reduced pressure. A brown-colored solid product was obtained, which was recrystallized from chloroform and pet. ether mixture. Recrystallized yield = 82 %; melting point = 112 °C.

*Synthesis of $Bu_2SnL_{(2)}A$ (**1b**)*

A dry THF solution of sterically demanding substituted pyrazolone $L_{(2)}H$ (309.8 mg, 1.34 mmol) and mandelic acid AH (204.6 mg, 1.34 mmol), was added to a methanolic solution of sodium (61.8 mg, 2.68 mmol). The reaction mixture was refluxed over a period of 6 h. Subsequently, the mixture of sodium salts of both ligands was mixed with a dry THF solution of dibutyltin dichloride (408.8 mg, 1.34 mmol). After then, the components of the reaction underwent refluxing for approximately 8 h. The solid sodium chloride (0.157 g) that was produced as a byproduct of the reaction was filtered. The volatile solvent from the remaining reaction mixture was removed under reduced pressure. A brown-colored solid product was obtained, which was recrystallized from chloroform and pet. ether mixture. Recrystallized yield = 80 %; melting point = 100 °C.

*Synthesis of $Bu_2SnL_{(3)}A$ (**1c**)*

A dry THF solution of sterically demanding substituted pyrazolone $L_{(3)}H$ (368.7 mg, 1.32 mmol) and mandelic acid AH (201.5 mg, 1.32 mmol), was added to a methanolic solution of sodium (60.6 mg, 2.63 mmol). The reaction mixture was refluxed over a period of 6 h. Subsequently, the mixture of sodium salts of both ligands was mixed with a dry THF solution of dibutyltin dichloride (401.6 mg, 1.32 mmol). After then, the components of the reaction underwent refluxing for approximately 8 h. The solid sodium chloride (0.154 g) that was produced as a byproduct of the reaction was filtered. The volatile solvent from the remaining reaction mixture was removed under reduced pressure. A pale–orange-colored solid product was obtained, which was recrystallized from chloroform and pet. ether mixture. Recrystallized yield = 81 %; melting point = 108 °C.

*Synthesis of $Bu_2SnL_{(4)}A$ (**1d**)*

A dry THF solution of sterically demanding substituted pyrazolone $L_{(4)}H$ (423.0 mg, 1.35 mmol) and mandelic acid AH (205.8 mg, 1.35 mmol), was added to a methanolic solution of sodium (62.2 mg, 2.70 mmol). The reaction mixture was refluxed over a period of 6 h. Subsequently, the mixture of sodium salts of both ligands was mixed with a dry THF solution of dibutyltin dichloride (411.1 mg, 1.35 mmol). After then, the components of the reaction underwent refluxing for approximately 8 h. The solid sodium chloride (0.158 g) that was produced as a

byproduct of the reaction was filtered. The volatile solvent from the remaining reaction mixture was removed under reduced pressure. A pale–orange-colored solid product was obtained, which was recrystallized from chloroform and pet. ether mixture. Recrystallized yield = 78 %; melting point = 109 °C.

RESULTS AND DISCUSSION

Dibutyltin(IV) complexes of the type $Bu_2SnL_{(n)}A$ were synthesized by the reactions of dibutyltin dichloride with sodium salts of substituted pyrazolones ($L_{(n)}H$)) and mandelic acid (AH) in 1:1:1 mole ratio in dry refluxing THF solvent (Scheme 1).

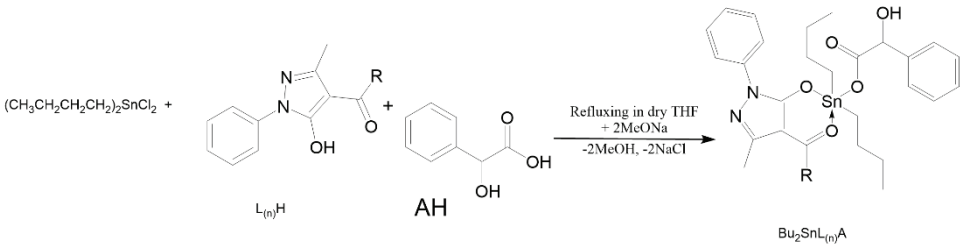

Where: R = $–CH_3$, $Bu_2SnL_{(1)}A$ (**1a**); R = $–CH_2CH_3$, $Bu_2SnL_{(2)}A$ (**1b**); R = $–C_6H_5$, $Bu_2SnL_{(3)}A$ (**1c**); R = *p*-$ClC_6H_4–$, $Bu_2SnL_{(4)}A$ (**1d**)

Scheme 1. Reactions of dibutyltin dichloride with sterically demanding substituted pyrazolones ($L_{(n)}H$) and mandelic acid (AH).

The plausible structures of synthesized dibutyltin(IV) complexes $Bu_2SnL_{(n)}A$ were elucidated by vibrational (IR), nuclear magnetic resonance (^1H, ^{13}C, ^{119}Sn) spectroscopy and mass spectrometry.

FT-IR spectra

The FT-IR spectra of the newly generated dibutyltin(IV) complexes (**1a**–**d**) have been recorded as KBr pellets in the range 4000–400 cm^{-1}. In the infrared spectra of dibutyltin(IV) complexes, the appearance of medium intensity bands in the region 655–606 cm^{-1} and 515–419 cm^{-1} may be attributed to the stretching vibrations of the Sn–O and Sn–C bonds, respectively.[26]

A band in the region of 1567–1539 cm^{-1} was seen in the IR spectra of sterically demanding substituted pyrazolones ($L_{(n)}H$), which could be attributed to carbonyl ν(>C=O) stretching vibrations.[3] This band appeared at 1531, 1529, 1533 and 1534 cm^{-1} in the IR spectra of the synthesized complexes $Bu_2SnL_{(1)}A$ (**1a**), $Bu_2SnL_{(2)}A$ (**1b**), $Bu_2SnL_{(3)}A$ (**1c**) and $Bu_2SnL_{(4)}A$ (**1d**), respectively. This shift in the position of the carbonyl ν(>C=O) stretching vibration to lower wave number indicates a bidentate nature of sterically demanding substituted pyrazolones ($L_{(n)}H$) in these complexes.

The coordination behavior of mandelic acid (AH) with tin atom is inferred from the $\nu(COO)_{asym}$ and $\nu(COO)_{sym}$ vibrations. The IR spectrum of mandelic

acid exhibited absorption bands at 1580 cm^{-1} for $\nu(COO)_{asym}$ vibration and at 1417 cm^{-1} for $\nu(COO)_{sym}$ vibration.[3] In the IR spectra of the complexes, these absorption bands appeared in the regions 1581–1564 cm^{-1} for $\nu(COO)_{asym}$ and 1384–1360 cm^{-1} for $\nu(COO)_{sym}$ vibrations. The $\Delta\nu$ ($\Delta\nu = \nu(COO)_{asym} - \nu(COO)_{sym}$) values are important data for determining the mode of bonding of carboxylates in the complexes. The calculated values of $\Delta\nu$ is of the order 193––204 cm^{-1} in the dibutyltin(IV) complexes. The increase in value of $\Delta\nu$ from 163 cm^{-1} in free mandelic acid to 193–204 cm^{-1} in dibutyltin(IV) complexes indicates the monodentate nature of carboxylic group of mandelic acid in these dibutyltin(IV) complexes.[27] A broad band appeared in the region 3478–3298 cm^{-1} in the IR spectra of the complexes, due to secondary –OH group of mandelic acid, indicates the non-involvement of this group in bonding. The absorption band appeared in the regions 1493–1415 cm^{-1} and 1601–1594 cm^{-1} may be attributed to $\nu(>C=C</>C=N–)$ and $\nu(–C_6H_5)$, respectively in the complexes.

^{1}H-NMR spectra

The ^{1}H-NMR spectrum of dibutyltin(IV) complex **1b** was recorded in $CDCl_3$ whereas, the ^{1}H-NMR spectra of dibutyltin(IV) complexes **1a**, **1c** and **1d** were recorded in $CDCl_3$ with few drops of DMSO-d_6, using TMS as an internal standard. The chemical shift values of these dibutyltin(IV) complexes are tabulated in Table S-I of the Supplementary material to this paper.

The broad signal of enolic –OH appeared in the δ region 10.67–12.77 ppm in the ^{1}H-NMR spectra of sterically demanding substituted pyrazolones ($L_{(n)}H$),[28] while the carboxylic proton (COO–H) appeared at δ 11.81 ppm in the ^{1}H-NMR spectrum of mandelic acid (AH).[3] These broad signals disappeared in the ^{1}H-NMR spectra of dibutyltin(IV) complexes which clearly show deprotonation of these ligands. The singlet observed in the ^{1}H-NMR spectra of dibutyltin(IV) complexes at δ 2.36 ppm (**1a**), 2.43 ppm (**1b**), 1.79 ppm (**1c**) and 1.82 ppm (**1d**) is due to the ring methyl protons ($–CH_3$) of substituted pyrazolone ($L_{(n)}H$) moiety. In the ^{1}H-NMR spectrum of $Bu_2SnL_{(1)}A$ (**1a**), a singlet at δ 2.39 ppm appeared for the terminal methyl protons, whereas the terminal $–CH_2CH_3$ group in the complex $Bu_2SnL_{(2)}A$ (**1b**) appeared as a quartet at δ 2.73 ppm (for CH_2 protons) and signal for CH_3 protons merged with butyl proton signals.

The signals for alcoholic –OH and –CH protons of mandelic acid were observed in the δ regions 3.64–3.73 ppm and 5.11–5.13 ppm, respectively, in the ^{1}H-NMR spectra of the complexes **1a**–**d**. Aromatic protons appeared as a multiplet in the δ region 7.17–7.89 ppm whereas protons of butyl groups, directly appended to tin, were observed in the δ region 0.66–1.68 ppm.

^{13}C-NMR spectra

The ^{13}C-NMR spectrum of dibutyltin(IV) complex **1b** was recorded in $CDCl_3$ whereas, the ^{13}C-NMR spectra of dibutyltin(IV) complexes **1a**, **1c** and **1d** were

recorded in $CDCl_3$ with few drops of DMSO-d_6, using TMS as an internal standard. Table S-II lof the Supplementary material lists the obtained chemical shift values.

In the ^{13}C NMR spectra of the sterically demanding substituted pyrazolones ($L_{(n)}H$), the signals for carbonyl (>C=O) carbon were observed at δ 196.2 ppm in $L_{(1)}H$, 197.97 ppm in $L_{(2)}H$, 192.05 ppm in $L_{(3)}H$ and 190.9 ppm in $L_{(4)}H$.[28] The positions of these carbonyl carbon (C6) signals experienced some shift in the ^{13}C-NMR spectra of dibutyltin(IV) complexes, which indicate that carbonyl group (>C=O) is participating in bonding. This suggests bidentate nature of sterically demanding substituted pyrazolone ($L_{(n)}H$). There are also some shifts observed in the positions of C_3, C_4 and C_5 carbon signals in the ^{13}C-NMR spectra of the complexes. The carboxylic carbon signal was observed at δ 173.33 in the ^{13}C-NMR spectra of mandelic acid (AH).[3] In the ^{13}C-NMR spectra of the dibutyltin(IV) complexes involving mandelic acid as a coligand, the carboxylic carbon signals are observed in the δ range 174.17–179.77 ppm. The shifting of carboxylic carbon signals indicate monodentate bonding behaviour of carboxylic group. The carbon signals of methyl group (C7) and phenyl groups are observed in the δ region 16.44––17.52 ppm and 120.92–148.97 ppm, respectively. The carbon signals of butyl groups directly bonded to tin atom appeared as splitted signals in the δ region 13.40–32.38 ppm in ^{13}C-NMR spectra of the dibutyl(IV) complexes (Table S-II).

^{119}Sn-NMR spectrum

The ^{119}Sn-NMR chemical shift (^{119}Sn) values provide insights into the geometry and the coordination number of tin in organotin(IV) complexes. The ^{119}Sn--NMR spectrum of dibutyltin(IV) complex **1a** was recorded in DMSO-d_6. The ^{119}Sn chemical shift value of dibutyltin(IV) complex $Bu_2SnL_{(1)}A$ (**1a**) is observed at δ – 125.86 ppm. This ^{119}Sn-NMR value reveals the presence of five coordinated tin centre in dibutyltin(IV) complex.[29] The coordination sphere of tin consists of two butyl groups, a chelating *O*,*O*'-bidentate substituted pyrazolone ($L_{(n)}H$) and a monodentate mandelic acid (AH).

Mass spectra

The mass spectral data of dibutyltin(IV) complexes **1a** and **1d**, were obtained using Xevo G2-S Q (Tof, Waters, USA) mass spectrometer (APCI), whereas the mass spectral data of dibutyltin(IV) complexes **1b** and **1c**, were obtained using Agilant MassHunter-6470A LC/MS system using electrospray ionization (ESI). The obtained ion peaks (*m*/*z* values) along with their intensity in % are presented in the Table S-III of the Supplementary material.

The mass spectrum of dibutyltin(IV) complex **1a** exhibits low-intensity molecular ion peak, $[M]^+$. The mass spectral data for complexes **1a**–**d** reveal a similar

fragmentation pattern. The resulting fragments closely match the anticipated structures of complexes. The absence of high intensity peaks in the *m*/*z* region above the molecular weight of complexes, indicates the monomeric nature of the dibutyltin(IV) complexes.

The obtained results of vibrational (IR), nuclear magnetic resonance (^{1}H, ^{13}C, ^{119}Sn) spectroscopies and mass spectrometry suggested a penta-coordinated geometry for tin in these complexes (Fig. 1).

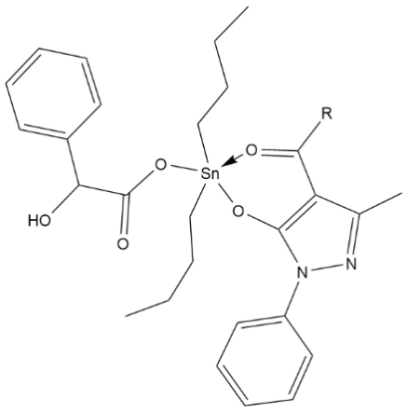

Fig. 1. Structure of dibutyltin(IV) complexes of sterically demanding substituted pyrazolone and mandelic acid, where: R = -CH_3, $Bu_2SnL_{(1)}A$ (**1a**); R = –CH_2CH_3 , $Bu_2SnL_{(2)}A$ (**1b**); R = –C_6H_5, $Bu_2SnL_{(3)}A$ (**1c**); R = *p*-ClC_6H_4–, $Bu_2SnL_{(4)}A$ (**1d**).

DFT calculations

The optimized molecular structures and molecular properties of synthesized dibutyltin(IV) complexes, $Bu_2SnL_{(n)}A$ (**1a**–**d**) have been studied in gas phase, using DFT-B3LYP functional in Spartan 20 computational modeling software. The ground state energy, E_{HOMO}, E_{LUMO}, dipole moment and other global reactivity parameters of the complexes $Bu_2SnL_{(n)}A$ have been calculated and obtained data are summarized in Table I.

Fig. 2 represents the optimized structures of the dibutyltin (IV) complexes $Bu_2SnL_{(n)}A$ (**1a**–**d**). The ground state energy of the synthesized complex $Bu_2SnL_{(4)}A$ (**1d**) is –2229.09439 a.u., the lowest among all the complexes, indicating that $Bu_2SnL_{(4)}A$ (**1d**) is the most stable complex. The ability to donate electron is associated with E_{HOMO}, while the ability to accept electrons is linked to the E_{LUMO}.[30] Furthermore, the energy gap between HOMO and LUMO serve as key indicator of the reactivity of the complexes.

The ΔE gap is found to be 3.88 eV for the complex $Bu_2SnL_{(4)}A$ (**1d**) which is lowest among all the complexes. The lowest ΔE gap suggests the highest reactivity of this complex. As shown in Figs. 3 and 4, the charge density of HOMO in complexes **1a**–**c** is localized on the five membered pyrazole ring having phenyl group forming a delocalized π system, whereas in complex **1d**, the charge density of

HOMO is mainly localized on the five membered pyrazole ring having phenyl group and phenyl ring of mandelic acid moiety.

TABLE I. Selected molecular properties of optimized geometries of dibutyltin(IV) complexes; $IP = -E_{HOMO}$; $EA = -E_{LUMO}$; $\mu = -(IP + EA)/2$; $\chi = (IP + EA)/2$; $\eta = (IP - EA)/2$; $S = 1/2\eta$[30]

Property	Complex **1a** $Bu_2SnL_{(1)}A$	Complex **1b** $Bu_2SnL_{(2)}A$	Complex **1c** $Bu_2SnL_{(3)}A$	Complex **1d** $Bu_2SnL_{(4)}A$
Molecular formula	$C_{28}H_{36}N_2O_5Sn$	$C_{29}H_{38}N_2O_5Sn$	$C_{33}H_{38}N_2O_5Sn$	$C_{33}H_{37}ClN_2O_5Sn$
Molecular weight	599.300	613.327	661.371	695.816
Energy, a.u.	–1577.76033	–1617.07528	–1769.49513	–2229.09439
E_{HOMO} / eV	–6.05	–5.91	–6.03	–6.11
E_{LUMO} / eV	–1.53	–1.58	–1.88	–2.23
ΔE / eV	4.52	4.33	4.15	3.88
Dipole moment, D	2.77	3.92	1.96	5.26
Polarizability	84.70	86.23	90.14	91.38
Ionization potential, eV	6.05	5.91	6.03	6.11
Electron affinity, eV	1.53	1.58	1.88	2.23
Chemical potential, μ	–3.79	–3.745	–3.955	–4.17
Elecrtonegativity, χ	3.79	3.745	3.955	4.17
Chemical hardness, η	2.26	2.165	2.075	1.94
Chemical softness, S	0.2212	0.2309	0.2409	0.2577
Area, Å^2	577.93	601.34	638.82	656.87
Volume, Å^3	547.22	565.63	613.19	627.71
PSA / Å^2	59.977	59.619	59.138	59.371
Ovality	1.79	1.82	1.83	1.85

For the LUMO of complexes **1a**–**d**, the charge density is localized on five membered pyrazole ring and carbonyl carbon of substituted pyrazolone moiety. This theoretical study reveals that localization of charge density on substituted pyrazolone moiety plays a crucial role for determining the reactivity of dibutyltin(IV) complexes.

The optimized molecular structure of the complexes $Bu_2SnL_{(n)}A$ (**1a**–**d**) have been studied, and the selected bond lengths and bond angles are listed in Tables II and III, respectively.

In the optimized structures of dibutyltin complexes (**1a**–**d**), the sum of the equatorial angles 108.98 (C9–Sn1–C13), 87.62 (C9–Sn1–O2) and 163.35° (C13––Sn1–O2) is 359.95° in complex **1a,** 110.95 (C10–Sn1–C14), 89.68 (C14–Sn1––O1) and 158.96° (C10–Sn1–O1) is 359.59° in complex **1b**, 113.90 (C5–Sn1––C12), 92.18 (C12–Sn1–O3) and 153.61° (C5–Sn1–O3) is 359.69° in complex **1c**, and 132.61 (C7–Sn1–C11), 109.68 (C7–Sn1–O3) and 115.95° (C11–Sn1–O3) is 358.24° in complex **1d**. The O–Sn–O bond angle between axial positions are 148.04° (O1–Sn1–O3) in complex **1a**, 149.42° (O2–Sn1–O3) in complex **1b**, 152.00° (O2–Sn1–O1) in complex **1c** and 167.53° (O4–Sn1–O2) in complex **1d**.

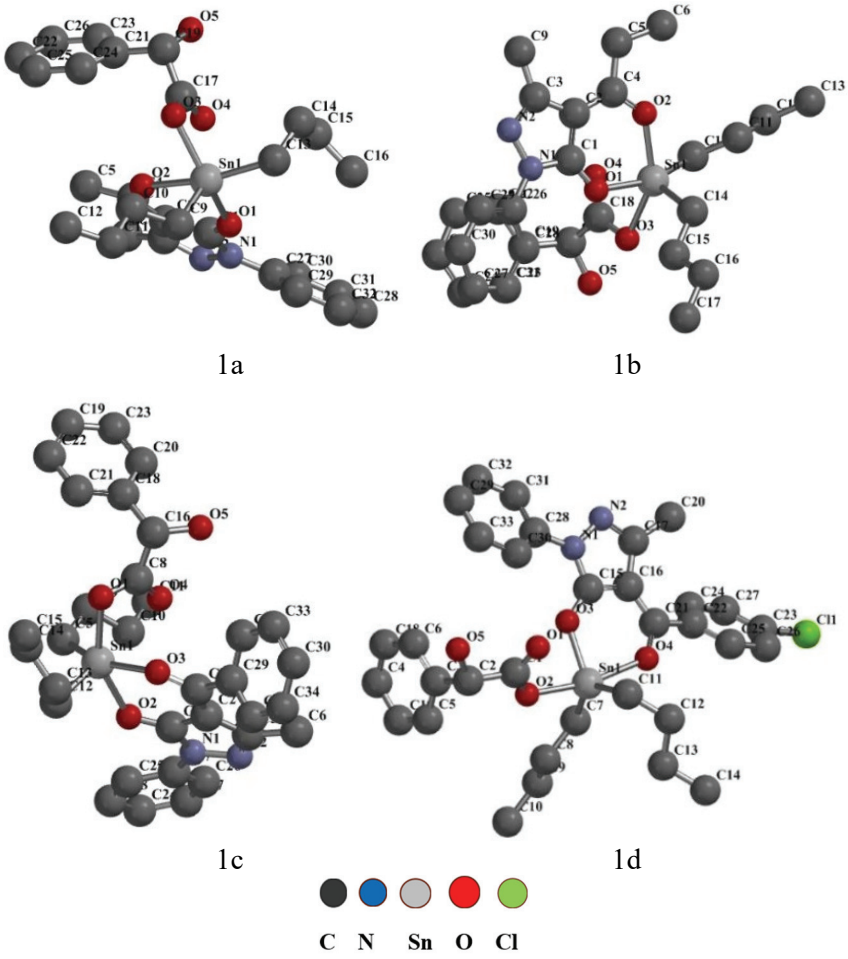

Fig. 2. The optimized molecular structures of dibutyltin(IV) complexes $Bu_2SnL_{(n)}A$ (**1a**–**d**).

These observations suggest that carbon atoms of two butyl groups and covalently bonded oxygen atom of substituted pyrazolone occupy the equatorial plane with tin atom, whereas the axial position were occupied by second oxygen atom of substituted pyrazolone and oxygen atom of carboxylate group. Thus, a distorted trigonal bipyramidal geometry may be suggested for these dibutyltin(IV) complexes (Fig. 2).

The theoretically calculated Mulliken charge at selected atoms in dibutyltin(IV) formulations have been depicted in Table IV. The charge distribution analysis reveals that the positively charged tin atom is surrounded by negatively charged carbon (from butyl groups) and oxygen (from substituted pyrazolones and carboxylic acid) atoms.

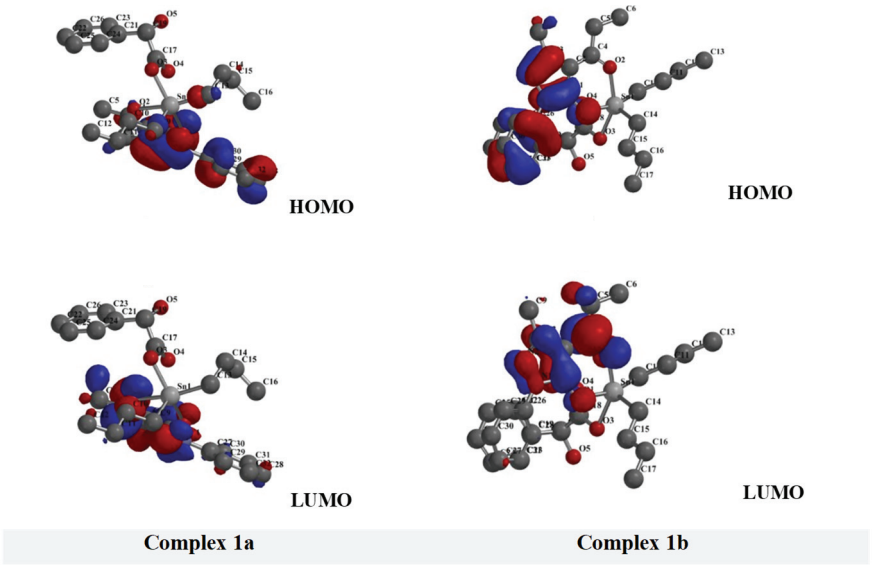

Fig. 3. FMOs of optimized molecular geometries of dibutyltin(IV) complexes (**1a**,**1b**)

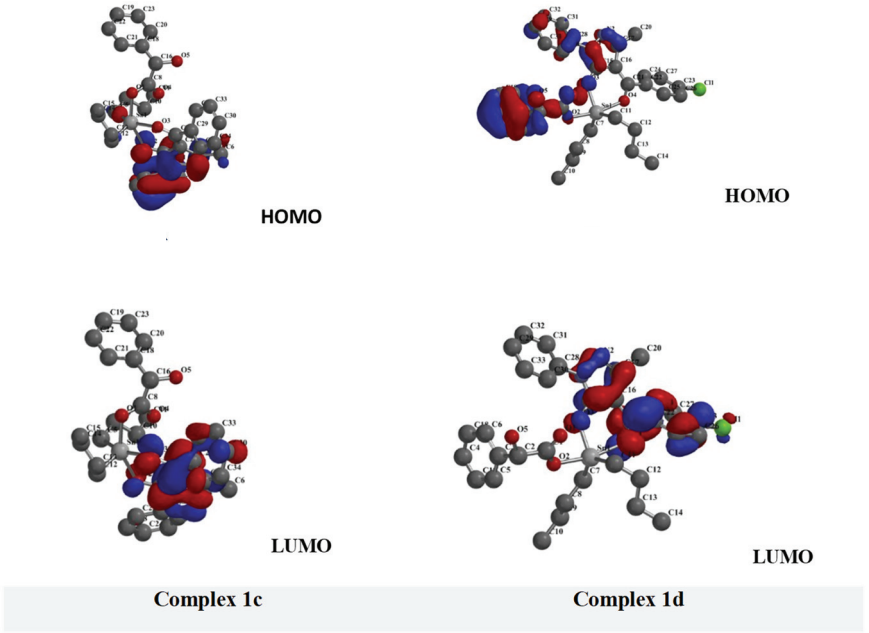

Fig. 4. FMOs of optimized molecular geometries of dibutyltin(IV) complexes (**1c** and **d**).

The negative charge on oxygen atoms of substituted pyrazolone (–0.736(O1), –0.637(O2) in complex **1a**, –0.720(O2), –0.661(O1) in complex **1b**, –0.724(O2),

-0.660(O3) in complex **1c** and –0.737(O3), –0.638(O4) in complex **1d**) is higher compared to oxygen atom of carboxylic acid (–0.627(O3) in complex **1a**, -0.654(O4) in complex **1b**, –0.653(O1) in complex **1c** and –0.687(O2) in complex **1d**) indicate stronger bonding interaction between substituted pyrazolone and tin atom.

TABLE II. Selected bond distances (in Å) of optimized geometries of dibutyltin(IV) complexes (**1a -1d**)

Complex **1a** $Bu_2SnL_{(1)}A$	Complex **1b** $Bu_2SnL_{(2)}A$	Complex **1c** $Bu_2SnL_{(3)}A$	Complex 1**d** $Bu_2SnL_{(4)}A$
2.153 (Sn1–C9)	2.152 (Sn1–C14)	2.150 (Sn1–C12)	2.136 (Sn1–C7)
2.162 (Sn1–C13)	2.158 (Sn1–C10)	2.157 (Sn1–C5)	2.143 (Sn1–C11)
2.104 (Sn1–O1)	2.135 (Sn1–O1)	2.139 (Sn1–O2)	2.042 (Sn1–O3)
2.192 (Sn1–O2)	2.153 (Sn1–O2)	2.140 (Sn1–O3)	2.265 (Sn1–O4)
2.188 (Sn1–O3)	2.195 (Sn1–O3)	2.133 (Sn1–O1)	2.074 (Sn1–O2)
1.276(O3–C17)	1.285(O3–C18)	1.288(O1–C8)	1.301(O2–C1)
1.263(C17=O4)	1.258(C18=O4)	1.248(C8=O4)	1.234(C1=O1)
1.291 (O1–C1)	1.281 (O1–C1)	1.285 (O2–C1)	1.296 (O3–C15)
1.429 (C1=C2)	1.432 (C1=C2)	1.432(C1=C2)	1.429 (C15=C16)
1.412 (C2–C4)	1.406(C2–C4)	1.405 (C2–C7)	1.416 (C16–C21)
1.272 (C4=O2)	1.281 (C4=O2)	1.281 (C7=O3)	1.273 (C21=O4)

TABLE III. Selected bond angles (in °) of optimized geometries of dibutyltin(IV) complexes (**1a**–**d**)

Complex **1a** $Bu_2SnL_{(1)}A$	Complex **1b** $Bu_2SnL_{(2)}A$	Complex **1c** $Bu_2SnL_{(3)}A$	Complex **1d** $Bu_2SnL_{(4)}A$
108.98(C9–Sn1–C13)	110.95(C10–Sn1–C14)	113.90(C5–Sn1–C12)	132.61(C7–Sn1–C11)
87.62(C9–Sn1–O2)	89.68(C14–Sn1–O1)	92.18(C12–Sn1–O3)	109.68(C7–Sn1–O3)
163.35(C13–Sn1–O2)	158.96(C10–Sn1–O1)	153.61(C5–Sn1–O3)	115.95(C11–Sn1–O3)
94.48(C13–Sn1–O1)	87.77(C10–Sn1–O2)	90.36(C5–Sn1–O2)	85.98(C7–Sn1–O4)
96.29(C13–Sn1–O3)	97.60(C10–Sn1–O3)	96.68(C5–Sn1–O1)	94.42(C7–Sn1–O2)
82.29(O2–Sn1–O1)	82.28(O1–Sn1–O2)	81.51(O2–Sn1–O3)	86.14(O2–Sn1–O3)
148.04(O1–Sn1–O3)	149.42(O2–Sn1–O3)	152.00(O2–Sn1–O1)	167.53(O4–Sn1–O2)
78.83(O3–Sn1–O2)	82.26(O3–Sn1–O1)	80.23(O1–Sn1–O3)	82.01(O3–Sn1–O4)
119.94(O3–C17=O4)	119.51(O3–C18=O4)	121.84(O1–C8=O4)	125.05(O2–C1=O1)
126.52(Sn1–O1–C1)	126.41(Sn1–O1–C1)	125.61(Sn1–O2–C1)	129.51(Sn1–O3–C15)
130.62(O1–C1=C2)	130.01(O1–C1=C2)	129.58(O2–C1=C2)	131.00(O3–C15=C16)
122.60(C1=C2–C4)	122.67(C1=C2–C4)	121.94(C1=C2–C7)	121.76(C15=C16–C21)
121.78(C2–C4=O2)	122.19(C2–C4=O2)	122.31(C2–C4=O3)	121.55(C16–C21=O4)
132.42(C4=O2–Sn1)	133.28(C4=O2–Sn1)	133.26(C7=O3–Sn1)	131.96(C21=O4–Sn1)

This observation is further supported by mass spectral data. The presence of a peak at *m*/*z* 449.2868 (100 % intensity) in complex **1a**, 463.6000 (16.66 % intensity) in complex **1b**, 511.9000 (6.66 % intensity) in complex **1c** and 545.6388 (72.72 % intensity) in complex **1d** corresponds to $[M\text{-}A]^+$ fragment ion (Table S-

-III). This indicates strong bonding interaction between oxygen atom of substituted pyrazolone and tin atom.

TABLE IV. Mulliken atomic charge on selected atoms of dibutyltin(IV) formulations(**1a-1d**)

Complex **1a** $Bu_2SnL_{(1)}A$	Complex **1b** $Bu_2SnL_{(2)}A$	Complex **1c** $Bu_2SnL_{(3)}A$	Complex **1d** $Bu_2SnL_{(4)}A$
+1.574 (Sn1)	+1.562(Sn1)	+1.557 (Sn1)	+1.539 (Sn1)
–0.650 (C9)	–0.649 (C26)	–0.655 (C12)	–0.654 (C7)
–0.647 (C13)	–0.637 (C22)	–0.640 (C5)	–0.643 (C11)
–0.736(O1)	–0.720(O2)	–0.724(O2)	–0.737(O3)
+0.683(C1)	+0.690(C13)	+0.692(C1)	+0.679(C15)
–0.117(C2)	–0.115(C12)	–0.111(C2)	–0.124(C16)
+0.436(C4)	+0.437(C11)	+0.337(C3)	+0.333(C21)
–0.637(O2)	–0.661(O1)	–0.660(O3)	–0.638(O4)
–0.627(O3)	–0.654(O4)	–0.653(O1)	–0.687(O2)
+0.665(C17)	+0.661(C21)	+0.661(C8)	+0.641(C1)
–0.608(O4)	–0.579(O5)	–0.673(O4)	–0.533(O1)

CONCLUSION

Four dibutyltin(IV) complexes (**1a**–**d**) were synthesized, and their structures elucidated using spectroscopic evidences and DFT-B3LYP functional. The synthetic method included incorporation of dibutyltin(IV) into structurally different substituted pyrazolone and mandelic acid, resulting in the formation of hybrid dibutyltin(IV) formulations. ^{119}Sn-NMR chemical shift value revealed the presence of pentacoordinated tin centre in the dibutyltin(IV) complex. DFT/B3LYP functional was used for the theoretical investigation of dibutyltin(IV) complexes, $Bu_2SnL_{(n)}A$. Optimized molecular structure, optimized energy and other global reactivity parameters of the complexes were studied. The Mulliken charge distribution analysis of dibutyltin(IV) complexes reveals the charge distribution on various atoms of complexes. On the basis of spectroscopic and theoretical evidences**,** a distorted trigonal–bipyramidal geometry was proposed in which substituted pyrazolone acts as bidentate ligand, coordinating through enolic oxygen (–O) as well as carbonyl (>C=O) oxygen, while the mandelic acid acts as monodentate ligand coordinating through carboxylic –C(O)O group.

SUPPLEMENTARY MATERIAL

Additional data and information are available electronically at the pages of journal website: https://www.shd-pub.org.rs/index.php/JSCS/article/view/13280, or from the corresponding author on request.

Acknowledgements. All authors are thankful to the Head, Department of Chemistry, University of Rajasthan, Jaipur, India, for providing necessary research facilities and MRC, MNIT, Jaipur and SAIF, Panjab University, Chandigarh, for providing facilities for spectroscopic analysis.

ИЗВОД

ДИБУТИЛКАЛАЈ(IV) ФОРМУЛАЦИЈЕ: СИНТЕТИЧКИ АСПЕКТ, СПЕКТРОСКОПСКА ИНТЕРПРЕТАЦИЈА И КОМПЈУТЕРСКА КАЛКУЛАЦИЈА

SUCHITRA BUDANIA, ANKUR M KUMAR, POONAM CHAND и ASHA JAIN

Department of Chemistry, University of Rajasthan, Jaipur-302004, Rajasthan, India

Овај истраживачки чланак приказује серију дибутилкалај(IV) комплекса, $Bu_2SnL_{(n)}A$ (**1a**–**d**), синтетисаних реакцијом натријумових соли супституисаних пиразолона ($L_{(n)}H$) и ароматичне карбоксилне киселине (AH) са дибутилкалај-дихлоридом у сувом THF растварачу. Новосинтетисани дибутилкалај(IV) комплекси су окарактерисани FT-IR, NMR (^1H, ^{13}C, ^{119}Sn) спектроскопијом и масеном анализом. Мод координације оба лиганда са централним атомом калаја објашњен је спектроскопском анализом комплекса. Спектроскопски резултати су открили да се супституисани пиразолонски лиганд координише са атомом калаја на бидентатни начин преко енолног кисеоника и карбонилног атома кисеоника. Насупрот томе, лиганд ароматичне карбоксилне киселине координише се монодентатно преко карбоксилног атома кисеоника, што резултира пентакоординационим окружењем око централног атома калаја. Рачунске калкулације коришћењем теорије функционала густине (DFT) пружају увид у оптимизоване молекуларне структуре, енергије, Маликенова наелектрисања и дисторзије у дужинама и угловима веза новоформираних комплекса. Дескриптори глобалне реактивности и граничне молекуларне орбитале (FMO) су израчунати како би се разумеле структурне и електронске особине дибутилкалај(IV) формулација. Теоретска студија истражује предложено пентакоординационо окружење око атома калаја, откривајући дисторзију у геометрији комплекса.

(Примљено 6. марта, ревидирано 15. маја, прихваћено 10. јула 2025)

REFERENCES

1. K. Ullah, S. Ali, A. Haider, S. Naz, S. Yousuf, K.S. Munawar, M. S. Jan, R. Zafar, R. Kumar, *J. Mol. Struct.* **1322** *(*2025**)** 140444 (https://doi.org/10.1016/j.molstruc.2024.140444)
2. M. S. Mansour, A. T. Ibrahium, A.A. El-Sherif, W. H. Mahmoud, *Appl. Organomet. Chem.* **38** (2024) e7656 (https://doi.org/10.1002/aoc.7656)
3. S. Budania, S. Saxena, A. Jain, *J. Indian Chem. Soc.* **101** (2024) 101198 (https://doi.org/10.1016/j.jics.2024.101198)
4. J. Devi, A. Boora, M. Rani, T. Arora, *Anti-Cancer Agents Med. Chem* **23** (2023) 164 (https://doi.org/10.2174/1871520622666220520095549)
5. X. M. Du, J. W. Ma, Q. L. Li, Y. Cui, C. L. Ma, *Appl. Organomet. Chem.* **38** (2024) e7522 (https://doi.org/10.1002/aoc.7522)
6. D. A. Berseneva, D. B. Shpakovsky, E. A. Nikitin, V. E. Goncharenko, Y. A. Gracheva, K. A. Lyssenko, Y. F. Oprunenko, E. R. Milaeva, *Russ. J. Coord. Chem.* **49** (2023) 622 (https://doi.org/10.1134/S1070328423600559)
7. S. Rahim, A. Sadiq, A. Javed, M. Kubicki, B. Kariuki, M. Assad, N. Muhammad, N. Fatima, M. Khan, A. F. AlAsmari, F. Alasmari, *J. Mol. Struct.* **1313** (2024) 138703 (https://doi.org/10.1016/j.molstruc.2024.138703)
8. M. Pooyan, Z. Shariatinia, F. Mohammadpanah, K. Gholivand, M. Dusek, V. Eigner, M. Satari, A. A. E. Valmoozi, *J. Mol. Liq.* **391** (2023) 123442 (https://doi.org/10.1016/j.molliq.2023.123442)

9. S. Ramzan, S. Rahim, S. T. Hussain, K. B. Holt, J. K. Cockcroft, N. Muhammad, Z. Ur--Rehman, A. Nawaz, S. Shujah, *Appl. Organomet. Chem.* **37** (2023) e7161 (https://doi.org/10.1002/aoc.7161)
10. S. Saroya, S. Asija, N. Kumar, Y. Deswal, *J. Indian Chem. Soc.* **99** (2022) 100379 (https://doi.org/10.1016/j.jics.2022.100379)
11. A. Sharma, A. Jain, S. Saxena, *Appl. Organomet. Chem.* **29** (2015) 499 (https://doi.org/10.1002/aoc.3321)
12. A. Boora, J. Devi, B. Kumar, B. Taxak, *BioMetals* **38** (2025) 153 (https://doi.org/10.1007/s10534-024-00644-8)
13. A. Kumawat, K. Soni, S. Saxena, A. Jain, *Appl. Organomet. Chem., C* **37** (2023) e7205 (https://doi.org/10.1002/aoc.7205)
14. P. Debnath, K. S. Singh, T. S. Devi, S. S. Singh, R. J. Butcher, L. Sieroń, W. Maniukiewicz, *Inorg. Chim. Acta* **510** (2020) 119736 (https://doi.org/10.1016/j.ica.2020.119736)
15. K. Soni, A. Kumawat, S. Saxena, A. Jain, *Bull. Chem. Soc. Jpn.* **97** (2024) 9 (https://doi.org/10.1093/bulcsj/uoae056)
16. A. M. Kumar, S. Budania, A. Jain, *Synth. Commun.* **54** (2024) 390 (https://doi.org/10.1080/00397911.2024.2306641)
17. S. Saroya, S. Asija, N. Kumar, Y. Deswal, *J. Indian Chem. Soc.* **99** (2022) 100379 (https://doi.org/10.1016/j.jics.2022.100379)
18. W. T. Piver, *Environ. Health Persp.* **4** (1973) 61 (https://ehp.niehs.nih.gov/doi/pdf/10.1289/ehp.730461)
19. M. Hoch, *Appl. Geochem.* **16** (2001) 719 (https://doi.org/10.1016/S0883-2927(00)00067-6)
20. S. Iftikhar, S. Hussain, S. Murtaza, D. Ali, S. Yousuf, M. A. Ali, A. Haider, M. Shahid, A. M. Alsuhaibani, M. S. Refat, *Appl. Organomet. Chem.* **38** (2024) e7581 (https://doi.org/10.1002/aoc.7581)
21. Y. Tan, Z. Zhang, J. Liu, Y. Tan, W. Jiang, *J. Mol. Struct.* **1322** (2025) 140697 (https://doi.org/10.1016/j.molstruc.2024.140697)
22. L. Pellerito, L. Nagy, *Coord. Chem. Rev.* **224** (2002) 111 (https://doi.org/10.1016/S0010-8545(01)00399-X)
23. F. Marchetti, C. Pettinari, C. Di Nicola, A. Tombesi, R. Pettinari, *Coord. Chem. Rev.* **401** (2019) 213069 (https://doi.org/10.1016/j.ccr.2019.213069)
24. M. Sirajuddin, S. Ali, A. Shahnawaz, F. Perveen, S. Andleeb, S. Ali, *J. Mol. Struct.* **1207** (2020) 127809 (https://doi.org/10.1016/j.molstruc.2020.127809)
25. B. S. Jensen, *Acta Chem. Scand*. **13** (1959) 1668 (https://doi.org/10.3891/acta.chem.scand.13-1668)
26. S. Sharma, A. Jain, S. Saxena, *Main Group Met. Chem.* **30** (2007) 63 (https://doi.org/10.1515/MGMC.2007.30.2-3.63)
27. G. B. Deacon, R. J. Phillips, *Coord. Chem. Rev.* **33** (1980) 227 (https://doi.org/10.1016/S0010-8545(00)80455-5)
28. R. K. Gupta, A. Jain, S. Saxena, *Main Group Met. Chem.* **33** (2010) 167 (https://doi.org/10.1515/mgmc.2010.33.4-5.167)
29. A. Joshi, S. Verma, A. Jain, S. Saxena, *Main Group Met. Chem.* **28** (2005) 31 (https://doi.org/10.1515/MGMC.2005.28.1.31)
30. S. Budania, S. Saxena, A. Jain, *IOP Conf. Ser. Mater. Sci. Eng.* **1248** (2022) 012106 (https://doi.org/10.1088/1757-899X/1248/1/012106).

Journal of the Serbian Chemical Society
JSCS@tmf.bg.ac.rs • www.shd.org.rs/JSCS
J. Serb. Chem. Soc. 90 (9) S332–S347 (2025) *Supplementary material*

SUPPLEMENTARY MATERIAL TO

Dibutyltin(IV) formulations: Synthetic aspect, spectroscopic interpretation and computational calculation

SUCHITRA BUDANIA, ANKUR M KUMAR, POONAM CHAND and ASHA JAIN*

Department of Chemistry, University of Rajasthan, Jaipur-302004, Rajasthan, India

J. Serb. Chem. Soc. 90 (9) (2025) 1041–1054

TABLE S-I. ^{1}H NMR spectral data of dibutyltin(IV) complexes of sterically demanding substituted pyrazolones ($L_{(n)}H$) and mandelic acid (AH) in (δ) ppm

Complex formula	RCO:C(OH)N(C_6H_5)N:CCH_3 ($L_{(n)}H$)				$C_6H_5CH(OH)COOH$ (AH)				Bu_2Sn
	OH	Ring C_6H_5	Ring CH_3	Terminal R (CH_3/ CH_2CH_3/C_6H_5/ p-ClC_6H_4)	COOH	C_6H_5	OH	CH	
$Bu_2SnL_{(1)}A$ (1a)	-	7.17-7.85 (m,10H)	2.36 (s,3H)	2.39 (s,3H)	-	*	3.69 (s,1H)	5.11 (s,1H)	0.70-1.67 (18H)
$Bu_2SnL_{(2)}A$ (1b)	-	7.18-7.89 (m,10H)	2.43 (s,3H)	2.73 (q,2H), ** (3H)	-	*	3.73 (s,1H)	5.13 (s,1H)	0.70-1.68 (18H)
$Bu_2SnL_{(3)}A$ (1c)	-	7.19-7.89 (m,15H)	1.79 (s,3H)	*	-	*	3.64 (s,1H)	5.11 (s,1H)	0.66-1.67 (18H)
$Bu_2SnL_{(4)}A$ (1d)	-	7.19-7.89 (m,14H)	1.82 (s,3H)	*	-	*	3.69 (s,1H)	5.11 (s,1H)	0.70-1.68 (18H)

s(singlet); t(triplet); q(quartet); m(multiplet); *(merge with ring phenyl); **(merge with butyl region); R= -CH_3 ($L_{(1)}H$), -CH_2CH_3 ($L_{(2)}H$), -C_6H_5 ($L_{(3)}H$), p-ClC_6H_4- ($L_{(4)}H$)

* Corresponding author. E-mail: aashajain27@gmail.com

TABLE S-II. ^{13}C NMR spectral data of dibutyltin(IV) complexes of sterically demanding substituted pyrazolones ($L_{(n)}H$) and mandelic acid (AH) in (δ) ppm

Complex formula.	$RCO:\overset{\frown}{C(OH)N(C_6H_5)N:}CCH_3$ **($L_{(n)}H$)**							$C_6H_5CH(OH)COOH$ **(AH)**			**Bu_2Sn**
	Ring C_6H_5	Terminal R= CH_3/ CH_2CH_3/ C_6H_5/ p-ClC_6H_4	C_3	C_4	C_5	C_6	C_7	COOH	C_6H_5	CH	
$Bu_2SnL_{(1)}A$ (1a)	120.93 - 148.92	27.99	162.01	104.76	138.48	193.15	17.52	179.60	*	73.51	13.42-28.73[ss]
$Bu_2SnL_{(2)}A$ (1b)	120.98 - 148.41	32.85 9.05	162.04	103.97	138.34	196.67	17.35	179.53	*	73.48	13.45-29.76
$Bu_2SnL_{(3)}A$ (1c)	120.92 - 149.35	*	162.60	104.61	139.47	192.42	16.44	179.77	*	73.56	13.40-32.38[ss]
$Bu_2SnL_{(4)}A$ (1d)	120.94 – 148.97	*	162.60	104.65	138.00	190.43	16.65	174.17	*	72.92	13.40-32.38[ss]

*merge with ring phenyl; [ss]splitted signals

TABLE S-III. Mass fragmentation pattern of dibutyltin(IV) complexes **1a-1d**

Fragments	Complex			
	$Bu_2SnL_{(1)}A$ (1a)	$Bu_2SnL_{(2)}A$ (1b)	$Bu_2SnL_{(3)}A$ (1c)	$Bu_2SnL_{(4)}A$ (1d)
$[M]^+$ (%intensity)	599.2868 (L.I.)	613.327 (n.o.)	661.327 (n.o.)	695.7827 (n.o.)
$[M-A]^+$ (%intensity)	449.2868 (100)	463.6000 (16.66)	511.9000 (6.66)	545.6388 (72.72)
$[F1]^+$ (%intensity)		381.7000 (15.55)		
$[F1-F2-CH_3]^+$ (%intensity)	335.0910 (4.61)	340.6000 (33.33)		
$[F1-F2-C_4H_9]^+$ (%intensity)			301.6000 (11.11)	
$[F1-F2-C_4H_9-CH_3]^+$ (%intensity)	279.1437 (37.39)	279.4000 (15.55)	279.4000 (100)	279.3088 (100)
$[F1-F2-2C_4H_9]^+$ (%intensity)	233.1190 (39.13)	231.4000 (30.00)		233.2572 (63.63)
$[SnO_2]^+$ (%intensity)	150.9696 (17.39)	149.2000	149.2000 (6.66)	151.0590 (18.18)
$[C_6H_5CO]^+/[C_6H_5N_2]^+$ (%intensity)		102.1000 (100)	102.1000 (17.77)	

$[M]^+ = [Bu_2SnL_{(n)}A]^+$; A = $C_8H_8O_3$; L.I. = Low Intensity; n.o. = not observed; F1 = M-A-C_6H_5; F2 = $CH_3/CH_2CH_3/C_6H_5/C_6H_4Cl$

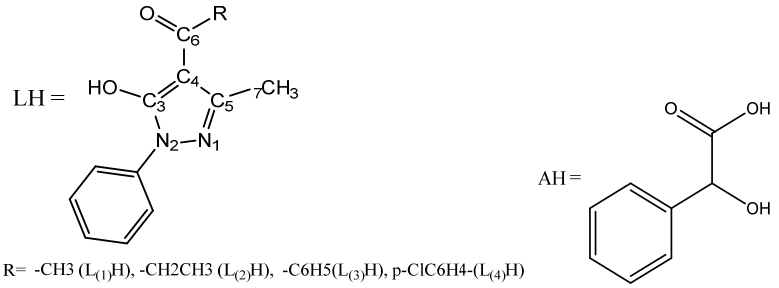

R= -CH3 ($L_{(1)}H$), -CH2CH3 ($L_{(2)}H$), -C6H5($L_{(3)}H$), p-ClC6H4-($L_{(4)}H$)

Table S-IV. ^{1}H NMR spectral data of sterically demanding substituted pyrazolones ($L_{(n)}H$) and mandelic acid (AH) in (δ) ppm

Ligand formula	$RCO:C(OH)N(C_6H_5)N:CCH_3$ **($L_{(n)}H$)**				**$C_6H_5CH(OH)COOH$ (AH)**			
	OH	Ring C_6H_5	Ring CH_3	Terminal R (CH_3/ CH_2CH_3/ C_6H_5/ p-ClC_6H_4)	COOH	C_6H_5	OH	CH
AH*					11.81(s)	7.19-7.70(m)	3.50(s)	5.01(s)
$L_{(1)}H$**	11.51(bs)	7.17-7.83 (m)	2.51 (s)	2.45 (s)				
$L_{(2)}H$**	10.67 (bs)	7.23-7.86 (m)	2.39 (s)	2.73(q), 1.21(t)				
$L_{(3)}H$**	12.77 (bs)	7.25-7.93 (m)	2.08 (s)	*				
$L_{(4)}H$**	11.37(bs)	7.26-8.00 (m)	2.14 (s)	*				

*ref. 3;**ref28

Table S-V.[13]C NMR spectral data of sterically demanding substituted pyrazolones ($L_{(n)}H$) and mandelic acid (AH) in (δ) ppm

Ligand formula	$RCO:\overline{C(OH)N(C_6H_5)N:CCH_3}$ **($L_{(n)}H$)**							**$C_6H_5CH(OH)COOH$ (AH)**		
	Ring C_6H_5	Terminal R= CH_3/ CH_2CH_3/ C_6H_5/ p-ClC_6H_4	C_3	C_4	C_5	C_6	C_7	COOH	C_6H_5	CH
AH*								173.33	125.96-136.12	75.12
$L_{(1)}H$**	120.4 - 147.0	26.2	160.4	104.1	137.1	196.2	15.4			
$L_{(2)}H$**	120.40- 147.32	32.29 7.94	160.10	103.27	137.06	197.97	15.48			
$L_{(3)}H$**	120.75 - 147.98	126.69 - 131.90	161.42	103.58	137.56	192.05	15.84			
$L_{(4)}H$**	120.8 – 147.6	126.8 – 138.0	161.1	103.5	138.1	190.9	15.8			

*ref. 3;**ref28

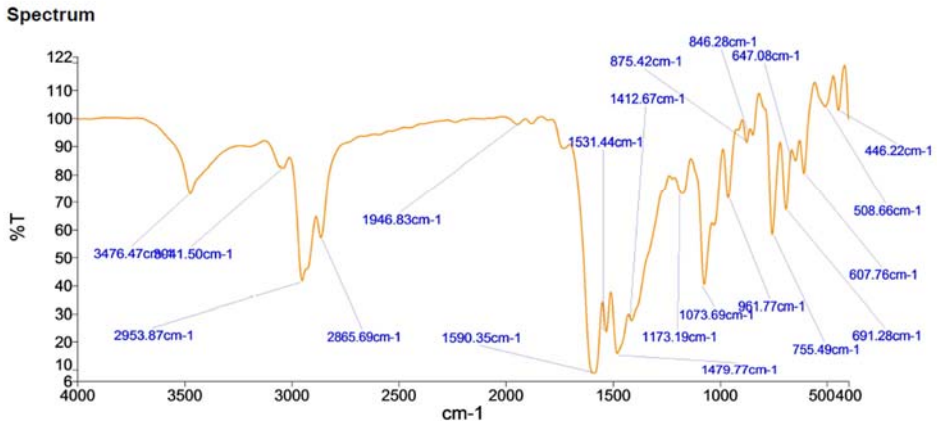

Fig S-1. IR Spectrum - Complex $Bu_2SnL_{(1)}A$(**1a**).

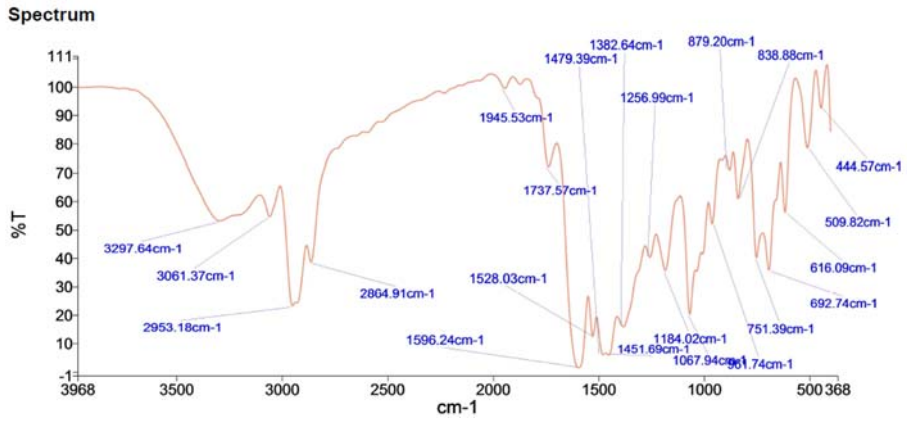

Fig S-2. IR Spectrum - Complex $Bu_2SnL_{(2)}A$ (**1b**).

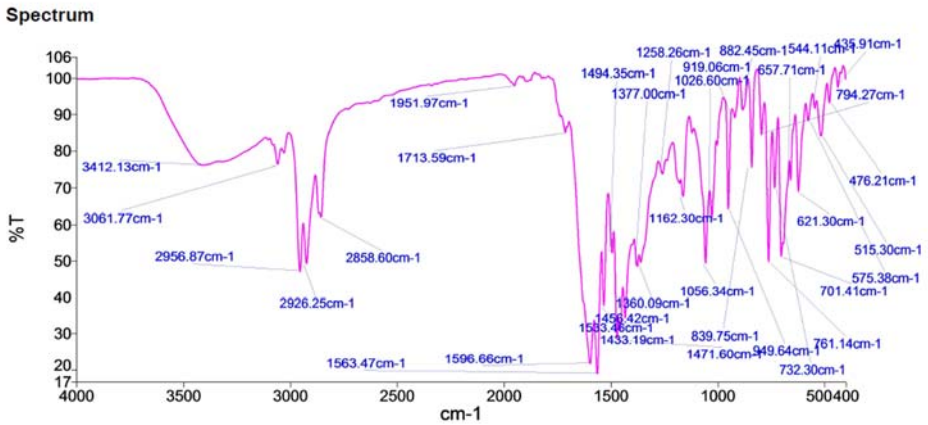

Fig S-3. **IR Spectrum** - Complex $Bu_2SnL_{(3)}A$ (**1c**).

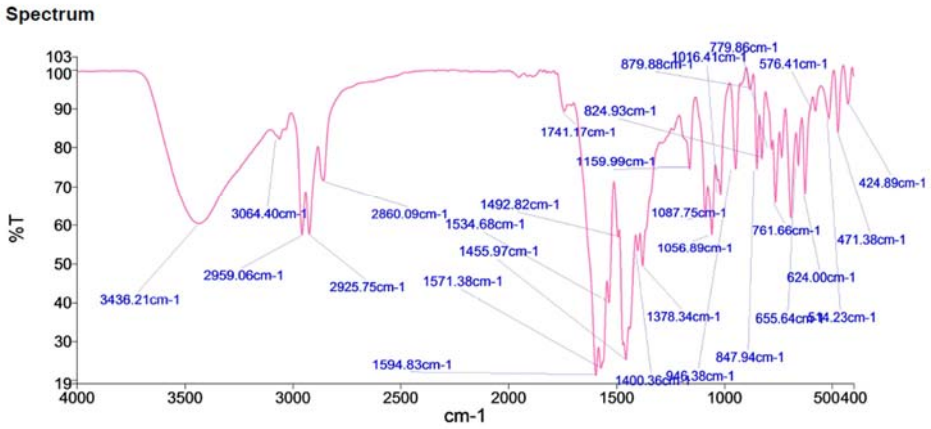

Fig S-4. **IR Spectrum** -Complex $Bu_2SnL_{(4)}A$ (**1d**).

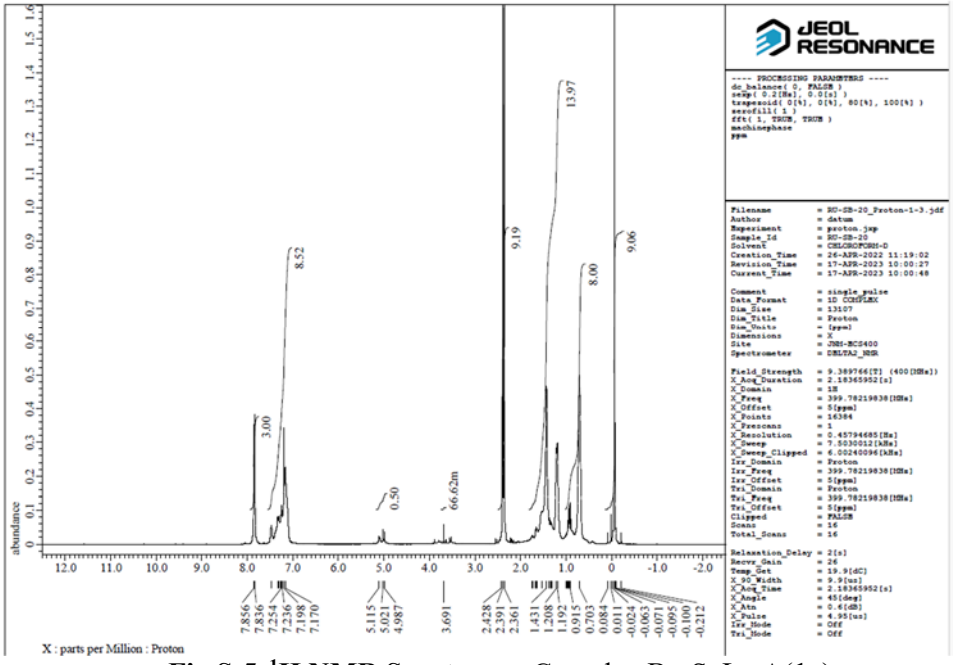

Fig S-5. ^{1}H NMR Spectrum - Complex $Bu_2SnL_{(1)}A$(**1a**).

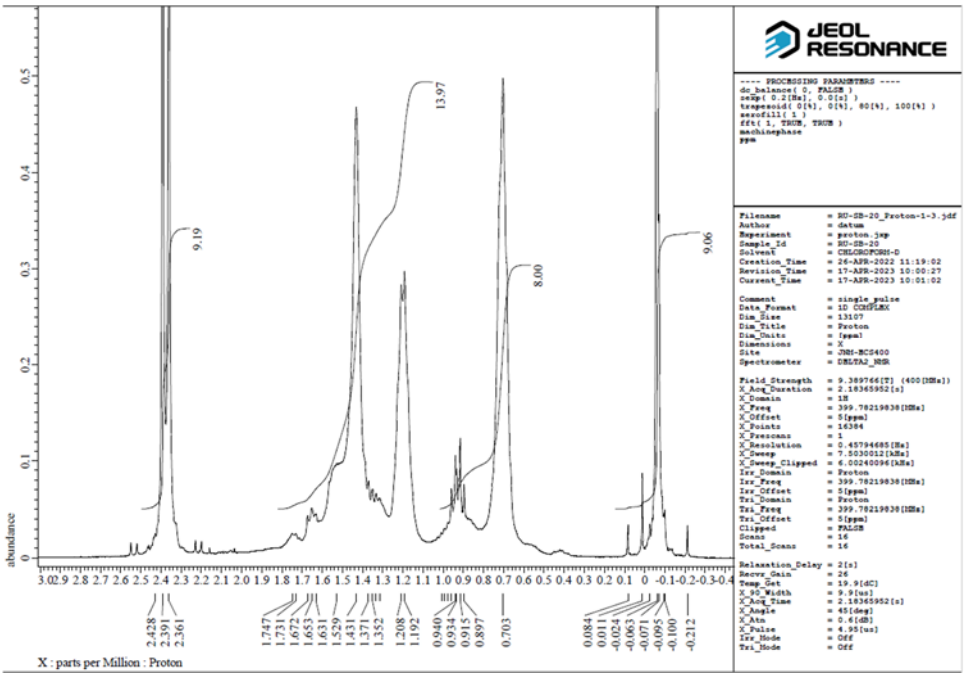

Fig S-6. ^{1}H NMR Spectrum - Complex $Bu_2SnL_{(1)}A$(**1a**) Expanded.

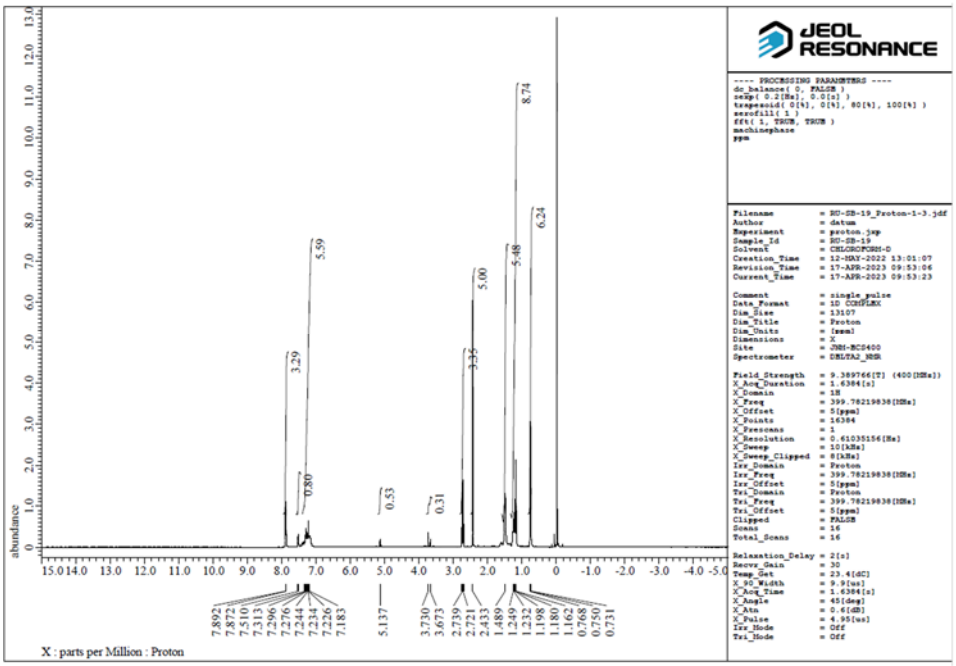

Fig S-7. ^{1}**H NMR Spectrum** - Complex $Bu_2SnL_{(2)}A$ (**1b**).

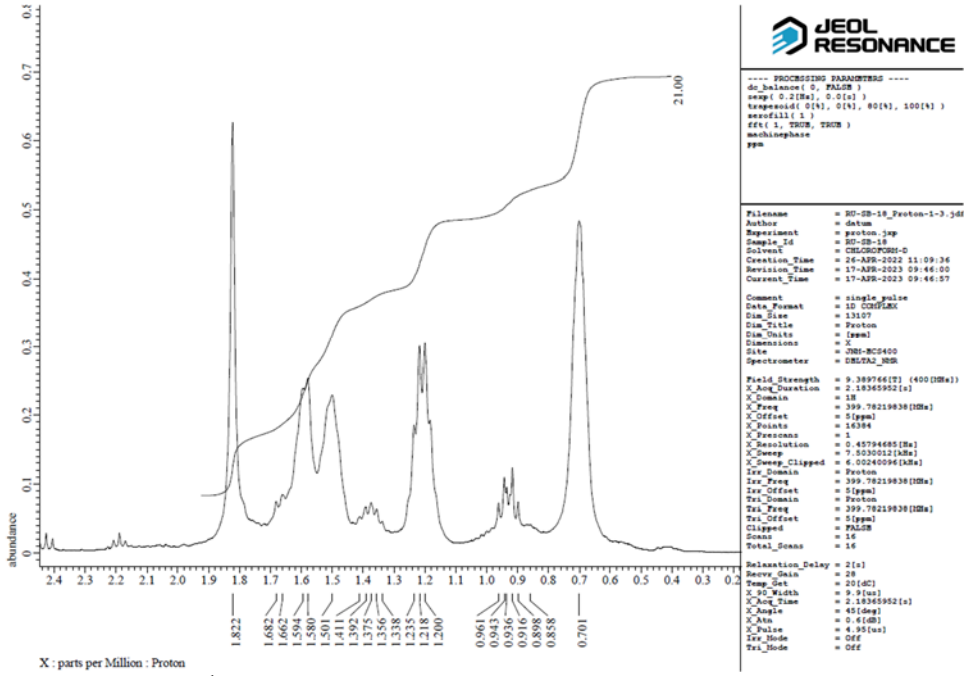

Fig S-8. ^{1}H NMR Spectrum - Complex $Bu_2SnL_{(2)}A$ (**1b**) Expanded.

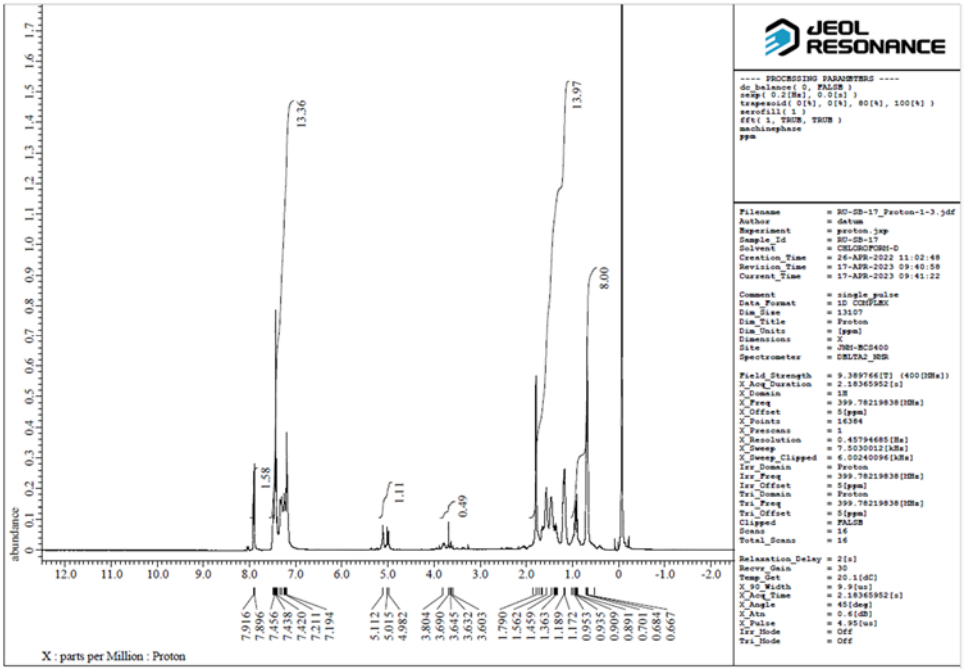

Fig S-9. ^{1}H NMR Spectrum - Complex $Bu_2SnL_{(3)}A$ (**1c**).

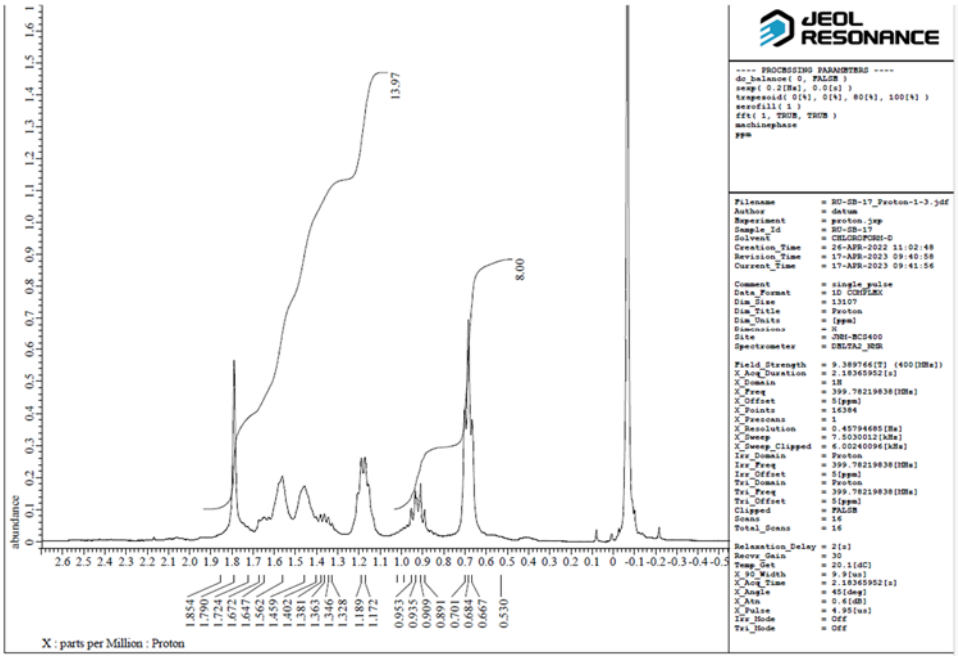

Fig S-10. **^{1}H NMR Spectrum** - Complex $Bu_2SnL_{(3)}A$ (**1c**)Expanded.

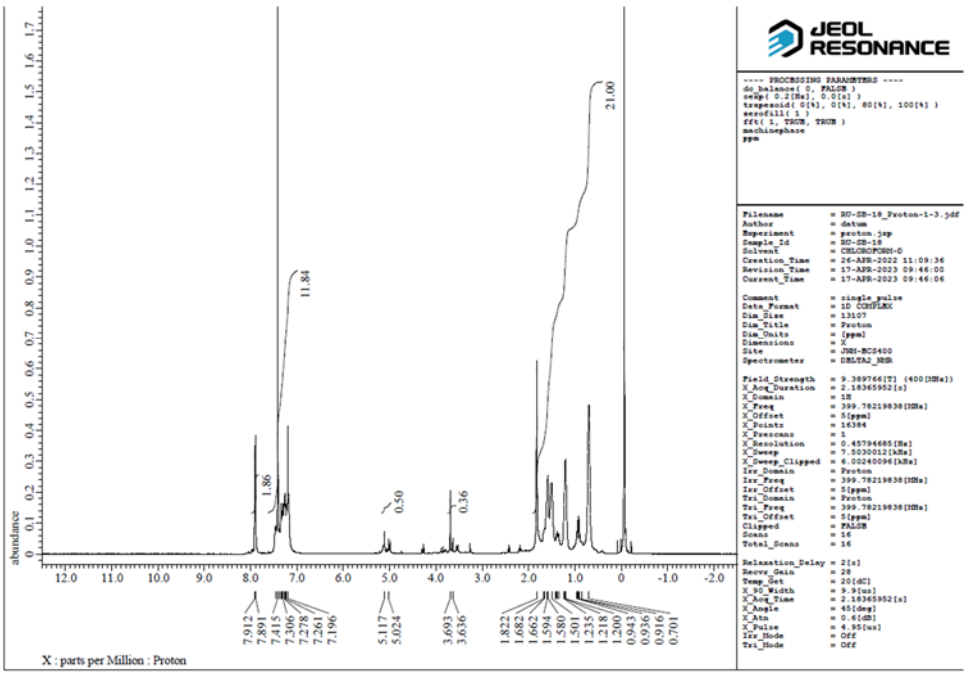

Fig S-11. **^{1}H NMR Spectrum** -Complex $Bu_2SnL_{(4)}A$ (**1d**).

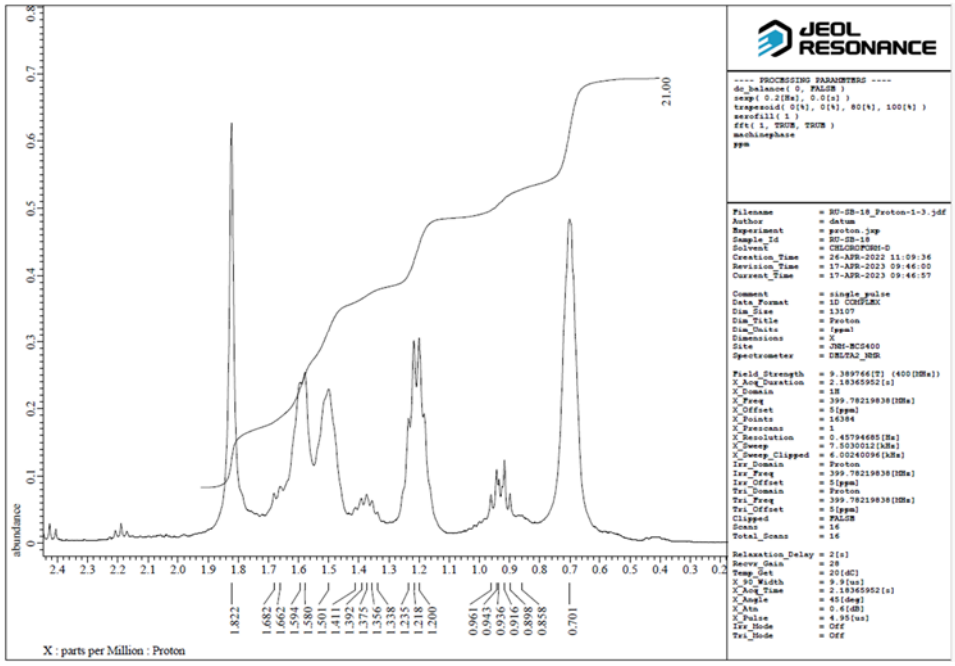

Fig S-12. **^{1}H NMR Spectrum** -Complex $Bu_2SnL_{(4)}A$ (**1d**) Expanded.

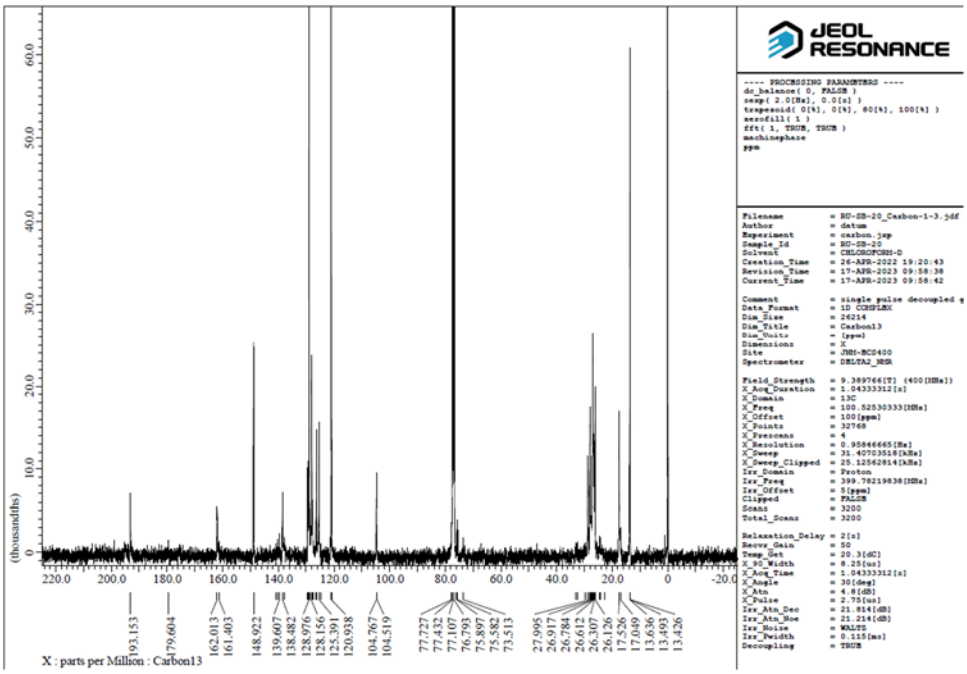

Fig S-13. **^{13}C NMR Spectrum** - Complex $Bu_2SnL_{(1)}A$(**1a**).

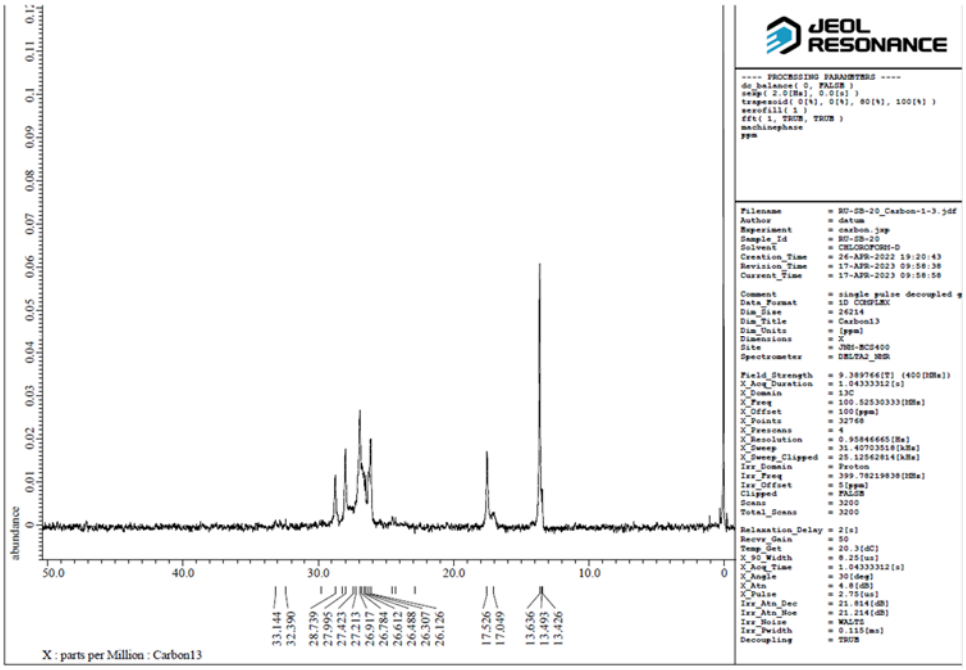

Fig S-14. 13C NMR Spectrum - Complex Bu2SnL(1)A(1a) Expanded.

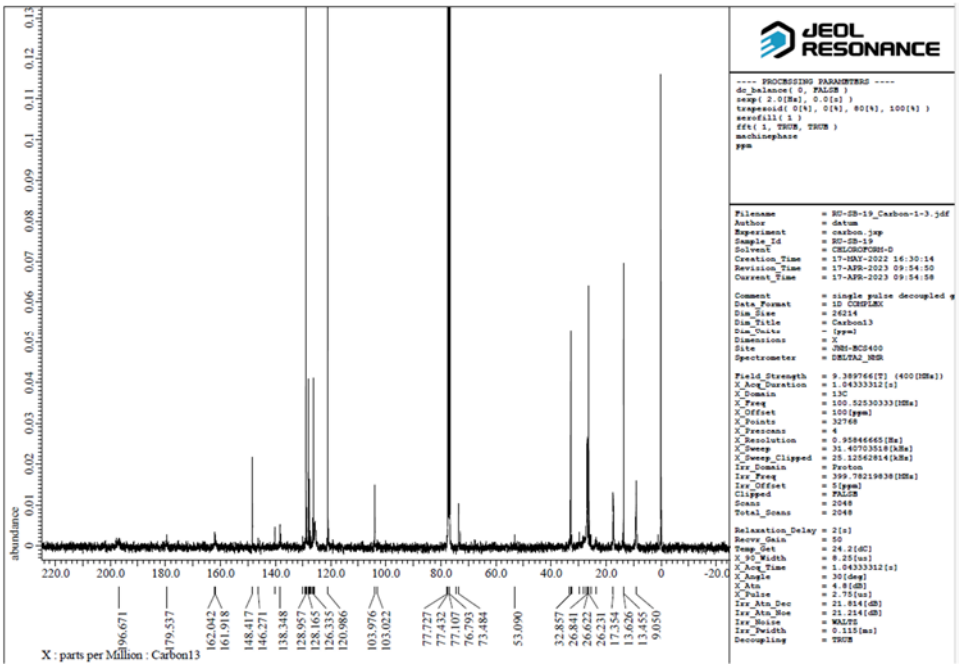

Fig S15. **^{13}C NMR Spectrum** - Complex $Bu_2SnL_{(1)}A$(**1a**) Expanded.

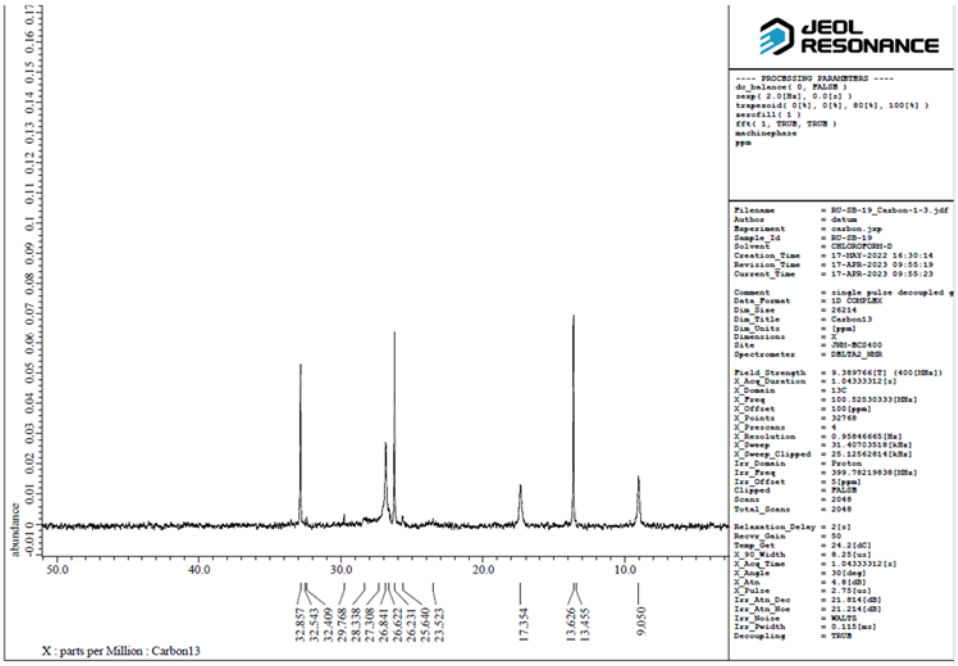

Fig S-16. **^{13}C NMR Spectrum** - Complex $Bu_2SnL_{(2)}A$ (**1b**) Expanded.

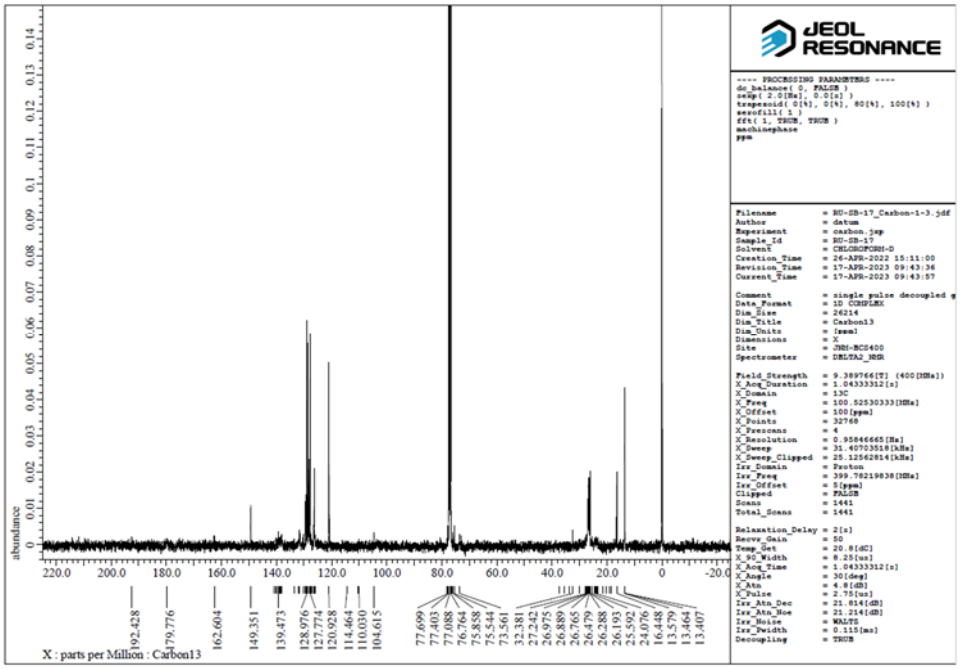

Fig S-17. ^{13}C NMR Spectrum - Complex $Bu_2SnL_{(3)}A$ (**1c**).

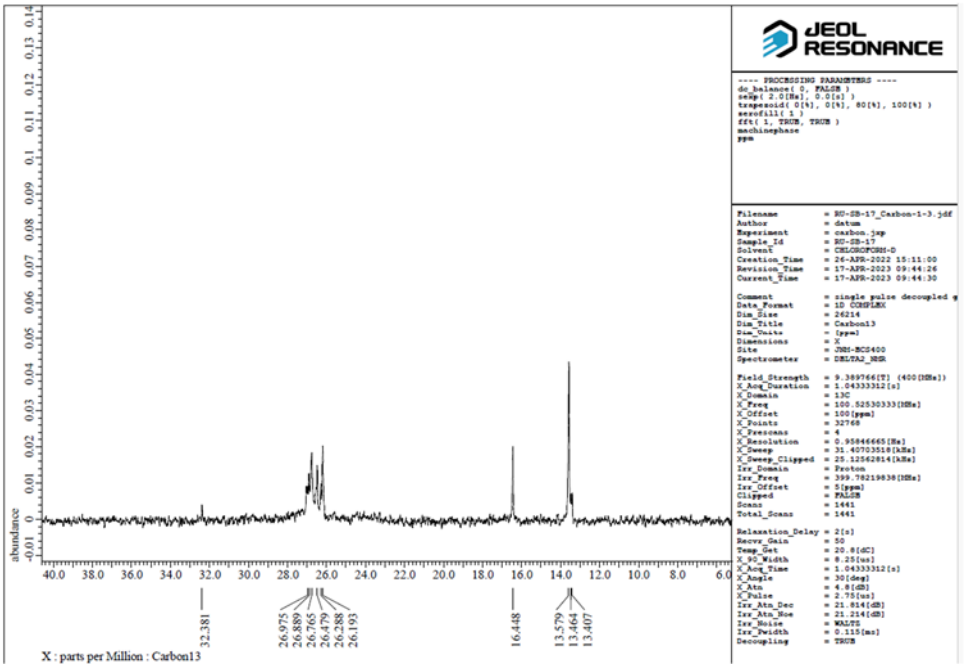

Fig S-18. **^{13}C NMR Spectrum** - Complex $Bu_2SnL_{(3)}A$ (**1c**).

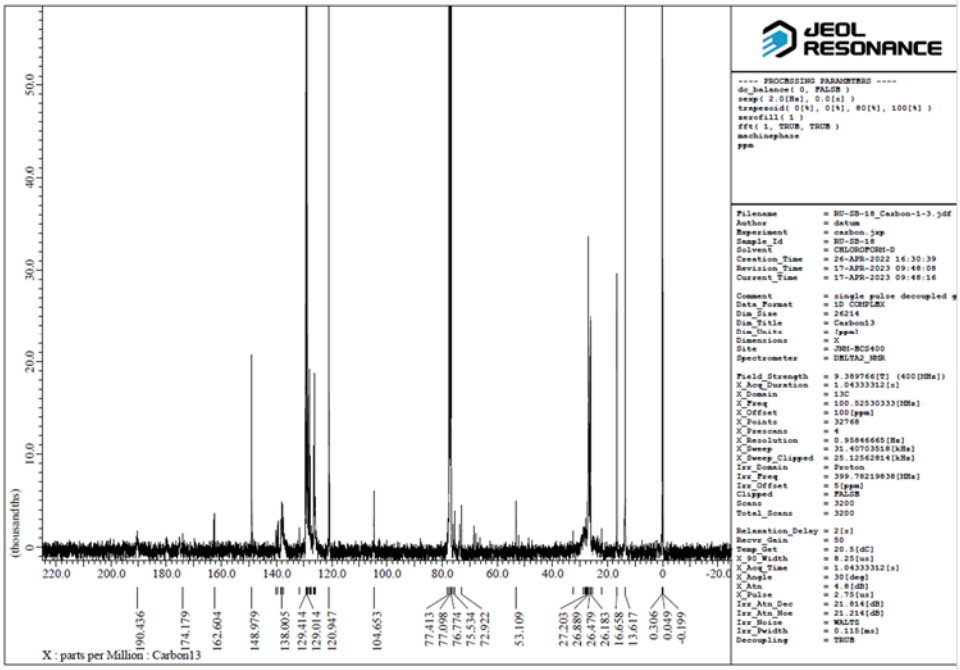

Fig S-19. **^{13}C NMR Spectrum** -Complex $Bu_2SnL_{(4)}A$ (**1d**).

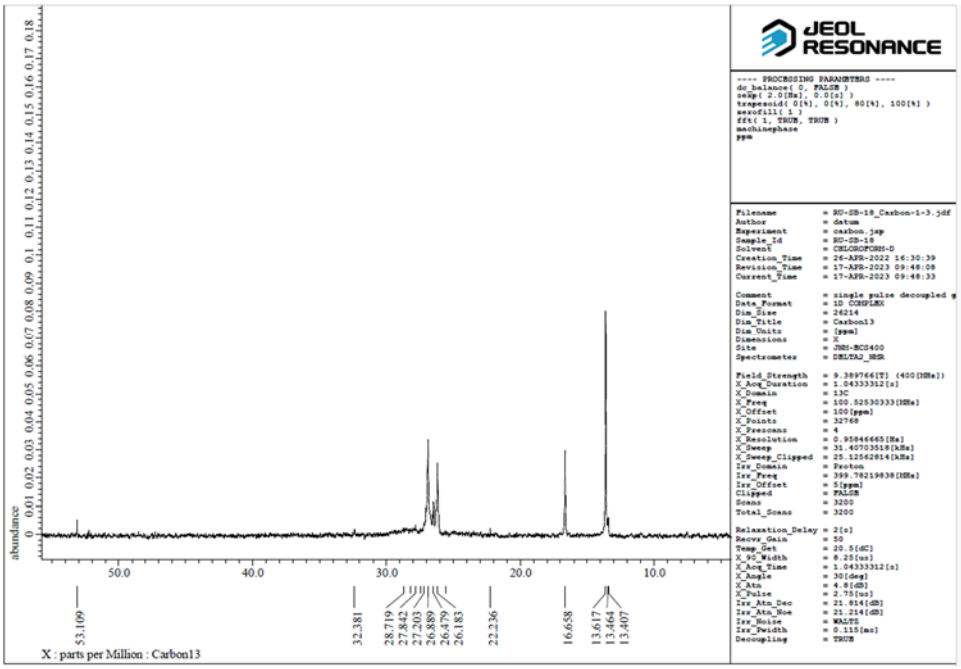

Fig S-20. ^{13}C NMR Spectrum -Complex $Bu_2SnL_{(4)}A$ **(1d)**Expanded.

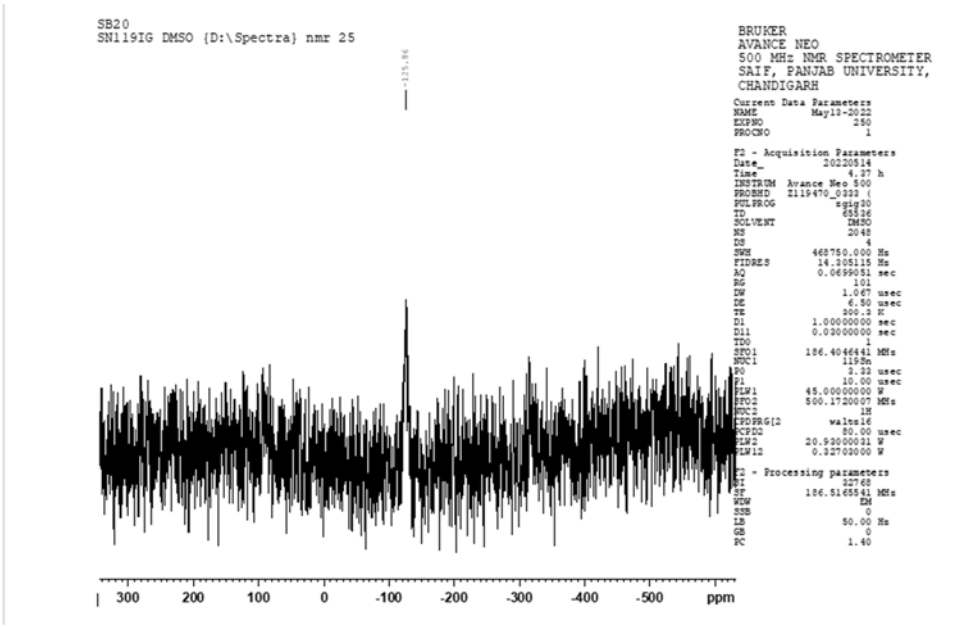

Fig S-21. ^{119}Sn NMR Spectrum - Complex $Bu_2SnL_{(1)}A$(1a).

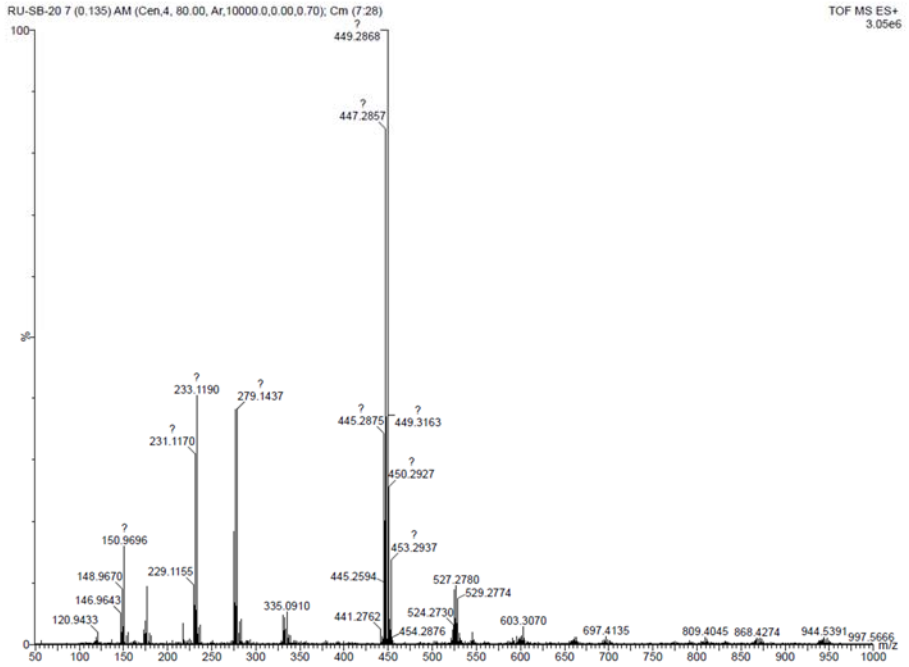

Fig S-22. **Mass Spectrum** - Complex $Bu_2SnL_{(1)}A$(**1a**).

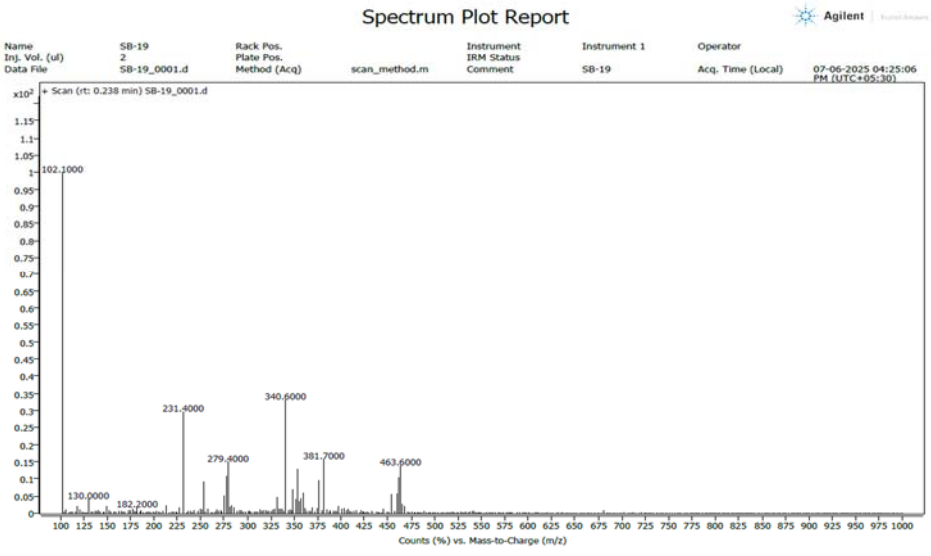

Fig S-23. Mass Spectrum - Complex $Bu_2SnL_{(2)}A$(1b).

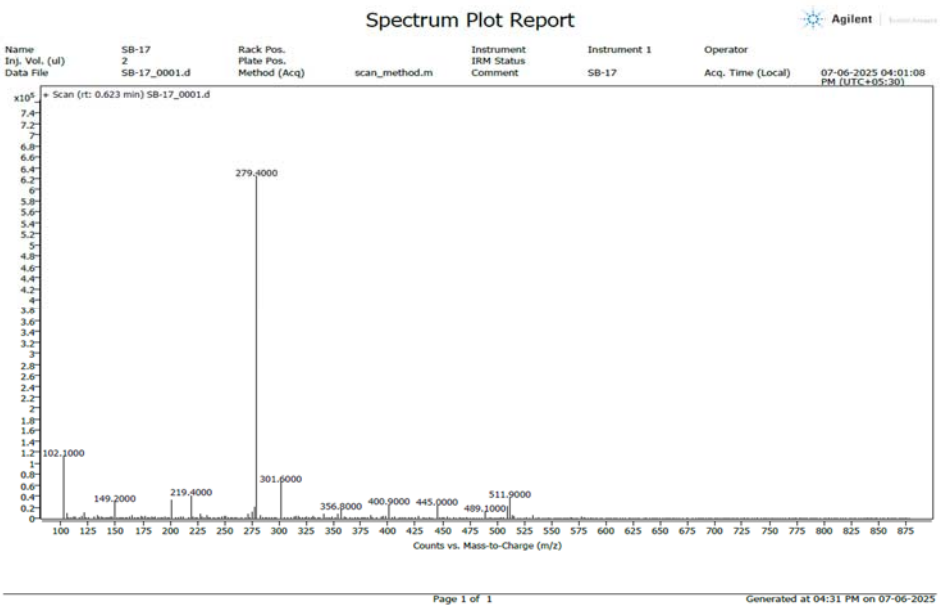

Fig S-24. Mass Spectrum - Complex $Bu_2SnL_{(3)}A$(1c).

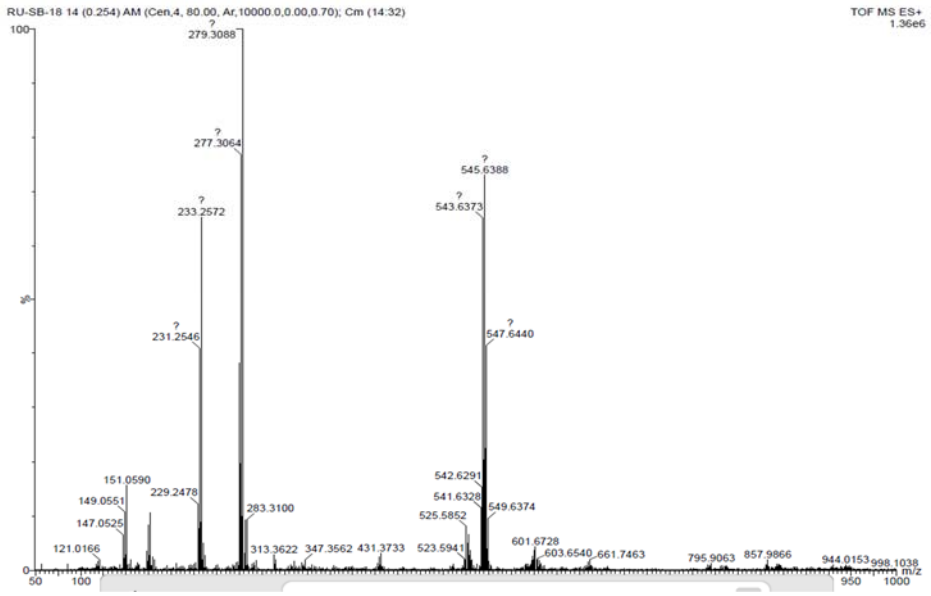

Fig S-25. Mass Spectrum -Complex $Bu_2SnL_{(4)}A$ (1d).

Journal of the Serbian Chemical Society
JSCS@tmf.bg.ac.rs • www.shd.org.rs/JSCS
J. Serb. Chem. Soc. *90* (9) 1055–1067 (2025)
JSCS–5439
Original scientific paper
Published 30 September, 2025

Environmental behavioral controls of polychlorinated biphenyls: Prediction of the soil sorption coefficient (K_{oc}) using multiple linear regression

AMINA CHAOUI[1,2], AMEL BOUAKKADIA[2,3], NOUREDDINE KERTIOU[2,3]* and HAMZA HADDAG[3]

[1]*Laboratory of Engineering and sciences of Advanced Materials (ISMA), ABBES Laghrour-University, Khenchela P.O 1252, 40004, Algeria,* [2]*Matter Sciences Department, Abbes Laghrour-University, Khenchela P.O 1252, 40004, Algeria and* [3]*Synthesis and Bio Catalysis Organic Laboratory, University of Badji Mokhtar-Annaba, Algeria*

(Received 19 February, revised 24 April, accepted 12 May 2025)

Abstract: The application of the quantitative structure property relationship (QSPR) approach helps to predict physicochemical properties of chemicals from their molecular structures. They are based on the translating and encoding of input information on theoretical molecular descriptors running by genetic algorithm techniques (GAs). In this research, the focus is mainly on the controlling and understanding the environmental fate and transport mechanisms of polychlorobiphenyls (PCBs) in soils. To achieve this goal, multiple linear regression (MLR) models were handed-down on a series of 188 PCBs to predict their soil sorption coefficient (log K_{oc}) which is critical to measuring their affinity. All statistical parameters obtained have indicated that the QSPR-MLR model has a very high predictive ability with a higher coefficient of determination (R^2 = = 0.9984) and lower root mean squared errors (*RMSE* = 0.0610). Moreover, the dominant molecular descriptors mentioned that the sorption process of these compounds on the surface of soils have been influenced by the size of molecule, polarizability and density.

Keywords: QSAR/QSPR study; polychlorinated biphenyls; molecular descriptors; partition coefficient; environmental chemistry.

INTRODUCTION

The study on the quantitative structure property relationship (QSPR) approaches, since their first formulation in the 1960s, is steadily growing following advances in environmental topics, medicine, pharmacology, biomedical and industrial research. The application of the QSPR method helps to predict physicochemical properties of compounds from their molecular structures. They are based

* Corresponding author. E-mail: kertiou.noureddine@univ-khenchela.dz
https://doi.org/10.2298/JSC250219035C

on the establishment of a mathematical model between theoretical molecular descriptors (MDs) and responses using linear and non-linear learning machines. These MDs encode and represent all input information running by genetic algorithm techniques (GAs). Besides, using these models helps researchers make predictions for new or untested compounds, thereby assessing their potential environmental impact and aiding in the development of safer and more sustainable chemicals. All the published papers, that have been done on the development of QSAR and QSPR models, revolve around their search to obtain the optimal model in order to predict the properties/activities or even though toxicities of chemicals under the guidelines of the five OECD[1] roles including here below: 1) a defined endpoint, 2) unambiguous algorithm, 3) a defined domain of applicability, 4) appropriate measures of goodness-of-fit, robustness and predictivity and 5) mechanistic interpretation of the molecular descriptors, if possible.[2]

Thus, in this research, the focus is mainly on the controlling and understanding the environmental fate and transport mechanisms of polychlorobiphenyls (PCBs) in soils. To achieve this goal, these chemometrics methods were applied to predict their soil sorption partition coefficient (K_{oc}) which is crucial for effective environmental management and pollution control (*e.g.*, some selected examples around modeling of PCBs using linear and non-linear QSAR/QSPR approaches.[3–10] log K_{oc} is a key parameter used to describe and to determine how organic compounds distribute themselves between aqueous and non-aqueous phases in the environment. It provides essential information for predicting the movement, bioavailability and potential environmental impact of organic pollutants.

PCBs, due to their resistance, lipophilicity, accumulation, their volatility and persistence for a long time, are frequently considered as hazardous compounds that can expose gravity impacts on human health, animals and on the environment. Several studies mentioned that PCB concentrations are highest in sediments and soil, particularly in industrial and urban area.[11,12] Over 90 % of PCB emissions originated from transformers and capacitor leaks and from fragmentizing operations.[13] That being the case, the movement of these organic compounds in soil is the primary and the principal cause of their toxic effects in the ecosystems. They migrate via the soil to vegetables, fruits, trees and eventually to humans through eating food, drinking water and breathing polluted air, causing disruption and contamination on biological systems in the form of diseases as cancer reproductive difficulties, immune system problems, kidney, stomach and Parkinson's diseases.[14–17] The number and the position of chlorines determine both the physical and the biological properties of each congener.[15]

In this study, the models were developed on a series of 188 polychlorinated biphenyls (PCBs) by leveraging the power of multiple linear regression techniques resulting from their simplicity, reproducibility and their higher predictive ability. The basis of these methods is the generation and selection of only influenced

molecular descriptors by using genetic algorithms. The following sections describe the methodologies and materials employed to build and validate QSPR models.

MATERIALS AND METHODS

Dataset collection and preparation

The collection of the experimental data is the significant and the unique source of input information accessible to QSPR modelers.[2] Experimental log K_{oc} values of 188 PCBs in this work were obtained from the literature[18] ranging from 4.2 to 8.03. The PCB codes, the formula, experimental and predicted log K_{oc} values of these PCBs as well as their Chemical Abstracts Service (CAS) numbers are listed in Table S-I of the Supplementary material to this paper. After this step, all molecular structures were drawn using the software ChemDraw[19] and saved as MDL.Molfile. A suggested format for the Hyperchem package[20] to optimize their geometries by the molecular mechanics force field method (MM+) on selecting the lowest energy. Besides, for more precise configuration a semi-empirical PM3 method was done to find the optimal conformation by computation Polak–Ribiere algorithm.

Descriptors calculation

Several molecular descriptors were calculated using Dragon software.[21] We sort these descriptors keeping only significant ones. Finally, 1143 molecular descriptors were retained for the QSPR model construction.

Dataset splitting

For the subsamples selection, a Kennard and Stone algorithm (CADEX) in MATLAB was applied. This non-random technique is usable just for only one splitting. So, it's considered as a deterministic method for the partitioning of the data into training and prediction sets in a way that ensures they are as uniformly spread out as possible. The algorithm, first determines which two samples are the furthest apart and have the largest Euclidean distance in order to determine which samples are the most representative. The remaining samples that are most distant from the previously chosen samples are then picked in each subsequent phase and appended to the bottom of the prior rank list. This process is repeated until a certain number of samples have been selected and ranked. The training set, is selected to build the model and learn the relationship between descriptors and property. It contains 132 compounds of PCBs (70 % of the total). While prediction set is used to evaluate the goodness-of-fit, robustness and the external predictive ability of the model. It contains 56 compounds of PCBs (30 % of the total).

MLR-model development and validation

The aim of multiple linear regression (MLR) is to model in the simplest way, capturing only the most relevant aspects of the chemical structure related to the end point.[2] QSARINS (version 2.2.4)[22,23] software served to achieve this step by running genetic algorithms. Different complemented steps were being verified in order to guarantee the goodness of the optimal MLR model selected. On the one hand, internal and external validation must be done with checking model predictivity of each training and predicting sub-sets, respectively. The internal validation was verified through: Determination Coefficient (R^2), adjusted squared regression coefficient (R^2adj), leave-one-out cross validation (Q^2_{LOO}), leave-many-out cross validation (Q^2_{LMO}), concordance correlation coefficient (*CCC*), root mean squared errors (*RMSE*), mean absolute error (*MAE*), *Y*-scrambling, standard error (*s*). And the external validation by CCC_{ext}, $RMSE_{ext}$, MAE_{ext}, standard error (s_{ext}).[2] Model performance was checked by QUIK rule, which referred to K_{XX} (the inter correlation of the independent variables) < K_{XY} (correlation We're not gonna

do it remove the external between independent variable matrix and dependent variable matrix) that indicate stability and reasonable prediction.[24] On the other hand, the definition of the applicability domain (AD) must be visualized by William's diagram aids in the knowledge and the definition of stable chemicals and the others which appeared as outlier. The outlier (the point with absolute value of standard deviation > 3) and high leverage points (the point where leverage values (h_i) were greater than the warning leverage (h^*)) could be simply and directly identified by Williams plot.[25] The leverage h_i is the i-th diagonal element of the Hat matrix, which links the target values to their predictions:[26]

$$hi = x_i^{\mathrm{T}} (\mathbf{X}^{\mathrm{T}}\mathbf{X})^{-1} x_i \quad (1)$$

Here, $\mathbf{X}$ is a 2D-descriptor matrix with n rows (compounds) and P columns (descriptors), $\mathbf{X}^{\mathrm{T}}$ is its transpose, $(\mathbf{X}^{\mathrm{T}}\mathbf{X})^{-1}$ is the inverse of the matrix $\mathbf{X}^{\mathrm{T}}\mathbf{X}$, and x_i is the row vector representing the descriptors of the query compound. A leverage value hi greater than the warning threshold h^* indicates that the compound i lies far from the center of the descriptor space and has a significant influence on the regression model. The critical value of leverage (h^*) is fixed at $3(p+1)/n$, where p is the number of predictor variables, and n is the number of observations. In this work, the ADs of the QSPR-MLR model were represented by the method of leverage value and Euclidean distance.[27]

RESULTS AND DISCUSSION

An excellent MLR-QSPR developed model was obtained based on two theoretical molecular descriptors (*EPS1* and *RDF030v*), the model is given as:

$$\log K_{\mathrm{oc}} = -1.8617 - 0.9159\,EPS1 - 0.0327\,RDF030v \quad (2)$$

For further assessing the predictive power of any model in QSPR field analysis internal and external validations are a necessary part. All statistical parameters of the QSPR-MLR model represented in Eq. (2) are presented in Table I.

TABLE I. Statistical parameters of QSPR model (internal validation); training set: n(tra) = 132

R^2	R^2_{adj}	*CCC*	Q^2_{LOO}	Q^2_{LMO}	R^2_{Yscr}	Q^2_{Yscr}	*s*	*F*	*RMSE*	*MAE*
0.9925	0.9924	0.9962	0.9922	0.9920	0.0148	–0.0318	0.0617	8525.0396	0.0610	0.0352

$R^2 = 0.9925 > 0.7$, $Q^2 = 0.9922 > 0.6$, $CCC = 0.9962 > 0.85$.[28,29] The difference between R^2 and Q^2 is low (no more than 10%).[2] R^2_{Yscr} and Q^2_{Yscr} values implied that the model had no accidental correlation ($R^2_{\mathrm{Yscr}} = 0.0148 < 0.3$, $Q^2_{\mathrm{Yscr}} = -0.0318 < 0.05$).[30] The great value of Fisher's parameter ($F = 8525.0396$) shows a highly significant model. Additionally, the lowest value of both *RMSE* (0.0610) and *MAE* (0.0352) factors indicate the less errors in predictions. Furthermore, a QUIK rule ($K_{XX} = 0.6727 < K_{XY} = 0.775$) showing a strength estimation. Despite the excellent internal results, this is not enough to propose it as a good model. So, an external validation (listed in Table II) must be undertaken to verify the predictive capabilities of our model, we resorted to its validation on a set designed for this purpose and chosen from the start.

TABLE II. Statistical parameters of QSPR model (external validation); prediction set: n(test) = 56

R^2_{ext}	CCC_{ext}	$RMSE_{ext}$	MAE_{ext}	Q^2-F1	Q^2-F2	Q^2-F3	r^2m
0.9757	0.9865	0.0880	0.0380	0.9746	0.9738	0.9844	0.9427

All values of Q^2-Fn > 0.70 and r^2m > 0.65,[2] with a noticeable decrease in the R^2_{ext} value by approximately 2 %. The regression line is shown in (Fig. 1), representing the relation between the measured values and the model's predictions, providing insight into the model's accuracy and predictive capabilities. In the training set, the observed log K_{oc} values were plotted against the corresponding experimental log K_{oc} values. A linear regression line was fitted to these points, ideally indicating a strong correlation and minimal deviation from the line of best fit. The closer the points are on this line, the more accurate the model is in predicting log K_{oc} values based on experimental data. The training set, used to develop the model, typically shows a high degree of fit, reflecting relationships within the data it was trained on. For the prediction set, which includes data not used during the model training, the observed log K_{oc} values were also plotted against the experimental log K_{oc} values. The fit of the linear regression line in this context demonstrates the model's generalizability and robustness in predicting set should align closely with the line, though some variability in environmental data. Upon examining the scatter plots and the linear regression lines, four outlier points were identified: PCB-000, PCB-095, PCB-155 and PCB-209. These points significantly deviated from the line adjustment, including a substantial discrepancy between the observed and the experimental log K_{oc} values. Such outliers suggest that the model's assumptions or inputs may not adequately account for specific characteristics or behaviors of these particular PCB compounds. PCB-000, PCB-209, PCB-155 and PCB-095 could represent unique cases where the chemical properties or environmental interactions differ significantly from the majority of the data set. A final point to highlight the MLR-QSPR model reliability is the definition of applicability domain (Fig. 1). It represents log K_{oc} experimental values *vs.* predictive values.

As shown (Fig. 2), the values of log K_{oc}(std) are between the limits ±3. One chemical compound PCB-209 (decachlorobiphenyl) from the training set, which appear clearly outside the limit set by the critical value h^* = 0.068 symbolized by the right parallel to the axis of log K_{oc}(std), is considered as influential compound. One other compound corresponding to PCB-000 (biphenyl) from training set appeared a little bit outside this interval with two others PCB-095 (2,2',3,5',6-pentachlorobiphenyl) from test set and PCB-155 (2,2',4,4',6,6'-hexachlorobiphenyl) are wrongly predicted. They are considered as outliers' compounds and cleaning of the data set is required. These outliers highlight the importance of further investigation to understand the underlying reasons for their deviation,

which could include experimental errors, unique chemical behaviors, or limitations in the model's scope. Addressing these outliers might involve refining the model or incorporating additional parameters to improve its overall accuracy and applicability. They were removed to observe their impact on the model accuracy and robustness. With removal of the outlier, the model was recalibrated and re-evaluated.

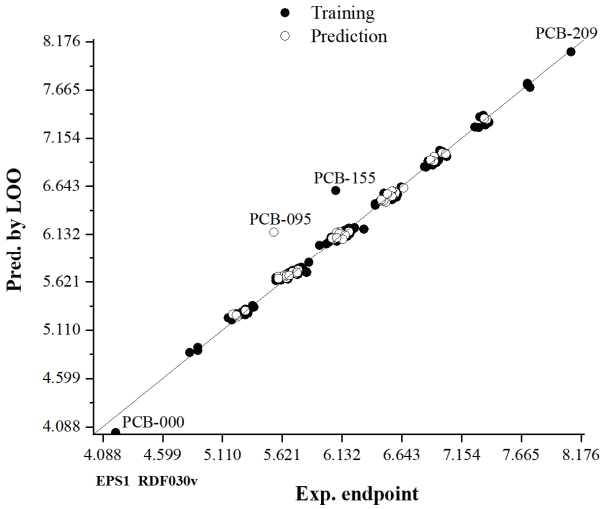

Fig. 1. Predicted *vs.* experimental log K_{oc} values for the training, validation sets.

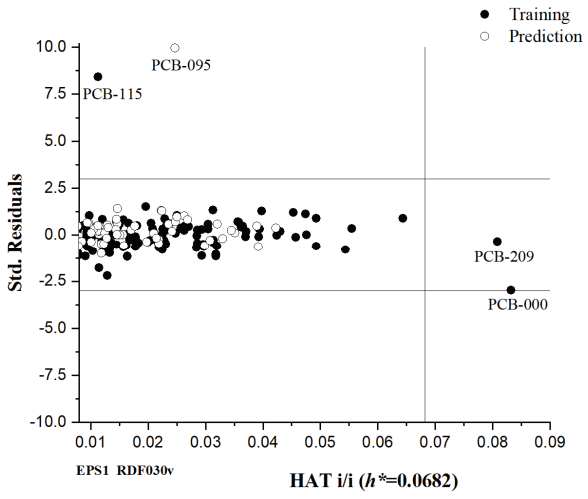

Fig. 2. Williams plot of the developed model.

Model refinement after outlier removal

PCBs, polychlorinated biphenyls are chemical compounds that consist of several isomers, differing in the position and number of chlorine atoms attached to the

biphenyl structure. In particular, PCB-095 and PCB-155 stand out from other PCBs due to their specific number of chlorine atoms and their configuration (Fig. 3).

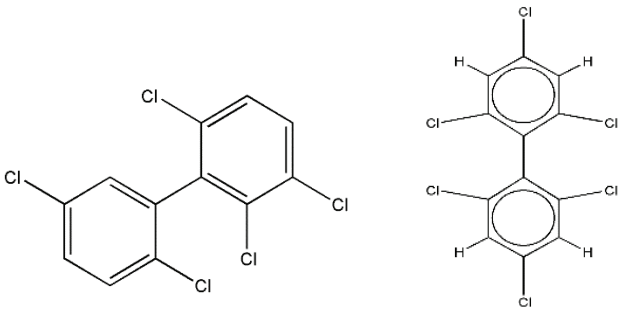

A B

Fig. 3. 2D structure of PCB-095 (A) and PCB-155 (B).

The arrangement of chlorine atoms on the biphenyl rings is unique to PCB--095 and PCB-155. For example, in PCB-095, the chlorine atoms can be located in ortho, meta, or para positions, which influences the reactivity and stability of the compound. In the case of PCB-155, some chlorine atoms occupy the ortho and meta positions, while other PCBs may have different configurations.

PCBs are mixture of several isomers based on the arrangement of chlorine atoms. PCB-095 has characteristics that distinguish it from other isomers, which can impact its environmental and toxicological properties.

The structural difference of PCB-095 compared to other PCBs lies in the number and position of chlorine atoms, which influences its chemical and environmental properties. Its polarity is intermediate, affected by its chlorinated structure. When compared to other PCBs, variations in the number and position of chlorine atoms lead to differences in polarity, thus impacting the solubility, toxicity, and environmental behavior of these compounds.

In summary, the structural distinction between PCB-095 and PCB-155, as well as other PCBs, is based on the number and position of chlorine atoms in their structure.

The QSPR-MLR models re-developed after the elimination of PCB-095 and PCB-155 is as follows in Tables III and IV.

TABLE III. Statistical parameters of re-developed QSPR model (internal validation);); training set: n(tra) = 131

R^2	R^2_{adj}	CCC	Q^2_{LOO}	Q^2_{LMO}	R^2_{Yscr}	Q^2_{Yscr}	s	F	$RMSE$	MAE
0.9966	0.9966	0.9983	0.9964	0.9964	0.0151	–0.0318	0.0416	18857.1091	0.0411	0.0313

The model is given as:

$$\log K_{oc} = -1.8940 + 0.9206EPS1 - 0.0348RDF030v \quad (3)$$

Based on the results obtained, it is observed that the elimination of PCB-095 and PCB-155 did not affect the robustness of the model and its internal and external predictive capacities.

TABLE IV. Statistical parameters of re-developed QSPR model (external validation); test set: n(ext) = 55

R^2_{ext}	CCC_{ext}	$RMSE_{ext}$	MAE_{ext}	Q^2-F1	Q^2-F2	Q^2-F3	r^2m
0.9968	0.9979	0.0352	0.0283	0.9959	0.9958	0.9975	0.9783

According to Fig. 4, it is clear that the predicted log K_{oc} values were very similar to the experimental ones, *i.e.*, all points lying excellently along the regression line except PCB-000 which refers to the biphenyl compound. The compound PCB 209 is located on the line, but it deviates significantly due to its distinct structure. This is confirmed by the Williams diagram, which places it outside the application domain.

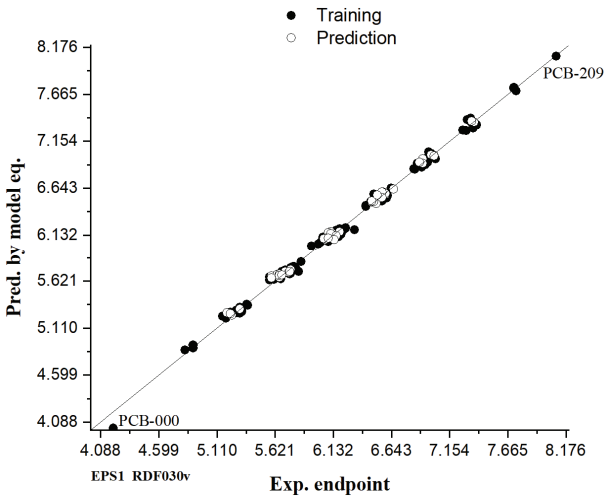

Fig. 4. Plot of predicted *vs.* experimental log K_{oc} partition coefficient.

The Fig. 5 shows that most data points from both training and prediction sets have leverage values below the critical threshold excluding PCB-000 and PCB--209 included in the training set, they have very unique structure, are considered influential chemical, and appear in the Williams graph to leverage higher than the warning h^* value of 0.069. In addition to being an influential point, PCB-000 is an outlier on the y-axis where it presents a standardized error lower than –3, along with PCB-120, which is also slightly aberrant. These points do not disproportionately influence the regression model. Consequently, the model predictions remain robust and unaffected by a few data points, maintaining overall stability.

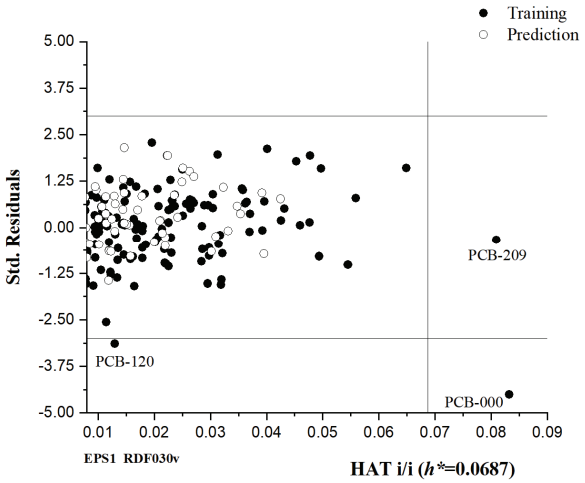

Fig. 5. Williams plot of the re-developed model.

Mechanistic interpretation

The *EPS1* descriptor is a measure used in molecular chemistry to describe the polarity and surface area of a molecule. It accounts for the surface area occupied by polar atoms, which is significant for understanding molecule solubility, permeability, and interactions with other molecules. The second descriptor *RDF030v* typically refers to a statistical measure that describes the spatial distribution of atoms within a molecule. Their negative coefficient implies that there is contradictory relationship between both *RDF030v* and log K_{oc} (the *RDF030v* value increases, log K_{oc} decreases). This could indicate that a higher number of atom pairs at the specified distance negatively impact the binding affinity, potentially due to steric interference or unfavorable spatial configuration. Specially, this descriptor might represent a particular distance range, capturing how atoms are distributed at a distance of 3.0 Å from a reference point within the molecule. This descriptor can provide insights into the three-dimensional arrangement and overall shape of the molecule.

After all statistical and graphical tests of the MLR-model created, the model represented in Eq. (3) is the most excellent. This is after removing the response outliers. It is challenging to determine the correct explanation for why the model failed to predict them, especially since all the chemicals have similar structures to each other. In addition to this, it is crucial to remember that variations in experimental conditions and measurement errors can also cause deviations from the expected results. Natural variations in soil composition and properties can also lead to differences in adsorption behavior. This means the model is reliable and produces consistent results. Also, we can see that the R^2 and Q^2 values for the permuted models (shown as red and yellow points, Fig. 6) are clustered near zero,

while the R^2 and Q^2 values of the actual model are significantly higher. This indicates that the original model is not due to chance correlations and that has identified a real relationship between the variables (the model is robust).

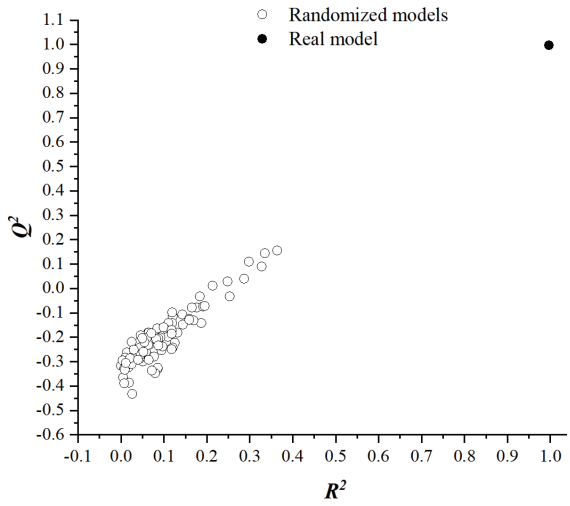

Fig. 6. *Y*-Scrambling plot.

Furthermore, variance inflation factor (*VIF*),[31] *T* and *p* values has several benefits (Table V) for improving the interpretation of the regression model results and enhancing its reliability. The larger *T* and the lower *VIF* and *p* values indicates that the independent variable (descriptor) has a significant effect on the dependent variable (log K_{oc}). *VIF* values are ensuring that there is no significant linear relationship between the independent variables.

TABLE V. Descriptions involved in the best developed MLR-models and corresponding *T* (test), *p* (statistically significant) and *VIF* (variance inflation factor) values

Descriptor	*T*	*P*	*VIF*
EPS1	196.45	0.000	1.601
RDF030v	–11.67	0.000	1.601

Comparison with previous work

To highlight the strengths of the MLR-QSPR model, a comparison of results with similar studies in the field was done and summarized in Table VI.

Our model's statistics are better than the two other models summarized in Table VI, except for the external validation (Q^2_{ext}). Yu *et al.*[3] model exhibits a $Q^2_{ext} = 0.9980$ greater than our model. This can be explained by the percentage of test compounds. We used 30 % of the dataset to externally validate our model

where Yu *et al.* used only ~19 % of their 138 PCBs. The external predictive ability of our model could be explained by relevant selection of descriptors.

TABLE VI. Comparison between our present work and previously published work for organic carbon/water partition coefficient (K_{oc}); KS – Kennard–Stone; SPM – SPM derived

No.	Ref.	Compd.	Dataset	Splitting method	Training	Test	R^2	Q^2_{LOO}	Q^2_{ext}	*RMSE*
1	Curr. study	PCBs	185	KS	130	55	0.9970	0.9968	0.9968	0,0378
2	Yu *et al.*[3]	PCBs	138	SPM	112	26	0.9960	0.9960	0.9980	0.0380
3	Yuan *et al.*[7]	PCBs	73	KS	55	18	0.9170	0.9020	0.8570	0.2530

CONCLUSION

To estimate the soil sorption partition coefficient and to determine which physicochemical molecular features have an influence on the sorption of a set of 188 polychlorinated biphenyls, a multiple linear regression QSPR model has been established in compliance with the OECD[1] principles. The entire database was divided into training and test sets by Kennard–Stone algorithm. Using QSARINS software, MLR model was developed using genetic algorithm techniques to select the main molecular descriptors. Two molecular descriptors were identified, namely *EPS1* and *RDF030v*, showing that the distribution behavior of the PCBs compounds is influenced by molecular size, polarizability and density. The final optimal model, obtained after removing outliers which had high R^2 and Q^2 values, had the distinct advantages of satisfactory stability and prediction performance as well as wide applicability domains. The proposed model can be used in the future to make reliable predictions for new compounds or compounds which have not yet been tested.

SUPPLEMENTARY MATERIAL

Additional data and information are available electronically at the pages of journal website: https://www.shd-pub.org.rs/index.php/JSCS/article/view/13257, or from the corresponding author on request.

ИЗВОД

ЕКОЛОШКА КОНТРОЛА ПОНАШАЊА ПОЛИХЛОРОВАНИХ БИФЕНИЛА: ПРЕДВИЂАЊЕ КОЕФИЦИЈЕНТА СОРПЦИЈЕ ЗЕМЉИШТА (K_{OC}) КОРИШЋЕЊЕМ МЕТОДЕ ВИШЕСТРУКЕ ЛИНЕАРНЕ РЕГРЕСИЈЕ

AMINA CHAOUI[1,2], AMEL BOUAKKADIA[2,3], NOUREDDINE KERTIOU[2,3] и HAMZA HADDAG[3]

[1]Laboratory of Engineering and sciences of Advanced Materials (ISMA), ABBES Laghrour-University, Khenchela P.O 1252, 40004, Algeria, [2]Matter Sciences Department, Abbes Laghrour-University, Khenchela P.O 1252, 40004, Algeria и [3]Synthesis and Bio Catalysis Organic Laboratory, University of Badji Mokhtar-Annaba, Algeria

Примена квантитативног односа структуре и особина (QSPR) помаже у предвиђању физичко–хемијских својстава на основу молекулских структура. Овај приступ заснован је на превођењу и кодирању улазних података о теоријским молекулским дескрипторима коришћењем техника генетских алгоритама. У овом истраживању, фокус је првенствено

на контроли и разумевању утицаја у животној средини и механизама транспорта полихлорованих бифенила (PCB) у земљишту. Да би се постигао овај циљ, модели вишеструке линеарне регресије (MLR) су примењени на серију од 188 PCB да би се предвидео њихов коефицијент сорпције земљишта (log K_{OC}) што је кључно за мерење њиховог афинитета. Сви добијени статистички параметри су показали да QSPR-MLR модел има веома високу предиктивну способност (R^2 = 0,9984 и *RMSE* = 0,0610). Поред тога, доминантни молекулски дескриптори указују на то да величина молекула, као и њихова поларизабилност и густина утичу на сорпциони процес ових једињења на површини земљишта.

(Примљено 19. фебруара, ревидирано 24. априла, прихваћено 12. маја 2025)

REFERENCES

1. S. Kherouf, N. Bouarra, A. Bouakkadia, D. Messadi, *J. Serb. Chem. Soc.* **84** (2019) 575 (https://doi.org/10.2298/JSC180820016K)
2. P. Gramatica, *Int. J. Quant. Struct. Prop. Relat.* **5** (2020) 63 (https://doi.org/10.4018/IJQSPR.20200701.oa1)
3. S. Yu, S. Gao, Y. Gan, Y. Zhang, X. Ruan, Y. Wang, L. Yang, J. Shi, *SAR QSAR Environ. Res.* **27** (2016) 2 (http://dx.doi.org/10.1080/1062936X.2016.1158734)
4. W. J. Doucette, *Environ. Toxicol. Chem.* **22** (2003) 1771 (http://doi.org/10.1897/01-362)
5. P. Gramatica, E. Giani, E. Papa, *J. Mol. Graph. Modell.* **25** (2007) 755 (https://doi.org/10.1016/j.jmgm.2006.06.005)
6. R. S. Kookana, R. Ahmad, A. Farenhorst, in *Non-First Order Degradation and Time-Dependent Sorption of Organic Chemicals in Soil,* W. Chen, A. Sabljic, S. A. Cryer, R. S. Kookana, Eds., ACS Symposium Series, Vol. 1174, American Chemical Society, Washington DC, 2014, pp. 222–236 (http://doi.org/10.1021/bk-2014-1174.ch012)
7. J. Yuan, S. Yu, T. Zhang, X. Yuan, Y. Cao, X. Yu, X. Yang, W. Yao*, Ecotox. Environ. Safety* **128** (2016) 171 (http://dx.doi.org/10.1016/j.ecoenv.2016.02.022)
8. Y. Wang, J. Chen, X. Yang, F. Lyakurwa, X. Li, X. Qiao, *Chemosphere* **119** (2015) 438 (http://dx.doi.org/10.1016/j.chemosphere.2014.07.007)
9. M. H. Fatemi, Z. G. Chahi, *SAR QSAR Environ. Res.* **23** (2012) 155 (http://dx.doi.org/10.1080/1062936X.2011.645876)
10. P. Singh, S. Pandit, R. Parthasarathi, in *Safety Evaluation and Risk Assessment*, H. Hong Ed., Elsevier Science, Amsterdam, 2023, pp. 77–87 (http://doi.org/10.1016/B978-0-443-15339-6.00026-6)
11. S. Mao, S. Liu, Y. Zhou, Q. An, X. Zhou, Z. Mao, Y. Wu, W. Liu, *Environ. Poll.* **271** (2021) 116171 (https://doi.org/10.1016/j.envpol.2020.116171)
12. Y. Dumanoglu, E. O. Gaga, E. Gungormus, S. C. Sofuoglu, M. Odabasi, *Sci. Tot. Environ. J.* **580** (2017) 920 (http://doi.org/10.1016/j.scitotenv.2016.12.040)
13. S. Kakareka, T. Kukharchyk, in *EMEP/CORINAIR Guidebook*, K. Breivik, Ed., European Environment Agency, Copenhagen, 2005 (https://www.eea.europa.eu/publications/EMEPCORINAIR5/Sources_of_PCB_emissions.pdf)
14. K. B. Moysich, R. J. Menzes, J. A. Baker, K. L. Falkner, *Rev. Environ. Health* **17** (2002) 263 (http://doi.org/10.1515/REVEH.2002.17.4.263)
15. D. O. Carpenter, *Rev. Environ. Health* **21** (2006) 1 (https://doi.org/10.1515/REVEH.2006.21.1.1)
16. L. M. Frazier, *J. Agromed.* **12** (2007) 27 (https://doi.org/10.1300/J096v12n01_04)
17. N. Othman, Z. Ismail, M. I. Selamat, S. H. S. Abdul Kadir, N. A. Shibraumalisi, *Int. J. Environ. Res. Public Health* **19** (2022) 13923 (https://doi.org/10.3390/ijerph192113923)

18. K. Jagiello, A. Sosnowska, S. Walker, M. Haranczyk, A. Gajewicz, T. Kawai, N. Suzuki, J. Leszczynski, T. Puzyn, *Struct. Chem.* **25** (2014) 997 (https://doi.org/10.1007/s11224-014-0419-1)
19. *ChemDraw*, CambridgeSoft Corporation, Cambridge, MA (http://camsoft.com/)
20. *Hyperchem^{TM}, release 6.03 for windows*, Hypercube, Inc., Gainesville, FL, 2000
21. R. Todeschini, V. Consonni, M. Pavan, *DRAGON Software for the Calculation of Molecular Descriptors, release 5.3 for windows*, Talete srl, Milano, 2006
22. P. Gramatica, N. Chirico, E. Papa, S. Cassani, S. Kovarich, *J. Comp. Chem.* **34** (2013) 2121 (https://doi.org/10.1002/jcc.23361)
23. P. Gramatica, S. Cassani, N. Chirico, *J. Comp. Chem.* **35** (2014) 1036 (https://doi.org/10.1002/jcc.23576)
24. L. Gu, T. Zhu, M. Chen, *J. Environ. Chem. Eng*. **9** (2021) 105615 (https://doi.org/10.1016/j.jece.2021.105615)
25. X. Zhao, Y. Zhao, Z. Ren, Y. Li, *Comp. Biol. Chem*. **79** (2019) 177 (http://doi.org/10.1016/j.compbiolchem.2019.02.008)
26. H. Yu, D. Wondrousch, F. Li, J. Chen, H. Lin, L. Ji, *Chem. Res. Toxicol.* **28** (2015) 1541 (http://doi.org/10.1021/acs.chemrestox.5b00127)
27. H. Liu, M. Wei, X. Yang, C. Yin, X. He, Sci. *Total Environ.* **574** (2017) 1371 (https://doi.org/10.1016/j.scitotenv.2016.08.051)
28. N. Chirico, P. Gramatica, *J. Chem. Inf. Model.* **52** (2012) 2044 (https://doi.org/10.1021/ci300084j)
29. E. Carnescchi, A. A. Toropov, A. P. Toropova, N. Kramer, C. Svendsen, J. L. Dorne, E. Benfenati, *Sci. Total Environ.* **704** (2020) 135302 (http://doi.org/10.1016/j.scitotenv.2019.135302)
30. T. Zhu, H. Yan, R. P. Singh, Y. Wang, H. Cheng, *Env. Sci. Poll. Res. J.* **27** (2020) 17550 (http://doi.org/10.1007/s11356-019-06389-z)
31. N. Bouarra, S. Kherouf, N. Nadji, L. Nouri, A. Boudjemaa, S. Djerad, K. Bachari, *Chem. Prod. Process Model*. **19** (2024) 251 (http://doi.org/10.1515/cppm-2023-0024).

Journal of the Serbian Chemical Society
JSCS@tmf.bg.ac.rs • www.shd.org.rs/JSCS
J. Serb. Chem. Soc. 90 (9) S348–S352 (2025) *Supplementary material*

SUPPLEMENTARY MATERIAL TO

Environmental behavioral controls of polychlorinated biphenyls: Prediction of the soil sorption coefficient (K_{oc}) using multiple linear regression

AMINA CHAOUI[1,2], AMEL BOUAKKADIA[2,3], NOUREDDINE KERTIOU[2,3]* and HAMZA HADDAG[3]

[1]*Laboratory of Engineering and sciences of Advanced Materials (ISMA), ABBES Laghrour--University, Khenchela P.O 1252, 40004, Algeria,* [2]*Matter Sciences Department, Abbes Laghrour-University, Khenchela P.O 1252, 40004, Algeria and* [3]*Synthesis and Bio Catalysis Organic Laboratory, University of Badji Mokhtar-Annaba, Algeria*

J. Serb. Chem. Soc. 90 (9) (2025) 1055–1067

TABLE S-I. List of studied compounds: PCB code, Formulae, observed and prediction values of log K_{oc}.

N°	Compounds	Formulae	log K_{oc} exp	log K_{oc} pred
1	PCB-000	$C_{12}H_{10}$	4.2	4.0244
2	PCB-006	$C_{12}H_8Cl_2$	4.83	4.8731
3	PCB-007	$C_{12}H_8Cl_2$	4.83	4.8719
4	PCB-013	$C_{12}H_8Cl_2$	4.9	4.8944
5	PCB-014	$C_{12}H_8Cl_2$	4.9	4.9257
6*	PCB-017	$C_{12}H_7Cl_3$	5.2	5.2793
7*	PCB-018	$C_{12}H_7Cl_3$	5.2	5.2789
8	PCB-019	$C_{12}H_7Cl_3$	5.28	5.3011
9	PCB-020	$C_{12}H_7Cl_3$	5.23	5.2662
10	PCB-021	$C_{12}H_7Cl_3$	5.19	5.2195
11*	PCB-022	$C_{12}H_7Cl_3$	5.24	5.2511
12	PCB-023	$C_{12}H_7Cl_3$	5.23	5.2823
13	PCB-024	$C_{12}H_7Cl_3$	5.16	5.2409
14*	PCB-025	$C_{12}H_7Cl_3$	5.31	5.316
15*	PCB-026	$C_{12}H_7Cl_3$	5.31	5.3154
16	PCB-027	$C_{12}H_7Cl_3$	5.31	5.2809
17	PCB-029	$C_{12}H_7Cl_3$	5.26	5.2789
18	PCB-031	$C_{12}H_7Cl_3$	5.31	5.2996
19*	PCB-032	$C_{12}H_7Cl_3$	5.23	5.2655
20	PCB-033	$C_{12}H_7Cl_3$	5.31	5.2695
21	PCB-034	$C_{12}H_7Cl_3$	5.31	5.3316
22	PCB-035	$C_{12}H_7Cl_3$	5.33	5.3036

* Corresponding author. E-mail: kertiou.noureddine@univ-khenchela.dz

N°	Compounds	Formulae	log K_{oc} exp	log K_{oc} pred
23	PCB-036	$C_{12}H_7Cl_3$	5.37	5.3677
24	PCB-037	$C_{12}H_7Cl_3$	5.33	5.2874
25	PCB-038	$C_{12}H_7Cl_3$	5.28	5.2775
26	PCB-039	$C_{12}H_7Cl_3$	5.38	5.3522
27	PCB-040	$C_{12}H_6Cl_4$	5.57	5.6343
28*	PCB-041	$C_{12}H_6Cl_4$	5.59	5.6773
29*	PCB-042	$C_{12}H_6Cl_4$	5.64	5.6773
30*	PCB-043	$C_{12}H_6Cl_4$	5.64	5.6922
31	PCB-044	$C_{12}H_6Cl_4$	5.64	5.6762
32	PCB-046	$C_{12}H_6Cl_4$	5.68	5.7182
33*	PCB-047	$C_{12}H_6Cl_4$	5.72	5.722
34*	PCB-048	$C_{12}H_6Cl_4$	5.66	5.6931
35*	PCB-049	$C_{12}H_6Cl_4$	5.71	5.7215
36	PCB-050	$C_{12}H_6Cl_4$	5.76	5.7606
37*	PCB-051	$C_{12}H_6Cl_4$	5.76	5.7443
38	PCB-052	$C_{12}H_6Cl_4$	5.83	5.7213
39	PCB-053	$C_{12}H_6Cl_4$	5.76	5.7415
40	PCB-054	$C_{12}H_6Cl_4$	5.63	5.6795
41	PCB-055	$C_{12}H_6Cl_4$	5.66	5.6624
42*	PCB-056	$C_{12}H_6Cl_4$	5.66	5.6613
43	PCB-057	$C_{12}H_6Cl_4$	5.71	5.7238
44*	PCB-058	$C_{12}H_6Cl_4$	5.71	5.7229
45	PCB-059	$C_{12}H_6Cl_4$	5.64	5.6829
46	PCB-060	$C_{12}H_6Cl_4$	5.67	5.6462
47	PCB-061	$C_{12}H_6Cl_4$	5.61	5.6373
48*	PCB-062	$C_{12}H_6Cl_4$	5.59	5.6523
49	PCB-063	$C_{12}H_6Cl_4$	5.71	5.7092
50	PCB-064	$C_{12}H_6Cl_4$	5.64	5.6677
51	PCB-065	$C_{12}H_6Cl_4$	5.57	5.6631
52	PCB-066	$C_{12}H_6Cl_4$	5.74	5.7107
53	PCB-068	$C_{12}H_6Cl_4$	5.79	5.7736
54	PCB-069	$C_{12}H_6Cl_4$	5.71	5.7393
55	PCB-070	$C_{12}H_6Cl_4$	5.73	5.7106
56*	PCB-071	$C_{12}H_6Cl_4$	5.66	5.6783
57	PCB-072	$C_{12}H_6Cl_4$	5.78	5.7733
58	PCB-073	$C_{12}H_6Cl_4$	5.71	5.738
59*	PCB-074	$C_{12}H_6Cl_4$	5.74	5.7105
60	PCB-075	$C_{12}H_6Cl_4$	5.72	5.7239
61*	PCB-076	$C_{12}H_6Cl_4$	5.68	5.6875
62	PCB-077	$C_{12}H_6Cl_4$	5.75	5.6967
63*	PCB-078	$C_{12}H_6Cl_4$	5.75	5.7198
64	PCB-079	$C_{12}H_6Cl_4$	5.8	5.7612
65	PCB-080	$C_{12}H_6Cl_4$	5.85	5.8256
66	PCB-081	$C_{12}H_6Cl_4$	5.76	5.7034
67	PCB-082	$C_{12}H_5Cl_5$	6	6.0294
68	PCB-083	$C_{12}H_5Cl_5$	6.04	6.0914
69*	PCB-084	$C_{12}H_5Cl_5$	6.09	6.134

N°	Compounds	Formulae	log K_{oc} exp	log K_{oc} pred
70	PCB-085	$C_{12}H_5Cl_5$	6.07	6.0715
71	PCB-086	$C_{12}H_5Cl_5$	6.02	6.0489
72	PCB-087	$C_{12}H_5Cl_5$	6.07	6.0704
73	PCB-088	$C_{12}H_5Cl_5$	6.11	6.1232
74	PCB-089	$C_{12}H_5Cl_5$	6.11	6.1068
75	PCB-090	$C_{12}H_5Cl_5$	6.12	6.1353
76*	PCB-091	$C_{12}H_5Cl_5$	6.11	6.1598
77	PCB-092	$C_{12}H_5Cl_5$	6.11	6.1345
78*	PCB-093	$C_{12}H_5Cl_5$	6.09	6.1494
79	PCB-094	$C_{12}H_5Cl_5$	6.16	6.1741
80*	PCB-095	$C_{12}H_5Cl_5$	5.55	6.157
81	PCB-096	$C_{12}H_5Cl_5$	6.13	6.0979
82*	PCB-097	$C_{12}H_5Cl_5$	6.07	6.0905
83	PCB-098	$C_{12}H_5Cl_5$	6.16	6.1778
84*	PCB-099	$C_{12}H_5Cl_5$	6.14	6.1358
85	PCB-100	$C_{12}H_5Cl_5$	6.24	6.2037
86*	PCB-102	$C_{12}H_5Cl_5$	6.19	6.1629
87	PCB-103	$C_{12}H_5Cl_5$	6.24	6.2011
88	PCB-104	$C_{12}H_5Cl_5$	6.2	6.1384
89	PCB-105	$C_{12}H_5Cl_5$	6.09	6.0569
90	PCB-106	$C_{12}H_5Cl_5$	6.09	6.0802
91*	PCB-107	$C_{12}H_5Cl_5$	6.14	6.1192
92*	PCB-108	$C_{12}H_5Cl_5$	6.14	6.1182
93*	PCB-109	$C_{12}H_5Cl_5$	6.07	6.0942
94*	PCB-110	$C_{12}H_5Cl_5$	6.06	6.0807
95	PCB-111	$C_{12}H_5Cl_5$	6.19	6.1804
96	PCB-112	$C_{12}H_5Cl_5$	6.04	6.1035
97*	PCB-113	$C_{12}H_5Cl_5$	6.11	6.14
98	PCB-114	$C_{12}H_5Cl_5$	6.09	6.0643
99	PCB-115	$C_{12}H_5Cl_5$	6.07	6.0788
100	PCB-116	$C_{12}H_5Cl_5$	5.94	6.013
101*	PCB-117	$C_{12}H_5Cl_5$	6.05	6.0892
102*	PCB-118	$C_{12}H_5Cl_5$	6.16	6.1218
103	PCB-119	$C_{12}H_5Cl_5$	6.16	6.1359
104	PCB-120	$C_{12}H_5Cl_5$	6.32	6.1851
105	PCB-121	$C_{12}H_5Cl_5$	6.19	6.1965
106*	PCB-122	$C_{12}H_5Cl_5$	6.14	6.0779
107	PCB-123	$C_{12}H_5Cl_5$	6.16	6.1289
108	PCB-124	$C_{12}H_5Cl_5$	6.16	6.1287
109*	PCB-125	$C_{12}H_5Cl_5$	6.09	6.0973
110	PCB-126	$C_{12}H_5Cl_5$	6.18	6.1124
111	PCB-127	$C_{12}H_5Cl_5$	6.22	6.1775
112	PCB-129	$C_{12}H_4Cl_6$	6.42	6.449
113*	PCB-130	$C_{12}H_4Cl_6$	6.47	6.4864
114	PCB-131	$C_{12}H_4Cl_6$	6.51	6.5407
115	PCB-132	$C_{12}H_4Cl_6$	6.52	6.5225
116	PCB-133	$C_{12}H_4Cl_6$	6.52	6.5487

N°	Compounds	Formulae	log K_{oc} exp	log K_{oc} pred
117	PCB-134	$C_{12}H_4Cl_6$	6.49	6.5676
118	PCB-135	$C_{12}H_4Cl_6$	6.57	6.5899
119	PCB-136	$C_{12}H_4Cl_6$	6.53	6.5171
120	PCB-137	$C_{12}H_4Cl_6$	6.49	6.4918
121	PCB-139	$C_{12}H_4Cl_6$	6.59	6.5664
122*	PCB-140	$C_{12}H_4Cl_6$	6.59	6.5661
123*	PCB-141	$C_{12}H_4Cl_6$	6.49	6.4905
124	PCB-142	$C_{12}H_4Cl_6$	6.46	6.4912
125*	PCB-143	$C_{12}H_4Cl_6$	6.54	6.5293
126	PCB-144	$C_{12}H_4Cl_6$	6.59	6.5635
127	PCB-145	$C_{12}H_4Cl_6$	6.56	6.5
128	PCB-146	$C_{12}H_4Cl_6$	6.54	6.5486
129*	PCB-147	$C_{12}H_4Cl_6$	6.57	6.5927
130	PCB-148	$C_{12}H_4Cl_6$	6.64	6.6334
131*	PCB-149	$C_{12}H_4Cl_6$	6.59	6.5781
132	PCB-150	$C_{12}H_4Cl_6$	6.61	6.5564
133*	PCB-151	$C_{12}H_4Cl_6$	6.56	6.5895
134	PCB-152	$C_{12}H_4Cl_6$	6.53	6.5329
135*	PCB-154	$C_{12}H_4Cl_6$	6.66	6.6221
136	PCB-155	$C_{12}H_4Cl_6$	6.08	6.5966
137*	PCB-156	$C_{12}H_4Cl_6$	6.51	6.4746
138	PCB-157	$C_{12}H_4Cl_6$	6.51	6.4737
139*	PCB-158	$C_{12}H_4Cl_6$	6.49	6.4914
140*	PCB-159	$C_{12}H_4Cl_6$	6.56	6.5361
141	PCB-160	$C_{12}H_4Cl_6$	6.42	6.4548
142	PCB-161	$C_{12}H_4Cl_6$	6.56	6.5507
143	PCB-162	$C_{12}H_4Cl_6$	6.56	6.5362
144*	PCB-163	$C_{12}H_4Cl_6$	6.47	6.5004
145	PCB-164	$C_{12}H_4Cl_6$	6.49	6.4988
146*	PCB-165	$C_{12}H_4Cl_6$	6.52	6.5606
147	PCB-166	$C_{12}H_4Cl_6$	6.42	6.4396
148	PCB-167	$C_{12}H_4Cl_6$	6.58	6.5407
149	PCB-168	$C_{12}H_4Cl_6$	6.56	6.5556
150	PCB-169	$C_{12}H_4Cl_6$	6.6	6.5293
151	PCB-170	$C_{12}H_3Cl_7$	6.85	6.844
152	PCB-171	$C_{12}H_3Cl_7$	6.94	6.9289
153	PCB-172	$C_{12}H_3Cl_7$	6.89	6.9062
154	PCB-173	$C_{12}H_3Cl_7$	6.87	6.9084
155	PCB-174	$C_{12}H_3Cl_7$	6.94	6.9448
156*	PCB-175	$C_{12}H_3Cl_7$	6.99	6.9962
157	PCB-176	$C_{12}H_3Cl_7$	6.96	6.9185
158*	PCB-177	$C_{12}H_3Cl_7$	6.92	6.9554
159	PCB-178	$C_{12}H_3Cl_7$	6.97	7.0238
160	PCB-179	$C_{12}H_3Cl_7$	6.94	6.9551
161	PCB-180	$C_{12}H_3Cl_7$	6.92	6.9051
162	PCB-181	$C_{12}H_3Cl_7$	6.94	6.9341
163	PCB-182	$C_{12}H_3Cl_7$	7.02	6.9888

N°	Compounds	Formulae	log K_{oc} exp	log K_{oc} pred
164*	PCB-183	$C_{12}H_3Cl_7$	7.02	6.9841
165	PCB-184	$C_{12}H_3Cl_7$	7.03	6.9583
166	PCB-186	$C_{12}H_3Cl_7$	6.91	6.8684
167	PCB-187	$C_{12}H_3Cl_7$	6.99	7.0114
168	PCB-188	$C_{12}H_3Cl_7$	7.01	6.9908
169	PCB-189	$C_{12}H_3Cl_7$	6.94	6.892
170	PCB-190	$C_{12}H_3Cl_7$	6.84	6.8519
171*	PCB-191	$C_{12}H_3Cl_7$	6.92	6.909
172	PCB-192	$C_{12}H_3Cl_7$	6.89	6.9119
173*	PCB-193	$C_{12}H_3Cl_7$	6.89	6.9193
174	PCB-194	$C_{12}H_2Cl_8$	7.3	7.2637
175*	PCB-196	$C_{12}H_2Cl_8$	7.37	7.351
176	PCB-197	$C_{12}H_2Cl_8$	7.39	7.3204
177*	PCB-198	$C_{12}H_2Cl_8$	7.35	7.3641
178	PCB-199	$C_{12}H_2Cl_8$	7.31	7.3781
179	PCB-200	$C_{12}H_2Cl_8$	7.36	7.2913
180	PCB-201	$C_{12}H_2Cl_8$	7.34	7.3563
181	PCB-202	$C_{12}H_2Cl_8$	7.34	7.3938
182	PCB-203	$C_{12}H_2Cl_8$	7.37	7.3527
183	PCB-204	$C_{12}H_2Cl_8$	7.39	7.3261
184	PCB-205	$C_{12}H_2Cl_8$	7.27	7.2711
185	PCB-206	$C_{12}H_1Cl_9$	7.72	7.719
186	PCB-207	$C_{12}H_1Cl_9$	7.74	7.6926
187	PCB-208	$C_{12}H_1Cl_9$	7.72	7.7321
188	PCB-209	$C_{12}Cl_{10}$	8.09	8.0695

TABLE S-II. Genetic algorithm settings in QSARINS software

GA until	02 (number of the descriptors in the model)
Generation per size	500
Population size	10
Mutation rate	20

Journal of the Serbian Chemical Society
JSCS@tmf.bg.ac.rs • www.shd.org.rs/JSCS
J. Serb. Chem. Soc. *90* (9) 1069–1087 (2025)
JSCS–5440
Original scientific paper
Published 30 September, 2025

Effect of microwave power level and processing time on the quality of palm shell charcoal (*Elaeis guineensis* Jacq.) briquettes

LINA LESTARI[1], SAPTO RAHARJO[2]*, I NYOMAN SUDIANA[1], LA ODE RUSMAN[1] and NIKEN SULASTRI[1]

[1]*Department of Physics, Faculty of Mathematics and Natural Sciences, Halu Oleo University, Kendari 93232, Indonesia and* [2]*Department of Chemistry, Faculty of Mathematics and Natural Sciences, Halu Oleo University, Kendari 93232, Indonesia*

(Received 30 August, revised 25 October 2024, accepted 24 July 2025)

Abstract: One of the developments in renewable energy sources is use of biomass. This research aims to analyze the effect of power (70, 150 and 230 W) and activation time of palm shell charcoal using microwave during different time intervals (360, 480 and 600 s) on the density, moisture, ash content and volatile matter of palm shell charcoal briquettes. Charcoal briquettes are obtained from the carbonization process at a temperature of 548.7°C for 6 h, grinding and sieving at 80–100 mesh, activation using a microwave at a fixed time of 480 s with variations in activation power of 70, 150 and 230 W and fixed 150 W with variations in activation time of 360, 480 and 600 s. The research results showed that the density of palm shell charcoal briquettes ranged from 0.51–0.54 g/cm^3, the water content ranged from 3.31–3.92 %, the ash content ranged from 7.13–7.86 % and the volatile matter ranged from 8.19–9.22 %. SEM characterization shows that microwave activation increases the number of pores evenly and enlarges the pores. From the research results, the power and activation time vastly improve the quality of palm shell charcoal briquettes.

Keywords: activation; carbonization; water content; ash content; volatile matter; pores.

INTRODUCTION

The use of fuel from fossil sources continue to increase even though the sources are decreasing. The development of renewable energy sources can replace fossil fuels to minimize the worst impacts.[1] The development of renewable energy sources, one of which is biomass energy, is very promising as an alternative energy.[2] The potential for biomass in Indonesia which can be used as an energy

* Corresponding author. E-mail: sapto.raharjo@uho.ac.id
https://doi.org/10.2298/JSC240830055L

source is very abundant, the annual biomass potential is 146.7 million t, and in 2020, 53.7 million tons of biomass was produced from waste.[3] Oil palm (*Elaeis guineensis* Jacq.) is a promising plantation commodity in Indonesia, particularly in Southeast Sulawesi. The region's oil palm plantations cover an impressive 70000 ha, producing a total of 61300 t in 2022.[4] As these plantations expand, so does the potential for biomass waste, a key ingredient in the production of charcoal briquettes, a promising alternative energy source. Every processing of 1 t of palm oil produce waste of 6.5 % or 65 kg of shells with a calorific value of 20,093 kJ/kg in dry conditions.[5] Palm oil shells contain high carbon lignocellulose content and have a higher specific gravity than wood, reaching 1.4 g/cm^3. Shells from palm kernels were chosen as the primary raw material for their abundant and sustainable availability. Indonesia is the world's largest producer of palm oil, with a growing amount of plantation acres. Palm kernel shells contain a significant amount of lignocellulose (25.88 % cellulose, 12.18 % hemicellulose and 42.20 % lignin), thus they have a higher density and calorific value than some other biomass. They use less energy and burn more effectively as a result. Palm kernel shells high fixed carbon content (59.1 %) and low ash content (0.20 %), offer good combustion qualities. Additionally, it is expected that the briquettes' quality will be improved by the microwave activation process, increasing their competitiveness with conventional fuels. Using palm kernel shells as a renewable energy source can reduce waste from the palm oil industry that could pollute the environment, reduce dependency on fossil fuels, and increase energy efficiency by utilizing underutilized resources.[5]

The advantages of charcoal briquettes are that they are more economical (cheap), have a high calorific value with a more extended burning period, also are smokeless and environmentally friendly. The characteristics of briquettes are influenced by several factors, namely carbonization temperature and time, carbonized charcoal fineness, charcoal powder density, and pressure in the moulding process. Good-quality briquettes have a smooth texture, are not easily broken and have good burning properties.[6] The burning characteristics of good quality briquettes include a short ignition time, long burning time at maximum temperature, low burning rate, no soot and little smoke. One way to improve the burning characteristics of charcoal briquettes is by activating the charcoal to reduce volatile matter levels so that the combustion rate is low (economical) and produces little smoke.[7] The main volatile substances that need to be removed include carbon monoxide, a high content of volatile substances in charcoal briquettes that will cause more smoke when lit. The high smoke content is caused by the reaction between CO and alcohol derivatives.[8] Light hydrocarbon compounds (CHx) from decomposing organic compounds in charcoal raw materials can burn quickly and less efficiently.[9] Water vapour, the remaining bound water in charcoal, can increase volatility and deteriorate combustion.[10]

Activation is a complex process that involves altering the physical properties of charcoal to reduce the level of volatile matter, thereby lowering the briquette burning rate.[6] The activation process also aims to reduce the water content and increase the fixed carbon and calorific value of the charcoal.[11] Lestari[12] stated that the quality of charcoal briquettes can be improved through the activation process. Previous research conducted by Bonsu *et al.*[13] analysed the characteristics of charcoal made from palm oil shells, which was used as the primary raw material for briquettes. The study reported that the charcoal had a moisture content of 6.7 %, an ash content of 0.20 %, a volatile matter content of 34.09 % and a fixed carbon content of 59.1 %.

It is of interest to investigate the influence of power (70, 150 and 230 W) and activation time using microwave with activation time variations of 360, 480 and 600 s on: the density, moisture, ash content and volatile matter of palm shell charcoal briquettes. This research aims to determine the effect of microwave power and activation time on the density, moisture content, and ash content of palm shell charcoal briquettes, as well as to evaluate the overall quality of the briquettes produced through microwave activation. This research determines the best power and time to produce quality briquettes that meet Indonesian National Standard (SNI) briquette quality by utilizing microenergy in charcoal activation.

EXPERIMENTAL

Research procedure

*Making palm shell charcoal briquettes (*Elaeis guineensis *Jacq.)*. Palm shell biomass waste (*E. guineensis* Jacq.) was obtained from PT, Tani Prima Makmur, Lerehoma Village, Konawe, Southeast Sulawesi. The carbonization reactor used in this study was a self-designed and locally modified version of the conventional "kiln drum" type commonly utilized by local communities. The reactor's structural design and functional performance were systematically developed and scientifically validated in the prior work by Lestari *et al.* (2024).[25] The biomass was sun-dried for 2–3 days to reduce moisture content before carbonization. Sago, used as an adhesive, was also sun-dried and sieved using an 80-mesh screen. Wood twigs were prepared as ignition material. Carbonization was carried out in a limited-air reactor. A total of 45 kg of dried palm shell was loaded into the reactor up to 75 % of its volume. The reactor was sealed, and ignition was initiated using dried twigs. Reactor temperature was monitored every 2 min using an infrared thermometer. The carbonization process was considered complete when the smoke emitted from the chimney changed from thick/dark to thin and clear. The resulting charcoal was ground and sieved sequentially through 80- and 100-mesh screens; the fraction retained between these meshes was collected. Activation was conducted by weighing 5 g of the sieved charcoal into a porcelain crucible and subjecting it to microwave irradiation at 720 W for 6 min. Briquette formation involved mixing the activated charcoal with sago adhesive in a 9:1 ratio (by weight), using 4 ml of distilled water preheated to 100 °C. The mixture was moulded and compacted using a hydraulic press at 15 MPa for 3 min to ensure uniform density and structural integrity. Briquette compaction tool (0–200 kg/cm^2) and a cylindrical briquette mould (outer diameter: 4 cm, inner diameter: 0.8 cm, height: 8 cm) are used for shaping the briquettes.

Experimental parameters

Determination of density. This test is carried out by determining how dense the mass of the briquettes is by comparing the mass of the briquettes with the volume dimensions of the palm shell charcoal briquettes:[14]

$$\text{Briquette density } (\rho) = \frac{m}{V_{\text{tot}}} \tag{1}$$

$$\text{Briquette volume } (V_{\text{tot}}) = \pi(r_2^2 - r_1^2)t \tag{2}$$

Description: m = mass of briquettes (g); r_1 = inner radius of the briquette (cm); r_2 = outer radius of the briquette (cm); t = briquette height (cm)

Determination of water content (moisture). This procedure is in accordance with the American Society of Testing and Materials (ASTM) D 2866-70. Testing the moisture content of charcoal briquettes is carried out by comparing the water content in the material during the heating process using an oven at a temperature of 105 °C for 3 h with the mass of the material before heating:

$$\text{Water content } (\%) = 100\frac{MS - MC - SP(105\ ^\circ\text{C}) - MCK}{MS} \tag{3}$$

Description: MS = sample mass (g); MCK = mass of empty cup (g); $MC + SP$(105 °C) = mass of cup + sample after heating at 105 °C (g).

Determination of ash content. The steps in measuring ash content are based on American Society of Testing and Materials (ASTM) D 2866-70. Put the palm shell briquette sample into a porcelain cup whose empty weight has been calculated. Next, put the porcelain cup containing the sample into the furnace at 700 °C until it turns ash for 3 h. Remove and cool the sample in a desiccator for 15 min. Determine the ash content with the following equation:

$$\text{Ash content } (\%) = 100\frac{MS - MC - SP(700\ ^\circ\text{C}) - MCK}{MS} \tag{4}$$

Description: $MC + SP$(700 °C) = mass of cup + sample after heating at 700 °C (g).

Volatile matter

Based on Cheng *et al.*[15] determines volatile matter using the following stages: put a sample of charcoal briquettes with known water content into a porcelain cup, then cover with aluminium foil. Inserting the sample into the furnace carefully and heating the sample at 750 °C for 15 min; cool the sample in a desiccator; next, open the porcelain cover and weigh the cup containing the charcoal briquette sample; calculate the level of volatile matter contained in the sample using the following equation:

$$\text{Volatile matter } (\%) = KZH(750\ ^\circ\text{C}) - \text{Water content } (\%) \tag{5}$$

Description: KZH = level of substance lost (%).

Fixed carbon. The fixed carbon content test is determined by subtracting 100 % from the percentage of water content, ash content, and volatile matter content:

$$\text{Fixed carbon } (\%) = 100 - M - AC - VM \tag{6}$$

Description: M = moisture (%); AC = ash content (%); VM = volatile matter (%).

Activated charcoal surface morphology

Surface morphology and elemental composition of the charcoal were analyzed using scanning electron microscopy coupled with energy dispersive spectroscopy (SEM-EDS). The SEM instrument used was the COXEM EM-30AXN (COSDAQ Listed Company, Korea), operating under both high and low vacuum modes, with a magnification range of 20–150,000× and acceleration voltage between 1–20 kV. Samples were coated with gold prior analysis. Elemental analysis was conducted using an Oxford Instruments Ultim Max Infinity EDS (Oxford, United Kingdom) equipped with a 30 mm standard compact detector, operated *via* AZtecOne software. EDS measurements were performed at three points on each sample to obtain average elemental compositions and standard deviation values. Charcoal activation was carried out using a microwave furnace (Sharp R-21D0(S)-IN, China) with a chamber capacity of 23 L, five adjustable power levels, operating at 220 V and 50 Hz. The activation parameters used in this study were specific microwave power levels and durations.

Fourier transform infrared spectroscopy (FTIR)

FTIR measurements were carried out using a Shimadzu type IRPestige-21 FTIR. The spectral data were recorded in the range of 4000–400 cm^{-1}. The procedure was carried out, namely the charcoal powder was sieved with a 100-mesh sieve. Charcoal powder with a mass of 0.02 mg was mixed with 0.2 mg KBr and homogenized by stirring with a stainless spatula. Then, pellets were made by pressing into a thin cylinder.

RESULTS AND DISCUSSION

*Quality analysis of palm shell charcoal briquettes (*El. guineensis *Jacq.)*

The quality of palm shell charcoal briquettes was analyzed by testing density, water, ash content, volatile matter and fixed carbon. Microwaves are electromagnetic waves with super high frequency (super high frequency, SHF), which is above 3 GHz. Microwaves can theoretically be converted into heat through interaction with dielectric materials. Carbon materials are generally sound microwave absorbers and are quickly heated using microwave radiation. This characteristic allows carbon materials to transform due to microwave heating, producing new carbon with the desired properties. Microwave oven have the fastest heating capability of all ovens, and also heat distribution, because the material absorbs microwaves and converts them into heat. Palm oil shells are shown in Fig. 1.

Fig 1. Raw palm kernel shells prior to carbonization and microwave activation.

The interaction between microwaves and carbon materials mainly involves an efficient and unique heating mechanism. Carbon materials, such as activated carbon and carbon nanotubes, have dielectric properties that effectively absorb microwave energy. When microwaves interact with carbon materials, the oscillating electric field causes the molecular dipoles and ions to vibrate and move, generating internal friction converted into heat. This process is known as dielectric heating. In addition, carbon materials with porous structures, such as activated carbon, have high surface areas and good electrical conductivity, enhancing microwave absorption efficiency. This allows for rapid and uniform heating in processes such as pyrolysis or carbonization. In some cases, the interaction between microwaves and carbon materials can generate microplasma on the material's surface. This plasma consists of highly reactive charged particles and can enhance the rate of chemical reactions or enable the synthesis of new materials at lower temperatures than conventional methods. Overall, the ability of carbon materials to absorb and convert microwave energy into heat makes them ideal candidates for various applications, including heating, material synthesis and catalysis.[24]

Palm oil waste contains lignin, cellulose, and primary hemicellulose elements, which indicate long carbon chains and high carbon content in palm oil waste. The very high carbon content can be a potential green precursor in producing carbon-based nanomaterials that can be applied in various situations.[16] The lignocellulose content of palm kernel shells was determined using the gravimetric method. The levels of hemicellulose, cellulose and lignin were calculated from measurements of neutral detergent fiber (NDF), acid detergent fiber (ADF) and subsequent residue analysis (see Supplementary material to this paper for details). The detailed results are presented in Table I.

TABLE I. Results of hemicellulose, cellulose and lignin content tests; analysis method: gravimetry

Component	Content, mass %
Hemicellulose	12.18±0.06
Cellulose	25.88±0.05
Lignin	42.40±0.02

Based on the data in Table I, the pretreatment process produced hemicellulose with a content of 12.18 %, cellulose with 25.88 % and lignin with a content of 42.40 %. The charcoal activation process aims to reduce the volatile matter content so that the combustion rate is low, also the water content is reduced and the charcoal's fixed carbon and calorific value are increased.

Microwave activation of charcoal involves exposing it to a specific power level (*e.g.*, 70 W) for different time intervals (*e.g.*, 480 s), causing a temperature change that transforms it into activated charcoal. Palm shell charcoal was activated using microwave at three power levels (70, 150 and 230 W) and three activation

times, namely 360, 480 and 600 s. These parameters were selected based on preliminary observation from both heating and color change. Below 150 W or less than 360 s, no noticeably heating effect happened. It tells that activation was less sufficient but conversely beyond 600 s or at powers greater than 230 W leading to charring and ashes formation, indicating overheating. The selected ranges were aimed to produce optimally identified conditions without any degradation of the material. Table II shows the results of analysis of density, water content, ash content, volatile matter and fixed carbon of palm shell charcoal briquettes fixed time 480 s.

TABLE II. Results of analysis of density, water content and ash content of palm shell charcoal briquettes at fixed time of 480 s

Power, W	Density g/cm^3	Water content %	Ash content %	Volatile matter %	Fixed carbon %
No activation	0.49±0.01	4.36±0.02	6.94±0.01	10.10±0.02	78.60±0.01
70	0.51±0.01	3.92±0.01	7.13±0.01	9.22±0.01	79.73±0.01
150	0.52±0.01	3.52±0.01	7.54±0.01	8.79±0.02	80.15±0.02
230	0.54±0.01	3.31±0.01	7.86±0.01	8.19±0.02	80.64±0.02

The values presented in Tables II and III represent the mean ± standard deviation from three replicates (n = 3) for each treatment. The standard deviation (±0.01) indicates the variation observed in the repeated measurements. Although the standard deviation values appear identical, this is due to rounding to two decimal places. Actual raw data showed slight differences, but they were within a narrow range, indicating high precision. These results were obtained through gravimetric and volumetric methods following ASTM standards, as detailed in the experimental section.

TABLE III. Results of analysis of density, water content and ash content at 150 W fixed power palm shell charcoal briquettes

Time, s	Density g/cm^3	Water content %	Ash content %	Volatile matter %	Fixed carbon %
No activation	0.49±0.01	4.36±0.02	6.94±0.01	10.10±0.02	78.60±0.01
360	0.52±0.01	3.76±0.01	7.34±0.03	8.91±0.02	79.99±0.01
480	0.52±0.01	3.52±0.01	7.54±0.02	8.79±0.02	80.15±0.02
600	0.53±0.01	3.40±0.02	7.68±0.01	8.40±0.01	80.52±0.01

Density

The density of charcoal briquettes may be viewed as an index between mass and volume, since it evidently influences mechanical strength, combustibility, and calorific value.[17] Increasing density might enhance briquette firmness and burning efficiency, but may also, if too dense, affect ignition easiness. According to Indonesian National Standard (SNI), the optimal density must balance burning time and

permeability to air.[18] In this study, the density of briquette samples ranged from 0.49 to 0.54 g/cm^3 (Tables II and III), and higher values were generated at higher microwave power and activation time. Density is accordingly influenced by particle size, homogeneity of material and pressure applied during the molding process.

The test results in Table II show that the density, of the palm shell charcoal briquettes produced, is 0.49–0.54 g/cm^3. The highest density value of 0.54 g/cm^3 was obtained at an activation power of 230 W, while the lowest density value was 0.49 g/cm^3 or charcoal briquettes without activation. Fig. 2A shows the surface morphology of the briquettes as observed through SEM imaging. As the activation power increases, the SEM images indicate a more compact and uniform surface structure with fewer visible pores. While SEM images cannot directly quantify density, the observed morphological changes suggest improved particle bonding and reduced void spaces, which may correlate with the measured increase in density reported in Table II. This is because as the activation power increases, the temperature produced by the microwave will be higher, resulting in stronger bonds between charcoal molecules. After all, when pressure is applied, the charcoal particles will be forced to fill the empty cavities and allow the adhesive to flow across the surface of the charcoal. So, it can reduce cavities or gaps that water can fill.[6] The increase in density at higher activation power may be associated with enhanced thermal effects that promote partial softening or restructuring of the carbon surface, potentially improving particle packing and reducing internal voids. Similar effects of thermal activation on carbon structure compaction have been noted in the previous studies by Zhang *et al.* (2022).[29]

When charcoal particles are pressed, pressure compacts the material by forcing particles to fill voids, thereby increasing density and improving structural integrity.[19] This process also enhances adhesive distribution along particle surfaces, promoting stronger bonding due to increased contact area.[20] The adhesive fills micropores in the charcoal structure, providing additional mechanical interlocking.[21]

Table III shows that briquettes, made with charcoal activated using a microwave at a fixed power of 150 W, have values of 0.52–0.53 g/cm^3. The density value experienced an insignificant increase as the activation time increased. This is because the activation process can cause the surface area of the charcoal briquettes to become more prominent, which results in greater absorption capacity so that the briquettes can absorb the adhesive used ideally and can fill the voids between particles, which will then increase their density.[29,30] Palm shell charcoal briquettes made from charcoal that has been activated using a microwave at a fixed activation power of 150 W have the highest density value of 0.53 g/cm^3, which is activated for 600 s. The size and homogeneity of the adhesive and charcoal mixture also influence the high or low density of palm shell charcoal briquettes. The more homogeneous the mixture of charcoal and adhesive is, the stronger the briquettes produced will be, and the higher the size of the charcoal particles, the higher the

density the charcoal briquettes will produce. The density of charcoal briquettes is also influenced by the pressure applied during the briquette compaction process. The more significant the pressure applied, the more water content will decrease because more is wasted as the compaction pressure increases. According to SNI 01-6235-2000, a good density value is 0.5–0.6 g/cm^3 based on the briquette quality standards. The density test results show that all palm shell charcoal briquettes made through the activation process in this study meet SNI standards, except for palm shell charcoal briquettes, which were made without activation (0.49 g/cm^3). The best density value of palm shell charcoal briquettes was produced from charcoal activated at 230 W of power for 480 s.

Water content (moisture)

The moisture content of charcoal briquettes greatly influences the calorific value. The smaller the water content value of the charcoal briquette, the higher the calorific value produced by the charcoal briquette.[22] Tables II and III show that briquettes made from activated palm shell charcoal produce lower water content values than briquettes made from charcoal without activation. The test results in Table II show that the water content value of the palm shell charcoal briquettes produced ranges from 3.31–4.36 %.

Based on Table II, the water content of palm shell charcoal briquettes tends to decrease significantly along with increased activation power. The higher the activation power, the lower the water content of palm shell charcoal briquettes. The decrease in water content is due to microwave activation, where higher power increases heat energy, promoting greater evaporation of water molecules from the charcoal. The water content value in palm shell charcoal briquettes with the activation time parameter, in Table III above, shows that briquettes made with charcoal activated using a microwave at a fixed power of 150 W have a value in the range of 3.40–3.76 %. The water content value experienced a significant decrease as the activation time increased. This is because the higher the activation time, the greater the surface area of the briquettes produced, causing the water in the briquettes to evaporate quickly, resulting in lower water content in the briquettes. The lowest water content was produced from charcoal briquettes activated at 150 W power for 600 s, namely 3.40 %. According to SNI 01-6235-2000, a good water content value is less than 8 % based on the briquette quality standards. The results of the water content test show that all palm shell charcoal briquettes made through the activation and non-activation processes in this study meet SNI standards.

Ash content

Ash content is the residue remaining after combustion, which no longer contains carbon. Inorganic substances that are not burned will remain behind and

become ash. Briquette ash content is the remaining part of the briquette combustion. The ash content is silica, which influences the calorific value produced in the briquettes. The high or low ash content in briquettes is influenced by the high content of inorganic materials contained in biomass waste and the level of adhesive used in making briquettes. Low ash content will produce good-quality charcoal briquettes. The test results in Table II show that the ash content value of the palm shell charcoal briquettes produced ranges between 6.94–7.86 %. The treatment of variations in activation power on palm shell charcoal significantly influences the ash content of charcoal briquettes. Increasing the activation power will cause an increase in the ash content of palm shell charcoal briquettes. The increase in ash content is caused by microwave heating that causes decomposition of organic material, therefore lowering the content of organic compounds in charcoal and increasing the ash content after burning. The ash content value in charcoal briquettes is also influenced by the raw materials used in the briquette. Materials that contain high levels of silica can cause high ash content, resulting in lower briquette quality.[6] The presence of excessive ash can also cause a decrease in heating value. The ash content value in palm shell charcoal briquettes with the activation time parameter. Table III shows that briquettes made with charcoal activated using a microwave at a fixed power of 150 W, have a value range of between 7.34–7.68 %. The highest ash content value was 7.68 % in the activation treatment, with an activation power of 150 W for 600 s. Ash content value increases significantly as the activation time increases. According to SNI 01-6235-2000, a good ash content value is less than 8 % based on the briquette quality standards. The ash content test results show that all treatments in this study meet SNI standards.

Volatile matter

Volatile matter can evaporate due to the decomposition of compounds still present in charcoal other than water, ash, and bound carbon.[23] The volatile matter content of palm shell charcoal briquettes ranged from 8.19 to 10.10 % (Table II), decreasing with increased activation power due to the higher heat energy driving off volatile substances. Similarly, Table III shows that longer activation times at 150 W led to a slight decrease in volatile matter (8.91–8.40 %), attributed to decomposition of volatile compounds at higher temperatures. The lowest value (8.19 %) was obtained at 230 W for 480 s, indicating efficient activation. All values met the SNI 01-6235-2000 standard, which recommends volatile matter content below 15 %. Lower volatile content enhances combustion efficiency and reduces smoke.[18]

Fixed carbon

The fixed carbon is the carbon fraction bound in charcoal apart from the water, ash, and volatile matter fractions. The main content of fixed carbon is carbon. The

water content, ash content and volatile matter values influence fixed carbon. The test results in Table II show that the fixed carbon value, of the palm shell charcoal briquettes produced, ranges 78.60–80.64 %. Table II shows that increasing the activation power will cause the fixed carbon content of palm shell charcoal briquettes to increase slightly. This is due to the decreasing values of water, ash and volatile matter content, which will cause an increase in fixed carbon levels. The lower the moisture, ash and volatile matter, the higher the fixed carbon content will be. The process of activating palm shell charcoal briquettes using a microwave can produce increased ash content that can affect the fixed carbon content. The fixed carbon value in palm shell charcoal briquettes, with the activation time parameter in Table III, shows that briquettes made with charcoal activated using a microwave at a fixed power of 150 W have a value range of 79.99–80.52 %. The fixed carbon value tends to increase slightly as the activation time increases. This is caused by the long activation process, which causes the decomposition or breakdown of the compounds in the carbonized material, increasing the fixed carbon content of the charcoal briquettes. The results of testing the fixed carbon content of palm shell charcoal briquettes showed that all treatments in this study met the SNI 01-6235--2000 fixed carbon standard (>77 %) with the best-fixed carbon value found in the 230 W activation treatment for 480 s, namely 80.64 %.

Activated charcoal surface morphology

SEM-EDS to characterized activated charcoal surface morphology analysis. The following is a picture of the morphological changes in charcoal without activation and charcoal activated with variations in microwave power (Fig. 2).

Fig. 2 shows the surface morphology of activated palm shell charcoal, which has a rough and irregular pore surface. Fig. 2B, charcoal activated with 70 W power for 480 s has new pores that are smaller. Charcoal activated with 150 W power for 480 s has larger pores (Fig. 2C). Meanwhile, in Fig. 2D, activated charcoal with 230 W of power for 480 s causes several pores to merge so that the number seems to decrease.

Furthermore, the surface morphology of charcoal activated at 150 W for varying times is shown in Fig. 3. In comparison to non-activated charcoal, the surface looks smoother and has fewer, uniformly spaced pores at 360 s (Fig. 3A). The pores start to grow after 480 s (Fig. 3B), and some of them start to combine at 600 s (Fig. 3C). The emergence of new pores and changes in the number and average diameter due to activation plays an important role, where porous charcoal easily binds adhesives in making briquettes homogeneous. In addition, the presence of pores will also provide enough space to trap the oxygen needed in burning briquettes. Activated charcoal materials for making briquettes must be tested for their safety against their potential for air pollution during combustion. EDS characterization is carried out to check whether the charcoal contains sulfur as a pollutant.

In Fig. 3, the activation time dramatically affects the structure and size of the carbon pores. The longer the activation time, the better the carbon pores produced, but if the activation time is increased again, the pore size will be more prominent.

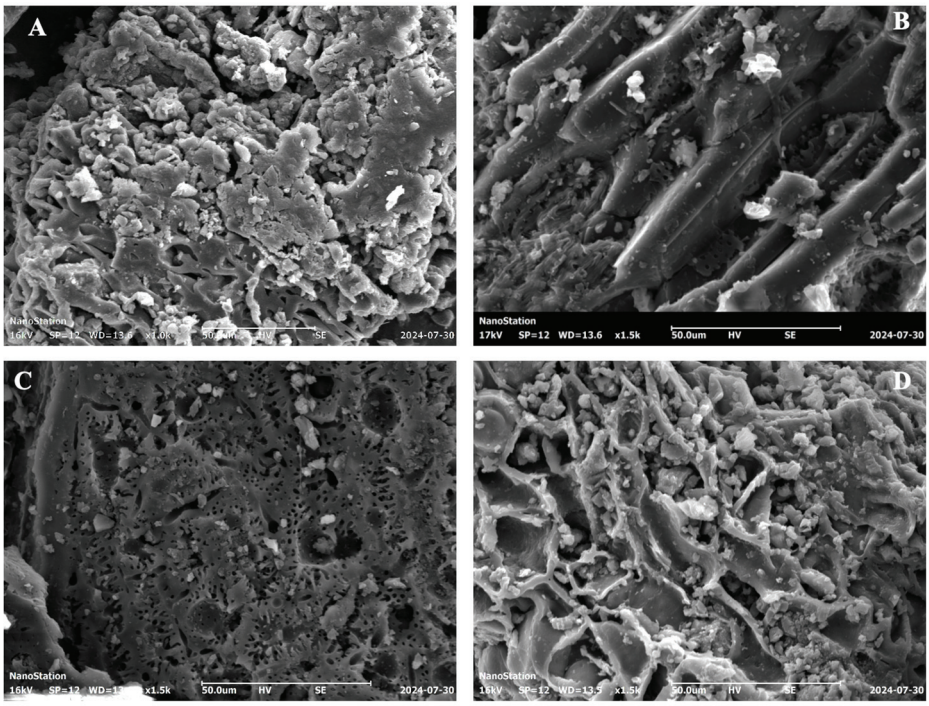

Fig. 2. Surface morphology of charcoal without activation (A) and charcoal activated by microwave for 480 s at: 70 (B), 150 (C) and 230 W (D).

Table IV shows that the weight composition of charcoal without activation. The predominant constituents are generally carbon and oxygen, though they can vary based on the activation circumstances. At lower power (*e.g.*, 70 W), microwave activation often increased carbon content; at higher power or longer exposure times; however, carbon content decreased, most likely as a result of structural oxidation. While activation at 150 W for 480 s revealed a lower carbon percentage (78.55 %) and higher oxygen content (showing more intensive oxidation), the sample activated at 70 W for 480 s had the highest carbon content (89.22 %), indicating negligible deterioration. Interestingly, no sulfur was found in any of the samples, indicating that burning the briquettes is safer for the environment. Furthermore, the increased ash content seen in proximate analysis is consistent with a slow rise in silicon and calcium in activated samples.

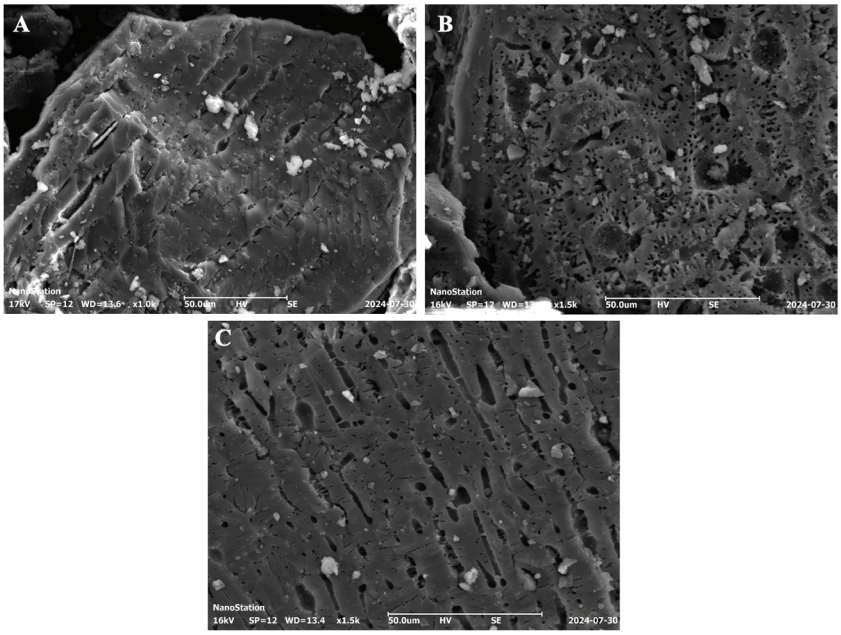

Fig. 3. Microwave at power activates the surface morphology of charcoal for 360 (A), 480 (B) and 600 s (C).

TABLE IV. Chemical composition of palm shell charcoal (*Elaeis guineensis* Jacq.)

Sample	Element	Amount, wt. %
Without activation	C	83.67±0.19
	O	15.62±0.12
	Ca	0.31±0.02
	K	0.29±0.02
	Si	0.09±0.00
	Al	0.01±0.06
Charcoal activated by microwave for 480 s at 70 W power	C	89.22±0.18
	O	8.88±0.09
	F	0.55±0.03
	K	0.42±0.05
	Ca	0.33±0.02
	Si	0.29±0.03
Charcoal activated by microwave for 480 s at 150 W power	C	78.55±0.13
	O	18.62±0.13
	Si	0.75±0.05
Charcoal activated by microwave for 480 s at 230 W power	C	83.19±0.22
	O	15.98±0.18
	F	0.37±0.02
	K	0.18±0.02
	Si	0.15±0.01

TABLE IV. Continued

Sample	Element	Amount, wt. %
Charcoal activated by microwave for 360 s at 150 W power	C	86.40±0.13
	O	10.80±0.20
	F	0.59±0.02
	K	0.46±0.03
	Si	0.36±0.03
Charcoal activated by microwave for 480 s at 150 W power	C	78.55±0.07
	O	18.62±0.07
	Si	0.75±0.03
	Ca	0.69±0.04
Charcoal activated by microwave for 600 s at 150 W power	C	81.03±0.13
	O	15.77±0.09
	Ca	1.56±0.06
	Si	0.51±0.05

EDS characterization shows that the absence of sulfur elements indicates that palm shell charcoal is safe to use during combustion without producing air pollutants. In addition, this characterization strengthens the proximate test of fixed carbon shown in Tables II and III. EDS characterization also shows an increase in Si content in activated carbon; this strengthens the proximate test of ash content, as shown in Table II and III.

Fourier transform infrared spectroscopy (FTIR)

The FTIR characterization results are shown in Fig. 4. The bands observed at approximately 3420 cm^{-1} are attributed to the hydroxyl group (O–H) vibration, consistent with the previous studies.[32] Absorption bands near 1035 cm^{-1} correspond to the C–O bond vibration, indicating the presence of alcohol groups.[33] A distinct double absorption band around 2920 cm^{-1} is associated with the Csp^3-H bond vibration (alkane), confirming the presence of alkane groups. Further, the methylene group (CH_2) vibration is evident around 1450 cm^{-1}, supporting the alkane presence. The carbonyl group (C=O) is identified by sharp absorption bands around 1735 cm^{-1}, and a band around 1600 cm^{-1} is consistent with C=C stretching in alkenes.[34] Additionally, the most intense absorption, between 570 and 600 cm^{-1}, likely corresponds to halogen compounds (C–X) or silicon oxide (Si–O) vibrations.[35]

FTIR results show that the activation process affects the functional groups present on the charcoal surface, especially in strengthening the presence of hydroxyl and alcohol groups, as well as increasing the complexity of inorganic groups. Microwave activation also has the potential to improve the chemical characteristics of charcoal for adsorption or energy applications, depending on the power and duration of treatment. The finding generated by O–H and C=O groups have indicated that there has been an increase in the oxygen-containing functional groups,

the existence of which affects the adsorption property through making such surfaces more polar. The indication concerning changes in peak intensity and existence of either Si–O bonds or C–X can also represent changes in pore structure and chemical composition upon activation. Such a relationship would suggest that microwave activation modifies not only the physical structure but also changes the chemical functionality of the material (as is shown by FTIR), which both complementarily influence the adsorption performance.

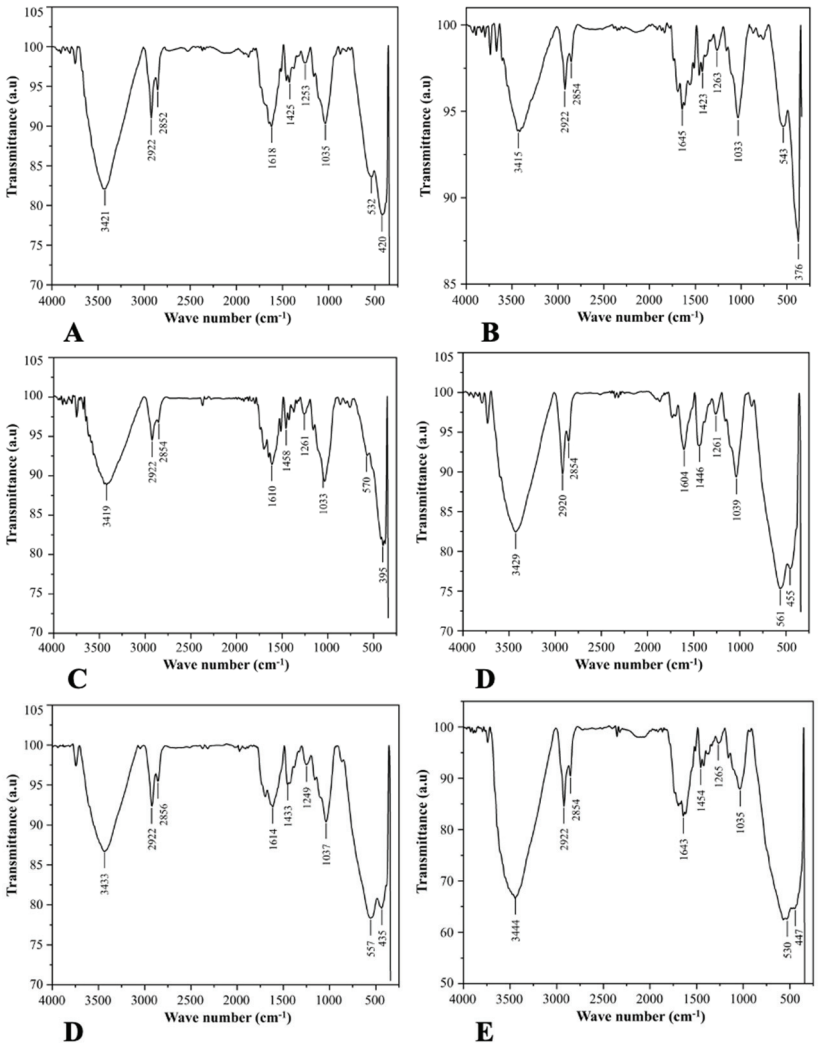

Fig. 4. FTIR spectra of palm shell charcoal (*Elaeis guineensis* Jacq.): sample 1 (without activation, A), charcoal activated by microwave: sample 2 (for 360 s at 150 W power, B), sample 3 (for 480 s at 70 W power, C), sample 4 (for 480 s at 150 W power, D), sample 5 (for 480 s at 230 W power, E) and sample 6 (for 600 s at 150 W power, F).

This study basically hinges around palm shell charcoal being the main precursor as it is plentiful and has a very low price coupled with very good adsorbing properties. The deciding factor for selecting this precursor was that it is high in carbon content and structurally compatible for activation. For example, coconut shell-based apparatus, wood-based biomass and agricultural residues. In addition to those, the FTIR spectrum from this work has revealed several functional groups such as O–H, C–O, Csp^3-H, CH_2, C=O, C=C and C–X or Si–O. Astuti (2020)[28] carried out research on palm kernel shell activated with $ZnCl_2$ and similarly found functional groups C–H, aliphatic C–O and aromatic C=C. The variation in FTIR was thus due to the activation methods, choice of activating agents, and precursor materials that have had significant influence on the physical and chemical property of activated carbon produced. Therefore, further optimization of method of activation is also necessary to improve the surface area of activated carbon and the adsorption characteristics of activated carbon produced in this study.

CONCLUSION

The study results indicate that an increase in microwave power and activation time play a significant role in affecting the physical and chemical properties of palm shell charcoal briquettes. Increased power and activation time increase the ash content, fixed carbon and density while diminishing both water content and volatile matter. Microwave activation increases pore formation, thus improving the properties and efficiency of combustion with an even more uniform and well-distributed porous structure, which allow better performance on adsorption properties. The absence of sulfur passes inspection through EDS characterization; hence the briquettes prove to be environmentally friendly and safe as they do not contribute to any air pollution caused by sulfur. Furthermore, there is an FTIR characterization to verify the presence of functional groups that include O–H, C–O, Csp^3-H, CH_2, (C–X) or silicon oxide (Si–O), C=O, as well as C=C that affect the chemical reactivity and potential adsorption of the material. It was observed that, upon the presence of oxygen-containing functional groups, activated palm shell charcoal can be used under high adsorption capacity applications, such as gaseous purification, effluent treatment, and industrial filtration. Besides combustion improvements, palm shell charcoal can also be considered an alternative fuel for household and industrial energy purposes with a reduced dependency on conventional fossil fuels. The developed porous structure generally is of high importance in increasing adsorption capacities, making the material suitable for removing contaminants, heavy metals or organic pollutants from water and air. Its functionalized surface chemistry also suggests future potential exploitation as a catalyst carrier in chemical processes, especially for biofuel production and environmental cleanup. In the agricultural sector, the material can serve as biochar in improving soil fertility and carbon sequestration. Microwave-activated palm shell charcoal indicates

great potential for variety applications in industries and environment, leaving room for more optimization and larger scale utilization. Future studies could focus on the long-term stability and economic feasibility of this material under practical conditions.

SUPPLEMENTARY MATERIAL

Additional data and information are available electronically at the pages of journal website: https://www.shd-pub.org.rs/index.php/JSCS/article/view/13028, or from the corresponding author on request.

Acknowledgements. We would like to express our deepest gratitude to all parties who have helped and supported us in preparing this journal.

И З В О Д

УТИЦАЈ СНАГЕ МИКРОТАЛАСА И ВРЕМЕНА ОБРАДЕ НА КВАЛИТЕТ УГЉЕНИХ БРИКЕТА ОД ЉУСКИ ПАЛМЕ (*Elaeis guineensis* JACQ.)

LINA LESTARI[1], SAPTO RAHARJO[2], I NYOMAN SUDIANA[1], LA ODE RUSMAN[1] и NIKEN SULASTRI[1]

[1]Department of Physics, Faculty of Mathematics and Natural Sciences, Halu Oleo University, Kendari 93232, Indonesia и [2]Department of Chemistry, Faculty of Mathematics and Natural Sciences, Halu Oleo University, Kendari 93232, Indonesia

Један од праваца развоја обновљивих извора енергије је употреба биомасе. Циљ овог истраживања је да се анализира утицај снаге (70, 150 и 230 W) и времена активације угља од палминих љуски микроталасима током различитих временских интервала (360, 480 и 600 s) на густину, влагу, садржај пепела и испарљиве материје угљених брикета од љуски палме. Угљени брикети су добијени процесом карбонизације на температури од 548,7 °C током 6 h, млевењем и просејавањем на 80–100 mesh, активацијом помоћу микроталаса у фиксном временском интервалу од 480 s са варијацијама снаге активације од 70, 150 и 230 W, као и активацијом са фиксних 150 W уз варијације времена активације од 360, 480 и 600 s. Резултати истраживања су показали да се густина угљених брикета од палминих љуски кретала од 0,51–0,54 g/cm^3, садржај воде од 3,31–3,92 %, садржај пепела од 7,13––7,86 %, а испарљиве материје од 8,19–9,22 %. СЕМ карактеризација показује да микроталасна активација равномерно повећава број пора и увећава поре. Према резултатима истраживања, снага и време активације значајно побољшавају квалитет угљених брикета од љуски палме.

(Примљено 30. маја, ревидирано 25. октобра 2024, прихваћено 24. јула 2025)

REFERENCES

1. A. Rahman, O. Farrok, M. M. Haque, *Renew. Sustain. Energy Rev.* **161** (2022) 112279 (https://doi.org/10.1016/j.rser.2022.112279)
2. M. M. Tun, D. Juchelkova, M. M. Win, A. M. Thu, T. Puchor. *Resources* **8** (2019) 81 (https://doi.org/10.3390/resources8020081)
3. BPS-Statistics Indonesia Sulawesi Tenggara Province (February 28, 2023). *Sulawesi Tenggara Province in Figures 2023*. (https://sultra.bps.go.id/en/publication/2023/02/28/1828fe18cd21a894338918f9/provinsi-sulawesi-tenggara-dalam-angka-2023.html) (July 19, 2024)

4. D. L. A. Gaveau, B. Locatelli, M. A. Salim, Husnayaen, T. Manurung, A. Descals, A. Angelsen, E. Meijaard, D. Sheil, *PloS One* **17** (2022) e0266178 (https://doi.org/10.1371/journal.pone.0266178)
5. Wu, T. C. Qiang, G. Zeng, H. Zhang, Y. Huang,Y. Wang, *Int. J. Hydrogen Energy* **42** (2017) 23871-23877 (https://doi.org/10.1016/j.ijhydene.2017.03.147)
6. S. Raharjo, L. Lestari, I. Saleh, I. N. Sudiana, A. Dewi. *J. World Sci.* **2** (2023) 310 (https://doi.org/10.58344/jws.v2i3.249)
7. A. O. Otieno, P. G. Home, J. M. Raude, S. I. Murunga, A. Gachanja. *Heliyon* **8** (2022) e10272 (https://doi.org/10.1016/j.heliyon.2022.e10272)
8. P. Martens, H. Czech, J. Tissari, M. Ihalainen, H. Suhonen, M. Sklorz, J. Jokiniemi, O. Sippula, R. Zimmermann, *Energy Fuels* **35** (2021) 14010 (https://doi.org/10.1021/acs.energyfuels.1c01667)
9. S. Nanda, F. Berruti, *J. Haz. Mat.* **403** (2021) 123970 (https://doi.org/10.1016/j.jhazmat.2020.123970)
10. C. Geng, W. Zhong, Z. Bian, X. Liu, *Fuel* **331** (2023) 125832 (https://doi.org/10.1016/j.fuel.2022.125832)
11. W. Spencer, G. Senanayake, M. Altarawneh, D. Ibana, A. N. Nikoloski, *Minerals Eng*. **212** (2024) 108712 (https://doi.org/10.1016/j.mineng.2024.108712)
12. L. Lestari, V. I. Variani, I. N. Sudiana, M. Z. Firihu, S. Raharjo, L. Agusu, A. Dewi, *J. Phys.: Conf. Ser*. **1153** (2019) 012076 (https://doi.org/10.1088/1742-6596/1153/1/012076)
13. B. O. Bonsu, M. Takase, J. Mantey, *Heliyon* **6** (2020) e05266 (https://doi.org/10.1016/j.heliyon.2020.e05266)
14. S. Y. Kpalo, M. F. Zainuddin, L. A. Manaf, A. M. Roslan, *Sustainability* **12** (2020) 2468 (https://doi.org/10.3390/su12062468)
15. J. Cheng, Y. Zhang, T. Wang, H. Xu, P. Norris, W. P. Pan, *Fuel* **225** (2018) 554 (https://doi.org/10.1016/j.fuel.2018.03.185)
16. N. Z. J. Zakaria, S. Rozali, N. M. Mubarak, S. Ibrahim, *Biomass Conv. Bioref.* **14** (2024) 13-44 (https://doi.org/10.1007/s13399-022-02430-3)
17. H. M. P. Marreiro, R. S. Peruchi, R. M. B. P. Lopes, S. L. F. Andersen, S. A. Eliziário, P. R. Junior, *Energies* **14** (2021) 8320 (https://doi.org/10.3390/en14248320)
18. P. Gustan, L. Efiyanti, S. Darmawan, N. A. Saputra, D. Hendra, A. D. Joseph, A. Inkriwang, R. Effendi*, J. Korean Wood Sci. Technol.* **51** (2023) 207 (https://doi.org/10.5658/WOOD.2023.51.3.207)
19. Z. Wang, Y. Cheng, K. Zhang, C. Hao, L. Wang, W. Li, W. B. Hu, *Fuel* 2**32** (2018) 495 (https://doi.org/10.1016/j.fuel.2018.06.004)
20. S. Khodabakhshi, P. F. Pasquale, E. Andreoli, *Carbon* **162** (2020) 604 (https://doi.org/10.1016/j.carbon.2020.02.058)
21. M. R. Sanghvi, H. T. Omkar, A. P. More *Polymer Bull.* **79** (2022) 10491 (https://doi.org/10.1007/s00289-021-04022-z)
22. C. Antwi-Boasiako, B. B. Acheampong, *Biomass Bioenergy* **85** (2016) 144 (https://doi.org/10.1016/j.biombioe.2015.12.006)
23. E. D. Vicente, A. Vicente, M. Evtyugina, R. Carvalho, L. A. Tarelho, F. I. Oduber, C. Alves, *Fuel Process. Technol*. **176** (2018) 296 (https://doi.org/10.1016/j.fuproc.2018.03.004)
24. Z. Li, K. Peng, N. Ji, W. Zhang, W. Tian, W. Z. Gao, *Nanoscale Adv*. **7** (2025) 419 (https://doi.org/10.1039/d4na00701h)

25. L. Lestari, S. Raharjo, I. N. Sudiana, L. O. Rusman, S. J. Manikam, *World Sci. **3*** (2024) 1198-1207 (https://doi.org/10.58344/jws.v3i9.1184)
26. K. Y. Foo, B. H. Hameed, *Biomass Bioenergy* **35** (2011) (7) 3257 (https://doi.org/10.1016/j.biortech.2011.09.116)
27. A. Awitdrus, Y. Pradita, R. Farma, Iwantono, *J. Technomater. Phys.* **1** (2019) 56 (https://doi.org/10.32734/jotp.v1i1.820)
28. W. Astuti, K. Wijaya, Rochmadi, *J. Mater. Res. Technol* **9** (2020) 5108 (https://doi.org/10.15294/jbat.v9i02.21991)
29. S. Zhang, M. Zheng, Y. Tang, R. Zang, X. Zhang, X. Huang, Y. Cheng, Y. Yamauchi, S. Kaskel, H. Pang, *Adv. Funct. Mater.* **32** (2022) 2204714 (https://doi.org/10.1002/adfm.202204714)
30. K. Malini, D. Selvakumar, N. Kumar, *J. CO_2 Util.* **67** (2023) 102318 (https://doi.org/10.1016/j.jcou.2022.102318)
31. W. Deng, M. Hu, J. Ma, Y. Su, R. Ruan, *J. Clean. Prod.* **259** (2020) 120907 (https://doi.org/10.1016/j.jclepro.2020.120907)
32. M. O. Yusuf, *Appl. Sci.* **13** (2023) 3353 (https://doi.org/10.3390/app13053353)
33. M. Asemani, A. R. J. Rabbani, *Pet. Sci. Eng.* **185** (2020) 106618 (https://doi.org/10.1016/j.petrol.2019.106618)
34. D. Karolina, M. S, Maja, D. S. Magdalena, Ż. Grażyna, *Spectrochim. Acta, A* **279** (2022) 121404 (https://doi.org/10.1016/j.saa.2022.121404)
35. N. S. Nemeş, A. Negrea, *Microb. Electrochem. Technol.* **1** (2023) 163 (https://doi.org/10.1002/9783527839001.ch6).

Journal of the Serbian Chemical Society
JSCS@tmf.bg.ac.rs • www.shd.org.rs/JSCS
J. Serb. Chem. Soc. 90 (9) S353–S355 (2025) *Supplementary material*

SUPPLEMENTARY MATERIAL TO

Effect of microwave power level and processing time on the quality of palm shell charcoal (*Elaeis guineensis* Jacq.) briquettes

LINA LESTARI[1], SAPTO RAHARJO[2]*, I NYOMAN SUDIANA[1], LA ODE RUSMAN[1] and NIKEN SULASTRI[1]

[1]*Department of Physics, Faculty of Mathematics and Natural Sciences, Halu Oleo University, Kendari 93232, Indonesia and* [2]*Department of Chemistry, Faculty of Mathematics and Natural Sciences, Halu Oleo University, Kendari 93232, Indonesia*

J. Serb. Chem. Soc. 90 (9) (2025) 1069–1087

EXPERIMENTAL

Research procedure

The source of palm shell biomass waste comes from PT. Tani Prima Makmur, Lerehoma Village, Anggaberi District, Konawe Regency. Making charcoal briquettes begins with sample preparation, adhesive material, and ignition material. Sample preparation involves drying palm oil shell waste in the sun to remove the waste's water content and speed up carbonization. Adhesive preparation involves drying the sago in the sun and sifting it using an 80-mesh sieve. Preparation of ignition material involves collecting wood or twigs and drying the ignition material until it is scorched so that it can start a fire in the carbonization process.

The carbonization process is a precise and careful procedure. 45 kg of dried palm oil shell waste was weighed and then carbonized using a carbonization reactor. This reactor, a device with a limited air supply system, ensures that the palm oil shells are burned without further burning. The weighed palm oil shells are put into the carbonization reactor until it fills 75% of the reactor volume, then the reactor is closed to reduce the amount of oxygen entering the reactor. The ignition material is put into the furnace and ignited until it ignites. The reactor temperature is measured every two minutes using an infrared thermometer to maintain the stability of the carbonization rate. The carbonization process of palm oil shells can be observed through the reactor chimney, providing a clear indication of the process's precision and care. When the chimney emits thick and dense smoke, it indicates that the palm oil shells have been carbonized, and when the smoke coming out of the chimney begins to thin and is clear in color, it indicates that the carbonization process has been completed.

Then, the finely ground charcoal is sieved using an 80-100 mesh sieve by arranging the two sieves with the 80 mesh sieve positioned above the 100 mesh sieve. The charcoal powder that passes through the 80 mesh sieve and remains on the 100 mesh sieve is the charcoal that

* Corresponding author. E-mail: sapto.raharjo@uho.ac.id

will be used for the following process. The sieving process is carried out to ensure the resulting charcoal powder has a uniform or homogeneous particle size.

The sifted palm shell charcoal powder was then weighed using a digital scale in the amount of 5 g and stored in a porcelain cup to be activated using a microwave furnace (SHARP R-21D0(S)-IN, China) with a chamber capacity of 23 liters, five adjustable power levels, operating at 220V and 50Hz. The activated palm shell charcoal is then mixed with the prepared sago adhesive. The composition of charcoal powder and adhesive material uses a ratio of 9:1, namely 9 g mass of charcoal and 1 g mass of adhesive material with 4 ml of distilled water solvent which has been heated at a temperature of 100°C. Mixing charcoal powder with adhesive aims to ensure that the charcoal particles bond together, have a good particle arrangement and do not crumble easily. The results of mixing charcoal powder and adhesive are then printed and compacted using a hydraulic press printing machine. The use of a hydraulic press printing machine is to ensure that the charcoal and adhesive mixture is compacted uniformly and with sufficient pressure, which is crucial for the structural integrity of the final product.

Gravimetric method (lignin, cellulose, and hemicellulose content)

To determine the lignin, cellulose, and hemicellulose content, the sample is first determined for Neutral Detergent Fiber (NDF) and Acid Detergent Fiber (ADF) content (Van Soest, 1985).

- Neutral Detergent Fiber (NDF)

$$\text{NDF content} = \frac{\text{b} - \text{a}}{Sample\ mass} \times 100\%$$

1. Weigh the sample approximately 0.4 grams, then put it into a 50 ml test tube
2. Add 40 ml of ADF solution, then close the tube tightly
3. Boil in boiling water for 1 hour while shaking occasionally.
4. Filter with sintered glass No. 1 of known weight (a gram) while being held with a vacuum pump.
5. Wash with approximately 100 ml of boiling water and 50 ml of alcohol.
6. Oven at 1050 C for 8 hours or leave overnight
7. Cool in a desiccator for approximately a half-hour, then weigh (b grams)

- Acid Detergent Fiber (ADF)

$$\text{ADF content} = \frac{\text{b} - \text{a}}{Sample\ mass} \times 100\%$$

1. Weigh the sample approximately 0.2 grams
2. Put it into a 50 ml test tube
3. Add 30 ml of NDF solution, then close the tube tightly
4. Boil in boiling water for 1 hour (shake occasionally)
5. Filter into sintered glass No.1 of known weight (a gram) while being sucked with a vacuum pump
6. Wash with approximately 100 ml of hot water (sufficient)
7. Wash with approximately 50 ml of alcohol
8. Oven at 1050 C for 8 hours or leave overnight
9. Cool in a desiccator for a half-hour, then weigh (b grams)

Lignin

Lignin is a combination of several closely related compounds containing carbon, hydrogen, and oxygen, but the proportion of carbon is higher than that of carbohydrate compounds.

$$\text{Lignin content} = \frac{\text{c} - \text{d}}{Sample\ mass} \times 100\%$$

1. Sintered glass containing ADF is placed on a Petri disk
2. Add 20 ml of 72% H2SO4, stir to ensure that the fibre is wetted with 72% H2SO4 and leave for 2 hours 20
3. Suck with a vacuum pump while rinsing with enough hot water
4. Oven for 8 hours at a temperature of 1000 C or leave overnight
5. Put in a desiccator, then weigh (c gran); put in an electric furnace or heat to 5000 C for 2 hours, let it cool slightly, then put in a desiccator for a half hour, then weigh (d)

Cellulose

$$\text{Cellulose content} = \%\ \text{ADF} - \%\ \text{Lignin} - \%\ \text{Insoluble ash}$$

Cellulose is the main component of plant cell walls. Cellulose is a glucose polymer with ß -1,4 glucoside bonds in a straight chain.

Hemicellulose

$$\text{Hemicellulose content} = \%\text{NDF} - \%\text{ADF}$$

Hemicellulose is a group of heterogeneous polysaccharides with low molecular weight. Hemicellulose is usually between 15 and 30 per cent of the dry weight of lignocellulosic materials (Taherzadeh, 1999). Hemicellulose is relatively more straightforward to hydrolyze with acid into monomers containing glucose, mannose, galactose, xylose and arabinose. Hemicellulose binds cellulose fibre sheets to form microfibrils that increase cell wall stability.

Table S1. Test results

Test Results	Hemiselulosa	Cellulose	Lignin
Repetition	Results (%)	Results (%)	Results (%)
1	12.24	25.83	42.22
2	12.12	25.92	42.21
3	12.17	25.90	42.18
Mean	12.18	25.88	42.20
Standard Deviation	0.06	0.05	0.02
Method Precision (%RSD)	0.50	0.18	0.05
%CV Horwits	10.983	9.805	9.109
	1.21767E-05	2.58833E-05	4.22033E-05
	-4.914471583	-4.586979795	-4.374653246
	3.457235791	3.293489897	3.187326623
0.67x% CV horwits	7.36	6.57	6.10

Journal of the Serbian Chemical Society
JSCS@tmf.bg.ac.rs • www.shd.org.rs/JSCS
J. Serb. Chem. Soc. *90* (9) 1089–1104 (2025)
JSCS–5441
Original scientific paper
Published 30 September, 2025

Water-splitting electrocatalytic properties and computational characterization of a symmetrically substituted porphyrazine

MARINA ALEXANDRA TUDORAN and BOGDAN-OVIDIU TARANU*

National Institute of Research and Development for Electrochemistry and Condensed Matter, Dr. A. Paunescu Podeanu Street No. 144, 300569 Timisoara, Romania

(Received 23 March, revised 19 June, accepted 10 July 2025)

Abstract: The porphyrazine 2,7,12,17-tetra-*tert*-butyl-5,10,15,20-tetraaza-21*H*,23*H*-porphine was studied regarding its electrocatalytic water-splitting activity in a wide pH range. Two different methods were employed to manufacture electrodes based on this compound: a solution-based method and a catalyst ink-based one. The most catalytically active electrode was obtained using the catalyst ink-based method. In 1 mol L^{-1} KOH solution it displays an H_2 evolution reaction overpotential of 0.6 V and a Tafel slope of 0.15 V dec^{-1}. Statistical analysis revealed a significant correlation between the pH and the O_2 evolution reaction overpotential. Quantum chemical calculations were performed to obtain a more detailed understanding of the porphyrazine's properties.

Keywords: electrocatalyst; hydrogen evolution reaction; oxygen evolution reaction; quantum chemical calculations; correlation analysis.

INTRODUCTION

Porphyrins, corroles, phthalocyanines, naphthalocyanines, subphthalocyanines and porphyrazines are classes of tetrapyrrole macrocyclic organic compounds and members of the porphyrinoids family.[1] Of these, porphyrazines, also known as tetraazaporphyrins, exhibit features differentiating them from porphyrins by having nitrogen atoms in the *meso*-positions of their macrocycle instead of carbon atoms, and from phthalocyanines by having their *β*-pyrrole positions available for functionalization.[2] Concerning their applications, these compounds are being studied as photosensitizers for photodynamic therapy and dye-sensitized solar cells, as photocatalysts, electrocatalysts, as well as fluorescent and optical sensors.[3–7] 2,7,12,17-Tetra-*tert*-butyl-5,10,15,20-tetraaza-21*H*,23*H*-porphine is a member of the tetraazaporphyrin class that has been the subject of some reported studies.[8–12] However, no published investigation regarding the electrocatalytic water-splitting

* Corresponding author. E-mail: b.taranu84@gmail.com
https://doi.org/10.2298/JSC250323043T

properties of this particular porphyrazine has been identified. Revealing the hydrogen evolution reaction catalytic activity of electrode materials is of appreciable current importance. Presently, green hydrogen generated via renewable energy-based water-splitting is highly desirable in the global effort of diminishing greenhouse gas emissions.[13] Considerable efforts to decrease greenhouse gas emissions, to slow down global warming and to contain the accelerated climate change are currently being made by many countries.[14] Different technologies are available for hydrogen generation through water-splitting,[15] but electrochemical water-splitting is one of the most promising for the production of green hydrogen.[16] The main reactions occurring during water electrolysis are the oxygen evolution reaction (OER) at the anode and the hydrogen evolution reaction (HER) at the cathode.[17] The former is the major bottleneck of the whole process due its sluggish electrochemical kinetics.[18] The benchmark electrocatalysts for the two reactions are Ir/Ru and Pt-based electrode materials.[19] Due to the scarcity and high costs characteristic of noble metals, it is difficult to use such materials for large-scale water-splitting. As a result, researchers have been investigating other compounds with electrocatalytic properties, either based on low-cost, Earth-abundant transition metals or metal-free carbon-based ones.[20–22] Regarding porphyrazines, even though no reported study of the water electrolysis activity of 2,7,12,17-tetra-*tert*-butyl-5,10,15,20-tetraaza-21*H*,23*H*-porphine was found, there are other members of the porphyrazine class that have been investigated as noble metal-free water-splitting electrocatalysts.[6]

The current work describes two investigations. One of them is experimental, while the other is theoretical. The experimental study concerns the electrochemical water-splitting activity of the aforementioned compound in a wide pH range by using porphyrazine-modified electrodes manufactured via different protocols. The theoretical part consists of quantum chemical calculations of the porphyrazine molecule in gas phase using three different hybrid density functional theory (DFT) methods, as well as statistical analysis. Although the computational modeling and experimental investigation are based on different principles, they are complementary methods which can provide a deeper understanding of the compound's structure and properties.

EXPERIMENTAL

Materials and reagents

2,7,12,17-Tetra-*tert*-butyl-5,10,15,20-tetraaza-21*H*,23*H*-porphine (Scheme S-1 of the Supplmentary material) was purchased from Sigma–Aldrich and used as received. The following organic solvents were procured and used to obtain the tetraazaporphyrin solutions: *N*,*N*-dimethylformamide (DMF), acetonitrile (CH_3CN), benzonitrile (PhCN), ethanol (EtOH), tetrahydrofuran (THF) and dichloromethane (DCM) from Sigma–Aldrich, Honeywell (Charlotte, NC, USA) and Merck. Nafion® 117 solution and carbon black, Vulcan® XC 72 were purchased

from Sigma–Aldrich and Fuell Cell Store (Bryan, TX, USA) and used to prepare the tetraazaporphyrin suspensions. The solid substrates utilized to manufacture the electrodes were glassy carbon (GC) tablets (∅ 8 mm) obtained from Andreescu Labor & Soft SRL (Bucharest, Romania). Sulfuric acid 98 %, potassium chloride and potassium hydroxide were procured from Merck to prepare the electrolyte solutions. All reagents were used as received and all electrolyte solutions were obtained with double-distilled water from a water double distillation unit (Fistreem, Cambridge, UK).

Electrode manufacturing methods

Two different methods were employed to obtain the porphyrazine-modified electrodes used in the electrochemical experiments aimed at evaluating the compound's water-splitting electrocatalytic properties. Regarding the first method, the tetraazaporphyrin was dissolved in organic solvents with different polarity, increasing as follows: DCM < THF < EtOH < PhCN < CH_3CN < DMF.[23,24] The solutions were utilized to modify the surface of the GC tablets *via* the drop-casting technique. A volume of 10 μL was applied to obtain one porphyrazine layer. After solvent evaporation at 40 °C a modified substrate was either used as an electrode in the electrochemical experiments or it was further modified with one or two more layers. The names of the electrodes are presented in Table I along with the solvents employed to dissolve the traazaporphyrin and the number of layers deposited on the GC support.

TABLE I. Names of porphyrazine-modified electrodes obtained with the solution-based method

Electrode name	Solvent	Porphyrin layers	Electrode name	Solvent	Porphyrin layers
$GC_{AP\text{-}DCM\text{-}1}$	DCM	1	$GC_{AP\text{-}PhCN\text{-}1}$	PhCN	1
$GC_{AP\text{-}DCM\text{-}2}$		2	$GC_{AP\text{-}PhCN\text{-}2}$		2
$GC_{AP\text{-}DCM\text{-}3}$		3	$GC_{AP\text{-}PhCN\text{-}3}$		3
$GC_{AP\text{-}THF\text{-}1}$	THF	1	$GC_{AP\text{-}CH3CN\text{-}1}$	CH_3CN	1
$GC_{AP\text{-}THF\text{-}2}$		2	$GC_{AP\text{-}CH3CN\text{-}2}$		2
$GC_{AP\text{-}THF\text{-}3}$		3	$GC_{AP\text{-}CH3CN\text{-}3}$		3
$GC_{AP\text{-}EtOH\text{-}1}$	EtOH	1	$GC_{AP\text{-}DMF\text{-}1}$	DMF	1
$GC_{AP\text{-}EtOH\text{-}2}$		2	$GC_{AP\text{-}DMF\text{-}2}$		2
$GC_{AP\text{-}EtOH\text{-}3}$		3	$GC_{AP\text{-}DMF\text{-}3}$		3

The solution-based GC modification strategy relies on the fact that porphyrazine molecules are capable of spontaneous self-assembly through non-covalent interactions into supramolecular aggregates.[25,26] Typically, the properties of these aggregates are different than those of the individual molecules.[27] The aggregation behavior depends on several factors, such as solvent type, the amount of material, the type of substituents, the presence or absence of a central metal ion, the surrounding environment (*e.g.*, the solid support and the atmosphere) and temperature.[26] The electrodes were manufactured by varying the solvent type and the number of deposited layers in the case of each solvent.

The second method employed to obtain tetraazaporphyrin-modified electrodes is the catalyst ink-based method.[28] The inks were obtained by dispersing in water an amount of porphyrazine or of porphyrazine and carbon black during a 30-min ultrasonication stage. The surface of the solid supports was modified by drop-casting a catalyst ink volume of 10 μL. The modified supports were dried at 40 °C and the resulting samples were used as electrodes in the electrochemical experiments. Table II shows the names of the electrodes and the compositions of the catalyst inks.

TABLE II. Names of porphyrazine-modified electrodes obtained with the catalyst ink-based method

Electrode name	Porphyrin amount mg	Carbon black mg	Nafion solution μL	Double-distilled water μL
GC_{AP}	10	–	50	450
GC_{CB-AP}	5	5	50	450

Electrochemical experiments

The setup used to perform the electrochemical investigations consisted of a standard glass cell for electrochemical experiments containing the electrolyte solution, a potentiostat (Voltalab, model PGZ 402, from Radiometer Analytical, Lyon, France) and three electrodes that were connected to the device and inserted into the solution. The auxiliary electrode was a Pt plate having a geometric surface (S_{geom}) of 0.8 cm^2. The Ag/AgCl (sat. KCl) electrode was utilized as reference electrode. The working electrode was each of the tetraazaporphyrin-modified electrodes after being placed inside a polyamide support that restricted the area exposed to the electrolyte solution to S_{geom} = 0.28 cm^2. To cover a wide pH range, the following electrolyte solutions were employed in the study: 0.1 mol L^{-1} KCl, 0.1 mol L^{-1} H_2SO_4, and 1 mol L^{-1} KOH. Before the HER experiments, the electrolyte solutions were bubbled with high-purity N_2. The linear sweep voltammograms (LSVs) obtained during the HER and OER tests were *IR*-corrected and their recording was carried out at a 5 mV s^{-1} scan rate (v).[29] The parameter j represents the geometric current density, while E is the electrochemical potential *vs.* reversible hydrogen electrode (RHE). The equations used to express the potential *vs.* the specified reference electrode, to calculate the oxygen and hydrogen evolution overpotentials (η_{OER} and η_{HER}) and the Tafel equation can be found in the Supplementary material as Eqs. (S-1), (S-2), (S-3) and (S-4), respectively.[30-32] Eqs. (S-5) and (S-6) are also relevant to the electrochemical study, as outlined in the Results and Discussion section.

Raman spectroscopy analysis

Raman spectra were recorded using a MultiView-2000 system (Nanonics Imaging Ltd., Jerusalem, Israel) with a Shamrock 500i spectrograph (Andor, Essex, UK).

Theoretical calculations

Quantum chemical calculations for the tetraazaporphyrin in the ground state were carried out using HyperChem 8.1 and Gaussian03 software. Pre-optimization of the molecule was conducted using HyperChem and the semi-empirical PM3 model. The obtained molecular configuration was then subjected to further optimization with the Gaussian 03 in DFT framework, without symmetry constraints, using the Becke 3-Lee-Yang-Parr (B3LYP), B3PW91 and MPW1PW91 functionals with STO-3G basis set. To verify that the obtained structure corresponds to a minimum on the potential energy surface, frequency calculations were performed at the same theoretical levels. Single point calculations were performed using 6-31G(d) basis set. Gaussian output files were visualized using Gauss View 6.0 software. A statistical analysis was performed using IBM SPSS 21 to ascertain the association between the studied electrochemical parameters.

RESULTS AND DISCUSSION

Results of the quantum chemical calculations

The structural parameters calculated with B3LYP/STO-3G, B3PW91/STO--3G and MPW1PW91/STO-3G are presented in Table S-I of the Supplementary material. Data obtained by Mongale *et al.* for the unfunctionalized porphyrazine were used for comparison.[33] The results obtained show that, with the exception of the C_{19}–C_{17} and C_{15}–C_{20} bonds, the carbon bond lengths for tetraaza-porphyrin were slightly higher than those of the unfunctionalized porphyrazine. In contrast, the values of the angles between carbon and nitrogen atoms were lower in the case of the tetraazaporphyrin, with the exception of the C_{15}–N_{21}–C_{13}, which was found to be lower in the case of the unfunctionalized porphyrazine. These variations arise from the alteration of the macrocycle's geometry, which occurs due to its functionalization with tert-butyl groups. The optimized structures for the tetraazaporphyrin and atom numbering are shown in Fig. S-1 of the Supplementary material.

The chemical activity of the compound was evaluated by examining the highest occupied molecular orbital (HOMO) and lowest unoccupied molecular orbital (LUMO) frontier molecular orbitals. The HOMO energy is indicative of the molecule's capacity to donate electrons in a chemical reaction, while the LUMO energy is indicative of its capacity to accept electrons.[33] The energy gap between the HOMO and LUMO energies denotes the energy required for a molecule to transition from the ground state to an excited state, being a critical factor in determining its reactivity tendency, optical polarizability, and kinetic stability.[34,35] The spatial distribution of the HOMO and LUMO orbitals and the corresponding energies are shown in Fig. S-2 and Table S-II of the Supplementary material. The HOMO and LUMO orbitals for the tetraazaporphyrin are localized at the carbon atoms of the macrocycle, which is similar to the unfunctionalized porphyrazine.[34] However, the value of the energy gap is slightly smaller, 2.303 (B3LYP/6-31G(d)), 2.538 (B3PW91/6-31G(d)) and 2.331 (MPW1PW91/6-31G(d)), compared to the 2.63 value reported by Mongale *et al.*[33] The vertical ionization potential and electron affinity for the tetraazaporphyrin were calculated using the ΔSCF formalism (Eqs. (S-7) and (S-8) from the Supplementary Material). The results are presented in Table S-II. The smallest values of both parameters were obtained with B3LYP/6-31G(d).

Table S-III of the Supplementary materialshows the values of the thermodynamic parameters. They can be used in calculating the Gibbs energy change, as part of the thermodynamic cycle,[36] and include the dipole moment, the zero-point vibrational energy, the sum of electronic energies with the zero-point correction and the thermal energy and enthalpy corrections. The rotational constants, thermal energy, heat capacity and entropy are also provided. Results indicate that the B3LYP/STO-3G method yields the highest values, except for the dipole moment,

zero-point vibrational energy, and thermal energy, for which higher values were obtained with the MPW1PW91/STO-3G method.

Natural charge, population and electronic configuration are commonly used to explain the electronic properties of molecules. Natural bond orbital (NBO) analysis was also employed to assess the nature of the bonding interaction with regard to charge transfer and orbital interactions, as well as to obtain a more comprehensive understanding of the dissociation process' activation.[37,38]

According to the results in Table S-IV of the Supplementary material, N atoms display only negative charges, H atoms display only positive charges and C atoms display both positive and negative charges – depending on the type of bonding they are involved in.

Polarizability and hyperpolarizability serve to characterize the response of a system to an applied electric field. Literature data indicates that organic molecules containing conjugated π-electrons exhibit high values of the first molecular hyperpolarizability.[39] It was also shown that increased polarization can result in enhanced adsorption, thereby decreasing surface adsorption resistance during the oxygen evolution reaction.[40] The complete set of equations employed for the calculation of the polarizability (α), the anisotropy of polarizability ($\Delta\alpha$), and the first hyperpolarizability (β) are available in the Supplementary material as Eqs. (S-9) to (S-11), with the results being presented in Table S-V of the Supplementary material. The highest polarizability values were obtained with the B3LYP/6--31G(d) method, while the highest hyperpolarizability value was acquired *via* the B3PW91/6-31G(d) method.

Experiments with electrodes obtained using the solution-based method

The results obtained by studying the water electrolysis catalytic activity of the electrodes manufactured with the solution-based method evidence the ways in which the organic solvents and the number of deposited tetraazaporphyrin layers influence the OER and HER overpotential values. The anodic polarization curves recorded in the acidic, neutral, and alkaline environments are presented in Figs. S-3, S-4 and S-5 of the Supplementary material. In most cases, the electrocatalytic activity of the porphyrazine-modified electrodes is lower than that of the unmodified GC electrode (GC_0). In the few situations in which it is higher the difference is not significant, with the exception of the $GC_{AP\text{-}PhCN\text{-}1}$ electrode immersed in 0.1 mol L^{-1} KCl solution (Fig. S-4a). When specifying the OER and HER overpotential values of different electrodes the current density value accepted as benchmark is 10 mA cm^{-2} for OER and −10 mA cm^{-2} for HER.[31] At this j value the η_{OER} for $GC_{AP\text{-}PhCN\text{-}1}$ and GC_0 is 1.24 and 1.32 V, respectively. As the current density increases this difference decreases until (at j = ~ 30 mA cm^{-2}) the η_{OER} value is the same for both specimens. Fig. S-6, S-7 and Fig. 1 show the cathodic polarization curves obtained on the electrodes manufactured with the solution-

based protocol in the 0.1 mol L^{-1} H_2SO_4, 0.1 mol L^{-1} KCl and 1 mol L^{-1} KOH electrolyte solutions. In the selected potential range only two electrodes display water-splitting electrocatalytic activity at −10 mA cm^{-2}: $GC_{AP\text{-}DMF\text{-}1}$ (η_{HER} = 0.916 V) and $GC_{AP\text{-}PhCN\text{-}3}$ (η_{HER} = 0.9 V). The LSVs for these specimens were recorded in the strong alkaline medium and can be seen in Fig. 1a and c, respectively. Out of the HER overpotential values determined for the electrodes obtained with the solution-based modification strategy the 0.9 V value is the lowest.

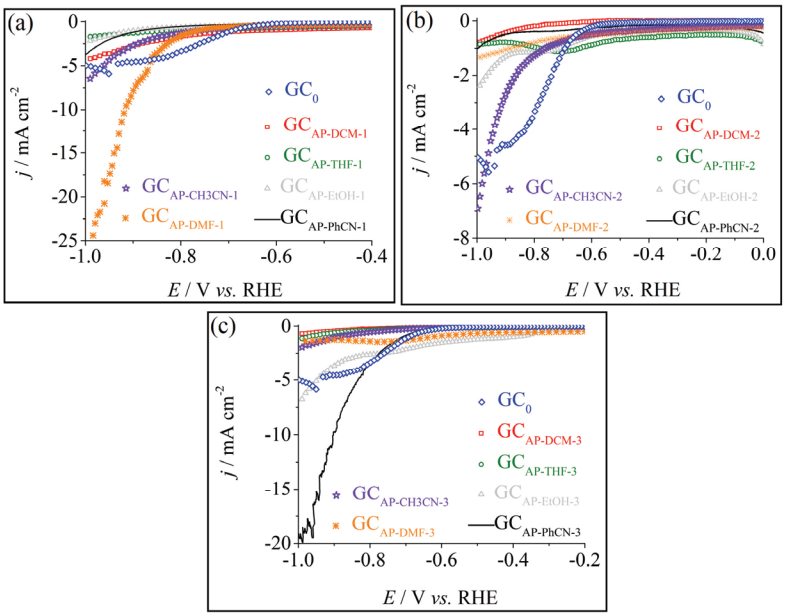

Fig. 1. Cathodic LSVs obtained on GC_0 and on: a) $GC_{AP\text{-}DCM\text{-}1}$, $GC_{AP\text{-}THF\text{-}1}$, $GC_{AP\text{-}EtOH\text{-}1}$, $GC_{AP\text{-}PhCN\text{-}1}$, $GC_{AP\text{-}CH3CN\text{-}1}$ and $GC_{AP\text{-}DMF\text{-}1}$; b) $GC_{AP\text{-}DCM\text{-}2}$, $GC_{AP\text{-}THF\text{-}2}$, $GC_{AP\text{-}EtOH\text{-}2}$, $GC_{AP\text{-}PhCN\text{-}2}$, $GC_{AP\text{-}CH3CN\text{-}2}$ and $GC_{AP\text{-}DMF\text{-}2}$; c) $GC_{AP\text{-}DCM\text{-}3}$, $GC_{AP\text{-}THF\text{-}3}$, $GC_{AP\text{-}EtOH\text{-}3}$, $GC_{AP\text{-}PhCN\text{-}3}$, $GC_{AP\text{-}CH3CN\text{-}3}$ and $GC_{AP\text{-}DMF\text{-}3}$. Electrolyte solution: 1 mol L^{-1} KOH; v = 5 mV s^{-1}.

Statistical analysis

The data collected during the electrochemical experiments carried out on the electrodes manufactured with the solution-based method were further exploited in statistical analysis. A correlation analysis was conducted to assess whether there is a significant relationship between the polarity of the organic solvents, the pH of the electrolyte solutions, and the number of layers drop-casted on the GC support on the one hand and the overpotential on the other. The only statistically significant correlation was obtained between the pH and the OER overpotential – $r_S(45)$ = = 0.447, $p < 0.01$ – indicating a medium association in the positive direction between the two parameters. The r_S^2 value specifies that approximately 20 % of

the variance in overpotential can be predicted from the pH. The correlation procedure is presented in the Supplementary material.

Experiments with electrodes obtained using the catalyst ink-based method

Fig. S-8 presents the anodic polarization curves recorded on the electrodes modified with the tetraazaporphyrin *via* the catalyst ink-based method. In all cases the unmodified GC electrode and the electrode manufactured using a catalyst ink containing only carbon black as the dispersed phase (GC_{CB}) are more electrocatalytically active compared with the modified specimens. The data collected during the HER investigation is shown in Fig. 2. GC_{CB} is more electrocatalytically active in the acidic and neutral environments (Fig. 2a and b), but the GC_{AP} and GC_{CB-AP} electrodes are significantly more active in the strongly alkaline solution (Fig. 2c). GC_{CB-AP} exhibits the highest water-splitting electrocatalytic activity found during the electrochemical experiments: $\eta_{HER} = 0.6$ V at $j = -10$ mA cm^{-2}.

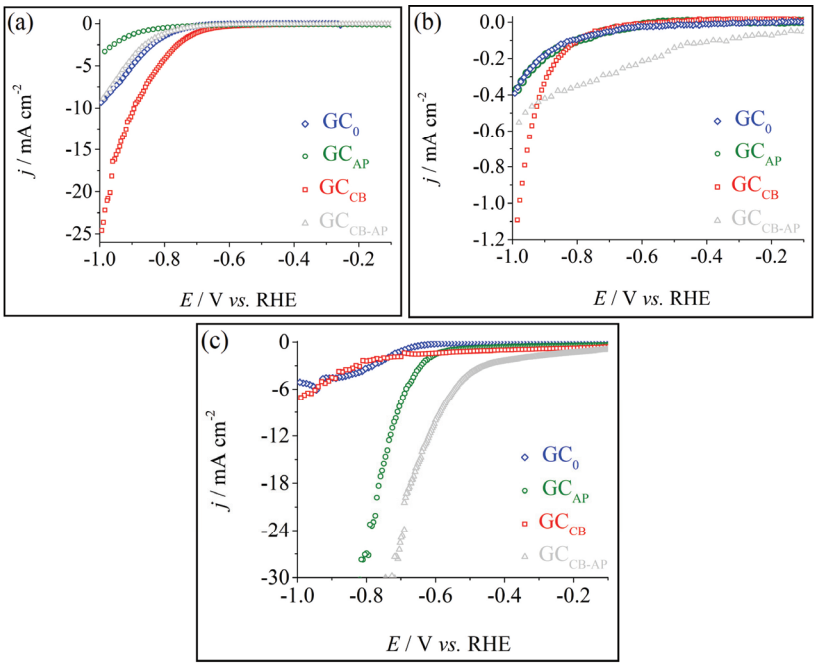

Fig. 2. Cathodic LSVs obtained on GC_0, GC_{CB}, GC_{AP} and GC_{CB-AP} in the following electrolyte solutions: a) 0.1 mol L^{-1} H_2SO_4, b) 0.1 mol L^{-1} KCl and c) 1 mol L^{-1} KOH; $v = 5$ mV s^{-1}.

The most active specimen was the focus of additional investigations aimed at outlining more of its water-splitting catalytic properties. The voltammetric and chronoamperometric data acquired during these experiments can be seen in Fig. 3. The electroactive surface area (*ECSA*) of the electrode was calculated based on the

value of the electric double-layer capacitance (C_{dl}), which is equal to the absolute value of the slope of the curve drawn by plotting the capacitive current density (j_{dl}) *vs.* the scan rate. Fig. 3a shows the graphical representation of two curves obtained for two GC_{CB-AP} specimens. The j_{dl} values were calculated with Eq. (S-5) using data from the cyclic voltammograms recorded at increasing scan rate values and presented in Fig. S-9 of the Supplementary material.[41] The curves from Fig. 3a are almost overlapping and the average value of their slopes (C_{dl}) can be found in Table III together with the values of other electrochemical parameters calculated in the study: the roughness factor (R_f) and *ECSA*. R_f is the ratio between the real surface of an electrode and its geometrical surface and is determined by dividing C_{dl} to the specific capacitance of a smooth electrode surface (C_s = 0.06 mF cm^{-2}).[42] Eq. (S-6) was employed to estimate the *ECSA* value.[43] This parameter is important in water-splitting studies due to its direct proportionality to the number of active sites involved in water electrolysis and also because it is used to investigate the OER and HER kinetics.[44–46]

TABLE III. The C_{dl}, R^2, R_f and *ECSA* values determined for the GC_{CB-AP} electrode

Electrode	C_{dl} / mF cm^{-2}	R^2	R_f	*ECSA* / cm^2
GC_{CB-AP}	1.416	0.9974	23.6	6.608

The HER kinetics at the interface between GC_{CB-AP} and the 1 mol L^{-1} KOH electrolyte solution were investigated as well. Fig. 3b shows the Tafel plot used to determine the Tafel slope, which in the present case was found to be 0.15 V dec^{-1} (R^2 = 0.9994). A low value of this parameter is preferable because it indicates faster reaction kinetics, but in strongly alkaline environments the surface of the working electrode can become covered to a large extent with hydrogen bubbles, leading to an increased slope value. When the slope is in the 0.04–0.12 V dec^{-1} range, the hydrogen evolution unfolds along a Volmer–Heyrovsky mechanism and the rates of the discharge and desorption steps are comparable, but in cases in which the slope is > 0.12 V dec^{-1} due to the high pH of the environment, a Volmer--limited mechanism is likely to unfold and the rate of the Heyrovsky step becomes slower than that of the Volmer step.[47–49]

The electrochemical stability of the GC_{CB-AP} electrode was also evaluated, with the results being presented in Fig. 3c. The chronoamperogram was recorded during a 7-hour period while maintaining constant the potential value corresponding to j = –10 mA cm^{-2}. Subsequently, a cathodic polarization curve was traced to evaluate the electrode's HER electrocatalytic activity and it is compared with the one obtained before the experiment (inset to Fig. 3c). The shape of the two LSVs is similar and an increase in the HER overpotential of just 14 mV is observed at j = –10 mA cm^{-2}. The electrode was analyzed by Raman Spectroscopy as well. Fig. S-10 of the Supplementary material shows the Raman spectra for the sample

before and after the stability test. The signals observed on the spectrum before the experiment are also observed on the one traced afterward. This result is evidence that the GC_{CB-AP} electrode did not undergo any significant structural modifications.

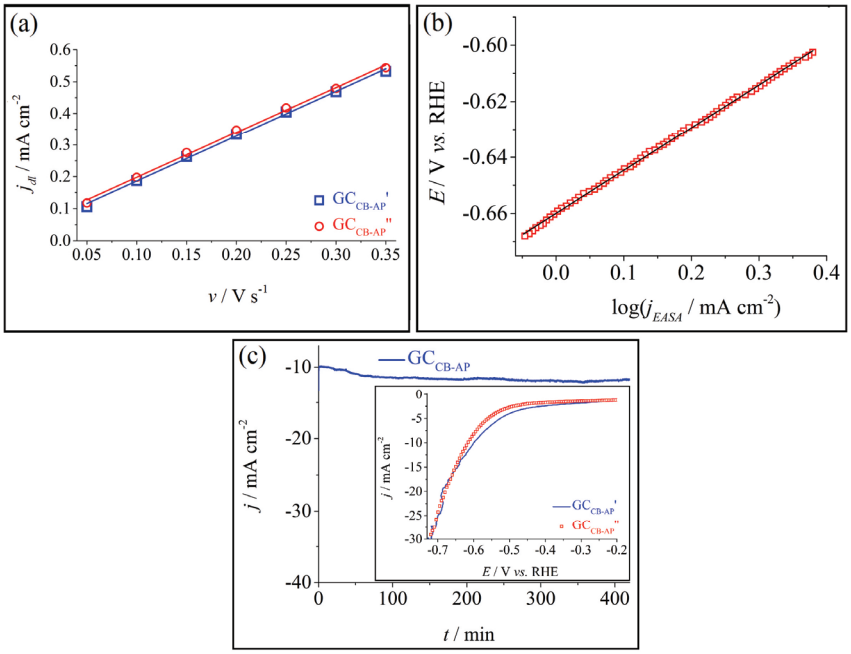

Fig. 3. a) The capacitive current density *vs.* scan rate plots obtained for two GC_{CB-AP} electrodes. b) Tafel plot for GC_{CB-AP} in 1 mol L^{-1} KOH solution. The current density (j_{ECSA}) was *ECSA*-normalized. c) Current density *vs.* time curve recorded on GC_{CB-AP} in 1 mol L^{-1} KOH solution and inset showing the polarization curves traced on GC_{CB-AP} before (GC_{CB-AP}') and after (GC_{CB-AP}'') the chronoamperometric experiment (1 mol L^{-1} KOH solution, v = 5 mV s^{-1}).

Considerations about the HER activity of the GC_{CB-AP} electrode

The GC_{CB-AP} sample obtained by employing the catalyst ink-based method displays the highest HER catalytic activity among the investigated specimens. It has been reported that the catalytic center of porphyrinoids is located in their macrocycle, more specifically at the N_4 site in case of the free-base compounds and the M-N_4 site in case of the metalated ones.[50–52] Since the tetraazaporphyrin used to modify the GC support is metal-free, its catalytic center is probably located at the N_4 site of its porphyrin-derived macrocycle. The previously mentioned relationship between ECSA and the number of active sites involved in the electrocatalytic process implies that a higher value of the former parameter corresponds

to a larger number of catalytic centers. GC_{CB-AP}'s ECSA (of 6.608 cm^2) is considerably higher than its geometric surface (of 0.28 cm^2), which points to a relatively high number of such centers. Porphyrinoid-modified electrodes exhibiting electrocatalytic activity, as is the case with GC_{CB-AP}, possess catalytic properties arising from surface structural features, increased π-resonance and charge transport phenomena.[53] One way in which charge transport unfolds is *via* π–π interactions between adjacent porphyrazine molecules, but the interface between the electrocatalyst and the conductive GC support is also involved. Because the nitrogen atoms located in the tetraazaporphyrin's macrocycle display higher electronegativity compared with the GC's carbon atoms, an electropositive doping effect is induced on the substrate's surface.[50] At the molecular level, the electron transport depends on the relationship between the macrocycle and its peripheral substituents, and the electronic effects of the substituents have an impact on the electrocatalytic water-splitting properties of porphyrinoids.[54] The tert-butyl moieties of the tetraazaporphyrin used to manufacture the GC_{CB-AP} electrode are electron-donating. As for the carbon black particles that were mixed with the porphyrazine to obtain the catalyst ink, their purpose is to improve the charge transport during water electrolysis. Basically, some of GC_{CB-AP}'s features have a positive impact on its catalytic activity (the relatively large number of catalytic centers, the electropositive doping effect of the GC and the carbon black particles), while others have a negative effect (the substituents' electron-donating effect). These characteristics and the electrolyte solution's high pH, whose influence on the Tafel slope has already been mentioned, are responsible for the electrode's HER activity. In Table IV this activity is compared to that of other porphyrinoid-based electrodes.

The η_{HER} and Tafel slope values are lower than some of the values from the table and are comparable to some of the remaining ones. The GC_{CB-AP} electrode displays higher electrocatalytic activity compared to electrodes modified with an A_3B Zn-porphyrin, a Co-phthalocyanine-based nanohybrid, amines-substituted Co-corroles, Fe- and Ni-porphyrin polymers, and a Co oxytyramine phthalocyanine polymer.[27,57,66–68] Also, the electrocatalytic activity of GC_{CB-AP} is similar to that of an electrode modified with a Zn-porphyrin–ferrocene imine gel and an imidazolyl-substituted free base porphyrin coated on carbon nanotubes. [59,64] In other words, the porphyrinoid-based electrocatalysts exhibiting lower or comparable activity to the tetraazaporphyrin studied herein belong to several compound classes - metallated and free base porphyrinoids, polymers and hybrids. Regarding the Tafel slopes, out of the 29 values reported in the literature and mentioned in the Table, 9 are higher than the value found for GC_{CB-AP} and 7 are comparable to it. This result is more than acceptable considering the simplicity of the manufacturing method used to obtain the electrode. More complex methods, such as the ones involving pulsed laser deposition, could further evidence the electrocatalyst's potential.

TABLE IV. The HER activity of GC_{CB-AP} and of other porphyrinoid-based electrodes studied in 1 mol L^{-1} KOH. The η_{HER} values are read at $j = -10$ mA cm^{-2}

Electrocatalyst or electrode	Substrate	η_{HER} / mV	Tafel slope, mV dec^{-1}	Ref.
Cu-CMP700	GC	430	167	55
Cu-CMP800	GC	380	135	55
Cu-CMP850	GC	350	135	55
Cu-CMP900	GC	430	135	55
CoP-2ph-CMP-800	GC	360	121	56
CoP-3ph-CMP-800	GC	380	–	56
CoP-4ph-CMP-800	GC	440	–	56
CoPc@MCA	GC	707	124	57
CoPc	GC	599	123	57
TiCP-PCP	Carbon fiber paper	310	–	58
ZnTAPP-NA	GC	546	121	59
CoTAPP-NA	GC	470	110	59
CoTPP-SD	Carbon fiber paper	475	–	60
CoCOP	Carbon fiber paper	310	161	60
PyCoPc/GO	GC	373	145	61
PyCoPc/GO-800	GC	253	96	61
CoPor-GDY	Carbon cloth	308	129	62
$G_{ZnP-DMF-1}$	Graphite	520	150	63
H_2TIPP@CNT-2	GC	599	127.6	64
CoTIPP@CNT-2	GC	485	102.3	64
NiTIPP@CNT-2	GC	529	104	64
CoTAPPCC	Ni foam	210	116	65
$G_{P4-NiPh-THF}$	Graphite	430	140	44
Co(tpfpc)	Carbon paper	960	275	66
Co(ttfphc)	Carbon paper	900	218	66
Co(ttfpdc)	Carbon paper	860	214	66
Fe-porphyrin polymer	Carbon paper	678	363	67
Co-porphyrin polymer	Carbon paper	437	195	67
Ni-porphyrin polymer	Carbon paper	644	345	67
Cu-porphyrin polymer	Carbon paper	436	236	67
Poly[CoOTPc]+KB	GC	390	80	68
Poly[CoOTPc]	GC	515	98	68
GC_{P1-CB}	GC	770	135	27
GC_{CB-AP}	GC	600	150	This work

CONCLUSION

A symmetrically substituted tetraazaporphyrin was tested as water-splitting electrocatalyst in a wide pH range. The electrodes modified with this porphyrazine were manufactured using two different methods. The best results were observed for the GC_{CB-AP} electrode obtained with the catalyst ink-based method. In strong alkaline medium it exhibits a η_{HER} value of 0.6 V (at $j = -10$ mA cm^{-2}) and a Tafel slope of 0.15 V dec^{-1}. The water electrolysis data collected by testing the electrodes modified with the solution-based method were used in statistical analysis,

which revealed a statistically significant correlation between the pH and the OER overpotential. Furthermore, the porphyrazine was investigated in gas phase by performing quantum chemical calculations. Overall, the three hybrid-DFT methods yielded comparable values for the key parameters of the molecular structure.

The results derived from experimental and theoretical approaches may function as a foundation from which extensive studies can be initiated, including the modeling of the chemistry and thermodynamics of redox processes and electron transfer, or more complex reaction mechanisms such as solute diffusion or surface diffusion.

The present work outlines the tetraazaporphyrin's applicative potential in the water-splitting domain and contributes to improving the current understanding of its features.

SUPPLEMENTARY MATERIAL

Additional data and information are available electronically at the pages of journal website: https://www.shd-pub.org.rs/index.php/JSCS/article/view/13305, or from the corresponding author on request.

Acknowledgements. The authors would like to thank Dr. Eugenia Fagadar-Cosma for the purchasing and providing of the porphyrazine and Dr. Florina Stefania Rus from INCEMC Timisoara (Romania) for performing the Raman analysis.

ИЗВОД

ЕЛЕКТРОКАТАЛИТИЧКА СВОЈСТВА ЗА РАЗЛАГАЊЕ ВОДЕ И РАЧУНАРСКА КАРАКТЕРИЗАЦИЈА СИМЕТРИЧНО СУПСТИТУИСАНОГ ПОРФИРАЗИНА

MARINA ALEXANDRA TUDORAN и BOGDAN-OVIDIU TARANU

National Institute of Research and Development for Electrochemistry and Condensed Matter, Dr. A. Paunescu Podeanu Street No. 144, 300569 Timisoara, Romania

Порфиразин 2,7,12,17-тетра-*трет*-бутил-5,10,15,20-тетрааза-21*H*,23*H*-порфин је испитиван у погледу његове електрокаталитичке активности разлагања воде у широком pH опсегу. За производњу електрода на бази овог једињења коришћене су две различите методе: метода заснована на раствору и метода заснована на суспензији катализатора. Каталитички најактивнија електрода је добијена методом заснованом на суспензији катализатора. У раствору KOH концентрације 1 mol L^{-1} ова електрода показује пренапетост реакције издвајања H_2 од 0,6 V и Тафелов нагиб од 0,15 V dec^{-1}. Статистичка анализа је показала значајну корелацију између pH и пренапетости реакције издвајања O_2. Квантно-хемијски прорачуни су извршени како би се добило детаљније разумевање својстава порфиразина.

(Примљено 23. марта, ревидирано 19. јуна, прихваћено 10. јула 2025)

REFERENCES

1. G. Singh, S. Chandra, *Electrochem. Sci. Adv.* **3** (2023) e2100149 (https://doi.org/10.1002/elsa.202100149)
2. A. Ghosh, J. Fitzgerald, P. G. Gassman, J. Almlof, *Inorg. Chem.* **33** (1994) 6057 (https://doi.org/10.1021/ic00104a014)

3. P. A. Pinheiro, G. F. M. Pereira, L. O. Cunha, J. P. S. C. Leal, M. E. Alvarenga, F. T. Martins, H. Silva, J. L. S. Milani, T. T. Tasso, *Photochem. Photobio. Sci.* **23** (2024) 1757 (https://doi.org/10.1007/s43630-024-00629-z)
4. D.-P. Medina, J. Fernandez-Ariza, M. Urbani, F. Sauvage, T. Torres, M. S. Rodriguez--Morgade, *Molecules* **26** (2021) 2129 (https://doi.org/10.3390/molecules26082129)
5. T. Koczorowski, B. Wicher, R. Krakowiak, K. Mylkie, A. Marusiak, E. Tykarska, M. Ziegler-Borowska, *Materials* **15** (2022) 7264 (https://doi.org/10.3390/ma15207264)
6. H. N. Silva, S. H. Toma, A. L. Hennemann, J. M. Goncalves, M. Nakamura, K. Araki, M. M. Toyama, H. E. Toma, *Molecules* **27** (2022) 4598 (https://doi.org/10.3390/molecules27144598)
7. S. A. Lermontova, T. S. Lyubova, I. S. Grigoryev, V. A. Ilichev, V. I. Plekhanov, N. Y. Shilyagina, I. V. Balalaeva, V. P. Boyarskiy, L. G. Klapshina, *Russ. J. Gen. Chem.* **93** (2023) S672 (https://doi.org/10.1134/S1070363223160053)
8. A. M. Alsharari, A. A. A. Darwish, M. Rashad, *Opt. Mater.* **105** (2020) 109870 (https://doi.org/10.1016/j.optmat.2020.109870)
9. N. Kobayashi, S. Nakajima, H. Ogata, T. Fukuda, *Chem.-Eur. J.* **10** (2004) 6294 (https://doi.org/10.1002/chem.200400275)
10. S. Yamazaki, M. Asahi, N. Taguchi, T. Ioroi, *J. Electroanal. Chem.* **848** (2019) 113321 (https://doi.org/10.1016/j.jelechem.2019.113321)
11. I. Fringu, D. Anghel, I. Fratilescu, C. Epuran, M. Birdeanu, E. Fagadar-Cosma, *Biomedicines* **12** (2024) 770 (https://doi.org/10.3390/biomedicines12040770)
12. A. A. Al-Zubaidi, A. A. A. Elfaki, A. A. A. Darwish, *J. Mol. Struct.* **1218** (2020) 128499 (https://doi.org/10.1016/j.molstruc.2020.128499)
13. I. Slobodkin, E. Davydova, M. Sananis, A. Breytus, A. Rothschild, *Nat. Mater.* **23** (2024) 398 (https://doi.org/10.1038/s41563-023-01767-y)
14. N. S. Hassan, A. A. Jalil, S. Rajendran, N. F. Khusnun, M. B. Bahari, A. Johari, M. J. Kamaruddin, M. Ismail, *Int. J. Hydrogen Energy* **52** (2024) 420 (https://doi.org/10.1016/j.ijhydene.2023.09.068)
15. J. E. Lee, I. Shafiq, M. Hussain, S. S. Lam, G. H. Rhee, Y.-K. Park, *Int. J. Hydrogen Energy* **47** (2022) 4346 (https://doi.org/10.1016/j.ijhydene.2021.11.065)
16. H. Sun, X. Xu, H. Kim, W. Jung, W. Zhou, Z. Shao, *Energy Environ. Mater.* **6** (2023) e12441 (https://doi.org/10.1002/eem2.12441)
17. Y. Yao, J. Lyu, X. Li, C. Chen, F. Verpoort, J. Wang, Z. Pan, Z. Kou, *DeCarbon* **5** (2024) 100062 (https://doi.org/10.1016/j.decarb.2024.100062)
18. X. Xie, L. Du, L. Yan, S. Park, Y. Qiu, J. Sokolowski, W. Wang, Y. Shao, *Adv. Funct. Mater.* **32** (2022) 2110036 (https://doi.org/10.1002/adfm.202110036)
19. C. Tian, R. Liu, Y. Zhang, W. Yang, B. Wang, *Nano Res.* **17** (2024) 982 (https://doi.org/10.1007/s12274-023-6003-5)
20. N. A. Kamaruzaman, W. M. K. W. M. Zin, K. H. Kamarudin, N. M. Saleh, F. Yusoff, *Int. J. Electrochem. Sc.* **18** (2023) 100187 (https://doi.org/10.1016/j.ijoes.2023.100187)
21. Y. Chen, X. Zhao, P. Dong, Y. Zhang, Y. Zou, S. Wang, *New Carbon Mater.* **39** (2024) 1 (https://doi.org/10.1016/S1872-5805(24)60831-0)
22. E. Nikoloudakis, A. G. Coutsolelos, E. Stratakis, *Energy Fuel* **38** (2024) 19222 (https://doi.org/10.1021/acs.energyfuels.4c03322)
23. L. R. Snyder, J. J. Kirkland, J. L. Glajch, *Practical HPLC Method Development*, John Wiley & Sons, Hoboken, NJ, 1997 (https://doi.org/10.1002/9781118592014)
24. Z. Szabadai, L. Sbarcea, L. Udrescu, *Analiza fizică și chimică a medicamentului*, Victor Babes publishing house, Timisoara, 2016 (ISBN 978-606-786-020-7)

25. W. Szczolko, T. Koczorowski, B. Wicher, M. Kryjewski, Z. Krakowska, E. Tykarska, T. Goslinski, *Dyes Pigments* **206** (2022) 110607 (https://doi.org/10.1016/j.dyepig.2022.110607)
26. E. Gonca, *J. Coord. Chem.* **70** (2017) 2344 (https://doi.org/10.1080/00958972.2017.1350267)
27. B.-O. Taranu, F. S. Rus, E. Fagadar-Cosma, *Coatings* **14** (2024) 1 (https://doi.org/10.3390/coatings14081048)
28. J. Chang, Q. Lv, G. Li, J. Ge, C. Liu, W. Xing, *Appl. Catal., B* **204** (2017) 486 (https://doi.org/10.1016/j.apcatb.2016.11.050)
29. Y. Ge, Z. Lyu, M. Marcos-Hernandez, D. Villagran, *Chem. Sci.* **13** (2022) 8597 (https://doi.org/10.1039/D2SC01250B)
30. B.-R. Wulan, S.-S. Yi, S.-J. Li, Y.-X. Duan, J.-M. Yan, X.-B. Zhang, Q. Jiang, *Mater. Chem. Front.* **2** (2018) 1799 (https://doi.org/10.1039/C8QM00239H)
31. A. Raveendran, M. Chandran, R. Dhanusuraman, *RSC Adv.* **13** (2023) 3843 (https://doi.org/10.1039/D2RA07642J)
32. O. van der Heijden, S. Park, R. E. Vos, J. J. J. Eggebeen, M. T. M. Koper, *ACS Energy Lett.* **9** (2024) 1871 (https://doi.org/10.1021/acsenergylett.4c00266)
33. M. K. Mongale, D. A. Isabirye, M. M. Kabanda, T. O. Aiyelabola, E. E. Ebenso, *Asian J. Chem.* **29** (2017) 496 (https://doi.org/10.14233/ajchem.2017.20205)
34. J. H. Luo, Q. S. Li, L. N. Yang, Z. Z. Sun, Z. S. Li, *RSC Adv.* **4** (2014) 20200 (https://doi.org/10.1039/C4RA02204A)
35. M. E. Ayalew, *J. Biophys. Chem.* **13** (2022) 29 (https://doi.org/10.4236/jbpc.2022.133003)
36. K. Arumugam, U. Becker, *Minerals* **4** (2014) 345 (https://doi.org/10.3390/min4020345)
37. S. Sarfaraz, M. Yar, A. Hussain, A. Lakhani, A. Gulzar, M. Ans, U. Rashid, M. Hussain, S. Muhammad, I. Bayach, N.S. Sheikh, K. Ayub, *ACS Omega* **8** (2023) 36493 (https://doi.org/10.1021/acsomega.3c05477)
38. S. Sarfaraz, M. Yar, N. S. Sheikh, I. Bayach, K. Ayub, *ACS omega* **8** (2023) 14077 (https://doi.org/10.1021/acsomega.3c00721)
39. V. K. Kumar, R. Sangeetha, D. Barathi, R. Mathammal, N. Jayamani, *Spectrochim. Acta, A* **118** (2014) 663 (https://doi.org/10.1016/j.saa.2013.08.089)
40. X. Li, Y. Du, L. Ge, C. Hao, Y. Bai, Z. Fu, Y. Lu, Z. Cheng, *Adv. Funct. Mater.* **33** (2023) 1 (https://doi.org/10.1002/adfm.202210194)
41. B. O. Taranu, S. D. Novaconi, M. Ivanovici, J. N. Goncalves, F. S. Rus, *Appl. Sci. (Basel)* **12** (2022) 6821 (https://doi.org/10.3390/app12136821)
42. M. L. F. Ciriaco, M. I. Silva-Pereira, M. R. Nunes, F. M. Costa, *Port. Electrochim. Acta* **17** (1999) 149 (https://doi.org/10.4152/pea.199902149)
43. A. Karmakar, S. Kundu, *Mater. Today Energy* **33** (2023) 1 (https://doi.org/10.1016/j.mtener.2023.101259)
44. B.-O. Taranu, E. Fagadar-Cosma, P. Sfirloaga, M. Poienar, *Energies* **16** (2023) 1 (https://doi.org/10.3390/en16031212)
45. B.-O. Taranu, P. Vlazan, P. Svera, M. Poienar, P. Sfirloaga, *J. Alloy. Compd.* **892** (2021) 162239 (https://doi.org/10.1016/j.jallcom.2021.162239)
46. M. Poienar, P. Svera, B.-O. Taranu, C. Ianasi, P. Sfirloaga, G. Buse, P. Veber, P. Vlazan, *Crystals* **12** (2022) 1803 (https://doi.org/10.3390/cryst12121803)
47. C. Wan, Y. Ling, S. Wang, H. Pu, Y. Huang, X. Duan, *ACS Central Sci.* **10** (2024) 658 (https://doi.org/10.1021/acscentsci.3c01439)

48. F. Bao, E. Kemppainen, I. Dorbandt, R. Bors, F. Xi, R. Schlatmann, R. van de Krol, S. Calnan, *ChemElectroChem* **8** (2021) 195 (https://doi.org/10.1002/celc.202001436)
49. Z. Y. Wu, B. C. Hu, P. Wu, H. W. Liang, Z. L. Yu, Y. Lin, Y. R. Zheng, Z. Li, S. H. Yu, *NPG Asia Mater.* **8** (2016) e288 (https://doi.org/10.1038/am.2016.87)
50. S. Seo, K. Lee, M. Min, Y. Cho, M. Kim, H. Lee, *Nanoscale* **9** (2017) 3969 (https://doi.org/10.1039/c6nr09428g)
51. W. Zhang, W. Lai, R. Cao, *Chem. Rev.* **117** (2017) 3717 (https://doi.org/10.1021/acs.chemrev.6b00299)
52. A. Facchin, C. Durante, *Adv. Sustain. Syst.* **6** (2022) 2200111 (https://doi.org/10.1002/adsu.202200111)
53. B. O. Taranu, E. Fagadar-Cosma, *Processes* **10** (2022) 611 (https://doi.org/10.3390/pr10030611)
54. B.-O. Taranu, *J. Serb. Chem. Soc.* **90** (2025) 447 (https://doi.org/10.2298/JSC241004105T)
55. S. Cui, M. Qian, X. Liu, Z. Sun, P. Du, *ChemSusChem* **9** (2016) 2365 (https://doi.org/10.1002/cssc.201600452)
56. H. Jia, Y. Yao, Y. Gao, D. Lu, P. Du, *Chem. Commun.* **52** (2016) 13483 (https://doi.org/10.1039/C6CC06972J)
57. J. Liu, C. Wang, H. Sun, H. Wang, F. Rong, L. He, Y. Lou, S. Zhang, Z. Zhang, M. Du, *Appl. Catal., B* **279** (2020) 1 (https://doi.org/10.1016/j.apcatb.2020.119407)
58. A. Wang, L. Cheng, X. Shen, W. Zhu, L. Li, *Dyes Pigments* **181** (2020) 1 (https://doi.org/10.1016/j.dyepig.2020.108568)
59. G. Cai, L. Zeng, L. He, S. Sun, Y. Tong, J. Zhang, *Chem. Asian J.* **15** (2020) 1963 (https://doi.org/10.1002/asia.202000083)
60. A. Wang, L. Cheng, W. Zhao, X. Shen, W. Zhu, *J. Colloid Interf. Sci.* **579** (2020) 598 (https://doi.org/10.1016/j.jcis.2020.06.109)
61. L. Chen, R. U. R. Sagar, J. Chen, J. Liu, S. Aslam, F. Nosheen, T. Anwar, N. Hussain, X. Hou, T. Liang, *Int. J. Hydrogen Energy* **46** (2021) 19338 (https://doi.org/10.1016/j.ijhydene.2021.03.075)
62. Q. Pan, X. Chen, H. Liu, W. Gan, N. Ding, Y. Zhao, *Mater. Chem. Front.* **5** (2021) 4596 (https://doi.org/10.1039/D1QM00285F)
63. B.-O. Taranu, E. Fagadar-Cosma, *Nanomaterials (Basel)* **12** (2022) 1 (https://doi.org/10.3390/nano12213788)
64. Y. Wang, D. Song, J. Li, Q. Shi, J. Zhao, Y. Hu, F. Zeng, N. Wang, *Inorg. Chem.* **61** (2022) 10198 (https://doi.org/10.1021/acs.inorgchem.2c01415)
65. Y. Dou, X. Yang, Q. Wang, Z. Yang, A. Wang, L. Zhao, W. Zhu, *J. Colloid Interf. Sci.* **644** (2023) 256 (https://doi.org/10.1016/j.jcis.2023.04.082)
66. S. Sahoo, E. K. Johnson, X. Wei, S. Zhang, C. W. Machan, *Energy Adv.* **3** (2024) 2280 (https://doi.org/10.1039/D4YA00257A)
67. N. Ocuane, Y. Ge, C. Sandoval-Pauker, D. Villagran, *Dalton Trans.* **53** (2024) 2306 (https://doi.org/10.1039/D3DT03371F)
68. N. Kousar, Giddaerappa, L. K. Sannegowda, *Int. J. Hydrogen Energy* **50** (2024) 37 (https://doi.org/10.1016/j.ijhydene.2023.06.296).

Journal of the Serbian Chemical Society
JSCS@tmf.bg.ac.rs • www.shd.org.rs/JSCS
J. Serb. Chem. Soc. 90 (9) S356–S371 (2025) *Supplementary material*

SUPPLEMENTARY MATERIAL TO

Water-splitting electrocatalytic properties and computational characterization of a symmetrically substituted porphyrazine

MARINA ALEXANDRA TUDORAN and BOGDAN-OVIDIU TARANU*

National Institute of Research and Development for Electrochemistry and Condensed Matter, Dr. A. Paunescu Podeanu Street No. 144, 300569 Timisoara, Romania

J. Serb. Chem. Soc. 90 (9) (2025) 1089–1104

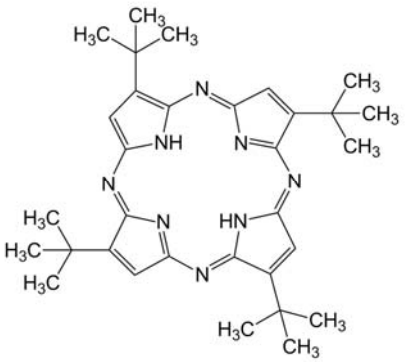

Scheme S-1. The chemical structure of 2,7,12,17-tetra-tert-butyl-5,10,15,20-tetraaza-21H,23H-porphine.

EQUATIONS

Equations employed in the electrochemical study

Equations (S-1) to (S-6) have been used during the study of the water-splitting electrocatalytic properties of 2,7,12,17-tetra-tert-butyl-5,10,15,20-tetraaza-21H,23H-porphine.[1-5]

Equation (S-1) is employed to represent the electrochemical potential value measured *vs.* the Ag/AgCl(sat. KCl) reference electrode in terms of the Reversible Hydrogen Electrode (RHE).

$$E_{RHE} = E_{Ag/AgCl(sat.\ KCl)} + 0.059\ \mathrm{pH} + E^{\circ}_{Ag/AgCl(sat.\ KCl)} \quad \text{(S-1)}$$

* Corresponding author. E-mail: b.taranu84@gmail.com

where E_{RHE} / V is the converted potential *vs.* RHE; $E_{Ag/AgCl(sat.\ KCl)}$ / V is the measured potential *vs.* the Ag/AgCl (sat. KCl) reference electrode and $E°_{Ag/AgCl(sat.\ KCl)}$ = 0.197 V.

Equation (S-2) is used to calculate the OER overpotential.

$$\eta_{OER} = E_{RHE} - 1.23 \quad \text{(S-2)}$$

where η_{OER} / V is the oxygen evolution overpotential.

Equation (S-3) is used to calculate the HER overpotential.

$$\eta_{HER} = |E_{RHE}| - 0 \quad \text{(S-3)}$$

where η_{HER} / V is the H_2 evolution overpotential.

Equation (S-4) is used to calculate the Tafel slope.

$$\eta = b \times \log(j) + a \quad \text{(S-4)}$$

where η / V is the overpotential; j / A cm^{-2} is the current density; b / V dec^{-1} is the Tafel slope and a is the exchange current density.

Equation (S-5) is used to calculate the capacitive current density.

$$j_{dl} = \frac{j_a + j_c}{2} \quad \text{(S-5)}$$

where j_{dl} / A cm^{-2} is the capacitive current density; j_a / A cm^{-2} is the absolute value of the anodic j at a given scan rate and at an E value from the range with only double-layer adsorption and desorption features and j_c / A cm^{-2} is the absolute value of the cathodic j at a given scan rate and at an E value from the range with only double-layer adsorption and desorption features.

Equation (S-6) is employed to estimate the electrochemically active surface area based on the electric double-layer capacitance. The latter is usually measured by recording cyclic voltammograms at various scan rate values followed by the determination of the slope of the curve from the graphical representation of the capacitive current density *vs.* the scan rate.

$$ECSA = \frac{C_{dl} \times S_{geom}}{C_s} \quad \text{(S-6)}$$

where $ECSA$ / cm^2 is the electrochemically active surface area; C_{dl} / F cm^{-2} is the electric double-layer capacitance; S_{geom} / cm^2 is the geometric surface of the electrode and C_s / F cm^{-2} is the specific capacitance of a smooth electrode surface.[6]

Equations employed in the theoretical study

The vertical ionization potential (*VIP*) and electron affinity (*VEA*) of a neutral system are calculated using the ΔSCF formalism, as the difference between the electronic energy of the cation and the electronic energy of the neutral molecule (Equation (S-7)), and the difference between the electronic energy of the neutral molecule and the electronic energy of the anion (Equation (S-8)), respectively.[7-9]

$$VIP = E_{cation} - E_{neutral} \quad \text{(S-7)}$$

$$VEA = E_{neutral} - E_{anion} \quad \text{(S-8)}$$

where $E_{neutral}$ is the electronic energy of the neutral molecule; E_{cation} is the electronic energy of the cation and E_{anion} is the electronic energy of the anion – the last two being evaluated at the geometry of the neutral molecule.

Polarizability (α):

$$\alpha = \frac{1}{3}\left(\alpha_{xx} + \alpha_{yy} + \alpha_{zz}\right) \quad \text{(S-9)}$$

Anisotropy of polarizability ($\Delta\alpha$):

$$\Delta\alpha = \frac{1}{\sqrt{2}}\left[\left(\alpha_{xx} - \alpha_{yy}\right)^2 + \left(\alpha_{yy} - \alpha_{zz}\right)^2 + (\alpha_{zz} - \alpha_{xx})^2 + 6\alpha_{xz}^2 + 6\alpha_{xy}^2 + 6\alpha_{yz}^2\right]^{1/2} \quad \text{(S-10)}$$

First hyperpolarizability (β):

$$\beta = \left[\left(\beta_{xxx} + \beta_{xyy} + \beta_{xzz}\right)^2 + \left(\beta_{yyy} + \beta_{yzz} + \beta_{yxx}\right)^2 + \left(\beta_{zzz} + \beta_{zxx} + \beta_{zyy}\right)^2\right]^{\frac{1}{2}} \quad \text{(S-11)}$$

To convert the values of polarizability, anisotropy of polarizability and hyperpolarizability measured in atomic units (a.u.) to electrostatic units (e.s.u.), the following formulas were used: for α, 1 a.u. = 0.1482×10^{-24} e.s.u., and for β, 1 a.u. = 8.6393×10^{-33}.

The equations were calculated using the x, y, z components from Gaussian 03W output, which are presented in Table S-V.

QUANTUM CHEMICAL CALCULATIONS

TABLE S-I. Calculated structural parameters of the optimized 2,7,12,17-tetra-tert-butyl-5,10,15,20-tetraaza-21H,23H-porphine

		Tetra-tert-butyl-tetraazaporphyrin			*Unfunctionalized porphyrazine*[a]
		B3LYP/ STO-3G	**B3PW91/ STO-3G**	**MPW1PW91/ STO-3G**	**B3LYP/ 6-31G(d)**
Bond length / Å	$C_{14} - C_{19}$	1.48709	1.48214	1.47895	1.453
	$C_{19} - C_{17}$	1.37053	1.36743	1.36392	1.378
	$C_{19} - C_{25}$	1.54594	1.53946	1.53573	-
	$C_{14} - N_{22}$	1.41549	1.40919	1.40511	1.371
	$C_{14} - N_{16}$	1.38882	1.38374	1.37953	1.323
	$N_{16} - C_{15}$	1.39013	1.38519	1.38099	1.338
	$N_{22} - H_{45}$	1.25823	1.25231	1.24972	-
	$C_{15} - C_{20}$	1.46894	1.46355	1.46111	1.475
	$N_{21} - C_{13}$	1.41526	1.40926	1.40493	1.361
	$C_{20} - H_{44}$	1.09331	1.09219	1.09037	-
Bond angle / °	$C_{17} - C_{19} - C_{14}$	105.51967	105.40852	105.42534	-
	$C_{19} - C_{14} - N_{22}$	110.73804	110.75401	110.76539	-
	$C_{14} - N_{16} - C_{15}$	113.74181	113.76580	113.82715	123.1
	$C_{14} - N_{22} - C_{12}$	105.78746	105.88973	105.89271	110.5
	$C_{15} - C_{20} - C_{18}$	107.80646	107.78086	107.71391	-
	$C_{15} - N_{21} - C_{13}$	105.71806	105.79135	105.80913	105.0

[a] Data from Mongale *et al.*[10]

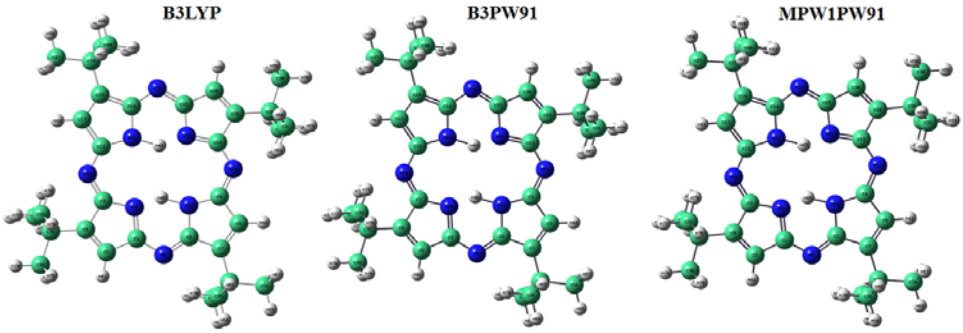

Fig. S-1. Optimized structure and atom labelling of 2,7,12,17-tetra-tert-butyl-5,10,15,20-tetraaza-21H,23H-porphine using STO-3G basis set.

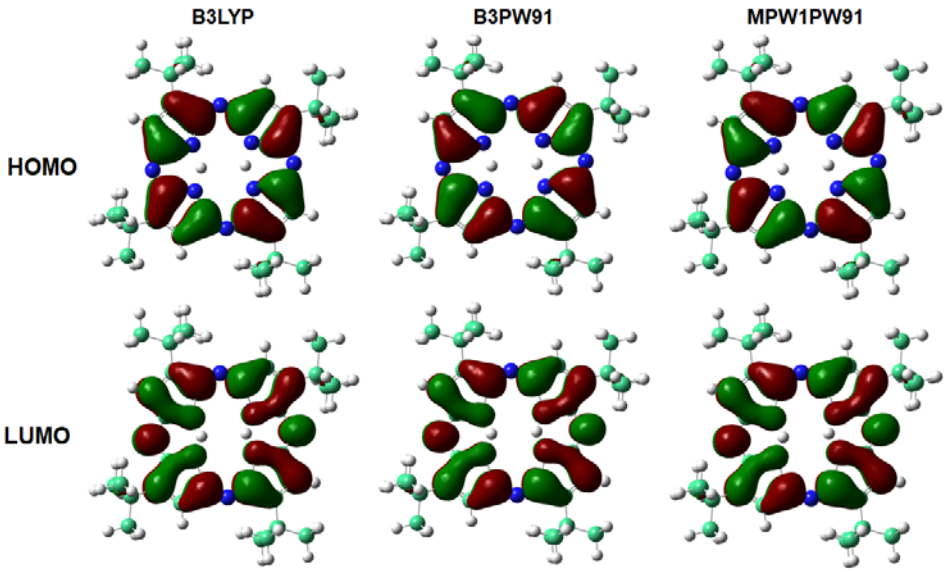

Fig. S-2. The atomic orbital composition of the HOMO and LUMO orbitals for 2,7,12,17-tetra-tert-butyl-5,10,15,20-tetraaza-21H,23H-porphine using 6-31G basis set.

TABLE S-II. Calculated energy values of HOMO (E_{HOMO}), LUMO (E_{LUMO}), energy gap (E_{gap}), vertical ionization potential and electron affinity of 2,7,12,17-tetra-tert-butyl-5,10,15,20-tetraaza-21H,23H-porphine.

Parameter	B3LYP/6-31G(d)	B3PW91/6-31G(d)	MPW1PW91/6-31G(d)
E_{HOMO} / eV	-5.497791	-5.699699	-5.619426
E_{LUMO} / eV	-3.194618	-3.161420	-3.287953
E_{gap} / eV	2.303173	2.538279	2.331473
VIP / eV	6.670086	6.781692	6.738326
VEA / eV	2.006947	2.10314	2.094558

TABLE S-III. Calculated thermodynamic parameters of 2,7,12,17-tetra-tert-butyl-5,10,15,20-tetraaza-21H,23H-porphine

Parameter		B3LYP/STO-3G	B3PW91/STO-3G	MPW1PW91/STO-3G
Zero-point vibrational energy / kcal mol^{-1}		466.29026	470.14528	474.06613
Total Electronic Energy with Zero-point correction		-1661.194191	-1660.787035	-1661.050020
Total Electronic Energy with Thermal energies		-1661.155169	-1660.748346	-1661.011627
Total Electronic Energy with Enthalpies		-1661.154225	-1660.747402	-1661.010683
Dipole moment / Debye		0.001500	0.000714	0.004386
Rotational constant / GHz	*X*	0.08238	0.08292	0.08339
	Y	0.07571	0.07614	0.07655
	Z	0.04092	0.04116	0.04139
Thermal energy / kcal mol^{-1}	**Total**	490.776	494.423	498.158
	Translational	0.889	0.889	0.889
	Rotational	0.889	0.889	0.889
	Vibrational	488.999	492.645	496.381
Constant volume heat capacity / cal mol-Kelvin^{-1}	**Total**	152.327	150.932	149.791
	Translational	2.981	2.981	2.981
	Rotational	2.981	2.981	2.981
	Vibrational	146.365	144.970	143.829
Entropy / cal mol-Kelvin^{-1}	**Total**	229.699	228.316	226.791
	Translational	44.736	44.736	44.736
	Rotational	38.374	38.356	38.339
	Vibrational	146.589	145.224	143.715

TABLE S-IV. Natural charge, population, and electronic configuration of 2,7,12,17-tetra-tert-butyl-5,10,15,20-tetraaza-21H,23H-porphine

	Atom	Natural charge	Natural population				Natural electronic configuration
			Core	*Valence*	*Rydberg*	*Total*	
B3LYP/6-31G(d)	**C14**	0.42413	1.99918	3.55160	0.02509	5.57587	[core]2S$^{(0.83)}$2p$^{(2.72)}$3p$^{(0.02)}$3d$^{(0.01)}$
	C19	-0.03832	1.99894	4.02020	0.01918	6.03832	[core]2S$^{(0.90)}$2p$^{(3.12)}$3p$^{(0.01)}$
	C17	-0.24989	1.99888	4.23900	0.01201	6.24989	[core]2S$^{(0.98)}$2p$^{(3.26)}$3p$^{(0.01)}$
	C25	-0.06437	1.99913	4.05314	0.01210	6.06437	[core]2S$^{(0.93)}$2p$^{(3.13)}$3p$^{(0.01)}$
	C15	0.41632	1.99925	3.55795	0.02647	5.58368	[core]2S$^{(0.84)}$2p$^{(2.72)}$3p$^{(0.02)}$3d$^{(0.01)}$
	C20	-0.26295	1.99884	4.25219	0.01191	6.26295	[core]2S$^{(0.97)}$2p$^{(3.28)}$3p$^{(0.01)}$
	C13	0.44709	1.99917	3.52796	0.02578	5.55291	[core]2S$^{(0.82)}$2p$^{(2.71)}$3p$^{(0.02)}$3d$^{(0.01)}$
	N22	-0.63946	1.99931	5.62598	0.01417	7.63946	[core]2S$^{(1.36)}$2p$^{(4.26)}$3p$^{(0.01)}$
	N16	-0.47341	1.99940	5.46035	0.01366	7.47341	[core]2S$^{(1.41)}$2p$^{(4.05)}$3p$^{(0.01)}$3d$^{(0.01)}$
	N21	-0.64084	1.99932	5.62720	0.01432	7.64084	[core]2S$^{(1.37)}$2p$^{(4.26)}$3p$^{(0.01)}$
	H44	0.25980	0.00000	0.73953	0.00067	0.74020	1S$^{(0.74)}$
	H41	0.25979	0.00000	0.73954	0.00067	0.74021	1S$^{(0.74)}$
B3PW91/6-31G(d)	**C14**	0.42194	1.99918	3.55368	0.02519	5.57806	[core]2S$^{(0.83)}$2p$^{(2.73)}$3p$^{(0.02)}$3d$^{(0.01)}$
	C19	-0.03970	1.99895	4.02155	0.01920	6.03970	[core]2S$^{(0.89)}$2p$^{(3.13)}$3p$^{(0.01)}$
	C17	-0.25715	1.99888	4.24619	0.01208	6.25715	[core]2S$^{(0.98)}$2p$^{(3.27)}$3p$^{(0.01)}$
	C25	-0.07279	1.99913	4.06194	0.01172	6.07279	[core]2S$^{(0.92)}$2p$^{(3.14)}$3p$^{(0.01)}$
	C15	0.41300	1.99925	3.56120	0.02655	5.58700	[core]2S$^{(0.97)}$2p$^{(3.28)}$3p$^{(0.01)}$
	C20	-0.27005	1.99885	4.25913	0.01208	6.27005	[core]2S$^{(0.82)}$2p$^{(2.71)}$3p$^{(0.02)}$3d$^{(0.01)}$
	C13	0.44546	1.99917	3.52938	0.02599	5.55454	[core]2S$^{(1.36)}$2p$^{(4.27)}$3p$^{(0.01)}$
	N22	-0.63824	1.99930	5.62433	0.01461	7.63824	[core]2S$^{(1.41)}$2p$^{(4.05)}$3p$^{(0.01)}$3d$^{(0.01)}$
	N16	-0.46988	1.99939	5.45645	0.01403	7.46988	[core]2S$^{(1.41)}$2p$^{(4.05)}$3p$^{(0.01)}$3d$^{(0.01)}$
	N21	-0.63983	1.99932	5.62573	0.01479	7.63983	[core]2S$^{(1.36)}$2p$^{(4.26)}$3p$^{(0.01)}$
	H44	0.26763	0.00000	0.73172	0.00065	0.73237	1S$^{(0.73)}$
	H41	0.26763	0.00000	0.73172	0.00065	0.73237	1S$^{(0.73)}$
MPW1PW91/6-31G(d)	**C14**	0.42661	1.99918	3.54854	0.02566	5.57339	[core]2S$^{(0.82)}$2p$^{(2.72)}$3p$^{(0.02)}$3d$^{(0.01)}$
	C19	-0.03982	1.99895	4.02124	0.01963	6.03982	[core]2S$^{(0.89)}$2p$^{(3.13)}$3p$^{(0.01)}$
	C17	-0.25830	1.99888	4.24700	0.01242	6.25830	[core]2S$^{(0.98)}$2p$^{(3.27)}$3p$^{(0.01)}$
	C25	-0.07408	1.99913	4.06313	0.01183	6.07408	[core]2S$^{(0.92)}$2p$^{(3.14)}$3p$^{(0.01)}$
	C15	0.41772	1.99925	3.55592	0.02710	5.58228	[core]2S$^{(0.83)}$2p$^{(2.73)}$3p$^{(0.02)}$3d$^{(0.01)}$
	C20	-0.27099	1.99884	4.25972	0.01243	6.27099	[core]2S$^{(0.97)}$2p$^{(3.29)}$3p$^{(0.01)}$
	C13	0.45025	1.99917	3.52411	0.02648	5.54975	[core]2S$^{(0.81)}$2p$^{(2.71)}$3p$^{(0.02)}$3d$^{(0.01)}$
	N22	-0.64418	1.99930	5.62998	0.01490	7.64418	[core]2S$^{(1.35)}$2p$^{(4.28)}$3p$^{(0.01)}$
	N16	-0.47430	1.99939	5.46058	0.01434	7.47430	[core]2S$^{(1.40)}$2p$^{(4.06)}$3p$^{(0.01)}$3d$^{(0.01)}$
	N21	-0.64574	1.99931	5.63136	0.01507	7.64574	[core]2S$^{(1.36)}$2p$^{(4.27)}$3p$^{(0.01)}$
	H44	0.26824	0.00000	0.73111	0.00065	0.73176	1S$^{(0.73)}$
	H41	0.26824	0.00000	0.73112	0.00065	0.73176	1S$^{(0.73)}$

TABLE S-V. Polarizability, anisotropy of polarizability, first hyperpolarizability and their components of 2,7,12,17-tetra-tert-butyl-5,10,15,20-tetraaza-21H,23H-porphine

DFT	**B3LYP/6-31G(d)**	**B3PW91/6-31G(d)**	**MPW1PW91/6-31G(d)**
α_{xx}	698.6429625	693.2942536	686.7598955
α_{xy}	-5.9861099	6.0337992	-5.8576367
α_{yy}	673.8693311	668.4113409	662.2107292
α_{xz}	0.0030171	-0.0019439	0.0032899
α_{yz}	0.0047666	0.0079143	0.0004745
α_{zz}	232.3156124	232.2472824	230.59394
α / e.s.u.	$7.927849856 \times 10^{-23}$	$7.874127212 \times 10^{-23}$	$7.80304895 \times 10^{-23}$
$\Delta\alpha$/ e.s.u.	$6.736660958 \times 10^{-23}$	$6.657801463 \times 10^{-23}$	$6.587727255 \times 10^{-23}$
β_{xxx}	-20.3999455	-22.8725558	-5.0131258
β_{xxy}	10.9304831	-4.595366	-2.0657743
β_{xyy}	0.2712327	2.8787402	-2.0809949
β_{yyy}	-25.2245749	-50.1636542	-26.9530695
β_{xxz}	10.4942587	2.7133526	3.1471885
β_{yyz}	11.155742	21.1487207	12.7231708
β_{xzz}	-4.3206832	0.7108711	-2.8860579
β_{yzz}	-4.4919258	-8.0685999	-4.9231165
β_{zzz}	-0.4285422	0.1992636	-0.3401646
β / e.s.u.	$3.233727869 \times 10^{-31}$	$6.046331071 \times 10^{-31}$	$3.337999671 \times 10^{-31}$

ELECTROCHEMICAL STUDY

Voltammetry results

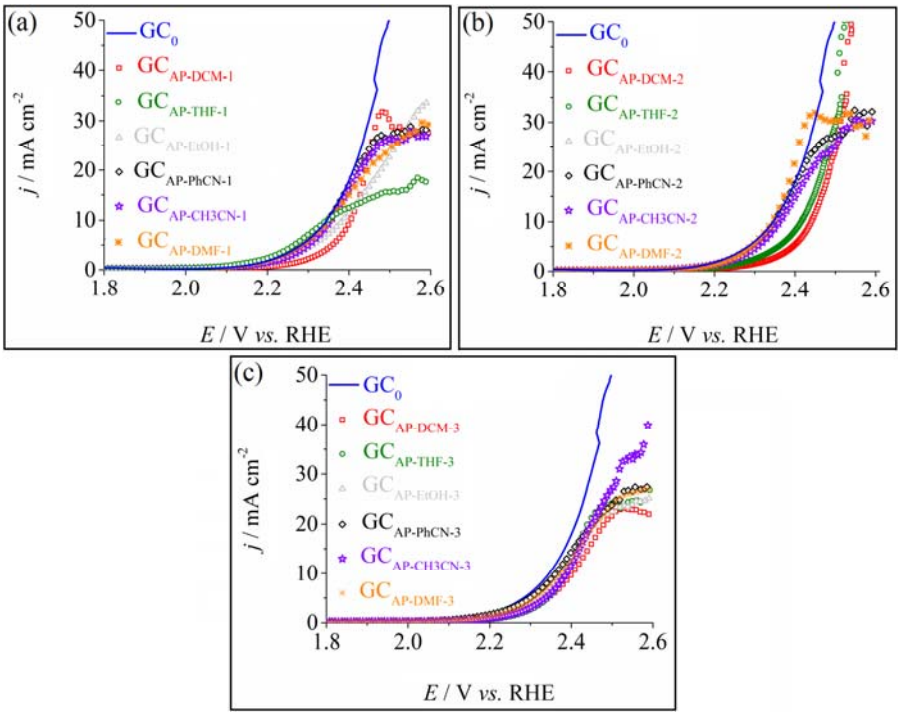

Fig. S-3. Anodic LSVs obtained on GC_0 and on (a) $GC_{AP-DCM-1}$, $GC_{AP-THF-1}$, $GC_{AP-EtOH-1}$, $GC_{AP-PhCN-1}$, $GC_{AP-CH3CN-1}$ and $GC_{AP-DMF-1}$; (b) $GC_{AP-DCM-2}$, $GC_{AP-THF-2}$, $GC_{AP-EtOH-2}$, $GC_{AP-PhCN-2}$, $GC_{AP-CH3CN-2}$ and $GC_{AP-DMF-2}$ and (c) $GC_{AP-DCM-3}$, $GC_{AP-THF-3}$, $GC_{AP-EtOH-3}$, $GC_{AP-PhCN-3}$, $GC_{AP-CH3CN-3}$ and $GC_{AP-DMF-3}$. Electrolyte solution: 0.1 mol L^{-1} H_2SO_4. v = 5 mV s^{-1}.

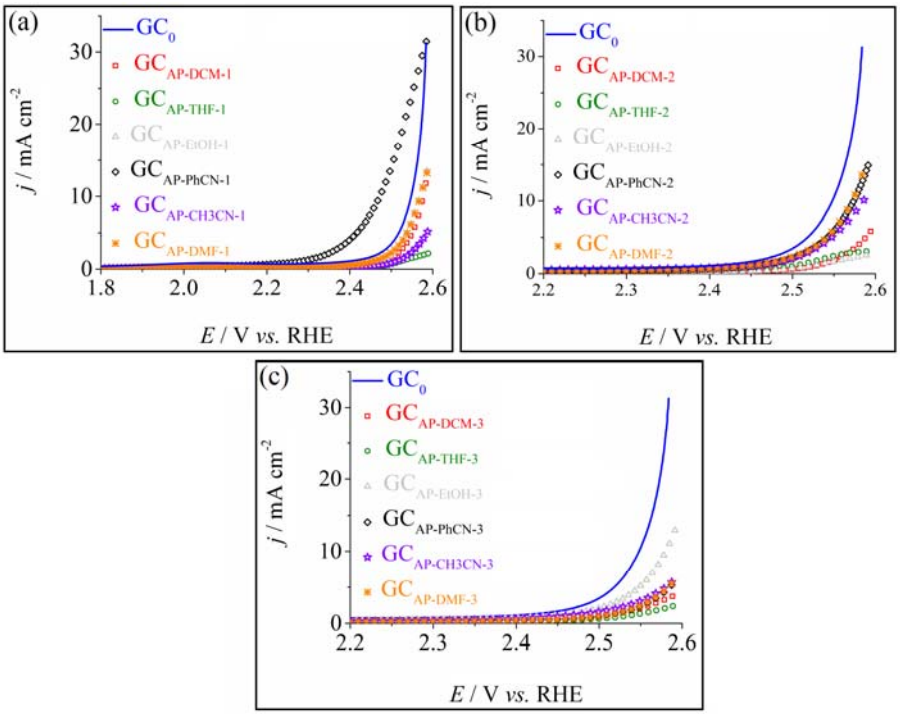

Fig. S-4. Anodic LSVs obtained on GC_0 and on (a) $GC_{AP\text{-}DCM\text{-}1}$, $GC_{AP\text{-}THF\text{-}1}$, $GC_{AP\text{-}EtOH\text{-}1}$, $GC_{AP\text{-}PhCN\text{-}1}$, $GC_{AP\text{-}CH3CN\text{-}1}$ and $GC_{AP\text{-}DMF\text{-}1}$; (b) $GC_{AP\text{-}DCM\text{-}2}$, $GC_{AP\text{-}THF\text{-}2}$, $GC_{AP\text{-}EtOH\text{-}2}$, $GC_{AP\text{-}PhCN\text{-}2}$, $GC_{AP\text{-}CH3CN\text{-}2}$ and $GC_{AP\text{-}DMF\text{-}2}$ and (c) $GC_{AP\text{-}DCM\text{-}3}$, $GC_{AP\text{-}THF\text{-}3}$, $GC_{AP\text{-}EtOH\text{-}3}$, $GC_{AP\text{-}PhCN\text{-}3}$, $GC_{AP\text{-}CH3CN\text{-}3}$ and $GC_{AP\text{-}DMF\text{-}3}$. Electrolyte solution: 0.1 mol L^{-1} KCl. v = 5 mV s^{-1}.

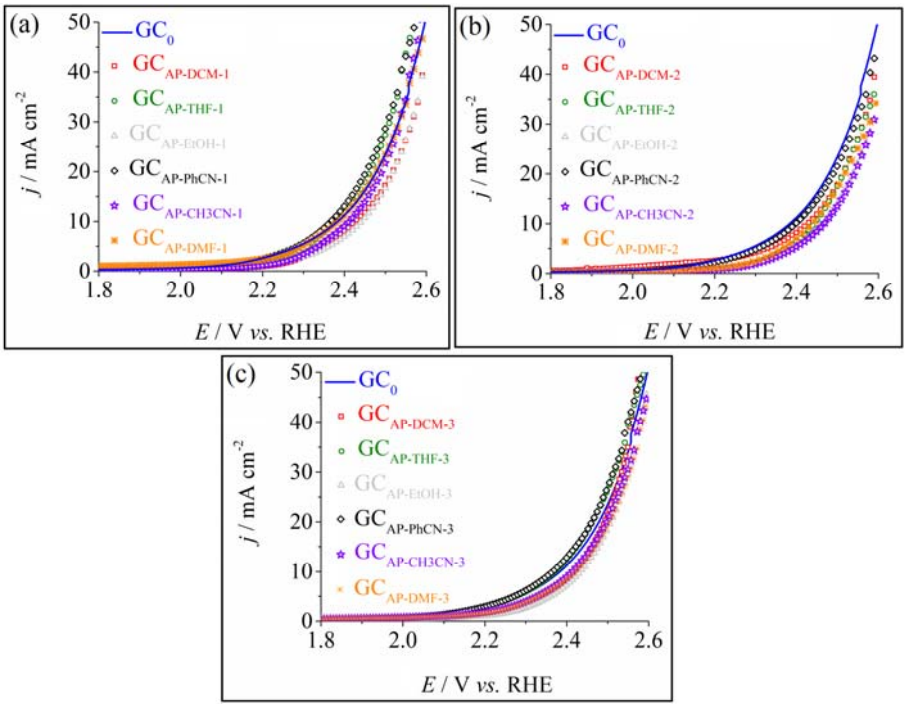

Fig. S-5. Anodic LSVs obtained on GC_0 and on (a) $GC_{AP-DCM-1}$, $GC_{AP-THF-1}$, $GC_{AP-EtOH-1}$, $GC_{AP-PhCN-1}$, $GC_{AP-CH3CN-1}$ and $GC_{AP-DMF-1}$; (b) $GC_{AP-DCM-2}$, $GC_{AP-THF-2}$, $GC_{AP-EtOH-2}$, $GC_{AP-PhCN-2}$, $GC_{AP-CH3CN-2}$ and $GC_{AP-DMF-2}$ and (c) $GC_{AP-DCM-3}$, $GC_{AP-THF-3}$, $GC_{AP-EtOH-3}$, $GC_{AP-PhCN-3}$, $GC_{AP-CH3CN-3}$ and $GC_{AP-DMF-3}$. Electrolyte solution: 1 mol L^{-1} KOH. v = 5 mV s^{-1}.

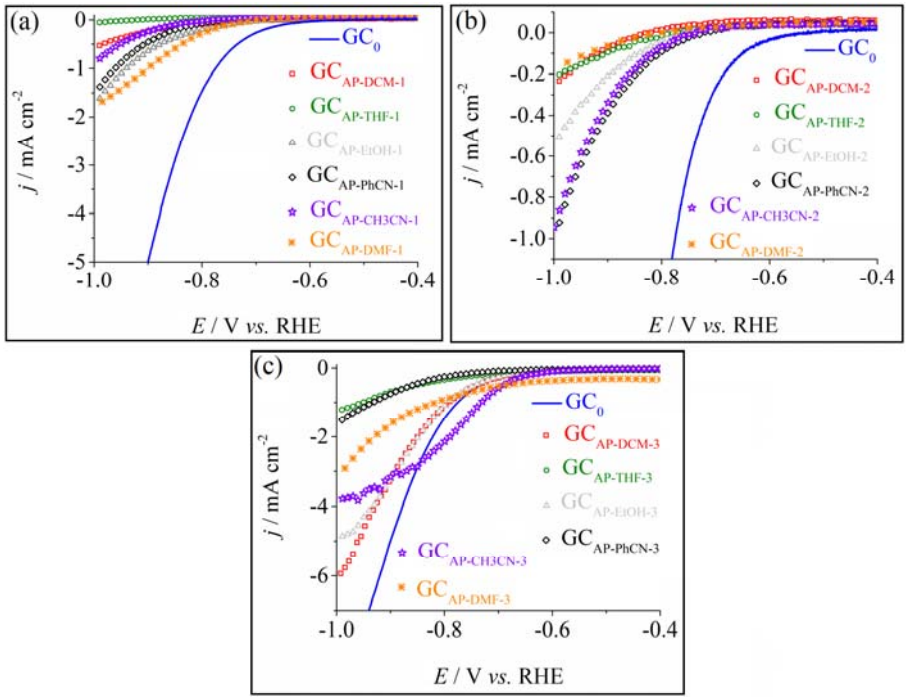

Fig. S-6. Cathodic LSVs obtained on GC_0 and on (a) $GC_{AP\text{-}DCM\text{-}1}$, $GC_{AP\text{-}THF\text{-}1}$, $GC_{AP\text{-}EtOH\text{-}1}$, $GC_{AP\text{-}PhCN\text{-}1}$, $GC_{AP\text{-}CH3CN\text{-}1}$ and $GC_{AP\text{-}DMF\text{-}1}$; (b) $GC_{AP\text{-}DCM\text{-}2}$, $GC_{AP\text{-}THF\text{-}2}$, $GC_{AP\text{-}EtOH\text{-}2}$, $GC_{AP\text{-}PhCN\text{-}2}$, $GC_{AP\text{-}CH3CN\text{-}2}$ and $GC_{AP\text{-}DMF\text{-}2}$ and (c) $GC_{AP\text{-}DCM\text{-}3}$, $GC_{AP\text{-}THF\text{-}3}$, $GC_{AP\text{-}EtOH\text{-}3}$, $GC_{AP\text{-}PhCN\text{-}3}$, $GC_{AP\text{-}CH3CN\text{-}3}$ and $GC_{AP\text{-}DMF\text{-}3}$. Electrolyte solution: 0.1 mol L^{-1} H_2SO_4. v = 5 mV s^{-1}.

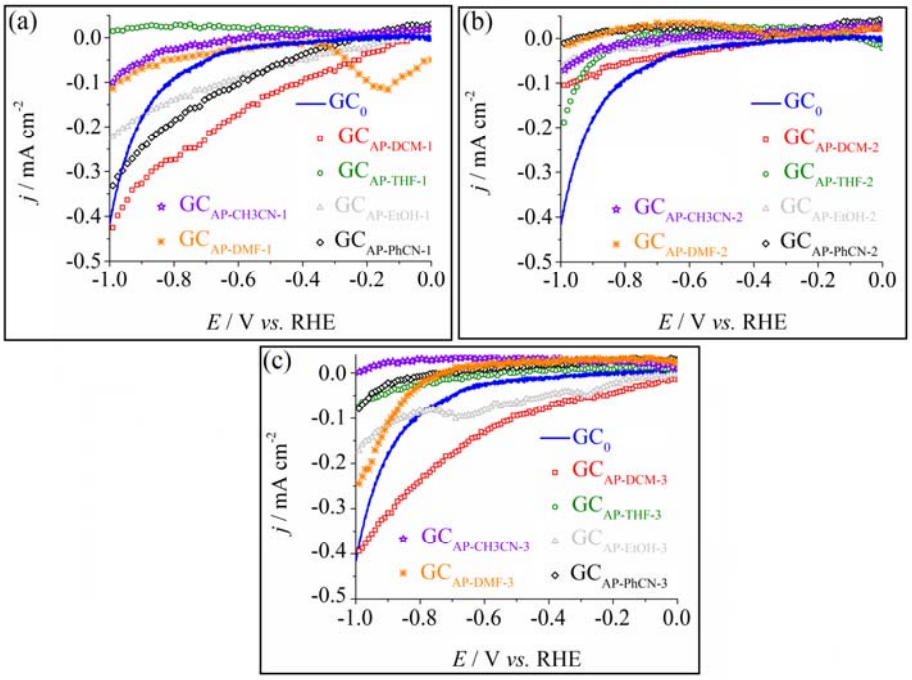

Fig. S-7. Cathodic LSVs obtained on GC_0 and on (a) $GC_{AP\text{-}DCM\text{-}1}$, $GC_{AP\text{-}THF\text{-}1}$, $GC_{AP\text{-}EtOH\text{-}1}$, $GC_{AP\text{-}PhCN\text{-}1}$, $GC_{AP\text{-}CH3CN\text{-}1}$ and $GC_{AP\text{-}DMF\text{-}1}$; (b) $GC_{AP\text{-}DCM\text{-}2}$, $GC_{AP\text{-}THF\text{-}2}$, $GC_{AP\text{-}EtOH\text{-}2}$, $GC_{AP\text{-}PhCN\text{-}2}$, $GC_{AP\text{-}CH3CN\text{-}2}$ and $GC_{AP\text{-}DMF\text{-}2}$ and (c) $GC_{AP\text{-}DCM\text{-}3}$, $GC_{AP\text{-}THF\text{-}3}$, $GC_{AP\text{-}EtOH\text{-}3}$, $GC_{AP\text{-}PhCN\text{-}3}$, $GC_{AP\text{-}CH3CN\text{-}3}$ and $GC_{AP\text{-}DMF\text{-}3}$. Electrolyte solution: 0.1 mol L^{-1} KCl. v = 5 mV s^{-1}.

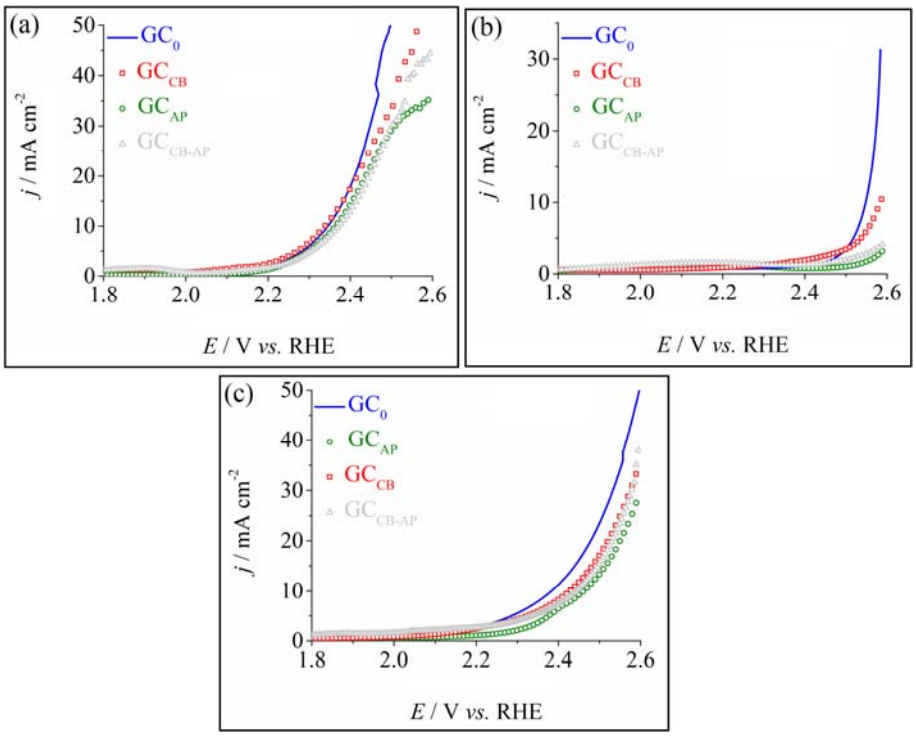

Fig. S-8. Anodic LSVs obtained on GC_0, GC_{CB}, GC_{AP} and GC_{CB-AP} in the following electrolyte solutions: (a) 0.1 mol L^{-1} H_2SO_4, (b) 0.1 mol L^{-1} KCl and (c) 1 mol L^{-1} KOH. v = 5 mV s^{-1}.

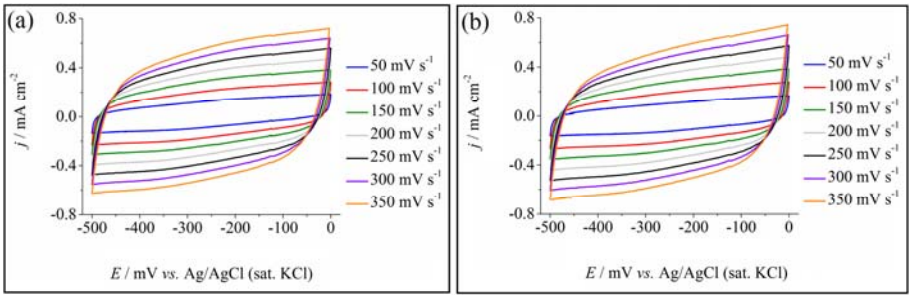

Fig. S-9. (a and b) CVs obtained on two GC_{CB-AP} electrodes in the E range from -500 to 0 mV, at increasing v values (50, 100, 150, 200, 250, 300 and 350 mV s^{-1}). Electrolyte solution: 0.1 mol L^{-1} KCl.

Raman spectra

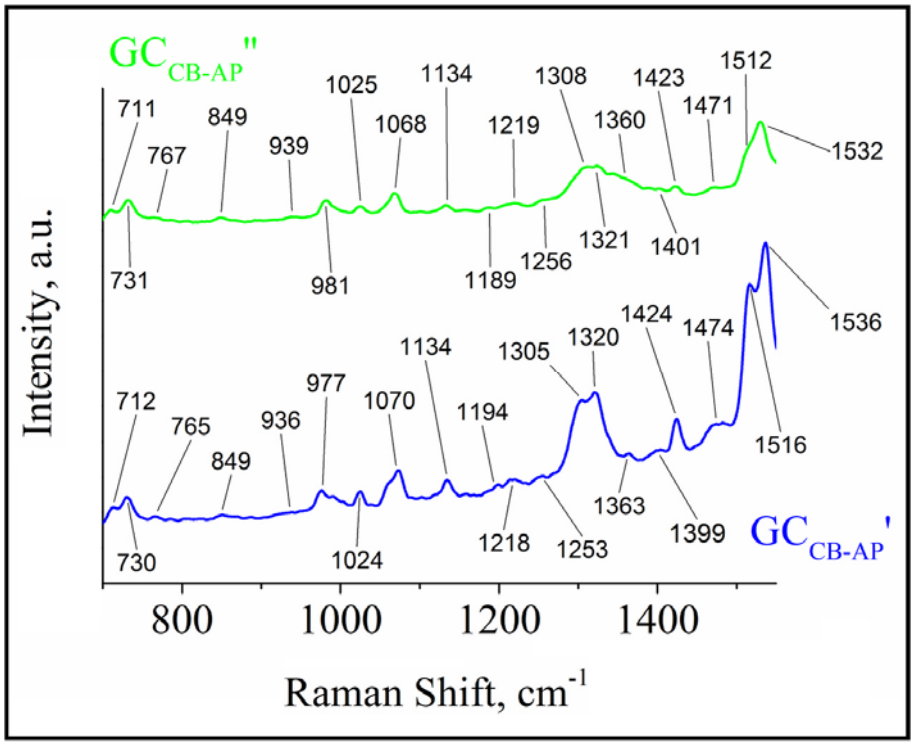

Fig. S-10. Raman spectra recorded on GC_{CB-AP} before a chronoamperometric stability test performed in 1 mol L^{-1} KOH solution (GC_{CB-AP}') and after the test (GC_{CB-AP}").

Statistical analysis

Before conducting the correlation analysis, a preliminary investigation was undertaken to ascertain the normality of the studied variables. This was achieved by employing a One-Sample Kolmogorov-Smirnov test. In the case of OER, the data for overpotential ($D(47) = 1.096$, $p > 0.05$) and polarity ($D(47) = 1.170$, $p > 0.05$) exhibited a normal distribution, while the data for pH ($D(47) = 1.856$, $p < 0.05$) and the number of layers ($D(47) = 1.778$, $p < 0.05$) were found to be non-normally distributed. Based on these results, Pearson statistics were computed to assess the relationship between overpotential and polarity, while Spearman's Rho statistic was computed to evaluate the relationship between the overpotential, the pH, and the number of layers. The results indicate no statistically significant correlation between overpotential, polarity, and number of layers. However, Spearman's correlation coefficient was found to be statistically significant for overpotential and pH (r_S (45) = 0.447, p < 0.01), thereby revealing a positive association between them. In the case of HER, the results of the One-Sample

Kolmogorov-Smirnov test show that the data for overpotential ($D(23) = 0.668$, $p > 0.05$), polarity ($D(23) = 0.847$, $p > 0.05$), and number of layers ($D(23) = 1.359$, $p = 0.05$) follow a normal distribution, whilst the pH data ($D(23) = 1.665$, $p < 0.05$) were found to be non-normally distributed. Based on these results, Pearson's statistics were computed to assess the relationships between overpotential, polarity, and number of layers, while Spearman's rho statistics were computed for the relationship between overpotential and pH. The obtained results revealed no statistically significant correlation between the overpotential and the other variables examined in the study.

REFERENCES

1. B.-R. Wulan, S.-S. Yi, S.-J. Li, Y.-X. Duan, J.-M. Yan, X.-B. Zhang, Q. Jiang, *Mater. Chem. Front.* **2** (2018) 1799 (https://doi.org/10.1039/C8QM00239H)
2. Raveendran, M. Chandran, R. Dhanusuraman, *RSC Adv.* **13** (2023) 3843 (https://doi.org/10.1039/D2RA07642J)
3. O. van der Heijden, S. Park, R. E. Vos, J. J. J. Eggebeen, M. T. M. Koper, *ACS Energy Lett.* **9** (2024) 1871 (https://doi.org/10.1021/acsenergylett.4c00266)
4. O. Taranu, S. D. Novaconi, M. Ivanovici, J. N. Goncalves, F. S. Rus, *Appl. Sci.-Basel* **12** (2022) 1 (https://doi.org/10.3390/app12136821)
5. Karmakar, S. Kundu, *Mater. Today Energy* **33** (2023) 1 (https://doi.org/10.1016/j.mtener.2023.101259)
6. M. L. F. Ciriaco, M. I. Silva-Pereira, M. R. Nunes, F. M. Costa, *Port. Electrochim. Acta* **17** (1999) 149 (https://doi.org/10.4152/pea.199902149)
7. V. Lemierre, A. Chrostowska, A. Dargelos, H. Chermette, *J. Phys. Chem. A* **109** (2005) 8348 (https://doi.org/10.1021/jp050254c)
8. P. Vibert, D. J. Tozer, *J. Chem. Theory Comput.* **15** (2018) 241 (https://doi.org/10.1021/acs.jctc.8b00938)
9. L. A. Curtiss, P. C. Redfern, K. Raghavachari, J. A. Pople, *J. Chem. Phys.* **109** (1998) 42 (https://doi.org/10.1063/1.476538)
10. M. K. Mongale, D. A. Isabirye, M. M. Kabanda, T. O. Aiyelabola, E. E. Ebenso, *Asian J. Chem.* **29** (2017) 496 (https://doi.org/10.14233/ajchem.2017.20205).

Journal of the Serbian Chemical Society
JSCS-info@shd.org.rs • www.shd.org.rs/JSCS
J. Serb. Chem. Soc. 90 (9) 1105–1117 (2025)
JSCS–5442
Original scientific paper
Published 30 September, 2025

Chitosan/sodium dodecyl sulphate microcapsules preparation: Influence of applied method

JELENA MILINKOVIĆ BUDINČIĆ[1]*, LIDIJA PETROVIĆ[1], MILIJANA ALEKSIĆ[2], JADRANKA FRAJ[1], LJILJANA ĐEKIĆ[3], SANDRA BUČKO[1], JAROSLAV KATONA[1], LJILJANA SPASOJEVIĆ[1], JELENA OSTOJIĆ[1], ŽELJANA RADONIĆ[1] and MINA BOSNIĆ[1]

[1]*University of Novi Sad, Faculty of Technology, Bulevar Cara Lazara 1, 21000 Novi Sad, Serbia,* [2]*Innovation and Entrepreneurship Center (IEC) Tehnopolis, Radoja Dakića, Nikšić Montenegro and* [3]*University of Belgrade, Faculty of Pharmacy, Vojvode Stepe 450, 11000 Belgrade, Serbia*

(Received 21 January, revised 17 March, accepted 3 June 2025)

Abstract: This study aims to compare and analyse the synthesis of microcapsules stabilized with chitosan/sodium dodecyl sulphate complex according to emulsion preparation methods. For this purpose, 20 % oil-in-water emulsions were obtained in two ways: by emulsifying the oil phase in aqueous solution of chitosan and its mixtures with anionic surfactant ("method I") and by subsequently dropping chitosan into an already prepared emulsion stabilized by anionic surfactant ("method II"). Good stability, positive zeta potential of the emulsions and uniform droplet size distribution obtained with both methods, enabled the preparation of chitosan-based microcapsules which were separated by spray drying and investigated in terms of yield, moisture content, particle mean diameter and size distribution. The results showed a uniform particle size distribution and approximately equal mean diameters of emulsion droplets (≈ 8 μm), *i.e.*, suspension particles (≈ 5μm), while the microcapsule yields and moisture content for method I were 15 and 1.14 %, and for method II were 1.2 and 2.85 %, respectively. These results indicate that method I may be more suitable for use in the pharmaceutical and food industries for the production of chitosan microcapsules with oil content. The study confirmed that small variations in preparation can lead to large changes in the microencapsulation process and microcapsule structure.

Keywords: chitosan; sodium dodecyl sulfate; emulsion; microcapsules.

* Corresponding author. E-mail: jelenamilinkovic@uns.ac.rs
https://doi.org/10.2298/JSC250121039B

INTRODUCTION

Microcapsule is a functional barrier between the core and the shell material to avoid chemical and physical reactions and to maintain the biological, functional and physicochemical properties of the core materials. Shell material properties determine the chemical and physical changes during capsule wall formation. Also, the shell material ultimately determines the choice of preparation method and the application direction of functional microcapsules.[1,2] Much attention has also been given to the use of chitosan, deacetylated chitin which is typically found in exoskeletons of arthropods and crustaceans and also in fungal cell walls, as polymer shell of the microcapsules. It's a polycationic polysaccharide compound that tends to interact with other substances, most often with the oppositely charged ones,[3–9] resulting in different morphology of novel microcapsules.[10] Since chitosan possesses a combination of properties such as biocompatibility, biodegradability, nontoxicity, as well as bioactivity: hypocholesterolemic, hypolipidemic, antimicrobial, antiviral, anticoagulant and antifungal, it has many applications in medicine, cosmetics and food industries.[11] Chitosan-based microcapsules have great potential for the development and applications of natural products that are widespread in the food, cosmetics and pharmaceutical industries.[1]

The capsule shell formation principle is based on the interaction between shell materials which include electrostatic interactions, covalent bonds and hydrogen bonds. Researchers have continuously explored a variety of preparation methods in the preparation process, such as the emulsification method, layer-by-layer (LBL) assembly method, sonochemical method, interface polymerization and spray drying method.[12–15]

Last couple of years, the most used microcapsule preparation and separation technique in the industry is spray drying. It consists of the rapid evaporation of the water phase from an emulsion by atomization with a pressure nozzle or a centrifugal wheel. The wide variety of materials that can be used, the simplicity of the procedure, its low cost and accessible equipment make spray drying the easiest and cheapest option to produce microencapsulated materials.[16] However, when using this method, great attention should be paid to choosing the shell material that could act as a barrier and protect the encapsulated bioactive compounds against oxygen, water, light and contact with other ingredients.[17] Furthermore, the characteristics of shell materials influence the controlled release of encapsulated bioactive compounds into the surrounding medium.[18,19]

Emulsions are colloid systems where one fluid is broken into small droplets within the other fluid and are often used in microencapsulation processes of liquid active components. The main problem occurring in emulsions is a phase separation that is due to flocculation and coalescence.[20] The emulsion stabilized by the polymer/surfactant complex is generally more stable than the one stabilized by surfactant only because it is stabilized not only by the electrostatic repulsion of the

droplets but also by the steric hindrance of the bulky oppositely charged polymer/surfactant complexes.[21] Emulsion stability, which is related to the size distribution of dispersed droplets and rheological properties of the continuous phase, can be expressed using the creaming index, where higher creaming index values indicate lower emulsion stability.[22] Also, achieving the emulsion droplets decrease, as well as attaining sufficiently high viscosity in the continuous phase contribute directly to emulsion stability and encapsulation efficiency of the core material at the subsequent drying process for microencapsulation.[23]

Methods for the preparation of emulsions used in the encapsulation process significantly affect the core stability, process efficiency and degree of protection of active components. Most of these methods involve preparing primary emulsion and then adding the polymer,[24–28] but this method may not be suitable for every polymer/surfactant or polymer/polymer system. To this end, based on the relevance of emulsion properties to efficient microencapsulation, this study compared and analysed the synthesis of microcapsules stabilized with chitosan/sodium dodecyl sulphate complex according to emulsion preparation methods.

EXPERIMENTAL

Materials

Low molecular weight chitosan (LMWCh) (product number: 448869) was obtained from Sigma–Aldrich. LMWCh degree of deacetylation, determined by potentiometric titration, is found to be 81.8 %.[29] Sodium dodecyl sulphate (SDS), purity >99 %, was purchased from Merck. Medium-chain triglycerides (caprylic/capric triglyceride, Saboderm TCC, Comcen, Zemun, Serbia) were used as oil phase. In all experiments buffered water was used as a solvent and pH was adjusted using 0.2 M water solution of acetic acid (Zorka-Pharma, Šabac, Serbia) and 0.2 M water solution of sodium acetate (Centrohem, Stara Pazova, Serbia). Aerosil 200, silicon dioxide, was provided by Carl Roth (Karlsruhe, Germany).

Preparation of solutions

The experiments were carried out at pH 4. pH was measured at room temperature using 827 lab pH-meter (Metrohm, Herisau, Switzerland). Stock solution of 0.2 mass % LMWCh was prepared by dissolving a given mass of polymer in the buffered water while stirring and after relaxation at room temperature during 24 h, pH value of the solution was checked. SDS stock solution of 1 mass % was prepared using the same procedure. LMWCh:SDS mixtures were prepared by mixing required volumes of LMWCh and SDS stock solutions. Before measurements, mixtures were left for 24 h at room temperature.

Preparation of oil-in-water emulsions

Oil-in-water (O/W) emulsions were prepared at the oil:water mass ratio 20:80 (20 % O/W emulsions) at 30 °C in two ways. The first method (“method I”) of preparation was the emulsification of semi-synthetic oil – Saboderm TCC in the aqueous phase by homogenizer Ultra Turrax T25. Solution of 0.1 % LMWCh, solutions of 0.001, 0.2 and 1 % SDS and mixtures of LMWCh:SDS at mass ratios 100:1, 1:2 and 1:10 were used as the aqueous phase of the emulsions. Before the start of emulsification, the aqueous phase was homogenized for 5 min at 5000 rpm by homogenizer Ultra Turrax T25, then during the first minute of emulsification the oil

phase was gradually added and the emulsification was continued for up to 10 min under the same conditions.

The second method ("method II") involved emulsion preparation by method I but with SDS solution as a water phase and then dropping a solution of chitosan into an already formed emulsion with SDS. This method was used to obtain a 20 % O/W emulsion with a mass ratio of LMWCh:SDS 1:2.

Spray drying procedure

In order to avoid agglomeration, 2 % of Aerosil was added to the emulsions. Mini spray dryer (Büchi 190, Flawil, Switzerland) with a standard 0.7 mm nozzle was used to convert the emulsions into microcapsules powders. The inlet temperature was kept at 160 °C and the outlet at 100 °C. The drying parameters during the process, such as aspiration (0.6 m^3/min) and feeding (2.2 ml/min) were controlled.

Zeta potential measurements

Zeta potential of emulsions was determined using Zetasizer Nano ZS (Malvern Instruments, Malvern, UK). Viscosity (0.88 mPas) and refractive index (1.33) of the solvent at room temperature were used for data analysis. All measurements were carried out in triplicate.

Droplet/particle size distribution

Droplet size distribution of the emulsions and particle size distribution of the suspensions of microcapsules in water was assessed by microphotography which was taken on optical microscope, Biooptica BEL-3000 (Milano, Italy) at 40× magnification and analyzed using BELView software. Droplet mean diameter as well as particle mean diameter, expressed as volume-surface mean value, d_{vs} (μm) and standard deviation σ (μm) were calculated from the experimental data, respectively:

$$d_{vs} = \sum n_i d_i^3 / \sum n_i d_i^2 \quad (1)$$

$$\sigma = (\sum n_i (d_i - d_{vs})^2 / \sum n_i)^{1/2} \quad (2)$$

where d_i is droplet/particle diameter (μm) and n_i is number of droplets/particles. Droplet/particle size distribution curves were obtained by fitting the experimental data with the gamma-equation:

$$Y_p = G x^m e^{(-ax)} \quad (3)$$

Emulsion stability test

For stability test, the emulsions were transferred into 10 ml graduated cylinders and stored at room temperature for 7 days. The emulsions were observed for the changes in homogeneity and phase separation during storage. The total height of the emulsion (H_0) and the height of the serum layer (H_s) were also measured over time. The extent of creaming was characterized by the creaming index, H:

$$H = 100 H_s / H_0 \ (\%) \quad (4)$$

The higher the creaming index the worse the emulsion stability. All experiments were carried out in triplicate and reported as average values plotted with standard deviation errors.

Yield analysis

The microcapsule powders collected from the processing equipment were stored in tightly closed dark container, at 4 °C, before further analysis. The product yield was calculated as the ratio between the mass of the output powders, recovered from the equipment at the end of the process, and the mass of the solid content of the initial emulsion, fed to the spray-dryer chamber.

Moisture content

The moisture content of microcapsules was determined gravimetrically by oven drying at 105 °C up to a constant weight.[30] One gram of powder was used and the moisture was expressed as a percentile value. All of the experiments were conducted in triplicate.

RESULTS AND DISCUSSION

The possibility of using chitosan (0.1 %) and SDS (0.001, 0.2 or 1 %) to stabilize the medium-chain triglycerides emulsion in water was first investigated. The appearance of the obtained emulsions 24 h after preparation is shown in Fig. 1.

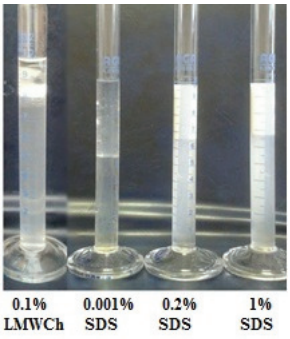

Fig. 1. O/W emulsions stabilized with LMWCh and SDS, 24 h after preparation.

The concentrations of SDS were selected based on the previous study[31] to cover the area before LMWCh/SDS coacervate formation (100:1), the coacervation area (1:2), as well as the area after coacervate formation (1:10), *i.e.*, 0.001, 0.2 and 1 % SDS, respectively. It can be noticed that emulsification properties of LMWCh and 0.001 % SDS are poor, after a few minutes there was a complete emulsion phase separation. This behavior of LMWCh is completely expected, due to its weak interface activity, as shown by our previous study.[29,31] Also, concentration of 0.001 % SDS is below critical micelles concentration of SDS[29] and insufficient for the formation of a stabile adsorption layer at the water-oil interface.

The stability of emulsions with 0.2 and 1 % SDS were monitored by visual observation of changes within the samples during 140 min of storage at room temperature and creaming index was determined. Results are presented in Fig. 2.

Concentrations of 0.2 and 1 % SDS were sufficient to provide a stable emulsion. In addition, the sample with 1 % SDS presented a slightly lower creaming index, suggesting that higher concentration of SDS provides a more stable emulsion. By observing the emulsions with 0.2 and 1 % SDS under a microscope (Fig. 2), immediately after preparation, it was noticed that they have spherical drops of different diameters. The mean droplet diameters were determined and they were 8.72±0.753 μm and 5.81±0.357 μm for emulsions with 0.2 and 1 % SDS, respectively.

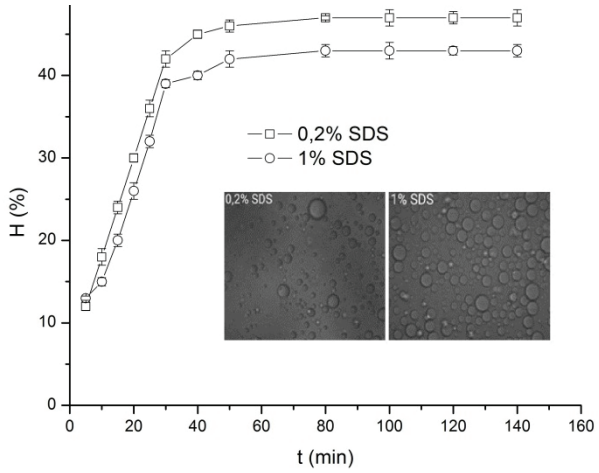

Fig. 2. Creaming index *H* and microphotograph of O/W emulsions stabilized by SDS.

It can be seen that the prepared emulsions stabilized with 0.2 and 1 % SDS have a droplet size below 9 μm and both emulsions had uniform droplet size distribution with low standard deviation. As expected, an emulsion with 1 % SDS has a lower value of mean droplet diameter than one with 0.2 % SDS, *i.e.*, as the concentration SDS increases, the droplet size decreases. This is ascribed to the enhanced water solubility of the oil molecules induced by the addition of ionic surfactants.[32]

To investigate the possibility of using LMWCh/SDS complexes for emulsion stabilization by method I, 20 % medium-length triglyceride emulsions in water were prepared which included a continuous phase with LMWCh:SDS solution mixture, and their appearance is shown in Fig. 3.

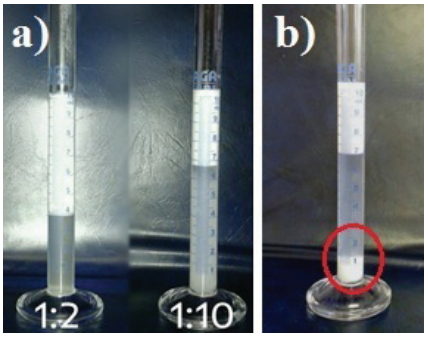

Fig. 3. Appearance of: a) O/W emulsions stabilized by LMWCh/SDS complex of different mass ratio 24 h after preparation; b) O/W emulsion stabilized by LMWCh/SDS complex in mass ratio of 1:10, 7 days after preparation.

Fig. 3a shows that stratification of emulsion to the cream and serum layer occurs due to the difference in density between the continuous and dispersed phase. Comparing the visual transparency of serum layers, it is observed that serum layer of the emulsion stabilized by LMWCh/SDS complex in mass ratio 1:10 was more

turbid and had higher creaming index than the other one. The creaming index of emulsions with LMWCh/SDS complexes in mass ratios 1:2 and 1:10 was monitored within 4 h and results are shown in Fig. 4.

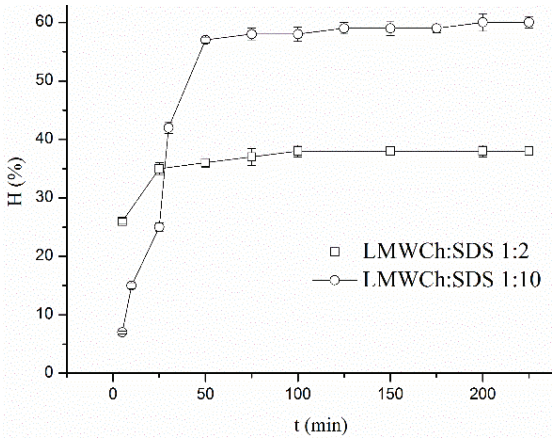

Fig. 4. Creaming index *H* of emulsions monitored within 4 h.

Changes in emulsion creaming index *H* with time (Fig. 4) indicate rapid separation of layers for emulsion stabilized with LMWCh/SDS complex in the mass ratio 1:10 during the first two hours of storage. Emulsion stabilized by LMWCh/SDS complex in the mass ratio 1:2 has slow separation of layers during the first hour of storage, which suggests better stability for this emulsion. After those times creaming index in booth emulsions remains almost unchanged.

Zeta potential of emulsion stabilized by LMWCh/SDS complex in mass ratio 1:2 was 22.3±4.05 μV and the droplets had a positive charge, while emulsion stabilized by LMWCh/SDS complex in mass ratio 1:10 had a negatively charged (–3.45±0.77 μV) which indicates that SDS molecules prevail in the adsorption layer. Based on our previous study,[29,31] the behavior of LMWCh/SDS complexes at interfaces and in the bulk was investigated in detail. When it comes to water solution the LMWCh/SDS mass ratio 1:2 complex is neutral and completely precipitated in the form of coacervates, while in emulsion containing the same complex, droplets bear positive charge. This phenomenon could be explained by share--induced reorganization in structure of formed complexes during emulsification process.[7,33] The reorganization during emulsification is a dynamic process where the emulsifier molecules adapt to changes in droplet size, phase interactions and surface coverage to stabilize the emulsion. In the context of emulsions, the polyelectrolyte complex can interact with both the oil phase and the aqueous phase, leading to a more complex behavior and potential changes. The reorganization of the polyelectrolyte complex at the interface during emulsification is critical to maintaining the stability and homogeneity of the emulsion.[34] Based on the general

knowledge polyelectrolyte complex interfacial behavior, two mechanisms are possible: the complex coacervates reorganize into a continuous protecting layer surrounding the oil droplets[35] or the coacervates adsorb on the oil droplet surface and stabilize the emulsion by a Pickering effect.[36,37]

As it can be seen from Fig. 3b emulsion stabilized by LMWCh/SDS complex in mass ratio 1:10 showed LMWCh/SDS coacervate sedimentation at the bottom of cylinder 7 days after preparation. Such findings along with negative charge of the droplets confirm that only SDS molecules are adsorbed at the interface.

Based on the above, for preparation of microcapsules with method II which is the usual method in literature,[24–26,28,38] 0.2 % SDS was selected for emulsion stabilization and LMWCh solution was dropped until LMWCh:SDS mass ratio of 1:2 was obtained.

Zeta potential of the emulsion prepared by method II was 17.1±3.29 μV, *i.e.*, the drops have a positive charge. The presence of a coacervate phase around the oil droplets (Fig. 5A and B) can be noticed in both emulsions, prepared by method I and method II, but their charge is not neutral. Positively charged emulsions have more advantages in the pharmaceutical and cosmetics industry due to potentially better bioavailability and biocompatibility.[39]

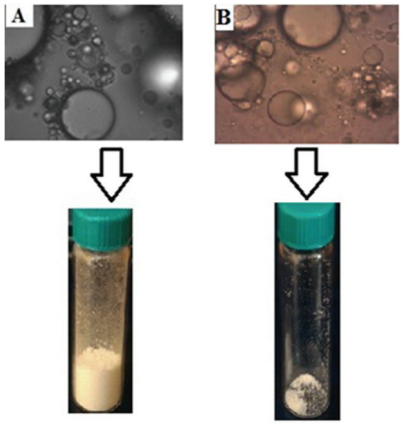

Fig. 5. Microphotograph of O/W emulsions stabilized by LMWCh/SDS complex in mass ratios 1:2 immediately after their preparation; A) method I and B) method II and obtained yield of microcapsules.

Microcapsules prepared by method I and method II and separated by spray drying were investigated in terms of yield, moisture content, particle mean diameter and size distribution.

Microcapsule production yield shows how much powder mass is produced after spray drying process and it is expressed by the percentage of core and shell materials present in the initial emulsion. Microcapsule yield was 15 % for microcapsules obtained by method I and 1.2 % for microcapsules obtained by method II. During the collection process after drying, the microcapsule powder obtained

in the method II was sticky and greasy probably due to the weak mechanical properties of their shell material.

Also, the low yield values obtained by method II are probably caused by the microcapsule preparation process itself. In the process of obtaining microcapsules by the method II it is most likely that stable coacervate did not form on the boundary surface, and it was partially formed in the continuous phase, as well. This is probably due to the weak affinity of LMWCh with SDS molecules at the boundary surface, which is a consequence of its weak surface activity, *i.e.*, before LMWCh reaches the boundary surface it binds to free SDS molecules in the continuous phase. For these reasons during the drying process the drops broke, which together with the coacervate from the continuous phase stuck to the walls of the drying chamber, *i.e.*, the powder adheres to the interior surface of the drying chamber due to high adhesive ability of LMWCh.[40]

The moisture content is an important variable related to the shelf life of powders and is often conducted to check on the spray-drying process. The moisture content of the microcapsules obtained by method I was 1.14 and 2.85 % for microcapsules obtained by method II. Its values are following the results from other studies.[30] This lower value for moisture content for microcapsules obtained by method I contributes to the powder stability during the storage and prevention of changes in physical and chemical characteristics.

For easier viewing, Table I shows a comparative analysis of the parameters tested for emulsions produced by both methods, microcapsules obtained from them by spry drying, as well as the mean diameters of re-dispersed microcapsules, which will be discussed below. The distribution parameters of the mean particle diameters of emulsion and re-dispersed microcapsules were obtained by processing microphotographs of their suspensions in water using BELview7 software. The particle size distribution curves of microcapsules that were obtained by fitting the experimental data with gamma equation are shown in Fig. 6.

TABLE I. Comparative analysis investigated parameters for both methods of emulsion preparation

Sample	Method I	Method II
Zeta potential of emulsion, μV	22.3±4.05	17.1±3.25
Particle mean diameter of emulsion, μm	8.72±0.753	7.32±1.052
Particle mean diameter suspensions of microcapsules, μm	5.12±0.372	5.70±0.819
Yield of microcapsules, %	15	1.2
Moisture content, %	1.14±0.275	2.85±0.652

As seen from the Table I and Fig 6, emulsions and suspensions of microcapsules were produced with mean diameters from 5.12 to 8.72 μm which is in accordance with the results of other studies.[41] Namely, after spray drying process all suspensions of microcapsules show slightly lower mean diameter and decreased

polydispersity compared to the starting emulsion. The spray drying process of emulsions affects the size and size distribution of the microcapsules, which is unsurprising taking into account that during drying process small droplets can be aspirated and large droplets can burst if the wall is not sufficiently resistant.[14] Also, both samples of microcapsules had uniform particle size distribution with low standard deviation. These results indicate equal properties of the microcapsule wall for both methods of their preparation. However, considering the appearance (sticky and oily), yield and moisture content of the microcapsule powders, it can be concluded that microcapsules are formed in smaller quantities when using method II. It is clear that yields of microcapsules and stability of the microcapsule shell as well as their characteristics were directly influenced by the emulsion preparation method. From all of the above method I can be considered better for the micro-encapsulation of oil in the system chitosan/sodium dodecyl sulphate.

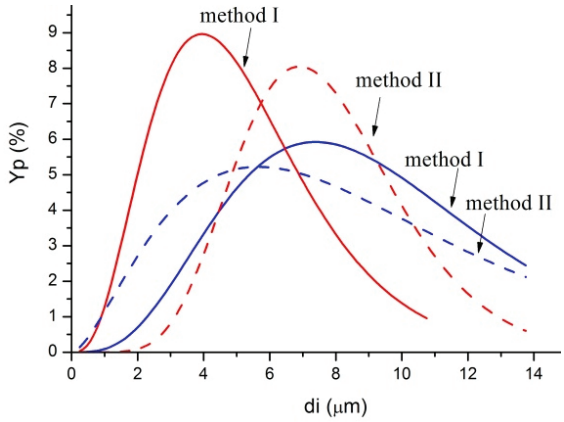

Fig. 6. Droplet and particle size distribution of the emulsions (blue) and suspensions (red) of microcapsules.

CONCLUSION

In this study, two preparation methods were proposed and demonstrated (method I: homogenization of oil in the already formed LMWCh/SDS complex and method II: subsequent dropping of chitosan into the already prepared emulsion with SDS) for chitosan-based microcapsules whose wall consisted of LMWCh/ /SDS complex. Microcapsules were obtained in powder form using spray drying as a method for their separation. Chitosan microcapsules were successfully prepared by both methods of preparation. For both methods, it was determined that the mean diameters suspensions of microcapsules have similar values (5.12±0.372 μm for method I, 5.70±0.819 μm for method II). However, the yield of the drying process was 15 % for microcapsules obtained by method I and 1.2 % for the method II of preparation, which indicates a small influence of the spray drying

method and a dominant influence of emulsions preparation method on formation stable or unstable shells of microcapsules. Also, a lower value of moisture content for microcapsules obtained by method I (1.14 %) could indicate their better stability during the storage by preventing changes in their physical and chemical characteristics. The results showed that method II, more commonly used in the literature for microencapsulation of oil in most polymer/surfactant and polymer/ /polymer systems, would not be proved to be the method of choice for the system chitosan/SDS. Therefore, method I gives a much higher yield of microcapsules and a lower moisture content than method II, which gives it an advantage in selection for obtaining oil-core microcapsules for the cosmetic and pharmaceutical industries. The study also confirmed that small variations in preparation can lead to large differences in the microcapsule structure.

Acknowledgement. This work was financed by Ministry of Education, Science and Technological Development of the Republic of Serbia, Grants No. 451-03-136/2025-03/ /200134, 451-03-137/2025-03/200134, 451-03-136/2025-03/200161 and 451-03-137/2025-03/ /200161.

ИЗВОД

ПРИПРЕМА МИКРОКАПСУЛА ХИТОСАН/НАТРИЈУМ-ДОДЕЦИЛ-СУЛФАТ: УТИЦАЈ МЕТОДЕ ПРИПРЕМЕ

ЈЕЛЕНА МИЛИНКОВИЋ БУДИНЧИЋ[1], ЛИДИЈА ПЕТРОВИЋ[1], МИЛИЈАНА АЛЕКСИЋ[2], ЈАДРАНКА ФРАЈ[1], ЉИЉАНА ЂЕКИЋ[3], САНДРА БУЧКО[1], ЈАРОСЛАВ КАТОНА[1], ЉИЉАНА СПАСОЈЕВИЋ[1], ЈЕЛЕНА ОСТОЈИЋ[1], ЖЕЉАНА РАДОНИЋ[1] и МИНА БОСНИЋ[1]

[1]*Технолошки факултет Универзитет у Новом Саду , Булевар Цара Лазара 1, 21000 Нови Сад,* [2]*Иновационо-подузетнички центар (IEC) Tehnopolis, Radoja Dakića, Никшић, Црна Гора и* [3]*Универзитет у Београду, Фармацеутски факултет, Војводе Степе 450, 11000 Београд*

Циљ овог рада је упоредна анализа микрокапсула стабилизованих комплексом хитозан/натријум-додецил-сулфат у зависности од методе припреме емулзија. У том циљу, 20 % емулзије уље у води добијене су на два начина: емулговањем уљне фазе у воденом раствору хитозана и његових смеша са анјонским сурфактантом („метод I") и накнадним укапавањем хитозана у већ припремљену емулзију стабилизовану помоћу анјонског сурфактанта („метод II"). Добра стабилност, позитиван зета потенцијал и уједначена расподела величина капи емулзија добијених обема методама, омогућили су припрему хитозанских микрокапсула које су издвојене сушењем распршивањем и којима је одређен принос, садржај влаге, средњи пречник и расподела величине честица. Резултати су показали уједначену распподелу честица по величини и приближно једнаке средње пречнике капи емулзија (≈ 8 μm), односно суспензија (≈ 5 μm), док су приноси микрокапсула и садржај влаге за метод I били 15 и 1,14 %, а за метод II 1,2 и 2,85 %, редом. Добијени резултати указују да метод I може бити погоднији за производњу хитозанских микрокапсула са уљним језгром у фармацеутској и прехрамбеној индустрији. Студија је показала и да мале варијације у припреми могу довести до великих промена у процесу микрокапсулирања и структури микрокпсула.

(Примљено 21. јануара, ревидирано 17. марта, прихваћено 3. јуна 2025)

REFERENCES

1. Q. Meng, S. Zhong, J. Wang, Y. Gao, X. Cui, *Carbohydr. Polym.* **300** (2023) 120265 (https://doi.org/10.1016/j.carbpol.2022.120265)
2. S. U. D. Wani, M. Ali, S. Mehdi, M. H. Masoodi, M. I. Zargar, F. Shakeel, *Int. J. Biol. Macromol.* **248** (2023) 125875 (https://doi.org/10.1016/j.ijbiomac.2023.125875)
3. M. Lundin, L. Macakova, A. Dedinaite, P. Claesson, *Langmuir* **24** (2008) 3814 (https://doi.org/10.1021/la702653m)
4. C. Onesippe, S. Lagerge, *Carbohydr. Polym.* **74** (2008) 648 (https://doi.org/10.1016/j.carbpol.2008.04.021)
5. L. Petrović, J. Milinković, J. Fraj, S. Bučko, J. Katona, L. Spasojević, *Colloid Polym. Sci.* **295** (2017) 2279 (https://doi.org/10.1007/s00396-017-4205-7)
6. J. Lazko, Y. Popineau, D. Renard, J. Legrand, *J. Microencapsul.* **21** (2004) 59
7. J. Milinković, L. Petrović, J. Fraj, S. Bučko, J. Katona, L. Spasojević, *Colloids Surfaces, A* **557** (2018) 9 (https://doi.org/10.1016/j.colsurfa.2018.06.085)
8. A. A. Sharipova, S. B. Aidarova, D. Grigoriev, B. Mutalieva, G. Madibekova, A. Tleuova, R. Miller, *Colloids Surfaces, B* **137** (2016) 152 (https://doi.org/10.1016/j.colsurfb.2015.03.063)
9. S. M. Anush, S. N. Raju, B. H. Gayathri, K. P. Ajeya, Y. R. Girish, S. Darshan, Y. P. Naveen, K. Prashantha, B. K. Narendra, A. Jayaram, *Express Polym. Lett.* **18** (2024) 102 (https://doi.org/10.3144/expresspolymlett.2024.8)
10. Z. A. Raza, S. Khalil, A. Ayub, I. M. Banat, *Carbohydr. Res.* **492** (2020) 108004 (https://doi.org/10.1016/j.carres.2020.108004)
11. M. Amidi, E. Mastrobattista, W. Jiskoot, W. E. Hennink, *Adv. Drug Deliv. Rev.* **62** (2010) 59 (https://doi.org/10.1016/j.addr.2009.11.009)
12. Q. Meng, S. Zhong, S. He, Y. Gao, X. Cui, *Colloids Interface Sci. Commun.* **44** (2021) 100503 (https://doi.org/10.1016/j.colcom.2021.100503)
13. L. Di Giorgio, P. R. Salgado, A. N. Mauri, *Food Hydrocoll.* **87** (2019) 891 (https://doi.org/10.1016/j.foodhyd.2018.09.024)
14. B. Muhoza, H. Yuyang, A. Uriho, J. D. Harindintwali, Q. Liu, Y. Li, *Food Hydrocoll.* **140** (2023) 108650 (https://doi.org/10.1016/j.foodhyd.2023.108650)
15. A. Napiórkowska, M. Kurek, *Molecules* **27** (2022) 5142 (https://doi.org/10.3390/molecules27165142)
16. I. Schmitz-Schug, U. Kulozik, P. Foerst, *Chem. Eng. Sci.* **141** (2016) 315 (https://doi.org/10.1016/j.ces.2015.11.008)
17. N. V. N. Jyothi, P. M. Prasanna, S. N. Sakarkar, K. S. Prabha, P. S. Ramaiah, G. Y. Srawan, *J. Microencapsul.* **27** (2010) 187 (https://doi.org/10.3109/02652040903131301)
18. D. Chaabane, I. Mirmazloum, A. Yakdhane, E. Ayari, K. Albert, G. Vatai, M. Ladányi, A. Koris, A. Nath, *Bioengineering* **10** (2023) 657 (https://doi.org/10.3390/bioengineering10060657)
19. J. Rodríguez, M. J. Martín, M. A. Ruiz, B. Clares, *Food Res. Int.* **83** (2016) 41 (https://doi.org/10.1016/j.foodres.2016.01.032)
20. E. Agama-Acevedo, L. A. Bello-Perez, *Curr. Opin. Food Sci.* **13** (2017) 78 (https://doi.org/10.1016/j.cofs.2017.02.014)
21. T. Vongsetskul, K. Phaenthong, R. Chanthateyanonth, P. Sunintaboon, P. Tangboriboonrat, *Chiang Mai J. Sci.* **42** (2015) 393 (http://epg.science.cmu.ac.th/ejournal/dl.php?journal_id=5760)
22. K. M. Albano, Â. L. F. Cavallieri, V. R. Nicoletti, *Food Rev. Int.* **35** (2019) 54 (https://doi.org/10.1080/87559129.2018.1467442)

23. S. Ferreira, C. R. Malacrida, V. R. N. Telis, *Can. J. Chem. Eng.* **94** (2016) 2210 (https://doi.org/10.1002/cjce.22596)
24. H. Aloys, S. A. Korma, T. M. Alice, N. Chantal, A. H. Ali, S. M. Abed, H. Ildephonse, *Am. J. Food Sci. Nutr. Res.* **3** (2016) 188 (http://www.openscienceonline.com/author/download?paperId=3564&stateId=8000&fileType=3)
25. C. Butstraen, F. Salaün, *Carbohydr. Polym.* **99** (2014) 608 (https://doi.org/10.1016/j.carbpol.2013.09.006)
26. Y. Li, L. Ai, W. Yokoyama, C. F. Shoemaker, D. Wei, J. Ma, F. Zhong, *J. Agric. Food Chem.* **61** (2013) 3311 (https://doi.org/10.1021/jf305074q)
27. Saehun Mun and D. J. McClements, *Langmuir* **22** (2006) 1551 (https://doi.org/10.1021/la052575l)
28. S. Mun, E. A. Decker, D. J. McClements, *Langmuir* **21** (2005) 6228 https://doi.org/10.1021/la050502w)
29. L. B. Petrović, J. R. Milinković, J. L. Fraj, S. D. Bučko, J. M. Katona, *J. Serb. Chem. Soc.* **81** (2016) 575 (https://doi.org/10.2298/JSC151119024P)
30. C. Dima, L. Pətraşcu, A. Cantaragiu, P. Alexe, Ş. Dima, *Food Chem.* **195** (2016) 39 (https://doi.org/10.1016/j.foodchem.2015.05.044)
31. J. R. Milinković, M. V. Aleksić, L. B. Petrović, J. L. Fraj, S. D. Bučko, J. M. Katona, L. M. Spasojević, *Acta Period. Technol.* **48** (2017) 221 (https://doi.org/10.2298/APT1748221M)
32. X. Xin, H. Zhang, G. Xu, Y. Tan, J. Zhang, X. Lv, *Colloids Surfaces, A* **418** (2013) 60 (https://doi.org/10.1016/j.colsurfa.2012.10.065)
33. J. M. Katona, S. D. Njaradi, V. J. Sovilj, L. B. Petrović, B. B. Marčeta, J. L. Milanović, *J. Serb. Chem. Soc.* **79** (2014) 457 (https://doi.org/10.2298/JSC130807132K)
34. D. J. McClements, S. M. Jafari, *Adv. Colloid Interface Sci.* **251** (2018) 55 (https://doi.org/10.1016/j.cis.2017.12.001)
35. B. Lindman, F. Antunes, S. Aidarova, M. Miguel, T. Nylander, *Colloid J.* **76** (2014) 585 (https://doi.org/10.1134/S1061933X14050111)
36. M. F. Li, Z. Y. He, G. Y. Li, Q. Z. Zeng, D. X. Su, J. L. Zhang, Q. Wang, Y. Yuan, S. He, *Food Hydrocoll.* **90** (2019) 482
37. S. Laquerbe, A. Carvalho, M. Schmutz, A. Poirier, N. Baccile, G. Ben Messaoud, *J. Colloid Interface Sci.* **600** (2021) 23 (https://doi.org/10.1016/j.jcis.2021.04.135)
38. S. Chatterjee, F. Salaün, C. Campagne, S. Vaupre, A. Beirão, *Carbohydr. Polym.* **90** (2012) 967 (https://doi.org/10.1016/j.carbpol.2012.06.028)
39. Y. Baspinar, H. H. Borchert, *Int. J. Pharm.* **430** (2012) 247 (https://doi.org/10.1016/j.ijpharm.2012.03.040)
40. M. Abdelmoula, H. Ben Hlima, F. Michalet, G. Bourduche, J.-Y. Chavant, A. Gravier, C. Delattre, M. Grédiac, J.-D. Mathias, S. Abdelkafi, P. Michaud, H. de Baynast, *Polysaccharides* **2** (2021) 110 (https://doi.org/10.3390/polysaccharides2010008)
41. I. C. Carlan, B. N. Estevinho, F. Rocha, *Powder Technol.* **318** (2017) 162 (https://doi.org/10.1016/j.powtec.2017.05.041).

Journal of the Serbian Chemical Society
JSCS-info@shd.org.rs • www.shd.org.rs/JSCS
J. Serb. Chem. Soc. 90 (9) 1119–1130 (2025)
JSCS–5443
Original scientific paper
Published 30 September, 2025

Ni–Bi–Sn ternary system liquidus surface projection

CHINGIZ I. ABILOV[1]*, IKHTIYAR B. BAKHTIYARLY[2], SAYYARA H. SADIGOVA[1], MEHRIBAN SH. HASANOVA[1] and ELMIRA K. GASIMOVA[1]

[1]*Azerbaijan Technical University, Baku, Azerbaijan and* [2]*Institute of Catalysis and Inorganic Chemistry named after academician M. Naghiyev of the Ministry of Science and Education of the Republic of Azerbaijan*

(Received 5 March, revised 8 May, accepted 15 June 2025)

Abstract: Physicochemical analysis investigations were conducted on six internal polythermic sections of the Ni–Bi–Sn ternary system, and phase diagrams of the sections were constructed. It was determined that two of the sections were quasibinary, and four were non-quasibinary. The projection of the liquidus surface of the ternary system was constructed. The equations for the nonvariant equilibrium reactions occurring in the ternary system were compiled and their coordinates were determined. The presence of promising solid solution areas was revealed in some of the internal sections of the ternary system, and their boundaries at room temperature were determined. The absence of new complex compounds and the presence of homogeneous regions indicate that the synthesized materials could be suitable for application as switching and contact layers in alternative energy sources.

Keywords: phase diagrams; alloys; primary crystallization; nonvariant reactions.

INTRODUCTION

Metallic nickel and its alloys are widely used in metallurgy as doping elements to enhance the mechanical properties of steel and increase resistance to heat and corrosion. They are also employed in the production of military ammunition, and in electronics and electrical engineering for materials like invar, platinite and nichrome. Nickel and its alloys also exhibit catalytic properties. Considering that nickel alloys find applications as both active (working element of the thermoelectric device) and passive (commutation layers) materials in thermoelectric energy converters,[1–5] the need to study the synthesis and properties of nickel-based alloys is clear.

Bi–Sn alloys are widely employed as contact materials in solid-state electronic devices and equipment. However, their low melting temperatures (both of the con-

* Corresponding author. E-mail: chingiz.ebilov@aztu.edu.az
https://doi.org/10.2298/JSC250305045A

stituent elements and the alloys themselves) can lead to heating when current passes through the contacts, potentially resulting in contact failure. Including a substance with a high melting point and good mechanical resistance, such as nickel, into these materials could offer a solution. Furthermore, the chemical compatibility of the interacting substances plays a crucial role. It is essential to consider the potential formation of new phases resulting from interactions between the contacting substances, the reactions that occur, and their formation temperatures, as these new phases can cause contact failure or reduce conductivity. Therefore, a thorough physicochemical analysis of the Ni–Bi–Sn system is of significant technological relevance.

Results of some studies on the Ni–Bi–Sn system have been reported in the literature. For example, Vassilev *et al*.[6] studied the solid phase equilibria of the ternary system at 733 and 903 K and scanning electron microscopy results indicated the presence of a ternary compound with the formula Ni_7Sn_2Bi. However, X-ray diffraction analysis did not confirm this compound. Thus, despite the modernity of these two investigation methods, inconsistencies exist in their reported results.

Thermodynamic functions of some ternary phases were calculated using parameters from the binary systems of the Ni–Bi–Sn triangle, and the system's phase equilibrium was subsequently studied based on these results.[7,8] Naturally, thermodynamic calculations alone cannot provide complete clarity on the ternary system's phase equilibrium. Furthermore, the activity coefficient of bismuth in the liquid phase at 1773 K was obtained using the isopiestic method, and these values were compared with theoretical calculations.[8]

The alloys of the Ni–Bi–Sn system were studied by X-ray diffraction analysis which indicated the presence of ternary compounds with the approximate formulas Ni_6Sn_2Bi and Ni_7Sn_2Bi.[9] According to the authors, the diffraction bands in the X-ray diffraction patterns of these ternary compounds coincide with the analogous diffraction maxima of NiBi and Ni_3Bi binary compounds. Consequently, the authors' conclusions are questionable, as assuming the existence of a new ternary compound based solely on X-ray phase analysis is methodologically unsound.

The Ni–Bi–Sn system was studied by SEM and differential scanning calorimetry, which showed that ternary eutectic reactions in the system occur at 116––129 °C.[10]

Thus, this brief literature review indicates that the Ni–Bi–Sn ternary system has not been fully studied and that existing studies present conflicting results. Therefore, a comprehensive study of the Ni–Bi–Sn system over a wide concentration and temperature range was deemed necessary, the results of which are presented herein. This study focuses significantly on investigating new sections, in addition to those traditionally examined in the literature.

EXPERIMENTAL

Ternary alloys were synthesized from special purity bismuth and tin (99.999 %), and TU-6-09 carbonyl grade nickel, using a single-temperature furnace with a vibratory mixer.[11,12] Depending on the composition, the synthesis temperature ranged from 1373 to 1573 K. To ensure equilibrium and complete reaction, the alloys were thermally treated (annealed) at temperatures of 363–523 K (composition-dependent) for 480 h. The alloys were obtained as dense masses with a dark-gray metallic colour. To clarify the nature of the chemical interaction between the components of the ternary system, differential thermal analysis (DTA), microstructural analysis (MSA) and X-ray phase analysis (XRD) were performed, and their microhardness and density were measured.

DTA was performed in the dynamic mode in an inert (helium) atmosphere with an STA 449F3 Jupiter simultaneous thermal analyzer (Netzsch, Germany) at a heating rate of 15 K/min using a Pt–Pt/Rh thermocouple. The analyzer operates under the control of the Proteus software. XRD analysis was performed on system samples with a D2 Phaser X-ray powder diffractometer (Bruker, Germany) using CuKα radiation and a Ni filter. The scanning speed was 2°/min. Device control and data analysis were managed using the Diffrac.Suite software package.[13,14]

MSA and microhardness measurements were performed on ground and polished samples using a “View” and “Micrometer-5101” microscopes, as well as on “PMT-3” microhardness tester with automatic load. The surfaces were etched with diluted nitric acid (2:1). Density was determined pycnometrically using toluene as the displacement liquid.

RESULTS AND DISCUSSION

The nature of chemical interactions in the Bi–Ni–Sn ternary system was investigated along the quasibinary sections Ni_3Sn–Bi and Ni_3Sn_2–Bi, and the non-quasibinary sections $Bi_{0.75}Sn_{0.25}$–$Ni_{0.5}Sn_{0.5}$, BiNi–Sn, $Bi_{0.6}Ni_{0.4}$–Sn and $Bi_{0.57}Sn_{0.43}$–Ni. The phase equilibria observed in these sections are described below.

Ni_3Sn–Bi Section

The Ni_3Sn–Bi phase diagram was constructed based on the results of physicochemical analysis. The section is quasibinary, and its phase diagram is of a simple eutectic type. However, its eutectic is degenerate. The eutectic occurs at ~270 °C. The phase transition in the Ni_3Sn compound, which occurs at 920 °C, is also identified in this phase diagram. However, due to the influence of bismuth, the temperature of this transition decreases to ~905 °C. A homogeneous region based on Ni_3Sn was observed in the section, and its boundary at room temperature corresponds to 1.5 mol % Bi. Given that nickel-containing alloys are recognized as effective materials for thermoelectric energy sources, the $(Ni_3Sn)_{1-x}Bi_x$ solid solutions identified in this section also hold significant promise for such applications.

Ni_3Sn_2–Bi Section

The phase diagram of this section also exhibits a simple eutectic type, indicating it is a quasi-binary system. The eutectic occurs at approximately 267 °C and

~99 mol % Bi. The phase diagram indicates no solid solution formation based on Ni_3Sn_2. As eutectic compositions inherently form composite materials and are utilized in switching and contact networks, the eutectic compositions identified in this section are promising for solid-state electronic applications.

To determine the coordinates of nonvariant points, monovariant curves, isotherms, and primary crystallization fields in the projection of the Ni–Bi–Sn ternary system, a series of non-quasibinary sections were investigated. Let us elaborate on some of these sections which sufficiently reflect the nature of chemical interactions in the ternary system.

$Bi_{0.75}Sn_{0.25}$–$Ni_{0.5}Sn_{0.5}$ Section

The initial components of this section ($Bi_{0.75}Sn_{0.25}$–$Ni_{0.5}Sn_{0.5}$ and $Ni_{0.5}Sn_{0.5}$) are analogous to mechanical mixtures in their respective Bi–Sn and Ni–Sn binary systems. Using the aforementioned physicochemical analysis methods, the phase diagram for the $Bi_{0.75}Sn_{0.25}$–$Ni_{0.5}Sn_{0.5}$ section was constructed (Fig. 1).

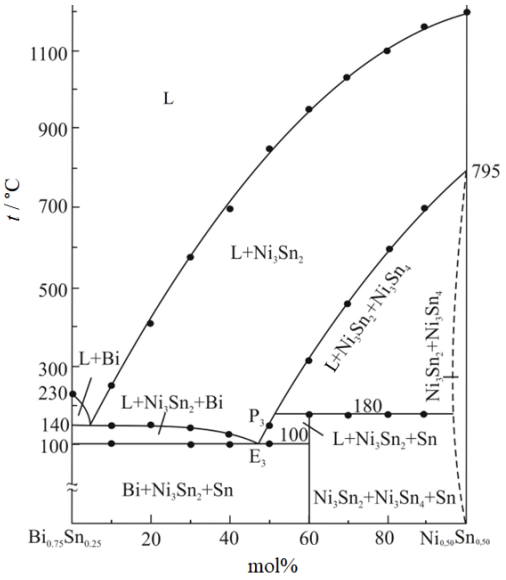

Fig. 1. Phase diagram of the $Bi_{0.75}Sn_{0.25}$–$Ni_{0.5}Sn_{0.5}$ section.

It is evident from the figure that the $Bi_{0.75}Sn_{0.25}$–$Ni_{0.5}Sn_{0.5}$ section is non-quasibinary and passes exclusively through the Bi–Ni_3Sn_2–Sn subsystem region, crossing two crystallization fields of Bi and Ni_3Sn_2. Consequently, its liquidus comprises two branches corresponding to the primary crystallization of Bi and Ni_3Sn_2.

These branches intersect where the section crosses the monovariant curve at 130 °C. At this point, binary crystallization (L+Ni_3Sn_2+Bi) begins and proceeds along the monovariant curve until it reaches the four-phase ternary eutectic point

(L ↔ Bi+Ni_3Sn+Sn) at 100 °C (48 mol % $Ni_{0.5}Sn_{0.5}$). In the sub-solidus region, within the concentration range of 0–60 mol % $Ni_{0.5}Sn_{0.5}$, a mixture of three phases (Bi+Ni_3Sn_2+Sn) precipitates. In the region rich in $Ni_{0.5}Sn_{0.5}$, the peritectic reaction L + Ni_3Sn_2 ↔ Ni_3Sn_4 starts at 795 °C (p_3), leading to the formation of the Ni_3Sn_4 compound. This reaction culminates in a four-phase ternary nonvariant peritectic equilibrium P_3 (L + Ni_3Sn_2 ↔ Ni_3Sn_4 + Sn) at 180 °C. Consequently, within the concentration range of 60–100 mol % $Ni_{0.5}Sn_{0.5}$, a mixture of Ni_3Sn_2 + Ni_3Sn_4 + Sn phases crystallizes. Practically no solubility was observed for either component.

The $Ni_{0.5}Sn_{0.5}$–Sn section is non-quasibinary. According to singular triangulation, it passes through the regions of three sub-systems formed by the quasibinary sections Bi–Ni_3Sn and Bi–Ni_3Sn_2: (Bi–Ni–Ni_3Sn (I), Bi–Ni_3Sn–Ni_3Sn_2 (II) and Bi–Ni_3Sn_2–Sn (III)), Fig. 2.

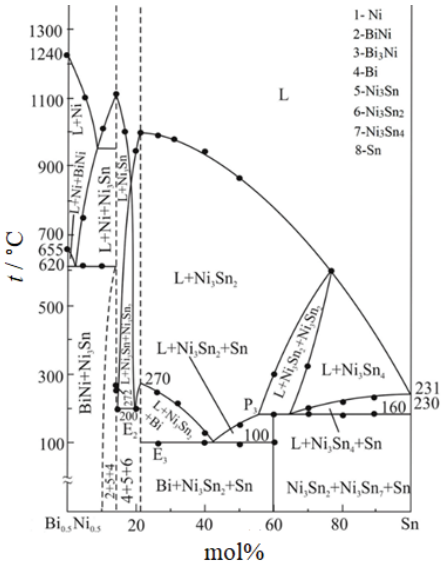

Fig. 2. Phase diagram of the $Bi_{0.5}Ni_{0.5}$–Sn section.

Therefore, the phase diagram of the $Bi_{0.5}Ni_{0.5}$–Sn section is divided into three parts. The first part (I) covers the concentration range of 0–14 mol % Sn. Here, the liquidus curve consists of two branches that intersect at the point where the section crosses the monovariant curve. These branches correspond to the primary crystallization of Ni and the Ni_3Sn compound.

The first component is within the composition of the BiNi compound, which is formed in the Bi—Ni binary system at 654 °C by the peritectic reaction L + Ni ↔ BiNi and melts incongruently. Here, the formation temperature of this compound begins to decrease. Finally, at 620 °C, both phases (L+Ni) that form the BiNi compound are in stoichiometric composition, so both are consumed simul-

taneously, and the process does not reach the four-phase ternary peritectic. As a result, two phases (BiNi+Ni_3Sn) precipitate in the subsolidus region.

The second part (II) of the $Bi_{0.5}Ni_{0.5}$–Sn section's phase diagram covers the concentration range of 14–22 mol % Sn. Here, the nature of the chemical interaction is relatively simple. The liquidus consists of two branches that characterize the primary crystallization of Ni_3Sn and Ni_3Sn_2, intersecting at the point where the section crosses the next monovariant curve. Crystallization ends at 200 °C with the four-phase ternary eutectic equilibrium L ↔ Bi + Ni_3Sn + Ni_3Sn_2.

In the subsolidus, a mixture of Bi+Ni_3Sn+Ni_3Sn_2 phases precipitates. In the third part (III), which falls within the Bi–Ni_3Sn_2–Sn quasi-ternary region (22–100 mol % Sn), the chemical interaction is somewhat more complex. Here, the $Bi_{0.5}Ni_{0.5}$–Sn section intersects two primary crystallization fields (Ni_3Sn_2 and Ni_3Sn_4), so it consists of two branches. The branches intersect at the point (76 mol % Sn) where the section crosses the monovariant curve that borders these primary crystallization fields, and binary crystallization (L+Ni_3Sn_2+Ni_3Sn_4) begins at that point.

In the phase diagram, within the concentration range of 22–60 mol % Sn, crystallization in the subsolidus ends with the four-phase ternary eutectic (E_3) reaction (L ↔ Bi + Ni_3Sn_2 + Sn) at 100 °C. Within the 60–100 mol % Sn concentration range, it ends with the four-phase ternary peritectic (P_3) equilibrium (L + Bi + Ni_3Sn_2 ↔ Ni_3Sn_4 + Sn) at 180 °C.

$Bi_{0.6}Ni_{0.4}$–Sn Section

This section is parallel to the $Bi_{0.5}Ni_{0.5}$–Sn section (Fig. 2) and passes through a relatively close concentration plane. In other words, the $Bi_{0.6}Ni_{0.4}$–Sn section also passes through the regions of three subsystems: Bi–Ni–Ni_3Sn (I), Bi–Ni_3Sn––Ni_3Sn_2 (II) and Bi–Ni_3Sn_2–Sn (III). Its phase diagram (Fig. 3) is non-quasibinary and is divided into three parts. With the exception of the first part (I), the nature of the chemical interaction in the second (II) and third (III) parts is almost identical.

In the first part (I), the liquidus consists of two branches because the section intersects the monovariant curve at the boundary of the primary crystallization fields of the Ni and Ni_3Sn phases (6 mol % Sn). Crystallization passes through the nonvariant peritectic equilibria P_1 (L + Ni ↔ BiNi + Ni_3Sn, 600 °C) and P_2 (L + BiNi ↔ Bi_3Ni + Ni_3Sn, 430 °C) and ends at the four-phase ternary eutectic equilibrium E_1 (L ↔ Bi + Bi_3Ni + Ni_3Sn, 250 °C). In the subsolidus, Bi+Bi_3Ni+Ni_3Sn phases crystallize together.

In the second (II) and third (III) parts of the phase diagram, the shape of the liquidus curve is similar to that in the $Bi_{0.5}Ni_{0.5}$–Sn section. However, crystallization ends with the nonvariant eutectic equilibria E_2 (II – 12–18 mol % Sn), E_3 (III – 18–66 mol % Sn), and the nonvariant peritectic equilibrium P_3 (III – 66––100 mol % Sn), with some differences in concentration ranges. As a result, dep-

ending on the concentration, a mixture of Bi+Bi_3Ni+Ni_3Sn_2, Bi+Bi_3Ni_2+Sn or Ni_3Sn_2+Ni_3Sn_4+Sn phases precipitates in the subsolidus.

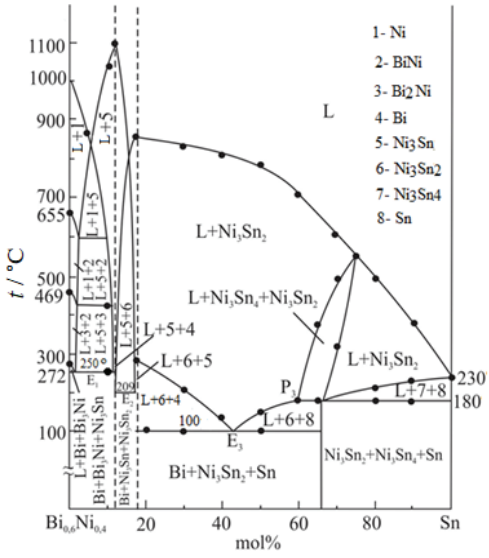

Fig. 3. Phase diagram of the $Bi_{0.6}Ni_{0.4}$–Sn section.

$Bi_{0.57}Sn_{0.43}$–Ni Section

This section is perpendicular to the non-quasibinary sections we have described (Fig. 4). $Bi_{0.57}Sn_{0.43}$ is the only binary eutectic (e_7) composition observed in the Bi–Sn system. Studying the phase equilibrium in the $Bi_{0.57}Sn_{0.43}$–Ni section allows us to follow the chemical interaction occurring in the following subsystems of the Bi–Ni–Sn ternary system: Bi–Ni–Ni_3Sn_4 (I), Bi–Ni_3Sn–Ni_3Sn_2 (II) and Bi––Ni_3Sn_2–Sn (III). The phase diagram is non-quasibinary, and the nature of the chemical interaction there is complex.

The $Bi_{0.57}Sn_{0.43}$–Ni section passes through four primary crystallization fields and intersects three monovariant curves. Therefore, the liquidus of the phase diagram consists of four branches of primary crystallization (Sn, Ni_3Sn_2, Ni_3Sn and Ni).

In the concentration range of 0–44 mol % Ni, the investigated section passes through the region of the Bi–Ni_3Sn_2–Sn (III) subsystem, and crystallization ends at 100 °C in the four-phase ternary eutectic equilibrium (L ↔ Bi + Ni_3Sn_2 + Sn). In the subsolidus, a mixture of three phases (Bi+Ni_3Sn_2+Sn) crystallizes.

In the phase diagram of the $Bi_{0.57}Sn_{0.43}$–Ni section, the chemical interaction in the Bi–Ni_3Sn–Ni_3Sn_2 (II) and Bi–Ni–Ni_3Sn (I) subsystems is further confirmed, as reflected in the previous sections. Specifically, in system (II) (44–56 mol % Ni concentration range), crystallization ends at 200 °C in the three-phase nonvariant

eutectic equilibrium (E_2, L ↔ Bi + Ni_3Sn + Ni_3Sn_2), and in the subsolidus, three phases (Bi+Ni_3Sn+Ni_3Sn_2) crystallize.

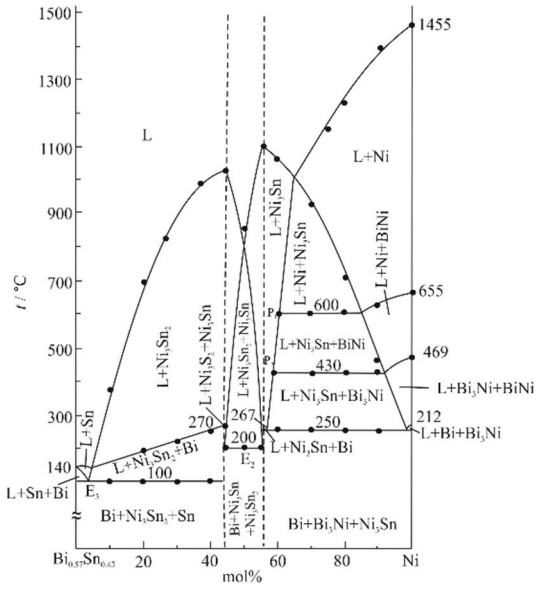

Fig. 4. Phase diagram of the $Bi_{0.57}Sn_{0.43}$–Ni section.

In the concentration range of 56–100 mol % Ni, in the region reflecting the Bi–Ni–Ni_3Sn (I) system, crystallization, as shown in the $Bi_{0.6}Ni_{0.4}$–Sn section, proceeds through the nonvariant peritectic equilibria P_1 (L + Ni ↔ BiNi + Ni_3Sn, 600 °C) and P_2 (L + BiNi ↔ Bi_3Ni + Ni_3Sn, 430 °C) and ends at the four-phase ternary eutectic equilibrium E_1 (L ↔ Bi + Bi_3Ni + Ni_3Sn, 250 °C). In the subsolidus, a mixture of Bi+Bi_3Ni+Ni_3Sn phases precipitates. It should be noted that, as can be seen from the phase diagrams, each of the investigated non-quasibinary sections has corresponding two-phase crystallization regions between their liquidus and solidus lines, which are clearly distinguished by concentration.

Among the studied polythermal sections, a significant solid solubility region based on the initial components was observed in only one, specifically the Ni_3Sn––Bi section. Furthermore, no new ternary or more complex compounds formed in any of the sections for which phase diagrams were constructed. This highlights a discrepancy between our findings and some results reported in the literature.[6–8] The significance of our results, which demonstrate the absence of such new complex compounds, is further emphasized by the principle outlined in reference:[15] the formation of new complex compounds at the contact interface of interacting metals, potentially due to localized heating, can lead to contact failure. Utilizing data from the literature on constituent binary systems, experimental results from the investigated polythermal sections, and analysis of additional samples not lying

on these sections, a projection of the liquidus surface for the Bi–Ni–Sn ternary system was constructed for the first time (Fig. 5).

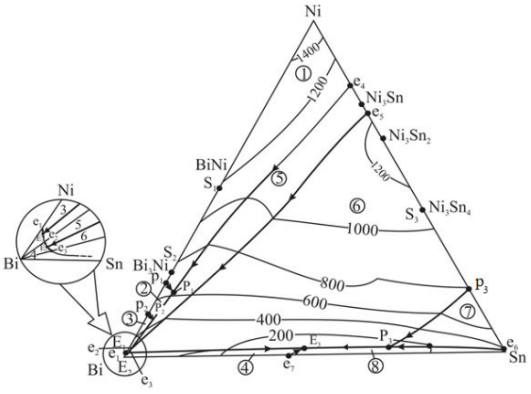

Fig. 5. Projection of the liquidus surface of the Ni–Bi–Sn ternary system with initial crystallization areas: 1 – Ni, 2 – BiNi, 3 – Bi_3Ni, 4 – Bi, 5 – Ni_3Sn, 6 – Ni_3Sn_2, 7 – Ni_3Sn_4, 8 – Sn; the phase equilibrium graph in the bismuth-rich part is highlighted in the lower left of the figure).

As can be seen from the figure, in the projection of the liquidus surface of the Ni–Bi–Sn ternary system, there are 8 primary crystallization fields characterizing the initial components and the newly formed phases, which are separated from each other by 13 monovariant curves (Table I). 7 of the 16 nonvariant equilibria existing in the projection of the system's liquidus surface are three-phase binary eutectics (e_1–e_7), 3 are three-phase binary peritectics (p_1–p_3), 3 are four-phase eutectics (E_1–E_3) and 3 are four-phase ternary peritectics (P_1–P_3).

TABLE I. Nonvariant reactions, monovariant curves, and their temperatures occurring in the Ni–Bi–Sn ternary system

No.	Nonvariant points, monovariant curves	Equilibrium reaction	t / °C
1	e_1	L ↔ Bi + Bi_3Ni	272
2	e_2	L ↔ Bi + Bi_3Sn	270
3	e_3	L ↔ Bi + Ni_3Sn_2	267
4	e_4	L ↔ Ni + Ni_3Sn	1130
5	e_5	L ↔ Ni_3Sn + Ni_3Sn_2	1160
6	e_6	L ↔ Ni_3Sn_4 + Sn	231
7	e_7	L ↔ Bi + Sn	140
8	p_1	L + Ni ↔ BiNi	654
9	p_2	L + BiNi ↔ Bi_3Ni	469
10	p_3	L + Ni_3Sn_2 ↔ Ni_3Sn_4	795
11	E_1	L ↔ Bi + Bi_3Ni + Ni_3Sn	250
12	E_2	L ↔ Bi + Ni_3Sn + Ni_3Sn_2	200
13	E_3	L ↔ Bi + Ni_3Sn_2 + Sn	100
14	P_1	L + Ni ↔ BiNi + Ni_3Sn	600
15	P_2	L + BiNi ↔ Bi_3Ni + Ni_3Sn	430
16	P_3	L + Ni_3Sn_2 ↔ Ni_3Sn_4 + Sn	180
17	e_1E_1	L ↔ Ni_3Sn + Bi	272–250
18	E_1 e_2E_1	L ↔ Bi_3Ni + Bi	250–270–200

TABLE I. Continued

No.	Nonvariant points, monovariant curves	Equilibrium reaction	t / °C
19	$E_2 e_3 E_3$	L ↔Ni_3Sn_2 + Bi	200–267–100
20	e_4P_1	L ↔ Ni + Ni_3Sn	1130–600
21	p_1P_1	L ↔ BiNi + Ni	654–600
22	P_1P_2	L ↔ BiNi + Ni_3Sn	600–430
23	P_2E_1	L ↔ Bi_3Ni + Ni_3Sn	430–250
24	e_5E_2	L ↔ Ni_3Sn + Ni_3Sn_2	1160–200
25	$E_3e_3E_2$	L ↔ Bi + Ni_3Sn_2	100–267–200
26	e_7E_3	L ↔ Bi + Sn	140–100
27	P_3E_3	L ↔ Ni_3Sn_2 + Sn	180–100
28	p_3P_3	L ↔ Ni_3Sn_4 + Ni_3Sn_2	795–180
29	e_6P_3	L ↔ Ni_3Sn_4 + Sn	231–180

The monovariant equilibrium curves were constructed based on the intersection points of the primary crystallization curves in the sections, and their directions were extrapolated according to the nonvariant equilibrium points (Table I) and the projection of the monovariant equilibrium curves drawn along the sides of the concentration triangle.

In the projection of the liquidus surface, isotherms were drawn every 200 °C by graphical interpolation. The consistency of the chemical interaction patterns observed in parallel and perpendicular polythermic non-quasibinary sections, and their mutual confirmation, leaves no doubt about the accuracy of the liquidus surface projection.

The direction of the monovariant equilibrium curves characterizing co-crystallization and the nature of the nonvariant equilibrium points (Table I) are consistent with the geometric parameters of the projection of the Ni–Bi–Sn ternary system's liquidus surface (Fig. 5).

CONCLUSION

The Ni–Bi–Sn ternary system was investigated for the first time using polythermic sections, and their respective phase diagrams were constructed. A projection of the liquidus surface for the ternary system was also determined. This projection revealed the nature of the chemical interactions, identifying 8 primary crystallization fields, 6 ternary nonvariant points and 13 monovariant curves. The absence of new ternary compound formation suggests that the synthesized alloys and eutectic compositions hold potential for use as switching and contact materials in solid-state electronics.

ИЗВОД

ПРОЈЕКЦИЈА ПОВРШИНЕ ЛИКВИДУСА ТЕРНАРНОГ СИСТЕМА Ni–Bi–Sn

CHINGIZ I. ABILOV[1] IKHTIYAR B. BAKHTIYARLY[2], SAYYARA H. SADIGOVA[1], MEHRIBAN SH. HASANOVA[1] и ELMIRA K. GASIMOVA[1]

[1]Azerbaijan Technical University, Baku, Azerbaijan u [2]Institute of Catalysis and Inorganic Chemistry named after academician M. Naghiyev of the Ministry of Science and Education of the Republic of Azerbaijan

Физичко–хемијске анализе спроведене су на шест унутрашњих политермичких пре—сека Ni–Bi–Sn тернарног система, те су конструисани фазни дијаграми тих пресека. Утврђено је да су два пресека била квазибинарна, док су четири била не-квазибинарна. Конструисана је пројекција површине ликвидуса тернарног система. Састављене су једначине за неваријантне равнотежне реакције које се дешавају у тернарном систему и одређене су њихове координате. Откривено је присуство обећавајућих подручја чврстог раствора у неким од унутрашњих пресека тернарног система, а њихове границе на собној температури су одређене. Одсуство нових комплексних једињења и присуство хомогених региона указују на то да би синтетизовани материјали могли бити погодни за примену као преклопни и контактни слојеви у алтернативним изворима енергије.

(Примљено 5. марта, ревидирано 8. маја, прихваћено 15. јуна 2025)

REFERENCES

1. M. Gurtaran, Zh. Zhang, X. Li, H. Dong, *J. Mater. Res. Technol.* **30** (2024) 7476 (https://doi.org/10.1016/j.jmrt.2024.05.136)
2. M. d'Angelo, C. Galassi, N. Lecis, *Energies* **16** (2023) 6409 (https://doi.org/10.3390/en16176409)
3. F. Garmroudi, M. Parzer, A. Riss, C. Bourgès, S. Khmelevskyi, T. Mori, E. Bauer, A. Pustogow, *Sci. Adv.* **9** (2023) (https://doi.org/10.1126/sciadv.adj1611)
4. M. Wolf, J. Flormann, T. Steinhoff, G. Gerstein, F. Nürnberger, H. J. Maier, A. Feldhoff, *Alloys* **1** (2022) 3 (https://doi.org/10.3390/alloys1010002)
5. A. Karati, V. S. Hariharan, S. Ghosh, A. Prasad, M. Nagini, K. Guruvidyathri, R. Ch. Mallik, R. Shabadi, L. Bichler, B. S. Murty, U. V. Varadaraju, *Scr. Mater.* **186** (2020) 375 (https://doi.org/10.1016/j.scriptamat.2020.04.036)
6. G. P. Vassilev, K. I. Lilova, J.-C. Gachon, *J. Alloys Compd.* **469** (2009) 264 (https://doi.org/10.1016/j.jallcom.2008.01.100)
7. S.-K. Seo, M. Cho, H. Lee, *J. Electron. Mater.* **36** (2007) 1536 (https://link.springer.com/article/10.1007/s11664-007-0256-8)
8. N. Milcheva, J. Romanowska, G. Vassilev, *Cent. Eur. J. of Chem.* **9** (2011) 149 (https://link.springer.com/article/10.2478/s11532-010-0128-6)
9. G. Vassilev, T. Kristinova, K. Lilova, J. Gachon, *J. Min. Metall., B* **43** (2007) 141 (https://doi.org/10.2298/JMMB0702141V)
10. N. Milcheva, P. Broz, J. Buršík, P. Vassilev, *Thermochim. Acta* **534** (2012) 41 (https://doi.org/10.1016/j.tca.2012.02.011)
11. Ch. Abilov, S. Sadigova, M. Hasanova, E. Kasumova, *Int. J. Mod. Phys., B* **36** (2022) 2250219 (https://doi.org/10.1142/S0217979222502198)
12. Ch. Abilov, M. Hasanova, E. Kasumova, N. Huseynova, E. Kurbanov, *AIP Conf. Proc.* **3122** (2024) 050013 (https://doi.org/10.1063/5.0216063)
13. Sh. Abdullaeva, F. Mammadov, I. Bakhtiyarly, *Zh. Neorg. Khim.* (*Russ. J. Inorg. Chem.*) **65** (2020) 98 (https://link.springer.com/article/10.1134/S0036023619110020)

14. E. N. Ismayilova, L. F. Mashadiyeva, I. B. Bakhtiyarly, M. B. Babanly, *Kondens. Sredy Mezhfaznye Granitsy* (*Condensed Matter and Interphases*) **25** (2023) 47 (https://journals.vsu.ru/kcmf/article/view/11036/11228)
15. M. I. Zargarova, K. Sh. Kakhramanov, A. A. Mageramov, R. V. Roshal, *Physicochemical basis for the selection of contact materials*, Elm, Baku, 1990 (ISBN: 5-8066-0371-7).

Journal of the Serbian Chemical Society
JSCS-info@shd.org.rs • www.shd.org.rs/JSCS
J. Serb. Chem. Soc. *90* (9) 1131–1146 (2025)
JSCS–5444
Original scientific paper
Published 14 September, 2025

The potential of electrochemical pesticide analyses by green synthesized, waste olive leaves-based, silver nanoparticles

EZGI ADAK[1,2], MERVE KESKIN[3] and HALIT ARSLAN[1]*

[1]*Department of Chemistry, Faculty of Science, Gazi University, 06500, Ankara, Turkiye,* [2]*Gazi University Graduate School of Natural and Applied Science, 06500, Ankara, Turkiye and* [3]*Vocational School of Health Services, Bilecik Seyh Edebali University, 11210, Bilecik, Turkiye*

(Received 18 November 2024, revised 24 January, accepted 24 July 2025)

Abstract: Pesticides are chemicals that negatively affect human health and the environment. Unconscious use of pesticides creates residues in foods or agricultural products and it also cause water and soil pollution. Quick and easy determination of pesticide residues is important for environmental inspections. For this reason, it is necessary to develop alternative methods to traditional methods such as chromatography for the determination of pesticide residues. Electrochemical sensors are new generation analytical devices developed for the determination of pesticides that enable rapid and practical analysis. Carbon paste electrodes used in the design of electrochemical sensors are modified using different materials such as silver nanoparticles. Silver nanoparticles used for modification could be synthesized using chemical methods, but these methods are harmful to the environment because toxic chemicals are used in the synthesis procedure. For this reason, the green synthesis technique was developed as an alternative to chemical techniques. In this study, waste olive leaves were used in green synthesis of silver nanoparticle as an electron precursor, the nanoparticles (OL-AgNPs) were characterized and modified carbon paste electrodes were prepared. The prepared modified carbon paste electrodes were used in the determination of thiocholine (as a product of hydrolysis of acetyl thiocholine by enzymatic reactions), H_2O_2 (as a product of many oxireductase enzyme reactions) and the widely used pesticides cyprodinil and mepanipyrim. The results showed that the modified carbon paste electrodes were more sensitive than the carbon paste electrodes for all analytes. It was clear that the modified carbon paste electrodes could be used in pesticide determinations.

Keywords: biological synthesis; modified carbon paste electrode; nanoparticle; sustainability; voltammetry; agricultural waste.

* Corresponding author. E-mail: halit@gazi.edu.tr
https://doi.org/10.2298/JSC241118056A

INTRODUCTION

Pesticides are chemicals used to increase agricultural products' yield and quality and protect forests and plantations.[1] Cyprodinil and mepanipyrim are the active ingredients of some commonly used pesticides.[2] Residues of these pesticides are found in agricultural products.[3] Unconscious and excessive use of these pesticides affects the environment and human health negatively.[2] Excessive pesticide residues cause many diseases and their determination in trace amounts is crucial.[4] Also, pesticides inhibit the important enzymes such as acetylcholinesterase (AChE) which is an key enzyme for the functioning of the central nervous system and muscle.[5] Thiocholine and acetate are the products of acetylthiocholine ester (ATCh) hydrolysis with acetylcholinesterase (AChE).[6] In addition to determination of thiocholine, H_2O_2 monitoring could be provide the indirectly measurement of choline which react with chloline oxidase, an oxireductase enzyme is important for central nervous system, in the pesticide determinations.[7] The irreversible inhibition of the activity of cholinesterases and acetylcholinesterase could have an important role to develop novel biosensors to determine pesticides.[7] Therefore, thiocholine and H_2O_2 are two important analytes for the determinations of pesticides by biosensors.

Traditional chromatographic methods such as mass spectrometry, capillary electrophoresis and high-performance liquid chromatography are used for the analysis of pesticides in the environment.[8] However, they have several drawbacks, including complexity, labor-intensive sample preparation and the need for expensive equipment and skilled personnel.[8] In addition, electrochemical methods are used for the determination of pesticides due to their high sensitivity and selectivity and short analysis time compared to other methods. The use of modified electrodes in electrochemical studies is becoming widespread.[9,10] Modified electrodes increase the selectivity and sensitivity of the electrodes could be prepared by adding conductive substances to the electrode material.[11–15] The range of electrochemical methods is expanded by this variety. Nanoparticles could be used when modifying electrodes.[16] Nanoparticles with sizes between 1–100 nm show unique physical and chemical properties.[17,18] They are widely used in many fields, especially in medicine, biotechnology, biomedical, textile, agriculture, defense industry, cosmetics and chemical sectors.[19,20] The most feasible technique for producing nanoparticles in a cost-effective, straightforward, safe and ecologically friendly manner without using hazardous chemicals, high pressure, heat, or energy is called green synthesis.[21,22] Agricultural and domestic wastes are increasing by the time as a result of population growth. The agricultural wastes such as olive, grape seeds, pine sawdust, almond, nut, hazelnut, pecan, corn, peach and many more can be used in green synthesis of nanoparticles.[23] Olive leaves are found in large quantities as residue in olive oil industries in Türkiye. Therefore, olive leaves can be evaluated as a cheap raw material that can be used as a useful resource for high

value-added products.[24] Phytochemicals present in plant extracts could be used as a precursor to reduce metal ions to metallic nanoparticles in the green synthesis process.[25,26] Due to their easy accessibility, using plant extracts in green synthesis of nanoparticles is an important research topic in the field of bionanotechnology today.[27–29] Factors such as the pH, temperature, reaction time, concentration of metal salt, dose of the plant extract and pressure affect the synthesis and application of metal nanoparticles through green synthesis from plant extract.[30] For example, it has been observed that as the pH value of the plant extract increases, the nanoparticle formation rate increases and the nanoparticle size decreases.[31] After green synthesis, characterization studies of nanoparticles should be carried out. Nanoparticles can be separated by their size, surface area, and distribution pattern. UV–Vis absorption spectroscopy, scanning electron microscopy (SEM), energy dispersive X-ray analysis (EDX), X-ray diffraction (XRD), Fourier transform spectroscopy (FTIR), *etc*., techniques are commonly used in the characterization of nanoparticles.[22,32] Metal nanoparticles are used in various industrial and biological applications.[19] They are widely used in nanotechnology fields due to their properties such as electrical conductivity.[33]

In this study, silver nanoparticles were synthesized and characterized. Their application in the determination of pesticides, H_2O_2 and thiocholine using electrochemical techniques was also examined. The synthesized silver nanoparticles were used to modify the carbon paste electrode to the voltammetric determination. The resulting silver nanoparticles modified carbon paste electrode showed a better performance than the carbon paste electrode. This study revealed that trace amounts of various pesticides and materials can be determined voltammetrically using a modified carbon paste electrode with silver nanoparticles.

EXPERIMENTAL

Apparatus and reagents

For electrochemical studies, CH Instruments, model 1230B, electrochemical analyzer was used.

Three electrode cell systems were used in experimental studies. Platinum wire (counter electrode) and Ag/AgCl (3 M KCl) reference electrode were employed, and as the working electrode, green synthesized waste olive leaves based-silver nanoparticles modified carbon paste electrode (OL-AgNPs-MCPE) was used in the electrooxidation studies.

Acetylthiocholine chloride (ATCh), acetylcholinesterase (AChE), mepanipyrim, cyprodinil, hydrogen peroxide, silver nitrate and all other chemicals were obtained from Sigma Aldrich.

Green synthesis and characterization of silver nanoparticles

To prepare olive leaves extract, waste olive leaves were obtained from Bodrum district of Muğla province during the olive harvest period. The supplied leaves were cleaned. It was then dried at 45 °C. After the dried plant leaves were ground, a certain amount was weighed, boiled pure water was added and kept for 60 min, and after cooling, they were filtered with filter paper and stored in a dark bottle at 4 °C until use. Then, the extract was mixed with 0.05 M $AgNO_3$

and stirred at 60 °C for 45 min. Finally, the obtained solution was centrifuged at 10000 rpm for 15 min to acquire, olive leaves-based, silver nanoparticles.[26]

The synthesized nanoparticles (OL-AgNPs) were characterized by UV absorption spectroscopy (T80+ high-performance double-beam spectrophotometer from PG Instruments), scanning electron microscopy (SEM, Zeiss/Supra 40 VP), energy dispersive X-ray (EDX), zeta potential (Malvern/Nano-ZS), Fourier transform infrared spectroscopy (FTIR, Thermo Fisher) and X-Ray diffraction analysis.

Preparation of electrodes

To prepare working electrode, a carbon paste electrode (CPE) was prepared by mixing carbon powder with mineral oil and the paste was filled into the electrode's hollow.[34] The mixture was dried for 24 h. After that, the prepared electrode was cleaned, polished and sanded to be used in electrochemical analyses (Fig. 1 a).[34]

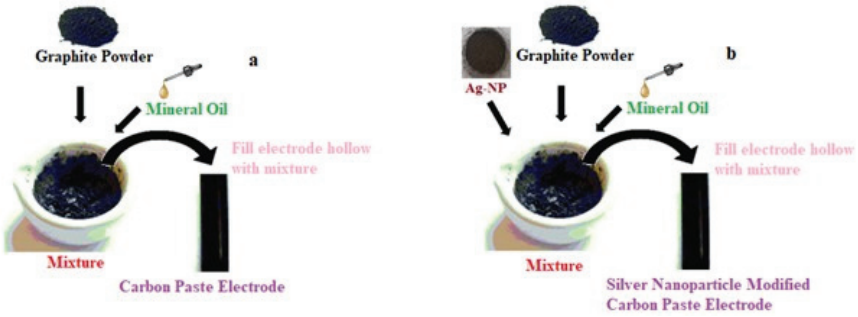

Fig. 1. Preparation of electrodes; a) carbon paste electrode (CPE) and b) silver nanoparticles modified carbon paste electrode (OL-AgNPs-MCPE).

A green synthesized waste olive leaves-based silver nanoparticles modified carbon paste electrode (OL-AgNPs-MCPE) was prepared by mixing carbon powder with mineral oil and 8 mg silver nanoparticles, respectively.[35] The pastes were filled into the hollow electrodes. The mixtures were dried for 24 h. The prepared electrode was polished and sanded to use in electrochemical analyses (Fig. 1 b).

Electrochemical measurements

All electrochemical measurements were performed by using square wave voltammetry. To determine H_2O_2, square wave voltammograms were applied, both carbon paste (CP) and modified carbon paste (MCP) electrodes in pH 2.0 Britton–Robinson (BR) buffer solution (f = 15 Hz; ΔE = 25 mV). Increasing concentrations of H_2O_2 solutions were added to the solution medium, voltammograms were taken and current changes were observed against increasing concentration. The analyses were performed, both CPE and OL-AgNPs-MCPE and the current changes were compared.

To determine the thiocholine, voltammograms were applied to both CP and MCP electrodes in 10 mL pH 7.5 BR buffer solution and 100 µL acetylcholine esterase (AChE) enzyme (f =15 Hz; ΔE = 25 mV). Increasing concentrations of acetylthiocholine solutions (ATCh) were added to the solution medium, voltammograms were taken and current changes were observed against increasing concentration. The analyses were performed both CPE and OL-AgNPs--MCPE and the current changes were compared. The catalyzes of acetylthiocholine to thiocholine by acetylcholine esterase is presented (Fig. 2). Acetylthiocholine is hydrolyzed by the enz-

yme acetylcholinesterase into thiocholine and acetic acid. The thiocholine is oxidized by dimerization *via* $2H^+$ loss. The oxidation reaction of thiocholine has been thoroughly investigated.

$$\text{Acetylthiocholine} + H_2O \xrightarrow{\text{AChE}} \text{Thiocholine} + \text{Acetic acid}$$

$$2\text{Thiocholine}_{(red)} \rightarrow \text{Thiocholine}_{(ox)}(\text{dimeric}) + 2H^+ + 2e^-$$

Fig. 2. Reaction mechanism of hydrolyzing acetylthiocholine by AChE.

To determine cyprodinil and mepanipyrim (Fig. 3), square wave voltammograms were applied to both CP and MCP electrodes in pH 2.0 BR buffer solution (f = 15 Hz; ΔE = 25 mV). Increasing concentrations of cyprodinil and mepanipyrim solutions were added to the solution medium, voltammograms were taken and current changes observed against increasing concentration. The analyses were performed both CPE and OL-AgNPs-MCPE and the current changes compared. All analyses were performed for cyprodinil and mepanipyrim separately.

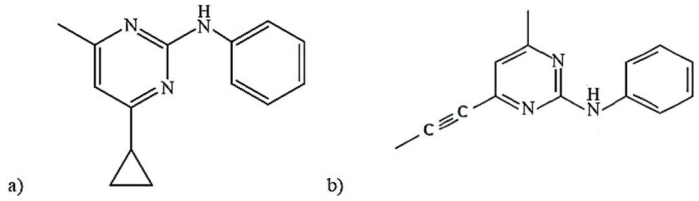

Fig 3. Chemical structre of cyprodinil (a) and mepanipyrim (b).

RESULTS AND DISCUSSION

UV–Vis spectroscopy can be used as an easy and dependable way to check the stability of the nanoparticles.[36] The progress of the reaction following its plasmon absorption bands at λ_{max} values was monitored for Ag nanoparticle evolution. Maximum absorbance at 415 nm was seen for silver nanoparticles by UV–Vis absorption spectroscopy technique. The literature search revealed that, a peak around 410 nm stands for silver nanoparticles.[37] The UV–Vis spectra at different pH, temperature, time and $AgNO_3$ concentration were recorded during the evolution of the Ag nanoparticles (Fig. 4).

The formation of silver nanoparticles can be observed through UV–Vis spectroscopy, with peak formation occurring between 395 and 425 nm. The pH of the plant extract used in the formation of silver nanoparticles has been found to be effective. As the pH of the plant extract increases, the amount of synthesized silver nanoparticles increases, and the size of the synthesized nanoparticles decreases.[38,39] To investigate the effect of the pH value of the olive leaf extract on nanoparticle formation, nanoparticles were synthesized using solutions with pH values ranging from 5.0 to 11.0, and measurements were taken using UV–Vis spectroscopy. It was observed that as the pH of the plant extract increased, the absorbance at 410 nm also increased, with the highest absorbance value measured at pH

10 (Fig. 5a). The obtained results were compatible with alternative methods of Ag nanoparticle synthesis in the literature.[40,41]

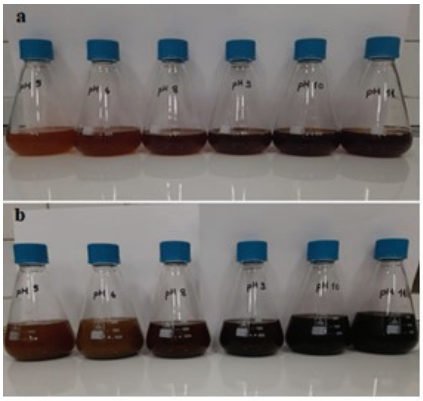

Fig. 4. a) The change in the color with changing pH of olive leaves extract in the pH range of 5.0––11.0 and b) silver nanoparticles synthesized using olive leaves extract in the pH range of 5.0––11.0 (60 min at 60 °C).

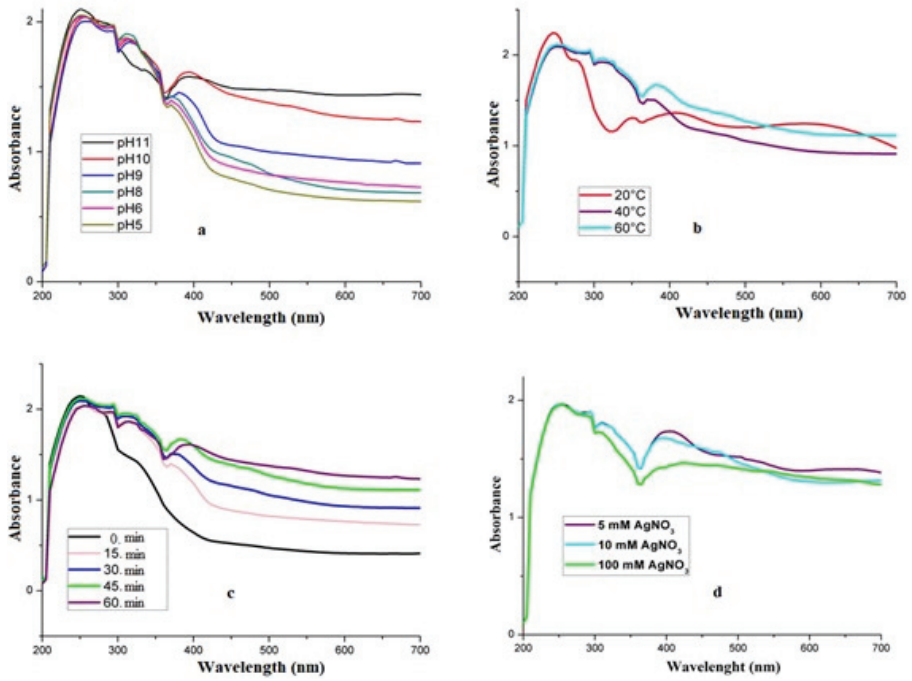

Fig. 5. UV–Vis spectra of silver nanoparticles for determination of optimal; a) pH, b) temperature, c) time and d) $AgNO_3$ concentration.

Another parameter affecting nanoparticle formation is temperature. It has been observed that as the temperature increases, the formation of nanoparticles also increases.[42] The formation of nanoparticles synthesized using extracts at temperatures ranging from 20 to 60 °C was monitored using UV–Vis spectroscopy. It was

observed that as the temperature increased, the absorbance peak at 410 nm also increased. Higher temperatures were not used in the experiments due to the potential degradation of the plant extract at elevated temperatures. The optimal value has been determined to be 60 °C (Fig. 5b).

The time parameter also affects nanoparticle formation.[43] The absorbance of the peak observed at 410 nm increased until the 45th min. At 60 °C, a decrease in absorbance was observed at the 60th min, which was thought to be due to aggregation and/or agglomeration. As a consequence, the optimal time for synthesizing silver nanoparticles using olive leaves extract was selected as 45 min (Fig. 5c). Studies have shown that higher $AgNO_3$ concentrations result in larger particle sizes.[44] High $AgNO_3$ concentrations negatively affect nanoparticle formation due to aggregation and/or agglomeration. Therefore, at lower $AgNO_3$ concentrations, more silver nanoparticles were formed, and higher absorbance values were measured at 410 nm. Finally, the optimization of synthesis was completed after determining the optimum $AgNO_3$ concentration (Fig 5d). A summary of the optimal parameters for synthesizing silver nanoparticles using olive leaves extract is given in Table I.

TABLE I. Optimum parameters for the green synthesized waste olive leaves-based silver nanoparticles

Parameter	Optimum value
pH	10
Temperature, °C	60
Time, min	45
$AgNO_3$ concentration, mM	5

A review of the literature reveals numerous studies in which silver nanoparticles are synthesized using aqueous extracts. The fluctuations observed in the UV peaks are not believed to be due to the use of aqueous extracts. Instead, these fluctuations are thought to be caused by the heterogeneity of the solution.

XRD was used to analyze the structure of OL-AgNPs. The five separate diffraction peaks of the 2θ values of 38.12, 44.28, 64.43, 77.48 and 81.54° can be assigned the planes of (111), (200), (220), (311) and (222), respectively (Fig. 6), indicating that the silver nanoparticles are crystalline and face-centered cubic (fcc) structure in nature.

FT-IR spectra of olive leaves extract and silver nanoparticles synthesized using olive leaves extract are given in Fig. 7, and corresponding data in Table II.

The spectra obtained as a result of the FT-IR analysis determined the presence of phytochemicals properties found in the essence of the olive leaves used in the synthesis of OL-AgNPs, and responsible for the reduction of silver nanoparticles. The band observed at 3309.81 cm^{-1} in the olive leaves extract, 3276.99 cm^{-1} in the synthesized OL-AgNPs, the bands observed at 1634.04, 1629.30, 666.83 and

644.56 cm^{-1} in the olive leaves extract and synthesized OL-AgNPs, respectively. Additionally, a band at 2358.35 cm^{-1} was detected in the FT-IR spectrum of OL--AgNPs. These functional molecules can be found with silver nanoparticles. The band observed at 3309.81 cm^{-1} indicate O–H stretching properties. These band indicates the presence of alcohols and phenols (O–H).[45] The band at 1634.04 cm^{-1} corresponded to the C=O stretching of alcohols.[46] And, the band at 666.83 cm^{-1} indicated chloroalkanes (C–X) stretching properties.[47] FT-IR results show that green synthesis of silver nanoparticles with plant extracts, primary and secondary metabolites such as sugars, phenolics, flavonoids, terpenes, etc. were functionally activated in the process.[48]

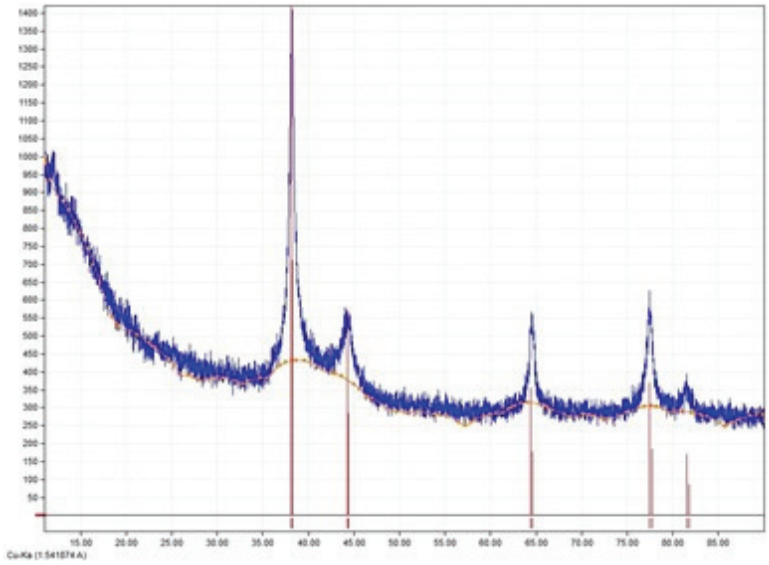

Fig. 6. XRD pattern of OL-AgNPs synthesized using olive leaves extract.

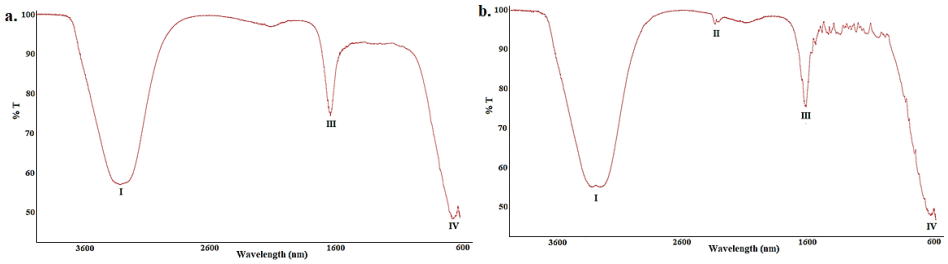

Fig. 7. FTIR spectra of: a) olive leaves extract and b) silver nanoparticles synthesized using olive leaves extract.

The zeta potential of OL-AgNPs was determined –26.7 mV (Fig. 8).

TABLE II. The peak list (cm^{-1}) of olive leaves extract and OL-AgNPs

Sample	I	II	III	IV
a. Olive leaves extract	3309.81	–	1634.04	666.83
b. Silver nanoparticles synthesized using olive leaves extract	3276.99	2358.35	1629.30	644.56

Zeta potential is the electrical charge on the surface of the surrounding material. For the high stability and stability of the AgNP colloid, the zeta potential should be in high negative value, which prevents the particles from sticking together or aggregating. Additionally, nanoparticles with increased negative charge values can enter the cell more easily.[49]

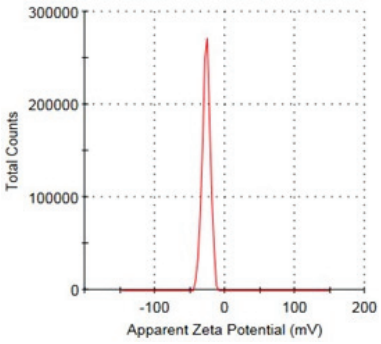

Fig 8. Zeta potential of OL-AgNPs.

Energy diffraction X-ray (EDX) is carried out to analyze the dispersed size distribution of nanoparticle components.[50] The elemental composition of silver in OL-AgNPs was determined as 86.25 % for the normalized atomic value. OL--AgNPs showed a characteristic optical absorption peak at nearly 2.8 keV due to surface plasmon resonance (Fig. 9).

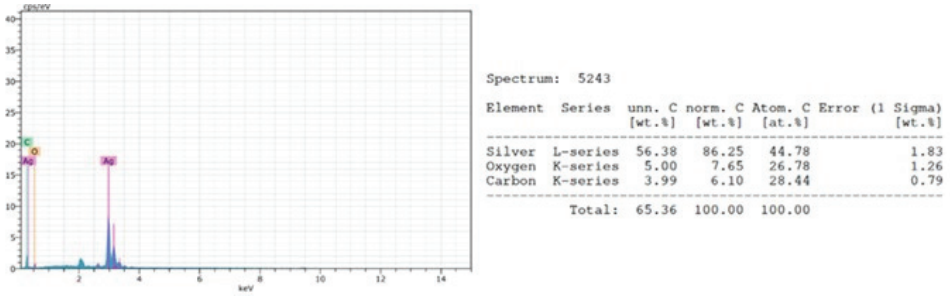

Fig. 9. Elemental composition of OL-AgNPs by EDX analysis.

Identification peaks for the main silver (Ag) emission energies were shown and these peaks match the spectrum, indicating that silver had been accurately

determined. The average particle sizes were found 85 nm (Fig. 10). The results obtained in this study were compatible with the literature (Table III).

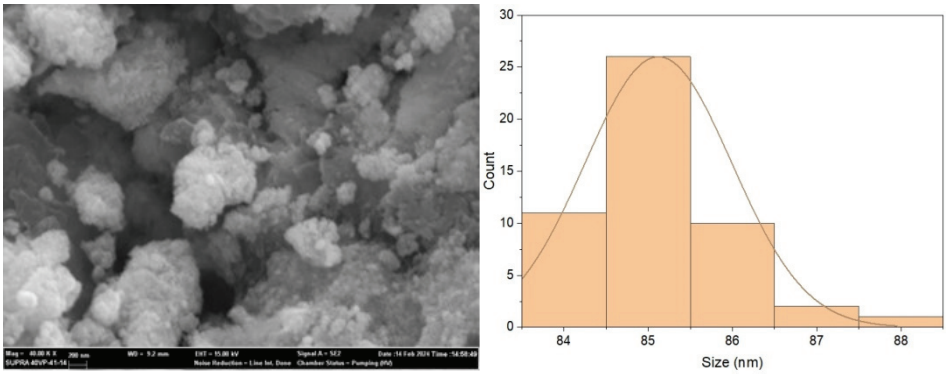

Fig. 10. SEM images and histogram of OL-AgNPs.

TABLE III. Comparison of optimum parameters for the green synthesized silver nanoparticles

Natural source of reducing materials	pH	Temperature °C	Time min	Size of silver particles, nm	Reference
Eucalyptus oleosa	–	25	960	45	51
Lemon	7	80	240	50	52
Hibiscus rosasinensis leaves	6	70	30	43	53
Olive leaves	8	22	52	50	54
Moringa oleifera leaves	–	Direct sunlight	60	57	55
Olive leaves	10	60	45	85	This study

Table IV provides the limit of detection (*LOD*) values for cyprodinil and mepanipyrim pesticides determined using different methods. It is anticipated that the electrodes prepared with the synthesized nanoparticles will enable the detection of these pesticides with lower *LOD* values.

TABLE IV. Comparison of *LOD*s of some methods developed for the determination of pesticides

Method used	Pesticide	*LOD*	Reference
Gas chromatographic determination	Cyprodinil	0.05 mg/kg	56
High-performance liquid chromatography–diode array detection	Cyprodinil	42.9 µg/L	57
QuEChERS method coupled with UPLC-MS/MS	Cyprodinil	below 0.4 µg/kg	58
Square wave stripping voltammetric determination	Cyprodinil	0.076 mg/L	59
QuEChERS method coupled with UPLC-MS/MS	Mepanipyrim	below 0.4 µg/kg	58
Single drop microextraction and gas chromatography––mass spectrometry	Mepanipyrim	0.03 µg L^{-1}	60
Liquid chromatography-tandem mass spectrometry	Mepanipyrim	0.10 µg /kg	61

1.0×10^{-3} M H_2O_2 stock solution was used to compare the sensitivity of CPE and OL-AgNPs-MCPE to H_2O_2. Fig. 11 shows that OL-AgNPs-MCPE is more than 50 times more sensitive to H_2O_2 than CPE.

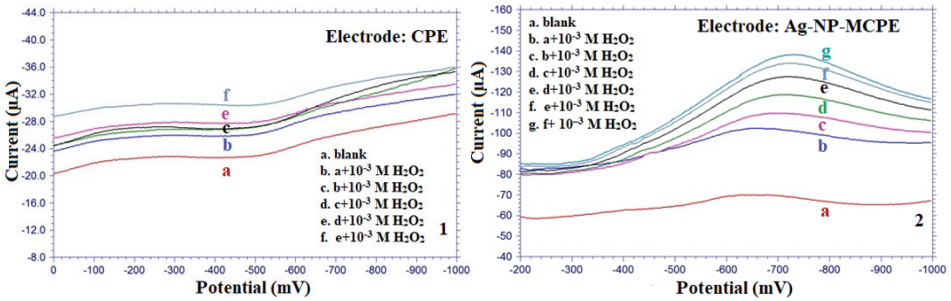

Fig. 11. Square wave voltammograms for H_2O_2 on: 1) CPE and 2) OL-AgNPs-MCPE (pH 2.0 BR buffer solution; f = 15 Hz; ΔE = 25 mV).

It was clear that the prepared OL-AgNPs-MCPE had a good performance in detection of H_2O_2. Different biosensors, which are based on measuring H_2O_2, could be designed by using OL-AgNPs-MCPE. 2.0×10^{-3} M mepanipyrim stock solution was used to compare the sensitivity of CPE and OL-AgNPs-MCPE to mepanipyrim. Fig. 11 shows that OL-AgNPs-MCPE was more than 4 times sensitive to mepanipyrim than CPE (Fig. 12).

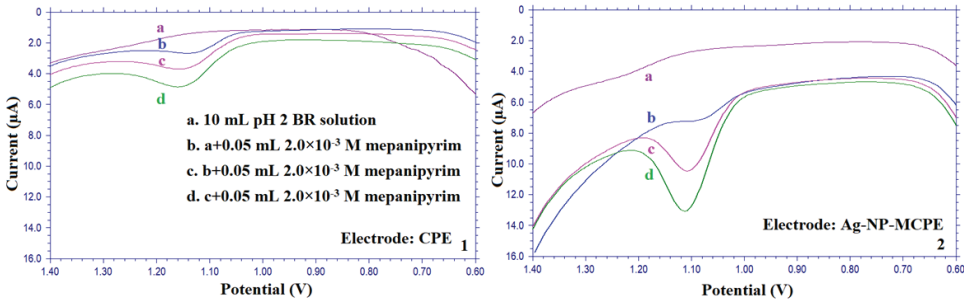

Fig. 12. Square wave voltammograms for mepanipyrim on: 1) CPE and 2) OL-AgNPs-MCPE (pH 2.0 BR buffer solution; f = 15 Hz; ΔE = 25 mV).

1.0×10^{-3} M cyprodinil stock solution was used to compare the sensitivity of CPE and OL-AgNPs-MCPE to cyprodinil. Fig. 12 shows that OL-AgNPs-MCPE was 3 times more sensitive to cyprodinil than CPE (Fig. 13).

1.0×10^{-4} M acetylthiocholine chloride (ATCh) and acetylcholinesterase (AChE) were used for the electrochemical determination of thiocholine. Fig. 13 shows that the peak was not observed at CPE for thiocholine. OL-AgNPs-MCPE is more

sensitive to thiocholine than CPE. The obtained currents at nearly 850 mV were plotted against the thiocholine concentration and the linearity showed (Fig. 14).

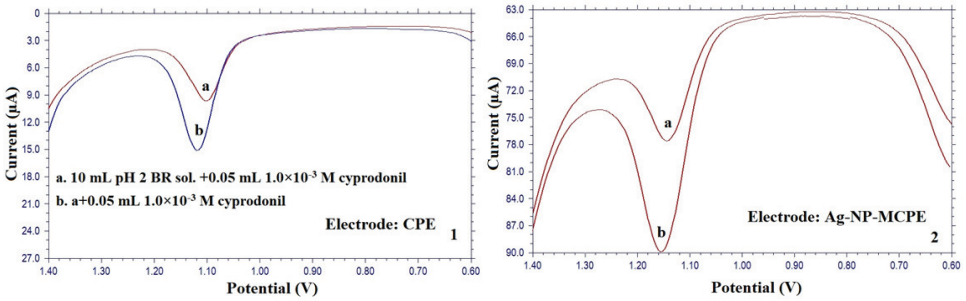

Fig. 13. Square wave voltammograms for cyprodinil on: 1) CPE and 2) OL-AgNPs-MCPE (pH 2.0 BR buffer solution; f = 15 Hz; ΔE = 25 mV).

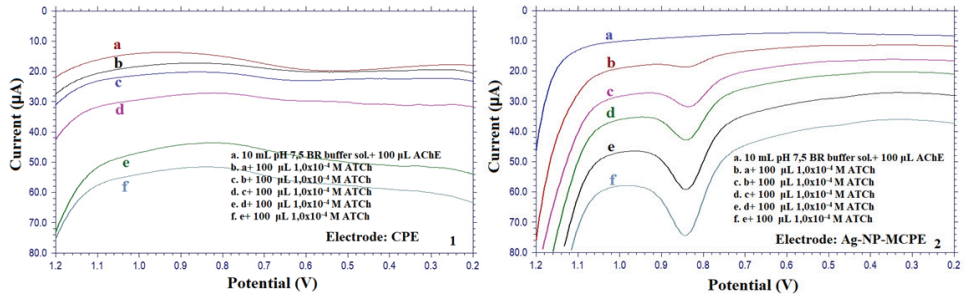

Fig. 14. Square wave voltammograms for thiocholine on 1) CPE and 2) OL-AgNPs-MCPE (pH 2.0 BR buffer solution; f = 15 Hz; ΔE = 25 m).

As a result, this study showed a successful approach to synthesizing silver nanoparticles using olive leaves extract, which could be used in electrochemical determination of H_2O_2, mepanipyrim, cyprodinil and thiocholine.

CONCLUSION

In this study, a new modified carbon paste electrode was prepared for the determination of the most commonly used pesticides (mepanipyrim and cyprodinil), H_2O_2 and thiocholine. For this purpose, eco-friendly silver nanoparticles were synthesized using waste olive leaves extract. In addition, the optimal parameters for synthesizing silver nanoparticles, using olive leaves extract, and characterization were studied. The application of silver nanoparticles in the preparation of modified carbon paste electrodes provides successful. Voltammetric determination of H_2O_2, mepanipyrim, cyprodinil and thiocholine. Consequently, the present study showed an innovative approach for synthesizing silver nanoparticles, using olive leaves extract, which can be used in various electrochemical determinations.

Acknowledgements. This study is a part of Ezgi Adak's doctoral thesis and we are also grateful to Gazi University Scientific Research Projects Coordination Unit (Project number: FDK-2022-7739) for providing financial support.

ИЗВОД

ПОТЕНЦИЈАЛ ЕЛЕКТРОХЕМИЈСКИХ АНАЛИЗА ПЕСТИЦИДА ПОМОЋУ НАНОЧЕСТИЦА СРЕБРА СИНТЕТИСАНИХ ЗЕЛЕНИМ ПУТЕМ НА БАЗИ ОТПАДНОГ ЛИШЋА МАСЛИНЕ

EZGI ADAK[1,2], MERVE KESKIN[3] и HALIT ARSLAN[1]

[1]Department of Chemistry, Faculty of Science, Gazi University, 06500, Ankara, Turkiye, [2]Gazi University Graduate School of Natural and Applied Science, 06500, Ankara, Turkiye и [3]Vocational School of Health Services, Bilecik Seyh Edebali University, 11210, Bilecik, Turkiye

Пестициди су хемикалије које негативно утичу на људско здравље и животну средину. Несавесна употреба пестицида доводи до присуства њихових остатака у храни и пољопривредним производима, као и до загађења воде и земљишта. Брзо и једноставно одређивање остатака пестицида је важно за контролу животне средине. Из тог разлога, неопходно је развити алтернативне методе за одређивање остатака пестицида које би могле заменити традиционалне технике, као што је хроматографија. Електрохемијски сензори су аналитички уређаји нове генерације развијени за одређивање пестицида који омогућавају брзу и практичну анализу. Електроде од угљеничне пасте, које се користе у дизајну електрохемијских сензора, модификоване су коришћењем различитих материјала као што су наночестице сребра. Наночестице сребра, које се користе за модификацију, могу се синтетизовати хемијским методама, али су ове методе штетне по животну средину, јер се у поступку синтезе користе токсичне хемикалије. Из тог разлога, развијена је техника зелене синтезе као алтернатива хемијским техникама. У овој студији, отпадни листови маслине коришћени су у зеленој синтези сребрних наночестица као прекурсора електрона. Наночестице (OL-AgNP) су окарактерисане и припремљене су модификоване електроде од угљеничне пасте. Електроде су коришћене у одређивању тиохолина (производа хидролизе ацетил тиохолина ензимским реакцијама), H_2O_2 (производа многих реакција ензима оксиредуктазе) и широко коришћених пестицида ципродинила и мепанипирима. Резултати су показали да су модификоване електроде од угљеничне пасте биле осетљивије од електрода од угљеничне пасте за све аналите. Јасно је показано да се модификоване електроде од угљеничне пасте могу користити у одређивању пестицида.

(Примљено 18. новембра 2024, ревидирано 24. јануара, прихваћено 24. јула 2025)

REFERENCES

1. D. J. Ecobichon, *Toxicology* **160** (2001) 27 (https://doi.org/10.1016/S0300-483X(00)00452-2)
2. S. Sabzevari, J. Hofman, *Sci. Total Environ.* **812** (2022) 152344 (https://doi.org/10.1016/j.scitotenv.2021.152344)
3. L. Wang, Y. Liang, X. Jiang, *Bull. Environ. Contam. Toxicol.* **81** (2008) 377 (https://doi.org/10.1007/s00128-008-9498-2)
4. W. M. Abdou, E. S. M. Yakout, *Tetrahedron* **49** (1993) 6411 (https://doi.org/10.1016/S0040-4020(01)80155-1)
5. G. Liu, S. L. Riechers, M. C. Mellen, Y. Lin, *Electrochem. Commun.* **7** (2005) 1163 (https://doi.org/10.1016/j.elecom.2005.08.025)

6. D. Du, J. Ding, Y. Tao, X. Chen, *Sensors Actuators,. B* **134** (2008) 908 (https://doi.org/10.1016/j.snb.2008.06.040)
7. M. Trojanowicz, M. L. Hitchman, *TrAC Trends Anal. Chem.* **15** (1996) 38 (https://doi.org/10.1016/0165-9936(96)88036-8)
8. C. Li, A. Begum, J. Xue, *Water Environ. Res.* **92** (2020) 1770 (https://doi.org/10.1002/wer.1431)
9. M. A. Munir, J. A. Jamal, M. M. Said, S. Ibrahim, M. S. Ahmad, *Scientifica* **2023** (2023) 5444256 (https://doi.org/10.1155/2023/5444256)
10. F. Arduini, S. Cinti, V. Scognamiglio, D. Moscone, *Microchim. Acta* **183** (2016) 2063 (https://doi.org/10.1007/s00604-016-1858-8)
11. H. Arslan, D. Şenarslan, B. S. Çevrimli, H. Zengin, D. Uzun, F. Arslan, *Bulg. Chem. Commun*. **50** (2018) 16 (http://bcc.bas.bg/BCC_Volumes/Volume_50_Number_1_2018/BCC-50-1-2018.pdf)
12. O. C. Bodur, E. H. Özkan, Ö. Çolak, H. Arslan, N. Sarı, A. Dişli, F. Arslan, *J. Mol. Struct.* **1223** (2021) 129168 (https://doi.org/10.1016/j.molstruc.2020.129168)
13. F. Arslan, H. Koçak, O. C. Bodur, E. H. Özkan, B. Arslan, N. Sarı, *Maced. J. Chem. Chem. Eng.* **41** (2022) 229 (https://doi.org/10.20450/mjcce.2022.2585)
14. M. A. Akbıyık, O. C. Bodur, M. Keskin, M. Kara, S. Dinç, H. Arslan, M. Ozmen, F. Arslan, *J. Electrochem. Soc.* **170** (2023) 037517 (https://doi.org/10.1149/1945-7111/acc364)
15. M. A. Munir, F. Rahmawati, J. A. Jamal, E. Rahmawati, F. Z. Fajriyaningsih, F. R. Putri, A. Gunawan, *Green Chem. Lett. Rev.* **17** (2024) (https://doi.org/10.1080/17518253.2024.2355235)
16. O. C. Bodur, M. Keskin, B. A. Avan, H. Arslan, *J. Serb. Chem. Soc.* **88** (2023) 521 (https://doi.org/10.2298/JSC221122013B)
17. J. F. Liu, S. J. Yu, Y. G. Yin, J. B. Chao, *TrAC Trends Anal. Chem.* **33** (2012) 95 (https://doi.org/10.1016/j.trac.2011.10.010)
18. S. Ü. Pektaş, M. Keskin, O. C. Bodur, F. Arslan, *J. Food Compos. Anal.* **129** (2024) 106133 (https://doi.org/10.1016/j.jfca.2024.106133)
19. R. J. Pinto, M. C. Neves, C. P. Neto, T. Trindade, in *Nanocomposites – New Trends and Developments*, F. Ebrahimi, Ed., InTech, Rijeka, 2012 (https://doi.org/10.5772/50553)
20. P. Nartop, *Pamukkale Univ. Muh. Bilim. Derg* **23** (2017) 759 (https://doi.org/10.5505/pajes.2016.04809)
21. P. Logeswari, S. Silambarasan, J. Abraham, *Sci. Iran.* **20** (2013) 1049 (https://core.ac.uk/reader/81124370)
22. M. Keskin, G. Kaya, S. Bayram, A. Kurek-Górecka, P. Olczyk, *Molecules* **28** (2023) 2762 (https://doi.org/10.3390/molecules28062762)
23. H. Nguyen, M. Jamali Moghadam, H. Moayedi, *J. Mater. Cycles Waste Manage.* **21** (2019) 1039 (https://doi.org/10.1007/s10163-019-00872-y)
24. R. Briante, M. Patumi, S. Terenziani, E. Bismuto, F. Febbraio, R. Nucci, *J. Agric. Food Chem.* **50** (2002) 4934 (https://doi.org/10.1021/jf025540p)
25. Z. Ahmad, A. Rauf, H. Zhang, M. Ibrahim, N. Muhammad, Y. S. Al-Awthan, O. S. Bahattab, *Green Process Synth.* **13** (2024) 20240001 (https://doi.org/10.1515/gps-2024-0001)
26. M. Can, M. Keskin, *J. Serb. Chem. Soc.* **90** (2025) 123 (https://doi.org/10.2298/jsc231110023C)
27. I. Hussain, N. B. Singh, A. Singh, H. Singh, S. C. Singh. *Biotech. Lett.* **38** (2016) 545 (https://doi.org/10.1007/s10529-015-2026-7)

28. S. Jadoun, R. Arif, N. K. Jangid, R. K. Meena, *Environ. Chem. Lett.* **19** (2021) 355 (https://doi.org/10.1007/s10311-020-01074-x)
29. A. I. Osman, Y. Zhang, M. Farghali, A. K. Rashwan, A. S. Eltaweil, E. M. Abd El--Monaem, I. M. A. Mohamed, M. M. Badr, I. Ihara, D. W. Rooney, P. S. Yap, *Environ. Chem. Lett*. **22** (2024) 841 (https://doi.org/10.1007/s10311-023-01682-3)
30. A. A. Yaqoob, K. Umar, M. N. M. Ibrahim, *Appl. Nanosci.* **10** (2020) 1369 (https://doi.org/10.1007/s13204-020-01318-w)
31. V. Armendariz, I. Herrera, J. R. Peralta-Videa, M. Jose-Yacaman, H. Troiani, P. Santiago, J. L. Gardea-Torresdey, *J. Nanoparticle Res.* **6** (2004) 377 (https://doi.org/10.1007/s11051-004-0741-4)
32. K. Vijayaraghavan, T. Ashokkumar, *J. Environ. Chem. Eng.* **5** (2017) 4866 (https://doi.org/10.1016/j.jece.2017.09.026)
33. S. Ahmad, S. Munir, N. Zeb, A. Ullah, B. Khan, J. Ali, M. Bilal, M. Omer, M. Alamzeb, S.M. Salman, S. Ali, *Int. J. Nanomedicine* **14** (2019) 5087 (https://doi.org/10.2147/IJN.S200254)
34. M. Özdemir, H. Arslan, *Artif. Cells Nanomed. Biotechnol.* **42** (2014) 27 (https://doi.org/10.3109/21691401.2013.768628)
35. P. K. Kalambate, C. R. Rawool, S. P. Karna, A. K. Srivastava, *Mater. Sci. Eng., C* **69** (2016) 453 (https://doi.org/10.1016/j.msec.2016.06.077)
36. R. K. Mishra, A. Sabu, S. K. Tiwari, *J. Saudi Chem. Soc.* **22** (2018) 949 (https://doi.org/10.1016/j.jscs.2018.02.005)
37. Panigrahi, S. Kundu, S. Ghosh, S. Nath, T. Pal, *J. Nanopart. Res.* **6** (2004) 411 (https://doi.org/10.1007/s11051-004-6575-2)
38. M. K. Alqadi, O. A. Abo Noqtah, F. Y. Alzoubi, J. Alzouby, K. Aljarrah, *Mater. Sci. Poland* **32** (2014) 107 (https://doi.org/10.2478/s13536-013-0166-9)
39. H. M. Kredy, *J. Pharm. Sci. Res.* **10** (2018) 2022
40. A. D. Dwivedi, K. Gopal, *Colloids Surfaces, A* **369** (2010) 27 (https://doi.org/10.1016/j.colsurfa.2010.07.020)
41. L. B. Anigol, J. S. Charantimath, P. M. Gurubasavaraj, *Org. Med. Chem. Int. J.* **3** (2010) 1 (https://doi.org/10.19080/OMCIJ.2017.03.555622)
42. J. Han, Y.Chen, X. Nie, *J. Clust. Sci.* **32** (2021) 899 (https://doi.org/10.1007/s10876-020-01852-1)
43. N. Manosalva, G. Tortella, M. C. Diez, H. Schalchli, A.B. Seabra, N. Durán, O. Rubilar, *World J. Microbio. Biotech.* **35** (2019) 88 (https://doi.org/10.1007/s11274-019-2664-3)
44. Y. Z. N. Htwea, W. S. Chow, Y. Sudab, M. Mariatti, *Materials Today: Proc.* **17** (2019) 568 (https://doi.org/10.1016/j.matpr.2019.06.336)
45. S. Renganathan, G. Geoprincy, B. N. Vidhya Srri, U. Poonguzhali, N. Nagendra Gandhi, *Asian J. Pharm. Clin. Res.* **6** (2013) 8
46. M. Vanaja, G. Annadurai, *App. Nanosci.* **3** (2013) 217 (https://doi.org/10.1007/s13204-012-0121-9)
47. P. Kumar, S. Senthamilselvi, A. Lakshmipraba, K. Premkumar, R. Muthukumaran, *Dig. J. Nanomat. Biostruc.* **7** (2012) 511 (https://chalcogen.ro/511_Kumar.pdf)
48. B. Sadeghi, F. Gholamhoseinpoor, *Spectrochim. Acta, A* **134** (2015) 310 (https://doi.org/10.1016/j.saa.2014.06.046)
49. S. Maddinedi, B. K. Mandal, S. K. Maddili, *J. Photochem. Photobiol., B* **167** (2017) 236 (https://doi.org/10.1016/j.jphotobiol.2017.01.003)
50. V. Singh, A. Shrivastava, N. Wahi, *African J. Biotechnol.* **14** (2015) 2554 (https://doi.org/10.5897/AJB2015.14692)

51. S. M. Pourmortazavi, M. Taghdiri, V. Makari, M. Rahimi-Nasrabadi, *Spectrochim. Acta, A* **136** (2015) 1249 (https://doi.org/10.1016/j.saa.2014.10.010)
52. T. C. Prathna, N. Chandrasekaran, A. M. Raichur, A. Mukherjee, *Colloids Surfacs, B* **82** (2011) 152 (https://doi.org/10.1016/j.colsurfb.2010.08.036)
53. A. Singh, B. Gaud, S. Jaybhaye, *Mater. Sci. Energy Technol.* **3** (2020) 232 (https://doi.org/10.1016/j.mset.2019.08.004)
54. M. M. Khalil, E. H. Ismail, K. Z. El-Baghdady, D. Mohamed, *Arab. J. Chem.* **7** (2014) 1131 (https://doi.org/10.1016/j.arabjc.2013.04.007)
55. J. S. Moodley, S. B. N. Krishna, K. Pillay, F. Sershen, P. Govender, *Adv. Nat. Sci.: Nanosci. Nanotechnol.* **9** (2018) 015011 (https://doi.org/10.1088/2043-6254/aaabb2)
56. P. Cabras, A. Angioni, V. L. Garau, E. V. Minelli, *J. AOAC Int.* **80** (1997) 867 (https://doi.org/10.1093/jaoac/80.4.867)
57. L. Vaquero-Fernandez, A. Saenz-Hernaez, J. Sanz-Asensio, P. Fernandez-Zurbano, M. Sainz-Ramırez, B. Pons-Jubera, M. Lopez-Alonso, S. Epifanio-Fernandez, M. Martınez--Soria, *J. Sci. Food Agric.* **8** (2008) 1943 (https://doi.org/10.1002/jsfa.3301)
58. X. Liang, X. Liu, F. Dong, J. Xu, D. Qin, Y. Li, Y. Zheng, *Food Add. Contam., A* **30** (2013) 713 (https://doi.org/10.1080/19440049.2013.768777)
59. E. A. Ayhan, R. İnam, *J. Food Meas. Charact.* **14** (2020) 1333 (https://doi.org/10.1007/s11694-020-00381-9)
60. L. Araujo, M. E. Troconis, D. Cubillán, J. Mercado, N. Villa, A, Prieto, *Environ. Monit. Assess* **185** (2013) 10225 (https://doi.org/10.1007/s10661-013-3327-8)
61. X. Chen, Z. Li, Z. Cao, X. Cao, M. Chen, *Chinese J. Chromat.* **31** (2013) 954 (https://doi.org/10.3724/sp.j.1123.2013.04028).